



# Lawrence Berkeley Laboratory

UNIVERSITY OF CALIFORNIA

## Materials & Molecular Research Division

SINTERING BEHAVIOR OF MULLITE-CONTAINING MATERIALS

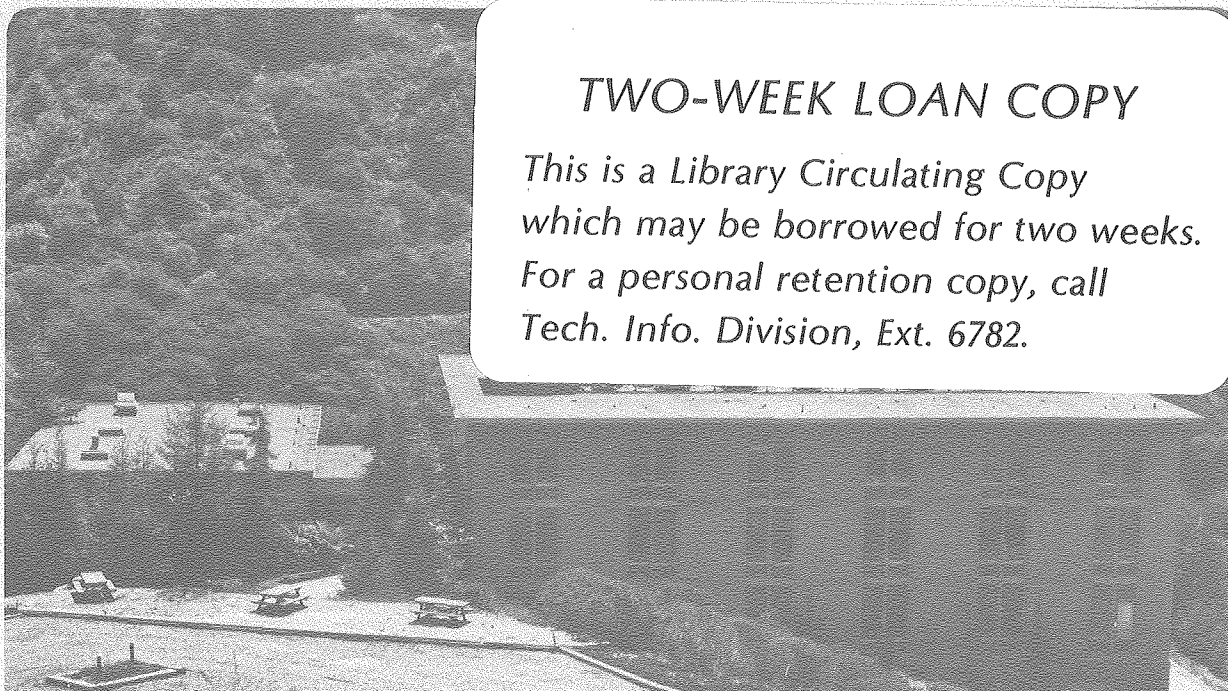
Michael David Sacks  
(Ph.D. thesis)

December 1979

RECEIVED  
LAWRENCE  
BERKELEY LABORATORY

MAR 28 1980

LIBRARY AND  
DOCUMENTS SECTION



### TWO-WEEK LOAN COPY

*This is a Library Circulating Copy  
which may be borrowed for two weeks.  
For a personal retention copy, call  
Tech. Info. Division, Ext. 6782.*

LBL 10372 C.2

## **DISCLAIMER**

This document was prepared as an account of work sponsored by the United States Government. While this document is believed to contain correct information, neither the United States Government nor any agency thereof, nor the Regents of the University of California, nor any of their employees, makes any warranty, express or implied, or assumes any legal responsibility for the accuracy, completeness, or usefulness of any information, apparatus, product, or process disclosed, or represents that its use would not infringe privately owned rights. Reference herein to any specific commercial product, process, or service by its trade name, trademark, manufacturer, or otherwise, does not necessarily constitute or imply its endorsement, recommendation, or favoring by the United States Government or any agency thereof, or the Regents of the University of California. The views and opinions of authors expressed herein do not necessarily state or reflect those of the United States Government or any agency thereof or the Regents of the University of California.

## SINTERING BEHAVIOR OF MULLITE-CONTAINING MATERIALS

### Table of Contents

ABSTRACT .....	v
I. INTRODUCTION .....	1
A. Sintering .....	1
1. General .....	1
2. Driving Force .....	1
3. Mass Transport Mechanisms .....	2
4. Stages of Sintering .....	3
B. Mullite .....	5
C. Research Objective .....	6
II. EXPERIMENTAL .....	7
A. Processing .....	7
1. "Powder" Process .....	7
2. "Gel" Process .....	12
B. Sintering Conditions .....	13
C. Properties .....	13
D. Microscopy .....	14
III. RESULTS AND DISCUSSION .....	16
A. "Powder" Process Materials .....	16
1. Chemical Composition .....	16
2. Densification Kinetics .....	20
(a) 60 IP Composition .....	20
(b) 73 IP, 73 PP, 75 IP Compositions .....	23

3. Microstructural Analysis of 73 IP Samples .....	24
4. Grain Growth in 73 IP .....	39
(a) Introduction .....	39
(b) Analysis of 73 IP Data .....	41
5. Analysis in Terms of Intermediate Stage Sintering Models	46
6. Effective Grain Size Concept .....	56
B. "Gel" Process Material .....	59
1. The Green State .....	59
2. "Final" Density .....	62
3. Densification Kinetics .....	62
C. Effects of Sintering Atmosphere .....	71
1. Introduction .....	71
2. Vacuum Sintering .....	72
3. Limiting Density and De-densification .....	75
(a) 60 wt% $Al_2O_3$ Composition .....	75
(b) 71.8 and 80 wt% $Al_2O_3$ Compositions .....	84
IV. SUMMARY AND CONCLUSIONS .....	91
ACKNOWLEDGMENT .....	94
REFERENCES .....	95
FIGURE CAPTIONS .....	100
FIGURES .....	112



## I. INTRODUCTION

### A. Sintering

#### 1. General

Sintering is an important step in the fabrication of ceramics, metals, and cermets. During the sintering process, an assembly of particles (i.e. the powder compact) is heated to a temperature at which mass transport mechanisms are operative. The initially porous compact is observed to shrink as void volume is eliminated. During solid state sintering, the sintering temperature is below the melting point of any of the constituent phases present.

From a scientific viewpoint, the interest in sintering involves determining the driving force, the mass transport mechanisms, and the kinetics of the process. An engineer involved with sintering technology is more concerned with obtaining a well-controlled microstructure (with its associated desired properties) by sintering at low temperatures for short times. In both cases, it is important to realize that processing variables will affect the microstructural evolution and the sintering kinetics. Powder characteristics, powder preparation procedures, forming processes, and pre-sintering heat treatments will all have an important influence on sintering behavior.

#### 2. Driving Force

During sintering, a decrease in free energy (i.e. the driving force) occurs due to the decreasing total solid-vapor interfacial area, and

energy, (that results when grain boundaries form between particles and when the pore phase is eliminated) relative to the increasing total solid-solid interfacial area, and energy, (that results when grain boundaries form)<sup>1</sup>. In addition to this driving force for densification, a driving force also exists for an increase in average particle (grain) size since this results in a reduction of the total solid-solid interfacial (i.e. grain boundary) area (and energy). From a thermodynamic viewpoint, a pore-free single crystal would be the most stable configuration.<sup>2</sup>

### 3. Mass Transport Mechanisms

In order for particle joining (grain boundary formation), neck growth (as in Figs. 31 and 32), and elimination of pores to occur, there must be mass transport. Six different mechanisms have generally been considered to contribute to the observed changes in various systems: viscous flow, plastic flow (dislocation mechanisms), evaporation-condensation, surface diffusion, grain boundary diffusion, and volume diffusion.<sup>2-10</sup>

Surface diffusion and evaporation-condensation mechanisms may lead to particle joining and neck growth and may affect the kinetics of densification and grain growth, but they cannot cause the densification (macroscopic shrinkage) observed during sintering because no mutual approach of particle centers can occur.

Viscous flow has been established as an important mechanism in the densification of systems containing significant amounts of liquid or glassy phase.

The importance of plastic deformation as a mass transport mechanism in sintering has been subject to controversy for nearly thirty years. During hot pressing (in which heat and pressure are applied to a powder), this mechanism is realistic in certain materials (i.e. especially in metals). Even under high pressures at elevated temperatures, dislocation motion is important in only some ceramic materials. In mullite, for example, samples tested in creep at 1400°C obey the Nabarro-Herring diffusional mechanism and do not have mobile dislocations.<sup>11</sup> In pressureless sintering, particularly in ceramics, the primary importance of diffusional processes (volume and grain boundary) of densification seems well-established.<sup>2,12</sup>

In order to realize pore elimination by a diffusional mechanism, vacancies must be transported from the pore surfaces to grain boundary sinks (and mass moves from grain boundaries to pore surfaces). The transport path may be through the lattice or along the grain boundaries. In both cases, vacancies at the grain boundaries are annihilated as grain centers approach each other, resulting in macroscopic shrinkage.

#### 4. Stages of Sintering

The sintering process is usually divided into stages based on geometrical changes that occur during the microstructural evolution from an assembly of individual particles to a dense, polycrystalline structure.<sup>1,2,12</sup> During the initial stage, grain boundaries form at contacts between particles. The pore phase exists as a continuous open channel. In an ideal system, with uniform size spheres of regular packing, this stage continues

until necks between particles impinge upon each other forming closed pores. In real systems, with heterogeneous packing and nonuniform particle sizes, the merging of necks may begin after only small amounts of shrinkage. During this intermediate stage, most of the pores are still continuous channels lying along grain boundaries, but the stage is distinguished from the initial stage by the occurrence of grain boundary motion and, thus, grain growth. Most of the densification occurs during the intermediate stage. As sintering proceeds, the continuous pore channels are pinched off into isolated closed pores. During the final stage of sintering, these closed pores shrink. The pores may remain on the grain boundaries or, alternatively, they may become entrapped within the grain interiors if the driving force for boundary migration is sufficiently large.

Many overlapping processes may occur during densification and grain growth which complicate the analysis. For example, mobile pores may migrate along with grain boundaries, depending on the relative rates of grain growth and densification. This can cause an increase in average pore size by a pore coalescence process as small grains disappear.<sup>13</sup> Non-densifying mechanisms of mass transport (surface diffusion and evaporation-condensation) may alter the neck geometry and, therefore, affect the rates of grain growth and densification. Rearrangement of particles in the initial stage of sintering may alter the densification rate by the formation and elimination of contacts among particles.<sup>14</sup> Several reviews are available which discuss the complex details of the sintering process.<sup>2,12,15</sup>

## B. Mullite

The  $\text{Al}_2\text{O}_3$  -  $\text{SiO}_2$  system is probably the most important in ceramic technology due to the abundance and widespread use of alumina, silica, and aluminum silicate minerals. Mullite, the only intermediate compound stable at high temperatures and normal pressures, is a commonly occurring phase in refractories, whitewares, and porcelains. Recent studies, with single crystal and high purity, high density polycrystalline mullite, have shown that only a fraction of mullite's potential capabilities, in regards to mechanical strength, creep resistance, and acid corrosion resistance, are achieved in normal processing.<sup>11,16-20</sup> Potential applications of improved mullite-containing ceramics are refractory materials for coal gasifier vessels,<sup>20,21</sup> radome materials,<sup>22</sup> and high temperature structural materials.

Many methods have been used in forming mullite, from high temperature decomposition of naturally occurring aluminum silicates (such as clay minerals) to chemical preparation techniques involving high purity raw materials. Several reviews of these methods are available.<sup>18,23,24</sup> Limited information is available, however, on the sintering behavior of mullite-containing materials. Although several studies have been made on the kinetics of hot pressing of mullite,<sup>16,25</sup> no quantitative studies of sintering kinetics (densification and grain growth) have been undertaken. Very little information is available on the correlation of processing variables with microstructural development and sintering behavior.

### C. Research Objective

Most attempts to formulate equations describing the kinetics of densification are based on ideal geometrical models devised for each of the stages discussed in section I.A.4. These simple models have contributed to our understanding of the sintering process, but have found little practical application. Because of the enormously complex geometrical changes that occur during the sintering of a real system, a precise prediction of densification kinetics seems unlikely at the present time. For this reason, detailed phenomenological studies of densification kinetics and the kinetics of microstructural changes (such as in grain size, pore size, etc.) are important in improving our understanding of the sintering process.

This study investigates the effects of several processing variables on the microstructural evolution and the sintering kinetics of mullite-containing materials. Qualitative and quantitative information is obtained on the effects of chemical composition, grinding of calcined powders (to increase the powder surface area), particle packing (i.e. the presence of inhomogeneities such as agglomerates/aggregates), and sintering atmosphere.

## II. EXPERIMENTAL

### A. Processing

Two processing schemes (Figs. 1 and 2) were used to form the aluminum silicate powders for sintering studies. In each procedure, the basic steps were (1) mixing of the two oxides, (2) calcining to form mullite, and (3) grinding to achieve particle size reduction. Details for the processes are given below.

#### 1. "Powder" Process

Starting materials were A-14<sup>\*</sup> aluminum oxide ( $\alpha$ -Al<sub>2</sub>O<sub>3</sub>) and silica flour<sup>†</sup> ( $\alpha$ -quartz, SiO<sub>2</sub>) which had purities of ~99.8% and ~99.6%, respectively. Semi-quantitative spectrographic analyses<sup>\*\*</sup> (Table 1) show that the major impurity in the A-14 was SiO<sub>2</sub> and the major impurity in the silica flour was Al<sub>2</sub>O<sub>3</sub>.

Compositions ranged from 60 wt% Al<sub>2</sub>O<sub>3</sub>/40 wt% SiO<sub>2</sub> to 90 wt% Al<sub>2</sub>O<sub>3</sub>/10 wt% SiO<sub>2</sub>. Mixing and de-agglomeration were achieved by wet (isopropyl alcohol) milling in (1) a porcelain ball mill (mixing condition "I") or (2) a teflon-lined vibratory mill<sup>††</sup> (mixing condition "P"). After stir-drying and screening (-120 mesh), mixtures were calcined at 1700°C for 8 h to form mullite, mullite and glass, or mullite and Al<sub>2</sub>O<sub>3</sub> (depending on the overall Al<sub>2</sub>O<sub>3</sub>/SiO<sub>2</sub> ratio — see Al<sub>2</sub>O<sub>3</sub>-SiO<sub>2</sub> phase diagram in Fig. 3.)

---

\*Alcoa Aluminum Co. of America, Bauxite, Ark.

†Ottawa Silica Co., Ottawa, Ill.

\*\*American Spectrographic Laboratories, Inc., S.F., Ca.

††Sweco, Inc., Los Angeles, Ca.

Table 1. Spectrographic Analysis of Raw Materials

	Alcoa A-14	Atomergic GZ5	Ludox AS	Ottawa Flour
Al	Principal Constituent		.05%	.2%
Si	.035%	.01%	Principal Constituent	
Na	<.02	.03	.4	<.02
Ca	.02	<.001	.003	.02
Mg	.001	<.001	.005	.035
K	<.5*	<.5*	<.5*	<.5*
Ti	.005	.002	.008	.025
Fe	.03	.005	.025	.05
Ga	.01	.001	-	-
Cu	<.001	<.001	.001	<.001
Mn	<.001	-	<.001	<.001
Zr	.01	-	.008	.003
Cr	<.001	-	-	.001
Ba	-	-	-	.004
Zn	-	-	-	-
B	.01	-	-	.01
Pb	-	-	<.005	<.005
Ni	-	-	-	<.001
Sr	-	-	-	.005

The above are reported as oxides of the elements indicated.

\*.5% was detection limit.



Experiments with a 73 wt%  $\text{Al}_2\text{O}_3$  showed that calcination time and temperature did not affect subsequent sintering as long as mullite reaction was complete. Reaction was considered complete when no  $\alpha\text{-Al}_2\text{O}_3$  was detected in the x-ray diffraction\* pattern (limit of detection ~1%). Within the precision of the indicated measurement, neither the particle size after comminution nor the green density after compaction was affected by the calcination time-temperature schedule. These results are shown in Table 2. Also included are data on a 73 wt%  $\text{Al}_2\text{O}_3$ /27 wt%  $\text{SiO}_2$  mixture which was not calcined prior to sintering.

After calcination, mixtures were subjected to coarse crushing in a mechanically operated mortar and pestle\*\* and wet (isopropyl alcohol) vibratory milling (grinding condition "P"). Unless noted otherwise, grinding time was 5 hrs. After stir-drying and screening (-120 mesh), powders were calcined at 800°C for 1 hr to volatilize any organic contamination. Powders were labeled according to composition and mixing/grinding conditions, e.g. 73 IP refers to a 73 wt%  $\text{Al}_2\text{O}_3$ /27 wt%  $\text{SiO}_2$  composition mixed by condition "I" and ground by condition "P". Semi-quantitative spectrographic analysis (Table 3) shows that processing introduces no significant additional cationic impurities and that, within experimental precision, the total cationic impurity is the same in all compositions (~.2 - .3%).

---

\*Norelco Diffractometer, Philips Electronic Instruments, NY.

\*\*Pulverisette, Alfred Fritsch Co., Germany.

Table 2. Properties as a Function of Calcination Schedule.

Calcination Temp(°C)	Calcination Time(hrs)	Compact Green Density(% $\rho_{th}$ )	Particle Size (microns)	Bulk Density(g/cm <sup>3</sup> after Sintering at 1700°C-12 h)	Phases Detected by X-ray Diffraction after Calcination
1600	24	58.2	2.1	2.78	Mullite-major $\alpha$ -Al <sub>2</sub> O <sub>3</sub> -minor
1600	48	58.5	2.0	2.85	Mullite-major $\alpha$ -Al <sub>2</sub> O <sub>3</sub> -trace
1650	8	58.5	2.1	2.85	Mullite-major $\alpha$ -Al <sub>2</sub> O <sub>3</sub> -trace
1650	16	58.1	2.1	2.87	Mullite-major $\alpha$ -Al <sub>2</sub> O <sub>3</sub> -trace
1650	24	58.2	2.2	2.89	Mullite
1700	2	58.3	2.0	2.82	Mullite-major $\alpha$ -Al <sub>2</sub> O <sub>3</sub> -minor
1700	4	58.0	1.95	2.87	Mullite-Major $\alpha$ -Al <sub>2</sub> O <sub>3</sub> -trace
1700	5.5	57.8	2.0	2.88	Mullite
1700	8	58.0	2.15	2.88	Mullite
1700	16	58.4	2.0	2.88	Mullite
No Calcination		54.1		2.22	Mullite <sup>†</sup>

†Phase after sintering.

Table 3. Spectrographic Analysis of Processed Materials.

	<u>60IP</u>	<u>73IP</u>	<u>73PP</u>	<u>75IP</u>	<u>80IP</u>	<u>73 "GEL"</u>
Al	Principal Constituents in Each Sample					
Si						
Mg	.02 %	.05 %	.015 %	.015 %	.015 %	.02 %
Fe	.06	.08	.05	.07	.05	.01
Na	<.02	<.02	<.02	<.02	<.02	.03
Ca	.04	.07	.04	.05	.04	.02
K	-	less than .5%* in each				-
B	.03	.025	.01	.02	.01	-
Pb	-	-	-	-	-	-
Mn	<.001	<.001	<.001	<.001	<.001	-
Ga	.005	.007	.006	.006	.006	<.001
Sn	-	-	-	-	-	-
Cu	.001	<.001	<.001	<.001	<.001	.005
Ti	.03	.03	.025	.025	.02	.006
Zn	-	-	-	-	-	-
Zr	.005	.02	.007	.007	.008	.005
Sr	.01	.003	.005	.003	<.003	<.003
Cr	<.001	.001	<.001	<.001	-	<.001
Ba	.003	.01	.002	.002	.002	.002
Pt	.015	-	.04	.015	.02	-

The above are reported as oxides of the elements indicated.

\*.5% was detection limit.

X-ray diffraction and microscopy have shown the most significant contamination in processing to be  $\alpha\text{-Al}_2\text{O}_3$  introduced by impact collisions during milling (high density alumina grinding media\* were used); thus the "PP" compositions have the largest  $\text{Al}_2\text{O}_3$  contamination.

Powder compacts were formed under uniaxial pressure ( $\sim 17 \text{ MN/m}^2$ ) followed by isostatically pressing at ( $\sim 170 \text{ MN/m}^2$ ).

## 2. "Gel" Process

The gel process, essentially the same as Gbate's process,<sup>25</sup> was used to reduce the time and/or temperature required to complete mullite formation. This allowed for reduced comminution (i.e. coarse crushing was unnecessary). Aqueous suspensions of alumina<sup>†</sup> and silica<sup>\*\*</sup> (spectrographic analyses in Table 1) were intimately mixed due to (1) rigorous mechanical agitation and (2) attraction of the oppositely charge alumina and silica particles. To prevent segregation, mixtures are gelled by pH adjustments or by evaporation of water by heating. Complete reaction (based on x-ray diffraction) occurred upon calcining the gel powders at  $1450^\circ\text{C}$  for 24 h. Spectrographic analysis (Table 3) for a 73 wt%  $\text{Al}_2\text{O}_3$  composition indicates a total impurity content of  $\sim .1\%$ . The low sodium content (.03%) indicates that the major impurity,  $\text{Na}_2\text{O}$  in the Ludox AS, volatilized during calcination.

---

\* Norton Co., Akron, OH.  
Coors Porcelain Co., Golden, CO.

<sup>†</sup> Atomergic GZ5, Atomergic Chemicals Corp., Plainview, NY.  
Mellor CR 125, Adolph Mellor Co., Providence, RI.  
(Manufacturer's specifications on both:  $\gamma\text{-Al}_2\text{O}_3$ , "agglomerate free,"  $\sim 99.98\%$  purity, surface area  $\sim 100 \text{ m}^2/\text{g}$ .)

\*\* Ludox AS Colloidal Silica, E. I. duPont de Nemours and Co., Inc., Wilmington, DE. (Manufacturer's specifications:  $\sim 99.5\%$  purity, surface area  $\sim 130 \text{ m}^2/\text{g}$ .)

Powder compacts were die formed under uniaxial pressure ranging from 140-310 MN/m<sup>2</sup>.

#### B. Sintering Conditions

Compacts were sintered in two different types of furnaces: (1) two electrically heated quench-type furnaces with MoSi<sub>2</sub> elements and (2) an electrically heated Brew furnace<sup>\*</sup> with tantalum elements. The lower temperature MoSi<sub>2</sub> element (1700°C Kanthal<sup>†</sup> Super) furnace is shown in Fig. 4. The higher temperature MoSi<sub>2</sub> element (1800°C Kanthal Super 33) furnace was similarly constructed except Pt 6%Rh - Pt 30%Rh thermocouples were used. The Brew furnace was controlled through a W 5%Re - W 26%Re thermocouple. For both types of furnaces, temperature was monitored and controlled by a Speedomax-H Recorder Series 60 Controller.<sup>\*\*</sup> A Trendtrack Programmable Controller<sup>††</sup> was also used with the Brew furnace. The atmosphere was air for the quench-type furnaces. Vacuum of ~10<sup>-6</sup> torr or ~1 atm argon were the atmospheres used for the Brew furnace.

#### C. Properties

"Average" particle size and surface area of powders were determined by an air permeability method<sup>††</sup> and by a multipoint BET adsorption method<sup>Δ</sup>, respectively.

Bulk density and open porosity were determined by the displacement method utilizing distilled water. % theoretical density (%ρ<sub>th</sub>) was estimated by using the apparent true density as determined from green compacts. In green compacts, the total porosity ≈ open porosity; the

---

<sup>\*</sup>Richard D. Brew & Co., Concord, NH.

<sup>†</sup>Kanthal Corp., Bethel, CT.

<sup>\*\*</sup>Leeds and Northrup Co., Philadelphia, PA.

<sup>††</sup>Fisher Subsize Sizer, Fisher Scientific Co., Pittsburg, PA.

<sup>Δ</sup>Quantasorb, Quantachrome Corp., Greenvale, NY.

latter quantity is measurable by the displacement method.

High temperature (1200°C and 1400°C) stress-strain testing under compression has been described in detail elsewhere.<sup>18</sup> The specimen dimensions were approximately .1" x .1" x .3" and the strain rate was  $\sim 1.0 \times 10^{-5}$ /sec.

#### D. Microscopy

Ceramographic polishing procedures consisted of grinding on (1) 220, 30, 15, and 6 micron metal bond diamond wheels or (2) glass plates with slurries of 120, 240, 600, 800, 1000 grit SiC powders and distilled water. This was followed by vibratory polishing<sup>\*</sup> using slurries of 6, 1 and 1/4 micron diamond paste<sup>†</sup> and oil.

Samples were observed by scanning electron microscopy (SEM),<sup>\*\*</sup> transmission electron microscopy,<sup>††</sup> and in reflected light by interference-contrast microscopy.<sup>Δ</sup> A light etch with diluted hydrofluoric acid solution and/or a thin ( $\sim 200\text{\AA}$ ) gold coating was sometimes needed to bring out features viewed in the optical microscope. Polished samples for viewing by SEM were thermally etched (1400-1550°C, depending on initial sintering conditions) in order to make the grain boundaries visible. Etching was followed by coating with a thin gold layer. An

---

\*FMC Corp., Syntron Div., Homer City, PA.

†Metadi Diamond Compound, Buehler Ltd., Evanston, IL.

\*\*AMR 1000, Advanced Metals Research Co., Bedford, MA.

††Philips 301, Philips Co., Amsterdam.

ΔNomarsky Differential Interference-Contrast Microscopy, Zeiss Ultraphot II, Metallograph, Carl Zeiss Co., West Germany.

EDAX\* (Energy Dispersive Analysis by X-rays) attachment was available for semi-quantitative compositional determination of phases.

In order to determine average grain size, photographs were placed underneath a transparent plastic sheet, on which parallel lines had been drawn. The grain size was obtained by counting the number of grain boundaries intercepting straight lines of known length. Corrections for the presence of porosity were made according to the method of Wurst and Nelson.<sup>26</sup> Magnification and statistical (multiplication by 1.56) corrections were also made.

Average pore intercept length was also determined. Segments of lines, formed by the interception of pore edges with the parallel lines, were measured individually. The value was corrected for magnification. However, no attempt was made to obtain an average pore size by applying a statistical correction because the pores were very irregular in shape and consisted of a broad distribution of sizes. Other measurements made on the polished sections were (1) average distance between first neighbors of pore intercept segments,  $\lambda_1$ , (2) number of point interceptions of pore edges per unit length,  $P_L$ , and (3) number of areal interceptions of pores per unit area,  $N_A$ .<sup>27</sup>

Average grain size and  $P_L$  measurements were made on the green compact. Despite impregnation with sulfur, the green compact was mechanically weak which caused difficulty in obtaining a polished section. Therefore, measurements on green compacts were the least accurate.

---

\*North American Philips Corp., Curryview, IL.

### III. RESULTS AND DISCUSSION

#### A. "Powder" Process Materials

##### 1. Chemical Composition

In order to get a basic understanding of the system, a broad composition range, 60 to 90 wt%  $\text{Al}_2\text{O}_3$ , was used in the initial experiments. The green density and average particle size were held approximately constant over the composition range ( $56\text{--}58\% \rho_{th}$  and  $2.1 \pm 0.2$  microns, respectively). Table 4 lists the bulk density, open porosity, and percentage of theoretical density values for these compositions sintered at  $1700^\circ\text{C}$  in air for 1, 4, and 12 hrs. Three groupings can be delineated:

- (1) 60 and 65 wt%  $\text{Al}_2\text{O}_3$  compositions, in the mullite and liquid phase region at  $1700^\circ\text{C}$  of the equilibrium  $\text{Al}_2\text{O}_3\text{--SiO}_2$  phase diagram (Fig. 3), sinter quickly (1 and 4 hr, respectively) to maximum density due to the presence of large amounts of liquid at the sintering temperature.
- (2) 71.8, 73 and 74 wt%  $\text{Al}_2\text{O}_3$  compositions (in the mullite solid solution range of the equilibrium phase diagram) sinter at a slower rate but eventually achieve a high density (12 hr fire).
- (3) Compositions with 75 wt%  $\text{Al}_2\text{O}_3$  and above sinter even more slowly. A sharp decrease in densification rate is observed between 74 and 75 wt%  $\text{Al}_2\text{O}_3$  compositions. The boundary between the mullite solid solution and mullite/alumina phase regions is at  $\sim 74$  wt%  $\text{Al}_2\text{O}_3$  at  $1700^\circ\text{C}$ .

Figure 5 shows microstructures for a range of compositions. 60 IP clearly shows the presence of a glass phase. At higher magnification



Table 4. Properties of Compositions Fired at 1700°C.

Composition, % Al <sub>2</sub> O <sub>3</sub>	Firing in Air, 1 hr.			Firing in Air, 4 hrs.			Firing in Air, 12 hrs		
	Bulk Density (g/cm <sup>3</sup> )	% Open Porosity	% Theor. Density	Bulk Density (g/cm <sup>3</sup> )	% Open Porosity	% Theor. Density	Bulk Density (g/cm <sup>3</sup> )	% Open Porosity	% Theor. Density
60 IP	2.91	0	97	2.90	0	96	2.89	0	96
65 IP	2.95	0	95	2.99	0	97	2.99	0	97
71.8 IP	2.51	20.6	79	2.78	8.7	87	2.97	0	93
73 IP	2.54	19.7	80	2.82	6.7	88	3.06	0	96
74 IP	2.56	16.6	80	2.72	11.1	85	3.00	0.5	94
75 IP	2.25	28.6	70	2.40	22.6	75	2.67	14.5	83
80 IP	2.43	26.7	72	2.64	17.6	78	2.83	11.9	84
85 IP	2.52	27.4	72	2.73	18.1	78	2.97	11.1	84
90 IP	2.64	26.3	72	2.82	21.4	77	3.34	2.2	91

(Fig. 6A), small amounts of glassy phase can be seen in 71.8 IP. Glass phase is not present in 75 IP (Fig. 6B). Free  $\text{Al}_2\text{O}_3$  particles (not shown) in this composition were detected by the use of EDAX. A feature of interest in the 73 IP and 74 IP samples (Fig. 7) are the rectangular shaped grains, forming unusual dihedral angles, which suggest the presence of a liquid film along some grain boundaries at the sintering temperature. Further evidence of small amounts of glass in these samples is shown in Fig. 8, a TEM micrograph of the 73 IP sample.

The amorphous nature of the small second phase areas discussed above is further confirmed by the stress-strain behavior at 1200°C in compression loading (Fig. 9). 71.8 IP, 73 IP, and 74 IP are similar in important microstructural features (grain size and density), yet the strength increases with higher  $\text{Al}_2\text{O}_3$  composition. The increase in strength can be accounted for by a decreasing glass phase content. The 75 IP sample also supports these conclusions because, despite a much lower density (83% vs. 95%), the glass-free 75 IP specimen is still as strong as the glass-containing 71.8 IP sample. We would expect that the deleterious effect of small amounts of glass phase on strength would be more severe at higher temperatures. This is confirmed in Fig. 10. Therefore, despite relatively pure materials and long reaction times, it appears that a glass phase, though decreasing to very small amounts, exists right up to the composition where free  $\text{Al}_2\text{O}_3$  begins to appear. The reason for this behavior, which is contrary to expectations based on the equilibrium phase diagram, is uncertain. However, it provides a plausible explanation for the decreased sintering rate on transition from 74 IP to 75 IP.

The possibility that glass phase exists due to insufficient calcination time (i.e. resulting in incomplete reaction) has been considered. In fact, a small amount of reaction between  $\text{Al}_2\text{O}_3$  and  $\text{SiO}_2$  is expected because grinding after calcination introduces some free  $\text{Al}_2\text{O}_3$ .  $\text{Al}_2\text{O}_3$  particles are apparently present in 73 IP samples at low firing temperatures (Fig. 11). However, particles are not in evidence at higher firing temperatures, yet the micrographs showing glass phase (Figs. 6, 7 8) are for samples fired at  $1700^\circ\text{C}$  (8, 12 hrs). Furthermore, on sintering for 100 hrs at  $1700^\circ\text{C}$ , glass phase coalesces into large "pockets" (Fig. 12). If reaction had been incomplete, we would not expect to see glass phase after extensive firing time.

Another explanation which would account for the observed results is the existence of a metastable high  $\text{Al}_2\text{O}_3$  mullite ( 74 wt%  $\text{Al}_2\text{O}_3$ , i.e. the mullite-alumina boundary composition) in "equilibrium" with the observed glass phase. In order to obtain the overall composition, an increasing amount of glass phase would be required with decreasing overall  $\text{Al}_2\text{O}_3$  composition. The existence of high alumina content mullite (as high as 83 wt%) is well documented.<sup>28,29</sup> However, past observations of high alumina mullite have always been associated with mullite grown from the melt (i.e. mullite crystallized on cooling from above the peritectic temperature).

## 2. Densification Kinetics

More detailed densification kinetics were studied on four compositions listed in Table 5. The surface area and green density were kept approximately constant. The 60 IP and 73 IP compositions show only mullite in the x-ray diffraction patterns since glass phase will not be detected; 60 IP has a large amount of glass (Fig. 5) and 73 IP has a trace (Fig. 8). 73 PP was subjected to the largest composition shift during processing (due to  $\text{Al}_2\text{O}_3$  contamination during vibratory milling) such that a trace of  $\alpha\text{-Al}_2\text{O}_3$  was detected by x-ray diffraction. 75 IP has a small amount of  $\alpha\text{-Al}_2\text{O}_3$  which is expected since the composition lies in the mullite and alumina phase region. The green microstructures of the four compositions are shown in Fig. 13.

### (a) 60 IP Composition

The kinetic data for 60 IP differs from the other three compositions due to the large amount of liquid phase present during sintering. In the density vs. time plot (Fig. 14), the rate is very highly temperature dependent. In addition to increased diffusivities at higher temperatures, the viscosity of the siliceous liquid decreases as the temperature increases. The data at 1620°C and 1660°C indicate that a final density, below the theoretical density, is being approached. At 1730°C,

Table 5. Powder Characteristics of A-14/SiO<sub>2</sub> Flour Compositions.

Composition	Surface Area (m <sup>2</sup> /g)	Green Density (% Theoretical)	X-ray Diffraction (phases present)
60 IP	1.9	58	Mullite
73 IP	1.8	58	Mullite
73 PP	2.1	58	Mullite (major) $\alpha$ -Al <sub>2</sub> O <sub>3</sub> (trace)
75 IP	1.7	58	Mullite (major) $\alpha$ -Al <sub>2</sub> O <sub>3</sub> (minor)

maximum density is achieved by the time sintering temperature is reached and a decrease in density is observed with increased sintering time. A density decrease with time is also observed at 1700°C (Table 9).

Observations of limiting densities and macroscopic de-densification, both in solid state and liquid phase sintering, are sometimes attributed to atmosphere effects (gas entrapment)<sup>30,31</sup>. When open pore channels are pinched off, gas is trapped at ambient pressure. Densification will stop when the internal gas pressure equals the surface tension driving force, i.e.  $P = 2\gamma/R$  where  $P$  is the internal gas pressure,  $\gamma$  is the surface tension, and  $R$  is the radius of a spherical pore. At this point, several possibilities can be envisioned:

- (1) If gas diffusion through the sample is very slow, densification will stop and a limiting density is observed.
- (2) In the opposite extreme of a very high rate of gas diffusion through the sample, final densification continues unaffected by the presence of the gas.
- (3) At intermediate rates, the kinetics of gas diffusion to the sample surface will control the rate of approach to final density.
- (4) When the rate of gas diffusion is slightly lower than in case (3), the surface becomes relatively inaccessible but exchange between adjacent pores can occur.

Case (4) can explain the observed results of density decrease with time. As sintering time increases, large pores can grow at the expense of small pores by a diffusional process. We would expect an increase in average pore size and a decrease in number of pores. A density decrease

will be observed because gas will expand on moving from small to large pores (i.e. because  $R_2 > R_1$ , then  $P_2 < P_1$  and by the gas law at constant temperature,  $P_1 V_1 = P_2 V_2$ ; therefore  $V_2 > V_1$ ).

Figure 15 illustrates that pore growth, not just elimination of small pores, has indeed occurred upon increased sintering time. Figure 16 shows micrographs for 60 IP sintered for 100 h at 1700°C in four different atmospheres. In vacuum ( $\sim 10^{-6}$  torr) sintering, pore closure is nearly complete which is consistent with the above arguments. The other microstructures, sintered at pressures of  $\sim 1$  atm or greater, show that large pores are present despite the long firing times. More detailed discussion on effects of sintering atmosphere is presented in Section III-C.

#### (b) 73 IP, 73 PP, 75 IP Compositions

Figure 17 shows density vs. time at 1660°C plots for all four compositions. As discussed earlier, densification is fastest for 60 IP due to large amounts of liquid phase present during sintering. Densification rate decreases with increasing alumina content. The sharp decrease from 73 IP (which has very small amounts of glass phase) to 73 PP indicates that the overall alumina content for the latter sample has shifted during processing (due to alumina contamination from milling) to a composition close to the mullite — mullite and alumina phase boundary.

Figures 18, 19 and 20 show densification vs. time plots for a range of temperatures (1540°C–1730°C) for 73 IP, 73 PP, and 75 IP. Figures 21, 22 and 23 show the corresponding plots of density vs. logarithm of time. The proportionality between  $\% \rho_{th}$  and  $\ln$  time over a large range of densities ( $\sim 60\% \rho_{th}$  to  $\sim 90-95\% \rho_{th}$ ) is consistent with the observed results in a

number of other systems.<sup>32-34</sup> This time dependence is predicted by several models for intermediate stage sintering<sup>35-38</sup> — i.e. the stage in which (1) the porosity evolves from continuous open channels along grain boundaries to discrete isolated closed pores at grain corners and (2) grain growth occurs. The significance of the  $\ln$  time relationship in terms of intermediate stage models will be discussed later (Section III A.5.)

### 3. Microstructural Analysis of 73 IP Samples

In addition to the time dependence of densification, microstructural features, such as grain and pore characteristics, can be utilized to test the validity of sintering models.

Figure 24 plots the average grain size vs. total pore fraction (i.e. porosity). A significant feature of this plot is that points for all temperatures fall on a single curve, i.e. average grain size is density (porosity) dependent only. If microstructural features remain constant, for a given density, it indicates that the mass transport mechanism(s) do not change over the range of sintering temperatures. The mechanism(s) may change, however, with density.

Figure 25 plots the mean pore intercept length,  $\bar{I}_{PL}$ , against porosity. Again, points for all temperatures fall on a single curve. Figure 25 also graphs an adjusted mean pore intercept length,  $\bar{I}_{PLA}$ , vs. porosity.  $\bar{I}_{PLA}$  is determined by counting the number of pores that are intercepted per unit test line, as opposed to counting the number of pore segments (see Fig. 26).  $\bar{I}_{PLA}$  accounts for the fact that irregularly-shaped, concave pores are important at high porosities. The merging of the curves in Fig. 25 at ~85% porosity indicates the point where all the pores have developed a high degree of convexity. The inflection in these



curves is significant because it indicates that the time dependence of  $\bar{I}_{PL}$  and  $\bar{I}_{PLA}$  is not constant over the range of measured porosities. (This conclusion is drawn from the fact that porosity has a single time dependence —  $\ln$  time — over the entire intermediate stage of densification. Any function of porosity — pore intercept size, grain size, etc. — must show an unchanging dependence on porosity over the same range in order for that function to also have a single time dependence over the entire intermediate stage.) The same conclusion (of changing time dependence) can be drawn regarding the average grain size from Fig. 24. These results are important because most intermediate stage models, which predict a semi-logarithmic relationship between density and time, require a single time dependence for some other parameter, such as average grain size.

Three more curves with inflections within the densification range of the intermediate stage are shown in Figs. 27 and 28. Figure 27 plots the number of interceptions of pores per unit area,  $N_A$ , vs. porosity.  $N_A$  is determined by counting the number of discrete pores in several micrographs of polished sections and then dividing by the total micrograph area (corrected for magnification). Figure 28 plots the estimated number of pores per unit volume,  $N_V$ , vs. porosity. The value of  $N_V$  is only an estimate because the relationship between  $N_V$  and  $N_A$  is a function of pore shape and pore size distribution. The difficulty in obtaining a mean pore size with irregularly-shaped, concave particles has already been alluded to in Section IID. Therefore,  $N_V$  is estimated by  $N_A/\bar{I}_{PL}$  ( $N_{VIPL}$ ) and by  $N_A/\bar{I}_{PLA}$  ( $N_{VIPLA}$ ).

Figures 24-28 are helpful in understanding the complex geometrical changes that occur during the sintering of a powder compact. The physical significance of the trends observed in these figures is now discussed in more detail by dividing densification into regions.

Region I: Green density to  $\sim 60\text{-}62\% \rho_{th}$

In this relatively small range of densification, rapid shrinkage and extensive microstructural changes occur. Figure 29 shows that the green compact evolves into a highly porous interconnected structure with dense solid regions separated by large pores. These dense solid regions are polycrystalline as illustrated in Fig. 30. Grain growth is also observed as the average grain size increases from  $\sim .76$  microns in the green compact to  $\sim .97$  microns in the sintered sample shown in Fig. 29.

This type of microstructural development would not be anticipated by analyses based on model systems. In model systems, in which particles are considered to be (1) uniform in size and in shape (usually spherical) and (2) packed in a regular fashion, uniform shrinkage is expected at each contact point.<sup>39</sup> In real systems, however, a range of particle (irregularly-shaped) sizes exists. In addition, pressing of the powder into a compact cannot be accomplished with absolutely uniform pressure being transmitted throughout the compact. Due to frictional effects, micro-variations in green density occur in the compact. Powder agglomeration and particle/agglomerate "bridging" effects also contribute to the development of inhomogeneity. The consequence, in terms of porosity, is not only a distribution of pore (irregularly-shaped) sizes but also a non uniform spatial distribution of pores.

Observed grain growth is most easily explained in non-ideal systems.<sup>40,41</sup> When particles are uniform in size the straight grain boundary cannot migrate from the neck region because an increase in the interfacial area (and, consequently, total interfacial energy) would be required (see Fig. 31). With particles of nonuniform sizes, the grain boundary will become curved (Fig. 32) since it intersects the surface at 90° in order to meet the requirements of the dihedral angle. This curvature creates the driving force for boundary migration. The curvature is increased when the particle size difference is greater. The green microstructure (Figs. 13, 49) of 73 IP shows clearly that a wide range of particle sizes exist. It is expected that a large driving force will quickly develop to eliminate small particles. The neck growth between particles need only occur to the point where the neck size is  $\approx$  the size of the smaller particle. At this point, the boundary will rapidly sweep through the grain. An important complication to the above analysis is that grain boundary energies are not necessarily isotropic. Anisotropy could allow grain boundary migration to occur from the onset of grain boundary formation (even in systems of uniform size particles).

The structure consisting of dense microregions and large pores has been observed by other researchers.<sup>14,42</sup> With carbon-doped  $\beta$ -SiC, Grescovich<sup>42</sup> and Rosolowski observed a decrease in specific surface area from  $\sim 11.5 \text{ m}^2/\text{g}$  at 1250°C to  $\sim 3 \text{ m}^2/\text{g}$  at 1900°C. However, no measurable macroscopic densification was observed over this range of sintering temperatures. With undoped silicon, a small amount ( $\sim 2$  linear percent) of macroscopic shrinkage was observed, but no surface area and densification information over a range of sintering temperatures was presented. In both

cases, dense solid polycrystalline regions were observed. Grescovich and Rosolowski interpret the development of dense regions, large pores, and accompanying grain growth in terms of a high ratio of surface and/or vapor phase mass transport (non-densifying mechanisms) to volume and/or grain boundary transport (densifying mechanisms). The primary evidence for this interpretation is the observation that doping  $\beta$ -SiC with boron and carbon causes: (1) no observable surface area decrease until  $\sim 1500^\circ\text{C}$  and (2) observable densification begins at  $\sim 1500^\circ\text{C}$  and proceeds more rapidly at higher temperatures. The suspected role of boron and carbon is to impede surface diffusion so that densifying mechanisms may operate.

Grescovich and Rosolowski observed that the dense polycrystalline microregions in undoped Si had a volume the size of thousands of the initial powder particles. The postulated mechanism for the extensive grain growth observed was the same as described previously: (1) necks form by surface diffusion and (2) curved grain boundaries are mobile and sweep through the smaller particle. Under the driving force of reverse curvature, the surface area of resultant grains can be reduced as grains assume a more compact shape (Fig. 33). Continuation of this process leads to aggregation of a group of particles into a dense, solid region composed of grains which are larger than the original powder. The fact that no observable densification occurs over a large range of temperatures in carbon-doped  $\beta$ -SiC lends support to this interpretation. However, small amounts of shrinkage in the present study and in the undoped silicon compacts of Grescovich and Rosolowski indicate a certain amount of volume and/or grain boundary diffusion transport. It is difficult to envision total elimination of pores in these dense polycrystalline microregions without some volume and/or grain boundary diffusion.

Although a range of particle sizes accounts for observed grain growth, the mechanism causing formation of dense regions separated by large pores is more easily visualized based on irregularity of packing. The presence of distinct aggregates and/or agglomerates, not observed in this study or that of Grescovich and Rosolowski, is not required to explain this type of structure. Exner sintered planar arrays of uniform size (60-63 microns) spherical copper particles. He observed that small pores in regions of regular arrangement of spheres are quickly filled (i.e. dense regions form). In more loosely, or irregularly packed regions, the size of larger pores increases as surrounding regions "pull away." This type of "rearrangement" accounts for observation of only small amounts of macroscopic densification.

It has been pointed out that, in a regularly packed arrangement of uniform spheres, shrinkage rate is initially independent of packing arrangement.<sup>39,40</sup> Each neck between particles can be considered an isolated system because diffusion distances are short compared to interneck distances. However, once the neck has grown to sufficient size, either by shrinkage-producing mechanisms (volume and/or grain boundary diffusion) or non-shrinkage - producing mechanisms (surface and/or vapor phase diffusion), packing affects densification because the average pore size changes with packing arrangement. In general, the average curvature of the neck region, which determines the driving force, varies inversely with average pore size. Thus, the difference in pore size alone can account for the type of structure developed in Region I.

Without consideration of pore size, Exner proposed that asymmetrical packing causes rearrangement.<sup>14</sup> Straightening of asymmetrical three particle chains was experimentally observed.

It should be realized that the above two approaches to explain Region I behavior have a common basis. Variation in pore size in a powder compact usually implies packing irregularity and irregularity (asymmetry) in packing requires a variation in pore sizes.

Although no time dependence of densification was determined for Region I, some observations may be noted. Table 6 lists density values, for the indicated times, obtained by extrapolation to values below those indicated by the solid lines on the  $\rho_{th}$  vs.  $\ln t$  plots at various temperatures for 73 IP (Fig. 21). Also listed are the actual measured densities for the indicated times. The times are given for the period from the moment the sample is plunged into the furnace hot zone to the time the sample is pulled out of the hot zone. Obviously, since sintering temperature cannot be obtained immediately (except at the surface), the actual sintering time at temperature is a somewhat smaller time. However, the measured density is always higher than the density from extrapolation, even without a time correction. This indicates a period of comparatively rapid densification (i.e. Region I) must have occurred. At higher temperatures (1700, 1730°C) and slightly longer times (20 min), the density points fall on the  $\ln t$  curve (Fig. 21) because (1) the region of rapid densification has become a relatively small percentage of the total densification and (2) the time correction is a smaller percentage of the total time.

Supporting evidence for a period of rapid densification is given by

Table 6. Comparison of Extrapolated and Measured Density Values.

Temp.(°C)	Time(min)	Extrapolated Density(% $\rho_{th}$ )	Measured Density(% $\rho_{th}$ )
1540	10	59.8	60.3
1580	10	60.1	61.9
1620	15	62.0	63.6
1660	15	64.5	65.6

Fig. 34 in which the total pore surface (interface) area per unit volume of the total system (pores plus matrix),  $S_V$ , is plotted against porosity. The large initial decrease in  $S_V$  is understandable considering the observed formation of clusters.  $S_V$  was determined from the polished microstructures by the relationship

$$S_V = 2P_L$$

where  $P_L$  is the number of point intersections of pores per unit length of test line (see Fig. 26)<sup>27</sup>. The expression is statistically exact and does not depend on pore shape or size distribution. Two points are given for  $S_V$  at the green density. One point was determined from the green microstructure while the other, much higher value, was obtained from the BET adsorption measurements on the 73 IP powder before compaction.

Region II and III:  $\sim 60\text{--}62\% \rho_{th}$  to  $\sim 73\% \rho_{th}$

Continuation of the  $\% \rho_{th}$  vs.  $\ln t$  plot from the first measured point to the point where the  $\ln t$  time proportionality begins is schematically illustrated in Fig. 35 for one temperature. Region II is the lower slope portion (dashed line). The upward change in slope is discussed in detail in section III B. For now, it is noted that the upward slope, on a  $\% \rho_{th}$  vs.  $\ln t$  time plot, does not mean an increase in densification rate ( $\frac{d\rho}{dt}$ ). This is obvious from the  $\% \rho_{th}$  vs. time plots (Figs. 18-20). According to the average grain size vs. porosity plot (Fig. 24), a slope decrease is observed at  $\sim 73\% \rho_{th}$  (see section III A.4. for discussion of grain growth behavior). Region III is the  $\ln t$  time portion of the densification curve up to  $\sim 73\% \rho_{th}$ .



Macroscopic densification, which can only occur by volume and/or grain boundary diffusion, must proceed at a reduced rate after the type of structure evolved in Region I develops. The number of grain boundaries that can act as vacancy sinks for pore volume reduction is reduced to those few which connect dense solid regions (examples are circled in Fig. 36). As a result, the effective diffusion distance has been greatly increased. It is also noted that variations in the spatial distribution of pores become important because shrinkage requires a coordinated change throughout the whole compact. Shrinkage of porous regions will be restrained by pore-free regions until differential stresses on grain boundaries are relieved. Coordinated changes are easier to accomplish when small grains are surrounded by small pores rather than dense microregions surrounded by large pores.

Implicit in the above discussion is the fact that densification rate is altered by the formation and the elimination of particle/particle and cluster/cluster (of particles) contacts during the densification process. Any net decrease in number of contacts would decrease the densification rate and, correspondingly, any net increase in number of contacts would increase the densification rate.

Figure 37 contains micrographs of 73 IP samples in the range of Regions II and III. Although the microstructural changes are not nearly as dramatic as for the first few percent of densification of the green compact, comparison of micrographs "A" ( $61.9\% \rho_{th}$ ) and "B" ( $65.6\% \rho_{th}$ ) indicate that the process of coalescence continues as small clusters of particles form larger dense microregions. Subtle differences are noted in the distribution of pore intercept sizes for "A" and "B" (Fig. 38).

Small pore intercept sizes ( $< .5\mu$ ) decrease from 44.0% ( $61.9\% \rho_{th}$ ) to 40.5% ( $65.6\% \rho_{th}$ ) while large pore intercepts ( $> 2.0\mu$ ) increase from 10.2% ( $61.9\% \rho_{th}$ ) to 12.2% ( $65.6\% \rho_{th}$ ). These changes, which explain the slight increase in  $\bar{I}_{PL}$  seen in Fig. 25, are consistent with our picture of dense microregion formation and opening of large pores.

As the density increases further (Fig. 37 D), reduction in the size of large pores between dense clusters begins to occur. This is reflected in the decreasing value of  $\bar{I}_{PL}$  (Fig. 25) and in the changes in pore intercept size distribution (Fig. 38). The large pore intercepts ( $> 2.0\mu$ ) decrease from 12.2% ( $65.6\% \rho_{th}$ ) to 7.5% ( $71.1\% \rho_{th}$ ) while intermediate pore intercept sizes ( $.5-1.0\mu$ ) increase from 25.2% ( $65.6\% \rho_{th}$ ) to 37.3% ( $71.1\% \rho_{th}$ ). Clusters of particles continue to coalesce as indicated by the decrease in small pore intercepts ( $< .5\mu$ ) from 40.5% ( $65.6\% \rho_{th}$ ) to 32.4% ( $71.1\% \rho_{th}$ ). Reduction in large pores, together with the increase in intermediate sizes, is consistent with the observed increases in  $N_A$  (number of pores per unit area - Fig. 27) and in  $N_{VIPL}$  and  $N_{VIPLA}$  (estimated number of pores per unit volume - Fig. 28). Long winding "tentacled" pores (as outlined in Fig. 39) have sections "pinched off" during the diffusional reduction of the pore phase.

A noticeable change in the microstructures (Fig. 37) upon densification is the smoothing and rounding of sharp edges on particle/clusters. This indicates that mass transport by surface diffusion and/or vapor transport is operational (along with densifying mechanisms). Vapor transport is eliminated as the mechanism, however, because (1) no significant weight loss is detected and (2) the thermodynamic data on mullite indicate very low partial pressures at these temperatures.

Region IV:      $\sim 73\% \rho_{th}$  to  $\sim 85\% \rho_{th}$

During this period of densification, two trends continue: (1) the estimated number of pores per unit volume,  $N_{VIPL}$  and  $N_{VIPLA}$ , increase (Fig. 28) and (2) the mean pore intercept size,  $\bar{I}_{pL}$ , decreases (Fig. 25). The distinguishing feature of these regions is that very little change in average grain size (Fig. 24) is observed. Grain growth behavior is analyzed in section III A.4. Changes in the pore phase are now discussed in more detail.

Region IV can be divided into three sub-regions according to the trends observed in the pore intercept size distribution data (Fig. 40 and Table 7). From  $73.5\% \rho_{th}$  to  $77.4\% \rho_{th}$ , very large pore intercepts ( $>2.0\mu$ ) are being eliminated. Large pore intercepts ( $1.0-2.0\mu$ ) are reduced to intermediate size intercept ( $.5-1.0\mu$ ) in the range  $77.4\% \rho_{th}$  to  $80.5\% \rho_{th}$ . Finally, from  $80.5\% \rho_{th}$  to  $84.5\% \rho_{th}$ , intermediate size pore intercepts are being reduced to small intercepts. These trends indicate that the "pinching off" process described earlier continues for the various pore intercept sizes. In most analyses of sintering in real systems, it is predicted that the average pore size will increase with increasing density because of the preferential elimination of small pores. It is worth re-emphasizing that the simultaneous decrease in mean pore intercept size,  $\bar{I}_{pL}$ , and increase in number of pores per unit volume,  $N_V$ , can only be explained by a process in which a larger pore fissions (or "pinches off") into two or more smaller pores. The observed changes in pore intercept size distribution must be interpreted with due regard to the dynamic nature of the sintering process. Small pores are most certainly being eliminated but the net increase in the fraction of small pores reflects the

Table 7. Pore Intercept Size Distribution Data for Region IV.

<u>Density (<math>\% \rho_{th}</math>)</u>	<u>Pore Intercept Size</u>			
	<u>&gt;2.0<math>\mu</math></u>	<u>1.0-2.0<math>\mu</math></u>	<u>.5-1.0<math>\mu</math></u>	<u>&lt;.5<math>\mu</math></u>
73.5	8.9%	22.3%	30.6%	38.1%
77.4	1.6%	25.1%	35.2%	38.2%
80.5	1.6%	14.3%	55.3%	40.9%
84.5	1.5%	11.8%	32.3%	54.4%

dominance of the fission process.

Some sintering models (see section III A.5.) predict pore growth, either by coalescence during grain boundary movement<sup>36</sup> or by Ostwald ripening.<sup>43</sup> In this study, it is clear that neither of these processes has occurred up to at least  $85\% \rho_{th}$  because pore growth requires a decrease in  $N_V$  and an increase in average pore size. While  $\bar{I}_{PL}$  does show a slight initial increase (until  $\sim 66\% \rho_{th}$ ), this clearly results from the opening of pores as clustered regions "pull away" due to localized densification.

It was pointed out earlier that the merging of the curves in Fig. 25 ( $\bar{I}_{PL}$  vs. porosity and  $\bar{I}_{PLA}$  vs. porosity) indicated that pores were approaching a high degree of convexity. This is illustrated directly in the micrographs (Fig. 41) for Region IV. It is clear that the development of convex pores signals the end of the observed (1) increase in  $N_V$  and (2) decrease in  $\bar{I}_{PL}$ .

Region V:  $\sim 85\% \rho_{th}$  to  $\sim 90\% \rho_{th}$

This region is dominated by the elimination of small pores as indicated by the pore intercept size histograms in Fig. 42. Small pores ( $< .5\mu$ ) decrease from 54.4% ( $84.5\% \rho_{th}$ ) to 47.7% ( $86.5\% \rho_{th}$ ) to 36.0% ( $90.5\% \rho_{th}$ ). This accounts for the (1) decrease in  $N_V$  (Fig. 28) and (2) increase in  $\bar{I}_{PL}$  (Fig. 25). These observations should not be interpreted as non-conservative pore coalescence (pore growth). Although some grain growth is observed in Region V (Fig. 24), the increase in average grain size is much too small to account for such large changes in  $N_V$  and  $\bar{I}_{PL}$ .

Figure 43 shows the pore intercept size histograms for samples sintered to approximately the same density with different time-temperature

schedules: 1660°C - 1455 min ( $90.5\% \rho_{th}$ ), 1700°C - 260 min ( $89.5\% \rho_{th}$ ), and 1730°C - 80 min ( $89.3\% \rho_{th}$ ). The close similarity of these histograms is one more indication that microstructure development is only dependent on density over the range of sintering temperatures used in this study.

Region VI:  $\sim 90\% \rho_{th}$  to  $\sim 95\% \rho_{th}$

This region continues the trends of (1) decreasing  $N_V$  (Fig. 28) and (2) increasing  $\bar{I}_{PL}$  (Fig. 25). It is separated from Region V because it represents a transition region from intermediate stage to final stage sintering. By the end of this period, only closed pores are present (Fig. 44). Significant grain growth occurs (Fig. 24). The migration of grain boundaries (Fig. 45A) past small pores (i.e. pore isolated within grains) is a common observation during final stage sintering.<sup>44</sup> The observations of increasing  $\bar{I}_{PL}$ , decreasing  $N_V$ , and rapid grain growth indicate that the occurrence of non-conservative pore growth is possible. However, the micrographs in Fig. 46 (A, B) indicate that the primary (but necessarily exclusive) cause for the observed trends is simply diffusional elimination of smaller pores (as in Region V). This accounts for the increase in average pore size and decrease in number of pores without invoking pore growth.

Region VII: Above  $\sim 95\% \rho_{th}$

The decreased rate of densification (Fig. 21), rapid grain growth (Fig. 24), separation of pores from grain boundaries (Figs. 45 and 46), and appearance of exaggerated grain growth (Figs. 45B, 46C) are all common observations in the final stage of sintering.<sup>44,45</sup> Since a small amount of densification is observed, it is still uncertain if the increasing  $\bar{I}_{PL}$  (Fig. 25) and decreasing  $N_V$  (Fig. 28) reflect the occurrence

of pore growth. The fact that very large pore intercept sizes ( $>2.4\mu$ ) reappear in the histograms (Fig. 47) suggests that some pore growth has occurred in Regions VI and VII.

#### 4. Grain Growth in 73 IP

##### (a) Introduction

Classical grain growth theory considers the process in which an increase in average grain size is observed with time at elevated temperatures in a dense, single phase body.<sup>46-48</sup> The grain boundary structure is the ideal geometry of cells in a foam in which minimization of grain boundary energy results in  $120^\circ$  angles between the intersection of 3 grain faces. Movement of individual grain boundaries toward their center of curvature at a velocity,  $\bar{V}$ , given by

$$\bar{V} = MF \quad (14)$$

where  $M$  is the mobility term, in which the factors arising from the mechanism of grain boundary movement are isolated, and is given by

$$M = M_o \exp\left(-\frac{D_b}{RT}\right) \quad (15)$$

where  $D_b$  is the diffusion coefficient for atoms at the boundary. The driving force is derived from the pressure gradient across the boundary due to curvature and is given by

$$F = \frac{d\mu}{dx} = \frac{d(V\Delta P)}{dx} \quad (16)$$

where  $\frac{d\mu}{dx}$  is the chemical potential gradient caused by  $\Delta P$ , the pressure

difference across the boundary which is given by

$$\Delta P = \gamma_{gb} \left( \frac{1}{r_1} + \frac{1}{r_2} \right) \quad (17)$$

where  $\gamma_{gb}$  is the grain boundary energy and  $r_1$  and  $r_2$  are the two radii of curvature of the boundary surface.

If (1) the velocity of the grain boundary is proportional to the rate of change in average grain size, i.e.  $\bar{V} \propto \frac{d\bar{G}}{dt}$  where  $\bar{G}$  is the average grain size, and (2)  $\left( \frac{1}{r_1} + \frac{1}{r_2} \right) \propto \left( \frac{1}{\bar{G}} \right)$ , then

$$\frac{d\bar{G}}{dt} \propto \bar{V} = M_o \exp \left( - \frac{D_b}{RT} \right) \gamma_{gb} \left( \frac{1}{\bar{G}} \right) \quad (18)$$

Upon integration,

$$\bar{G}^2 - \bar{G}_o^2 = Kt \quad (19)$$

In general, this rate law is only observed in high density, high purity metals at high temperatures.<sup>49</sup> Various investigators have taken into account the presence of impurities, inclusions (pores and second phase particles),<sup>50-52</sup> and liquid phase<sup>53-57</sup> to derive grain growth laws where  $n$  in the equation<sup>58</sup>

$$\bar{G}^n - \bar{G}_o^n = Kt \quad (20)$$

varies from 1-5. These laws are usually tested by assuming  $\bar{G}^n \gg \bar{G}_o^n$ . A plot of  $\ln \bar{G}$  vs.  $\ln$  time should yield a straight line with slope  $1/n$ .



In addition to the assumptions that  $\left(\frac{1}{r_1} + \frac{1}{r_2}\right) \propto \frac{1}{\bar{G}}$  and  $\bar{V} \propto \frac{d\bar{G}}{dt}$ , grain growth law derivations also assume that: (1) the grain boundary energy,  $\gamma_{gb}$ , is isotropic and independent of grain size, (2) the mobilities of all grain boundaries are equal and independent of grain size, and (3) the shape of the grain size distribution curve is constant during grain growth (independent of grain size).

A principal objection to the derivation presented above has been the assumption that the driving force is proportional to the average grain size. <sup>59</sup> Feltham considered the rate of change in size of any grain,  $G$ , in the distribution to be given by

$$\frac{dG}{dt} = K \ln\left(\frac{G}{\bar{G}}\right) \quad (21)$$

where grains larger than  $\bar{G}$  grow and those smaller will shrink. Hillert <sup>60</sup> based his derivation on

$$\frac{dG}{dt} \propto \left(\frac{1}{G_{cr}} - \frac{1}{G}\right) \quad (22)$$

where  $G_{cr}$  is the "critical" grain size above which grains grow and below which grains shrink. Both Feltham and Hillert derive laws that are essentially the same as equation 19 if the shape of the grain size distribution is time-invariant.

#### (b) Analysis of 73 IP Data

Fig. 48 plots the logarithm of average grain size vs. the logarithm

of time for the various temperatures (1540°C-1730°C). In addition to the experimental data shown in Fig. 48, smooth curves were generated by using the data in Figs. 21 and 24. From Fig. 24, the grain size at any given density can be determined and, from Fig. 21, the density at any time can be obtained. Hence, the grain size at any time can be generated. The generated points in Fig. 48 at any given temperature are given over the range of densities in which the  $\ln$  time relationship is observed for that particular temperature. The extrapolated points are determined by applying Figs. 21 and 24 and assuming the  $\ln$  time relationship in Fig. 21 can be extrapolated to higher and/or lower densities (for longer and/or shorter times, respectively) for any given density within the density range of intermediate stage sintering ( $\sim 62.5\text{--}95\% \rho_{th}$ ). It is clear from Fig. 48 that no single growth law exists. The growth law not only changes with density, but also varies with temperature. Measured slopes vary in the range .013 - .65 where the former value is more than an order of magnitude lower than the smallest value in a derived grain growth law (when  $n=5$ ,  $1/n = .2$ ). This behavior is contrary to the assumptions of all intermediate stage densification kinetics models (see section III.A.5).

Grain growth behavior can be discussed in terms of the densification regions outlined in section III.A.3. The green microstructure of the 73 IP material (Figs. 13 and 49) does not at all resemble the ideal geometry of cells in a foam. Fig. 49 shows a high magnification micrograph of the 73 IP material illustrating the existence of very small particles (more than an order of magnitude lower than the average particle

size). The mechanism of elimination of these particles (in which (1) necks form by surface diffusion and (2) the boundary sweeps through the smaller particle due to the large curvature introduced by the particle size difference) was discussed in detail in section III.A.3. During Region I densification, grain growth occurs by the rapid elimination of these fine particles. This is confirmed in the grain size histograms in Fig. 50 in which the percentage of grains less than 0.4 microns decreases from 60.3% in the green compact to 41.8% in the  $63.5\% \rho_{th}$  sample.

During densification Regions II and III, after the formation of dense microregions, grain growth still consists of the elimination of small particles by the mechanism described above. As indicated by the histogram in Fig. 50, the small particles ( $<0.4$  microns) have decreased to 16.5% at  $71.1\% \rho_{th}$ .

Grain size histograms for densities in the range  $71.1\% \rho_{th}$  -  $95.3\% \rho_{th}$  are shown in Fig. 51. Although the changes are less dramatic than in Fig. 50, the shape of the grain size distribution is becoming broader. The time dependence of the shape of the size distribution observed in Figs. 50 and 51 contradicts the assumptions made in the derivations of the grain growth laws (section III.A.4.a.).

The change in slope in Fig. 24 (grain size vs. porosity) upon transition from Region III to Region IV ( $\sim 73\% \rho_{th}$ ) reflects a change in mass transport mechanism(s), either for pore removal (densification) or grain growth. Since the time dependence is constant over the intermediate stage densification range (Fig. 21), the change in slope probably indi-

cates the end of grain growth by the mechanism in which small particles are eliminated by the two step process of surface diffusion and boundary migration. Grain growth in the dense microregions formed during Region I densification should occur by boundary movement according to classical grain growth theory. If we assume that the grain growth rate in these microregions remains constant, the decreased slope in Fig. 24 then reflects the fact that one less mechanism (the two step elimination of fine particles) is occurring. Implicit in this discussion is the assumption that the two grain growth mechanisms are independent of each other.

The slow grain growth during Region IV ( $\sim 73\% \rho_{th}$  to  $\sim 85\% \rho_{th}$ ) is indicated by the low slope regions in Fig. 48. Enhanced grain growth, as indicated by the upward slopes at 1660°C, 1700°C, and 1730°C in Fig. 48, is observed in Regions V and VI. Significant grain growth begins at a density ( $\sim 85\% \rho_{th}$ ) in which (1) pores have developed a considerable amount of convexity and (2) the fraction of closed pores becomes sizeable. In other words, pores are becoming pinched off and isolated on grain corners rather than existing as continuous channels along grain boundaries. This picture is consistent with enhanced grain growth because boundaries are less restrained by the pore phase. However, since grain growth was not important in fully dense microregions in the early stages (Regions I-IV), it is difficult to understand why grain growth becomes significant during Region V. The probable explanation has its basis in the size distribution of grains. Fig. 50 shows that the largest grain size present increases only slightly (2.6 to 3.0 microns) from  $58\% \rho_{th}$  to  $71.1\% \rho_{th}$ . Fig. 51

indicates a sizeable increase (3.0 to 6.0 microns) in the largest grain size upon densification from  $71.1\% \rho_{th}$  to  $95.3\% \rho_{th}$ . Half of this increase occurs just in the range  $89.5\% \rho_{th}$  to  $95.3\% \rho_{th}$ . In Fig. 52, the increase is even more dramatic (from 6.0 microns at  $95.3\% \rho_{th}$  to 29.0 microns at  $97.2\% \rho_{th}$ ). These results indicate that grain growth, after Region III, occurs primarily by a few large grains growing at the expense of their smaller neighbors. When such a process becomes severe, as indicated in Fig. 52, it is referred to as exaggerated, or abnormal, grain growth.<sup>49</sup>

Apparently, the driving force for grain growth in the dense microregions is extremely low. This is probably due to the large fraction of straight grain boundaries (see Fig. 30). A significant driving force does not develop until some large grains form (i.e. when large grains are present, the small grains develop a large relative curvature). The significance of the change in the pore phase (i.e. development of isolated, closed pores beginning at  $\sim 85\% \rho_{th}$ ) is that the largest grain size present is no longer restricted to the original cluster (dense microregion) size.

### 5. Analysis in Terms of Intermediate Stage Sintering Models

The first attempt to derive a quantitative model for intermediate stage densification kinetics was formulated by Coble.<sup>33,35</sup> He replaced the complex structure of the compact with a system of uniform, cylindrical interconnected pores located at three grain edges of uniform size polyhedral grains. The problem was reduced to the shrinkage of a single pore in a specified geometrical environment. Shrinkage was assumed to occur by diffusion of vacancies from pores to neighboring grain boundary sinks. The vacancy flux per unit area of boundary was taken to be uniform over each boundary. The form of the shrinkage equation derived depends on the assumed geometry and on the flux equation which is chosen.

Under conditions in which shrinkage is by bulk diffusion and grains have the shape of a tetrakaidecahedron, Coble obtained the following equation:

$$\frac{d\rho}{dt} = - \frac{dP}{dt} = \frac{ND_V \gamma_{SV}\Omega}{\ell^3 kT} \quad (1)$$

where  $\frac{d\rho}{dt}$  is the densification rate,  $P$  is the porosity which equals  $(1-\rho)$ ,  $T$  is the absolute temperature,  $N$  is a numerical factor,  $D_V$  is the volume diffusion coefficient,  $\gamma_{SV}$  is the surface energy,  $\Omega$  is the volume of a vacancy,  $\ell$  is the edge length of the model grain, and  $k$  is the Boltzmann constant. Since  $D_V = D_0 \exp(-\frac{Q}{RT})$  where  $Q$  is the activation energy for volume diffusion and  $\ell \propto G$  where  $G$  is the grain size,

$$\frac{dP}{dt} = - \frac{N' D_0 \exp(-\frac{Q}{RT}) \gamma_{SV}\Omega}{G^3 kT} \quad (2)$$

Coble then substituted the empirical grain growth law,  $G^3 = At$ , where  $A = A_0 \exp(-\frac{E}{RT})$  where  $E$  is the activation energy for grain growth. After integration,

$$P_0 - P = \frac{ND_0 \exp(-\frac{Q}{RT}) \gamma_{SV} \Omega}{A_0 \exp(-\frac{E}{RT}) kT} \ln\left(\frac{t}{t_0}\right) \quad (3)$$

Granting the assumptions (which have not been detailed here) of this semi-empirical model, the correct time dependence of densification is predicted for the experimental results of this study (73 IP, 73 PP, 75 IP). However, this model requires a cubic grain growth law which is not experimentally observed.

Slopes of the density (or porosity) vs.  $\ln$  time plots have also been used to test the model. Since the slope,  $m$ , is given by

$$m = \frac{K}{T} \exp\left(\frac{E-Q}{RT}\right) \quad (4)$$

where  $K$  is constant, a plot of  $\ln(mT)$  vs.  $1/T$  should give a straight line with slope of  $-\frac{(E-Q)}{R}$ , where the numerator represents the difference between activation energies for diffusion and grain growth. Plots for 73 IP, 73 PP, and 75 IP are shown in Fig. 53. A value of  $\sim 70$  kcal/mole was obtained in each case for  $(Q-E)$ . Since a single value of  $E$  cannot be obtained in this study over the whole intermediate stage of densification, a single value of  $Q$  cannot be determined.

Several difficulties with Coble's derivation have been pointed out. First, the porosity was defined in terms of the edge length of the model polyhedron (grain). It is not clear how the pore structure changes as grains grow in size. Secondly, the differentiation with respect to

time to obtain equation (1) was done by treating  $\ell$ , the grain edge length, as a constant with respect to time. It is incorrect, therefore, to integrate and obtain equation (3) by treating  $\ell(\propto G)$  as a variable with respect to time.<sup>61</sup> Coble's model must then be evaluated by using equation (2). This can be done by plotting  $\ln\left(\frac{d\rho}{dt} G^3 T\right)$  vs.  $1/T$  at constant density. This should yield a straight line with slope  $-\left(\frac{Q}{R}\right)$ . Since  $G^3$  is a constant for all temperatures at a given density in this study (Fig. 24), we can simply plot  $\ln\left(\frac{d\rho}{dt} T\right)$  vs.  $1/T$ . This is done in Fig. 54 for several densities of the 73 IP sample in which the values of  $\frac{d\rho}{dt}$  used were determined from the experimental results and by extrapolating the  $\rho_{th}$  vs.  $\ln$  time plots at low temperatures to  $92.5\rho_{th}$ . The data do not yield a straight line if all the plotted points are used. The fit is somewhat better when the extrapolated values are excluded, but these results are unreliable considering the small number of data points available. In both cases, a least squares fit yields an increasing activation energy with increasing density (although the increase is much more severe when the extrapolated values are used). Coble's model predicts a single-valued activation energy because a single geometry and single mass transport mechanism is assumed to apply over the entire intermediate stage of densification.

The results are the same with the 73 PP and 75 IP materials (assuming  $G$ , the grain size, is not a function of temperature as in Fig. 24) except that the values of  $Q$ , for a given density, increase in the order 73 IP < 73 PP < 75 IP (see Fig. 55). The lowest indicated value of  $Q$  (216 kcal/mole) is still considerably higher than the activation energy for bulk diffusion in mullite obtained by other methods



(~170 kcal/mole).

Wong's intermediate stage sintering model<sup>37</sup> used the same geometry as Coble's model, but he treated the diffusion problem as equivalent to a viscous shear flow problem. He utilized a rheological expression which relates the bulk viscosity and the rate of volume change of a viscous solid to the pressures on the solid. The bulk viscosity was expressed in terms of the porosity of the body and the effective shear viscosity. The vacancy flux was then equated to a creep rate with the shear viscosity coefficient being related to the bulk diffusion coefficient. The final equation has the same form as in Coble's model:

$$\frac{dP}{dt} = - \frac{K D_V \Omega \gamma_{SV}}{kT G^3} \quad (5)$$

where K is a constant which is different from the constants in equations (1)-(4).

Equation (5) was obtained without requiring G to be a constant with respect to time. Wong then substituted N, the number of interconnected voids per unit volume, for G:

$$\frac{dP}{dt} = - \frac{K' D_V \Omega \gamma_{SV} N^3}{kT} \quad (6)$$

He postulated that the reduction in N follows a cubic law,  $N^3 = 1/at$  where a is temperature dependent. After integration

$$P - P_0 = \frac{- K' D_0 \exp(-\frac{Q}{RT}) \gamma_{SV}}{a_0 \exp(-\frac{e}{RT}) kT} \ln\left(\frac{t}{t_0}\right) \quad (7)$$

where  $e$  is the activation energy for the reduction in the number of interconnected voids per unit volume. Granting the assumptions of this model (which have not been detailed here), the analysis in terms of experimental data is essentially the same as that carried out on Coble's model:

(a) In this case, we need to test the relationship  $N^3 = 1/at$ .  $N$  is estimated by multiplying  $N_{VIPL}$  (or  $N_{VIPLA}$ ) by the fractional open porosity.  $N$  is plotted against porosity in Fig. 56. It is clear that  $N$  could not possibly follow Wong's postulated relationship because (1)  $N$  is increasing up to  $\sim 85\% \rho_{th}$  (it should be decreasing according to  $N^3 = 1/at$ ) and (2) an inflection in the curve occurs.

(b) The previous plots of  $\ln(mT)$  vs.  $1/T$  do not change, but the slope would now equal  $(Q-e)$ . As before, a single value of  $Q$  cannot be obtained since  $e$  is not single-valued.

(c) A plot of  $\ln(\frac{d\rho}{dt} N^3 T)$  vs.  $1/T$ , at constant density, should yield a straight line with slope  $-(\frac{Q}{R})$ . Since  $N^3$  is constant for all temperatures at a given density in this study (Fig. 56), we would plot  $\ln(\frac{d\rho}{dt} T)$  vs.  $1/T$ , exactly as before.

36

Rosolowski and Grescovich based their model on an idealized pore-grain boundary geometry and calculated the vacancy flux from a single cylindrical pore assuming simultaneous grain boundary and volume diffusion mechanisms. They explicitly incorporated the effects of grain growth while making less restrictive assumptions (than Coble or Wong) regarding the size and shape of the grains. They obtained the following equation:

$$\begin{aligned} \ln(1 - P) = & \frac{\beta \Omega f e s}{h} \left( \frac{\ell}{r} \right)_{\text{ave.}} \left[ \int_{t_0}^t \frac{dt}{(d^3)_{\text{ave.}}} \right] \\ & + \frac{\lambda \Omega f e s}{h} \left[ \int_{t_0}^t \left( \frac{\ell}{r^2} \right)_{\text{ave.}} \left( \frac{1}{d^3} \right)_{\text{ave.}} dt \right] + \ln(1 - P_0) \end{aligned} \quad (8)$$

where the contribution of volume diffusion is incorporated in the first term and the contribution of grain boundary diffusion is incorporated in the second term of the right side of equation (8).  $(1-P)$  is the fraction of theoretical density,  $\ell$  is the pore length,  $r$  is the pore radius,  $t$  is time,  $d$  is grain size,  $f$  is the fraction of grain edges occupied by pores,  $e$  is the average number of edges per grain,  $s$  is a factor which accounts for the sharing of each pore by more than one grain,  $h$  is a constant related to the average geometry of the grains,  $\Omega$  is the molecular volume divided by the number of atoms of the sinter-rate-limiting species per molecule (the atomic volume for a monatomic solid), and

$$\beta = \frac{3ID_V \gamma_{SV}}{kT}, \quad \lambda = \frac{11.4 \delta D_{gb} \gamma_{SV}}{kT}$$

where  $D_V$  is the volume diffusion coefficient,  $D_{gb}$  is the grain boundary diffusion coefficient,  $\delta$  is the width of the grain boundary,  $\gamma_{SV}$  is the surface energy,  $I$  is a constant which depends on the ratio  $\ell/r$ , and  $kT$  has its usual meaning.

When the logarithm on the left of equation (8) is expanded in terms of  $P$  (porosity), the dominant term is just  $P$  because  $P$  is usually small ( $< .4$ ). When the cube of the average grain diameter depends linearly on time (i.e.  $G^3 = At$ , which is not observed in the present study), then

the volume diffusion term alone will generate a linear dependence of P (or relative density) on the logarithm of time. Rosolowski and Grescovich tested the model with data from several other studies by plotting

$$\ln(1 - P) \text{ vs. } \int_{t_0}^t \frac{dt}{(d_{\text{ave.}})^3} \quad (\text{A})$$

and

$$\ln(1 - P) \text{ vs. } \int_{t_0}^t \frac{dt}{(d_{\text{ave.}})^4} \quad (\text{B})$$

where the integrand of the grain boundary diffusion term in equation (8) is approximated by the integrand in (B). (A) yielded good straight lines over a large change in porosity. (B) yielded curved lines over the entire range of measured porosities indicating a poor fit. Plots of (A) and (B) for this study are shown in Fig. 57. Neither case yields straight lines.

One of the major assumptions in this model is that the grain growth rate is large enough so that coalescence dominates the change in the number of pores per unit volume. As discussed earlier in section III A.3., this is clearly not true for the experimental results with 73 IP. The results suggested that pore coalescence is negligible until  $\sim 90\% \rho_{\text{th}}$  (i.e. around the transition density from intermediate stage to final stage sintering).

<sup>43</sup>Kucynski treated densification as a non-conservative Ostwald ripening process in which (1) large pores grow at the expense of small ones and (2) pore shrinkage occurs, both by volume diffusion. He took a statistical approach in which a distribution of pore radii was allowed. A

continuity equation utilized in Ostwald ripening theories was modified to include a term associated with pore shrinkage. He derived equations for kinetics of densification and grain growth which have the form

$$P^{-n_1} - P_0^{-n_1} = At \quad (9)$$

and

$$a^{n_2} - a_0^{n_2} = Bt \quad (10)$$

respectively, where  $P$  is porosity,  $t$  is time,  $a$  is grain size,  $A$  and  $B$  contain terms which are not time dependent, and  $n_1$  and  $n_2$  are the exponents in the rate laws which are constants over the intermediate stage of densification. The relationship between porosity and grain size is given by

$$aP^{n_3} = a_0P_0^{n_3} \quad (11)$$

where  $n_3 = n_1/n_2$ . A plot of  $\ln a$  vs.  $\ln P$  should yield a straight line with slope of  $-n_3$ . This is not observed for the 73 IP material (Fig. 58), even when we consider the transition between the intermediate and final stages to occur at  $90\% \rho_{th}$ . The failure of this relationship to hold for the 73 IP data is not surprising in view of the fact that the densification kinetics do not follow the form of equation (9). In addition,  $n_2$  (the grain growth law exponent) is not constant with temperature or density in this study. The assumption of Ostwald ripening of pores is not valid in the present work because the occurrence of pore growth is negligible until at least  $90\% \rho_{th}$ . Furthermore, the exponent in equation (11) was defined by

$$n_3 = \frac{2+X}{3} \quad (12)$$

where  $X$  is taken as a positive constant defined by

$$X = \frac{d \ln N_V}{d \ln P} \quad (13)$$

where  $N_V$  is the number of pores per unit volume. It is clear from Fig. 58 that  $X$ , the slope of a  $\ln N_V$  vs.  $\ln P$  plot, is not a positive constant.

Several other intermediate stage sintering models will not be detailed, but they yield similar results to those previously discussed. Beere's model<sup>38</sup> yields the same time dependence of densification as the models of Coble and Wong. It is also dependent on a cubic grain growth law. The model of Ikegami et al.<sup>62</sup> has same time dependence of densification and of grain growth as in Kuczynski's model.

In summary, the preceding analysis of the experimental data has demonstrated that available intermediate stage sintering models are inadequate for the 73 IP material. The assumptions made in deriving the various models have not been detailed here, but in all cases idealized pore-grain boundary geometries were used. These geometries are unrealistic for the physically inhomogeneous 73 IP powder compacts. In addition, the pore-grain boundary geometry does not change with time in the regular, idealized fashion described by these models.

A wide range of rate laws for densification and grain growth have been observed experimentally. Simultaneous measurements of densification rate and grain growth rate are few. Even less common is the correlation of the observed rate laws with the microstructural evolution from green

compact to maximum density. In order to accurately assess whether a model is physically realistic, a detailed microstructural analysis is required.

The results of the present study not only indicate the inability of current models to deal with physical inhomogeneity in the powder compact but also suggests the inadequacy of grain size as a parameter used in sintering models. This is discussed in more detail in the following section.

## 6. Effective Grain Size Concept

In section III.A.5., difficulties in the use of grain size in sintering models were demonstrated to result from the failure to obtain a single growth law over the region in which a single time dependence of densification was observed. However, a more fundamental reason exists for discarding grain size as a parameter in the modeling of sintering in physically inhomogeneous systems. Grain size is used in the various models to characterize the diffusion distance that vacancies at pore surfaces must travel in order to be annihilated at grain boundary sinks. It is clear that the formation of dense microregions in our system (within 2 linear percent shrinkage) renders grain size an inaccurate measure of diffusion path length.

An "effective grain size", the size of the dense microregions, needs to be defined. From an experimental point of view, it is suggested that measures of diffusion path length are more appropriately defined in terms of the pore phase. Two possible measures are (1)  $\lambda_1$ , the average distance between first neighbors of intercepts of pore segments, and (2)  $\lambda$ , the mean free path between pores.  $\lambda$  is defined by applying the statistically exact expression<sup>26</sup>

$$\lambda = \frac{2(1-P)}{P_L}$$

where  $P$  is the fractional porosity and  $P_L$  is the number of interceptions of pore edges per unit length (see Fig. 26). Plots of (1)  $\lambda$  vs. porosity



and (2)  $\lambda_1$  vs. porosity at the various temperatures (1540°C - 1730°C) for 73 IP are shown in Fig. 59. The values of  $\lambda$  and  $\lambda_1$  increase smoothly with increasing relative density (decreasing porosity).

An interesting plot is given by the ratio  $(\lambda/\lambda_1)$  as a function of porosity (see Fig. 60). Clearly, the lowest possible value of  $(\lambda/\lambda_1)$  is unity. At this value, the microstructure consists of uniformly distributed pores. As densification continues, the ratio increases which indicates the development of a nonuniform spatial distribution of pores. The large change in slope in Fig. 60 (at  $\sim 90\% \rho_{th}$ ), as we approach final stage sintering, indicates that nonuniform spatial distribution of pores is an important contributing factor in the failure to obtain a microstructure that is theoretically dense. Shrinkage requires a coordinated change throughout the whole compact. This becomes difficult when the spatial distribution of pores becomes very nonuniform.

In Fig. 61, (1)  $\ln(\lambda^3 - \lambda_0^3)$  vs.  $\ln$  time and (2)  $\ln(\lambda_1^3 - \lambda_{10}^3)$  vs.  $\ln$  time were plotted by using the curves in Figs. 58 and 21 (similar to the way Fig. 48 was determined).  $\lambda_0$  and  $\lambda_{10}$  are the initial values of  $\lambda$  and  $\lambda_1$ , respectively, when the dense microregions first develop. These plots should yield straight lines with a slope of one if a cubic growth law holds. It is observed that the data fit straight lines over a large range of densities. However, the slope changes with temperature and only at 1660°C for the  $\lambda_1$  plot is the slope of unity obtained. This change in growth law with temperature is to be expected for any micro-

structural parameter in which the data points (at all temperatures) fall on a single curve when plotted against porosity (or density). This follows from the fact that the slopes of the  $\% \rho_{th}$  vs.  $\ln$  time plots increase with temperature; i.e. a single growth law would be observed for  $\lambda$  (and for  $\lambda_1$ ) if the slopes of the  $\% \rho_{th}$  vs.  $\ln$  time plots were constant with temperature. The theoretical significance of the slopes of the  $\% \rho_{th}$  vs.  $\ln$  time plots is not understood at the present time.

## B. "Gel" Process Material

### 1. The Green State

One "gel" composition - 73 wt%  $\text{Al}_2\text{O}_3$ /27 wt%  $\text{SiO}_2$  - was used in this portion of the study. The gelled mixed oxides agglomerate upon drying as seen in Fig. 62. These form partially sintered aggregates upon calcination. The calcined material was sintered (1) without any grinding and (2) with vibratory grinding from 0.5-12 h. Aggregates are rapidly broken down upon grinding (Fig. 63, upper micrographs). Table 8 illustrates this rapid comminution also; grinding for 0.5 h has reduced the "average" particle size to  $\sim 1/3$  the value of the uncalcined material. Rapid size reduction, indicating mechanically weak particles, is consistent with the fact that these aggregates are porous (i.e. only partial sintering of agglomerates has occurred). The relatively small surface area increase is also indicative of the breakdown of porous particles. In addition, the specific surface area of  $3.8 \text{ m}^2/\text{g}$  for 5.4 micron particles implies either (1) very irregular particle shape or (2) porous particles. For example, with solid spheres,  $S_g = \frac{3}{\rho R}$  where  $S_g$  is the specific surface area,  $\rho$  is the theoretical density of the material, and  $R$  is the particle radius. For mullite ( $\rho \approx 3.19 \text{ g/cm}^3$ ), a 5.4 micron diameter yields  $S_g = .35 \text{ m}^2/\text{g}$  which is approximately an order magnitude lower than the observed specific surface area.

Very large interaggregate pores are present in the zero grind time compact. Interaggregate pores decrease in size as aggregates decrease in size (with increasing grinding time). In fact, the largest pores present in each compact result for different reasons. In the zero grind time compact, the very large pores do indeed result from packing

Table 8. Powder Characteristics of "Gel" Mullite.

Grinding Time (hrs)	Average Particle Diameter (microns)	Surface Area (m <sup>2</sup> /g)	True Density (g/cc)	Green Density (% Theoretical)	Compaction Pressure (MN/m <sup>2</sup> )
0	5.4	3.8	3.19	53	310
0.5	1.7	4.8	3.18	54	210
1	1.4	5.1	3.19	54.5	210
5	.8	6.8	3.19	55	170
12	.7	7.4	3.20	55	140

of very large aggregates. In the twelve hour ground compact, the largest porosity present is the result of agglomeration effects during compaction. In the intermediate case of one hour grind time, both large aggregates and agglomerate effects appear to be responsible for large pores.

At high magnification (Fig. 63 bottom micrographs), it is seen that the individual crystallite size is approximately the same ( $\sim .1 - .5$  microns), regardless of grinding time. Aggregates, up to  $1 - 2 \mu$ , still exist in the twelve hour ground compact (Fig. 63 lower, far right micrograph) because vibratory milling becomes ineffective in achieving particle size reduction below  $\sim 1 - 2$  microns.

No quantitative pore size information was obtained on the green compacts. However, some qualitative observations can be made. First, consider the 12 h ground compact. Very small pores (order of magnitude  $\sim .1$  micron) exist within the small aggregates (intra-aggregate pores). A range of larger pore sizes ( $\sim 2 - 3$  microns and less) exists due to the range of aggregate sizes and due to the agglomeration effects. The 12 h ground compact's pore size distribution would appear to be at least bimodal. As we progress to shorter grinding times, the distribution is probably trimodal. In zero ground compacts, very large pores (order of magnitude  $\sim 10$  microns) exist between the large aggregates as well as very small (order of magnitude  $\sim .1$  micron) pores within aggregates. In addition, the large aggregates are not homogeneous (Fig. 64), and intermediate size (order of magnitude  $\sim 1$  micron) pores are present. Intermediate size pores also exist in the short grind time compacts due to the range aggregate sizes.

The importance of the green compact's character on the microstructural evolution during sintering and on the densification kinetics is discussed below.

## 2. "Final" Density

The effect of the green state on the maximum density achieved is shown in Fig. 65 ( $\% \rho_{th}$  vs. time plots at 1660°C for powders ground 0-12 h) and Fig. 66 (micrographs after sintering at 1660°C, 18 h for powders ground 0 - 12 h). Aggregate areas and agglomerated areas sinter to maximum density while interaggregate/interagglomerate areas remain porous. Large interaggregate pores in the green compact (short grind times) result in a lower final density for a given sintering time and temperature. These results indicate the importance of uniform packing of powder particles for achieving high densities. In each case, the individual particle size is small ( $\sim .1 - .5$  microns) and the overall green density is approximately the same ( $53 - 55\% \rho_{th}$ ). However, the packing becomes more uniform with more extensive grinding. Even after 12 h grinding time, packing is not completely uniform which probably accounts for the residual nonuniformly distributed porosity after extensive sintering (Fig. 66, far right).

## 3. Densification Kinetics

Figures 67 - 71 show the density vs. time plots for 0 - 12 h ground materials. It is observed that: (1) Densification kinetics are enhanced with increased grinding time. This is expected since surface area is increasing and particle size is decreasing with increasing grinding time. (2) As discussed above, a lower maximum density is associated with shorter grinding time. (3) At low temperatures for 0, 0.5, and 1 h

ground materials, an increase in densification rate is initially observed.

The data are replotted as density vs. logarithm of time in Figs. 72 - 76. The first point at each temperature on these curves is for a time measured from the moment the sample is plunged into the hot zone until the sample is quenched from the furnace. Therefore, the actual sintering time is somewhat less than indicated (except for the sample surface). Regions of different densification behavior are indicated by the upward changes in slope observed in all curves at low temperatures. Except for the first slope change at 1540°C and 1580°C in the 0 and 0.5 h ground samples, these changes are not associated with an increase in densification rate (as can be seen in Figs. 67-71 ). There is uncertainty in drawing the curve between the first and second points. In several instances in the 1 h, 5 h, and 12 h compacts, a slope change between the first and second points is indicated although

no experimental point is available to confirm such a break. This is done so that the transition between two particular regions occur at approximately the same density for each temperature. For example in the 5 h ground material (Fig. 73), the transition between (1) Region I and Region II occurs at  $\sim 60\% \rho_{th}$  and (2) Region II and Region III occurs at  $\sim 69\% \rho_{th}$ .

Before attempting to explain the observed experimental results, a qualitative analysis of the effect on sintering kinetics of packing a compact with widely different sizes of particles (and pores) is needed.

According to a model system analysis,<sup>40</sup> a linear densification rate is predicted for a simple cubic packed arrangement of uniform size spherical particles, with isotropic interfacial energies, until the (100) planar pores close. Assuming no thermodynamic barrier exists, densification would proceed at a decreasing rate until all pores are eliminated.

Consider the packing arrangement in Fig. 77. The largest size spheres are packed in a simple cubic manner. These spheres are composed of intermediate size particles which also form a simple cubic structure. In turn, the latter particles are composed of small particles with the same packing. The solid density fraction of such an arrangement is  $\sim .141$ . A density vs. time curve is constructed in Fig. 78 by adding the individual contributions of the three particle size regimes. A tenfold decrease in the linear densification rate portion of the curves was arbitrarily chosen for the transition from (1) small particles to intermediate size particles and (2) intermediate size particles to large particles.



Now, consider a system with a distribution of sizes, but with three modes in the distribution as in Fig. 79. In Fig. 80, a plot is constructed assuming intermediate stage behavior in which density is proportional to the logarithm of time from the onset of densification. The initial solid density, the range of densification for each particle size regime, and the time length of each densification stage are all arbitrarily chosen. In Figs. 78 and 80, sintering of each particle size regime was assumed to begin at the same time. In Fig. 81, the plot is constructed with densification of particle size regimes III (large) and II (intermediate) beginning when densification is nearly complete in regimes II (intermediate) and I (small), respectively. The basis for this construction is the observation in Section IIIA.3. that small particles densify quickly and, by their "pulling away," large pores open. In terms of the analysis by particle size regime, the overall densification curve of regime II, as an example, includes (1) the component of densification of regime II particles plus (2) the component of de-densification as pores open between these particles as the result of regime I sintering. Hence, the first portion of the regime II curve could easily have the indicated zero slope. The upward changes in slope in the  $\rho_{th}$  vs. logarithm of time plot do not indicate an increase in densification rate as confirmed by Fig. 81C.

Figures 82 and 83 schematically illustrate the effect of temperature on curves of the form in Figs. 80 and 81. This is constructed by changing the length of time required to complete a given densification range (smaller times for higher temperatures, longer times for lower temperatures). In this ideal case, the time was changed by the

same factor at each temperature from one particle size regime to the subsequent one. Clearly, this does not take into account the fact that a change in mass transport mechanisms, due to a change in temperature, is more likely to occur with small particles than with large particles.

There is a good deal of similarity between the mathematically generated curves in Fig. 83 and the experimentally determined  $\% \rho_{th}$  vs.  $\ln_{time}$  plots, particularly for the 12 h ground "gel" material. The agreement is better when the initial portion of the curves in Fig. 83 is neglected. This region does not accurately reflect the densification behavior in a real system because (1) the proportionality between  $\% \rho_{th}$  and  $\ln_{time}$  was assumed to begin from the onset of densification and (2) uncertainty arises since the density at zero time cannot be represented on a semi-logarithmic plot.

The amount of densification between the green density ( $55\% \rho_{th}$ ) and the first measured point ( $56.6\% \rho_{th}$  for  $1540^{\circ}\text{C}$ , 6 min) in the 12 h ground material is similar to that observed in the 73 IP samples ( $58\% \rho_{th}$  to  $60.3\% \rho_{th}$  for  $1540^{\circ}\text{C}$ , 10 min). More rapid densification might have been expected with the 12 h "gel" material since its specific surface area is  $\sim 4$  times that of the 73 IP material. Except for this initial period, an enhanced densification rate is observed for the "gel" material (compare Figs. 72 and 21). The similarity in initial periods for the two materials reflects the fact that the "gel" material consists of aggregates (about the size of the 73 IP particles) which are already partially sintered (due to the earlier calcination). Sintering within aggregates begins from the onset but no rapid period of densification, equivalent to cluster formation in the 73 IP samples, is observed.

In the 73 IP material, the initial upward slope described in Fig. 35 is now interpreted in terms of the transition from sintering of individual particles to sintering of dense (polycrystalline) clusters. The observed densification in the first region for the 12 h ground "gel" material (Fig. 72) is due to the elimination of very small intra-aggregate pores in the partially sintered aggregates. In Fig. 84, the high magnification micrograph (top) of the 1580°C - 1 h sample ( $64.3\% \rho_{th}$ ) shows that some aggregates are almost completely dense. The second region in Fig. 72, beginning at  $\sim 62\% \rho_{th}$ , consists of the elimination of larger intra-aggregate pores and small inter-aggregate pores. The third region, beginning at  $\sim 70\% \rho_{th}$ , reflects the sintering of larger inter-aggregate and of inter-agglomerate pores. These stages are clearly seen in the micrographs in Figs. 84, 85. The high magnification micrographs (Fig. 84) show that from 1580°C - 1 h ( $64.3\% \rho_{th}$ ) to 1580°C - 6 h ( $76.1\% \rho_{th}$ ) elimination of small pores (region II) is occurring. The low magnification micrographs (Fig. 85) show the elimination of large pores (region III) from 1580°C - 6 h ( $76.1\% \rho_{th}$ ) to 1580°C - 18 h ( $83.5\% \rho_{th}$ ).

The micrograph of the 1580°C - 6 h sample in Fig. 86 clearly reflects the micro-inhomogeneity of the "gel" materials. This sample has a density just beyond the transition density between regions II and III. Hence, aggregates undergoing final stage sintering (with very small entrapped pores and relatively large grains) are observed together with large porous regions (that were inter-agglomerate pores in the green compact) in which only necks have formed between grains.

A single slope is observed in the  $\% \rho_{th}$  vs.  $\ln$  time plot (Fig. 72) at 1620°C due to the overlap of regions II and III. At this temperature,

region I is completed prior to the first experimentally measured point. These results are consistent with the curves generated in Fig. 83. At 1660°C and 1700°C, the transition into final stage densification is observed at densities of  $\sim 93-95\% \rho_{th}$ .

The 0 h ground "gel" material is taken as an example that reflects the differences in densification behavior between short and long grind time "gel" materials. The unusual observation of an increased densification rate (Fig. 71) can only be explained on the basis of an increased number of particle contacts being formed. The appearance of the initial slow period of densification, followed by an increased densification rate, is observed in short grind time samples only. This indicates a difficulty in forming contacts between the large aggregates that are present in the short grind time materials.

The observed regions II and III behavior in the 12 h grind material is also expected in the 0 h grind material since small (intra-aggregate) and intermediate (intra- and inter-aggregate) size pores are present. Figure 87 plots the regions II and III behavior at 1580°C materials ground 0 - 12 h. An increase in the transition density is observed:  $\sim 62\%$  (0hr),  $\sim 66\%$  (0.5 h),  $\sim 66\%$  (1 h),  $\sim 69\%$  (5 h),  $\sim 71\%$  (12 h). This reflects the fact that the fraction of pores in the green compact that are small ( $< \sim .5 \mu$ ), which are eliminated in regions I and II, increases with grinding time. (Since the green density is approximately the same for the 0 - 12 h ground materials, the total pore volume is approximately the same. Materials ground for short times clearly have a sizeable fraction of very large pores in the green compacts (Fig. 63), while the long grind time samples have no large pores. Therefore, the long

grind time compacts must have a higher percentage of small pores).

In the 73 IP, 73 PP, and 75 IP samples, the proportionality between  $\%P_{th}$  and  $\ln$  time existed until final stage densification began at  $\sim 90 - 95\%P_{th}$ . This is also observed in the 5 and 12 h ground "gel" materials. In short grind "gel" materials, the proportionality ends at lower densities and is temperature dependent (Figs. 74-76). Region III behavior (removal of intermediate size pores) must end at lower densities in short grind time materials because there is at least one extra region — elimination of large pores between large aggregates. The apparent temperature dependence is more difficult to explain. It could indicate that mass transport mechanism(s) change with temperature. However, the results with 73 IP suggest that other alternatives should be considered. (In 73 IP, microstructural evolution — i.e. changes in mean grain size, mean pore intercept size, mean free path between pores, open porosity, etc. — is dependent on the density, but not on the sintering temperature).

Another possible explanation is that sintering time was not long enough to observe all the densification regions. The appearance of the micrographs (Fig. 66) is consistent with the previous analysis of large pores "opening up" as aggregates sinter and "pull away." In the idealized curves in Fig. 83, the observable densification of a particular particle size regime began at a density shortly before complete densification of the preceding regime. In the densification kinetics for short grind time "gel" samples, the removal of pore volume between large aggregates may not begin until complete densification of aggregates has occurred. For example, if sintering had been continued for longer times at 1620°C with the 0 h and 0.5 h ground materials, another region (with

a proportionality between  $\rho_{th}$  and  $\ln$  time) might have been observed in Figs. 75 and 76. At higher temperatures, the transition between such regions may not be as distinguishable, such as illustrated by the effect of increased temperature on the regions I - II and regions II - III transitions.

## C. Effects of Sintering Atmosphere

### 1. Introduction

In order to attain a particular microstructure (with its associated desired properties) by sintering, a materials technologist must be concerned with processing. This will include raw materials selection (composition, purity, particle size, etc.), raw materials preparation (mixing, beneficiation, grinding, etc.), forming (dry pressing, casting, extrusion, etc.), pre-sintering heat treatment (drying, calcination, etc.), and the sintering process itself (time, temperature, atmosphere, heating and cooling rate, etc.). Each microstructural feature (total porosity, average grain size, etc.) and their interrelationships will be affected by the preceding variables. From an economic point of view, it is desirable to achieve the desired microstructure by sintering at low temperatures for short times. This emphasizes the importance of the first three groups of variables listed above. In terms of achieving high densities, for example, three common approaches are (1) the use of fine particle size materials, (2) addition of second phase or solid solution additives, (3) forming to high green densities. Another approach, however, is to alter the sintering atmosphere which can change (1) the densification rate and (2) the "final" density achieved.

The importance of sintering atmosphere on the "final" density achieved has already been mentioned in section IIA.2. Sintering atmosphere can affect the densification rate by altering the bulk defect and/or surface structures. The atmosphere may affect the surface structure by processes such as chemisorption, decomposition, etc. These processes may alter the thermodynamic driving force for sintering since the ratio

of surface energy to grain boundary energy ( $\gamma_{SV}/\gamma_{SS}$ ) may vary with surface structure. The bulk defect structure is important because lattice diffusion takes place by the reverse flux of vacancies. In oxides, for example, the partial pressure of oxygen will affect the concentration of lattice vacancies. The densification rate will be directly affected if oxygen is the slower diffusing species. A number of studies have provided experimental evidence for both changes in surface energy and in diffusivity due to changes in sintering atmosphere.<sup>2,35,63-67</sup>

## 2. Vacuum Sintering

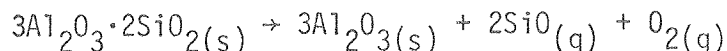
During the initial experiments with a broad range of compositions, vacuum sintering at 1700°C for 12 h was compared with air sintering under the same time and temperature conditions. These results (Fig. 88) show that vacuum firing yields a higher density for all compositions.

One must be extremely cautious in drawing conclusions about densification rate from data of the final density measured. However, the final stage appearance (exaggerated grain growth and entrapped pores) of the 73 IP and 74 IP samples (Fig. 89) in conjunction with the detailed densification kinetics in air sintering (73 IP, 73 PP, 75 IP), indicates an enhanced densification rate for samples above 71.8 wt%  $Al_2O_3$ . Since maximum density is reached very quickly with 60 IP and 65 IP samples, conclusions cannot be drawn regarding densification rate.

Unfortunately, a significant weight loss is associated with vacuum sintering (Fig. 90). The volatility of silica and siliceous glasses under conditions of low oxygen partial pressure and elevated temperature is well known.<sup>68,69</sup> Earlier studies have indicated that mullite, although more stable than  $SiO_2$ , decomposes at high temperatures under low partial



pressures of oxygen to:



Alumina is stable under low partial pressures of oxygen to higher temperatures than the present sintering conditions. Consequently, weight losses are large in 60 IP and 65 IP, with large siliceous glass contents, and decrease with increasing overall alumina content. Weight loss in air sintering is ~0.1wt% or less in each composition. This small loss can be accounted for by desorption of moisture, volatilization of organic contamination, etc.

Figure 91A shows surface decomposition in a 71.8 IP sample sintered in vacuum. The top half of the micrograph is a porous surface alumina layer. The EDAX display in Fig. 91B confirms this. The peaks from left to right are Al, Si, and Au. The dotted spectra is from the bulk interior (mullite) while the lined spectra, containing only Al and Au, is from the surface layer. The top half of Fig. 91 is a plot of weight loss vs. firing time at ~1715°C for vacuum and air firing of the 71.8 IP sample. The decreasing rate of weight loss in vacuum firing indicates that sintering of the porous surface alumina is occurring. This is confirmed in Fig. 92. Unfortunately, ~15% weight loss has occurred in the 71.8 IP sample in Fig. 92A. In addition, we would expect the coarse grained (see Fig. 92B), porous  $\text{Al}_2\text{O}_3$  surface layer to be very weak mechanically. Spontaneous cracking has also occurred in these samples (Figs. 92A and 92C).

It should be noted that the reported densities are obtained after grinding off the porous  $\text{Al}_2\text{O}_3$  surface layer. Some of the weight loss is

expected from the interior of the specimen since it is relatively accessible until pores close. Consequently, the percent theoretical density values reported are somewhat high because the theoretical density value is based on the starting composition. The inaccuracy is expected to be quite small for samples above 71.8 wt%  $\text{Al}_2\text{O}_3$  composition because (1) the total weight loss is small and (2) the difference in theoretical density of mullite ( $\sim 3.2$  g/cc) and  $\text{Al}_2\text{O}_3$  ( $\sim 4.0$  g/cc) is not very large.

Evidence for small weight losses before complete pore closure is given by the appearance of "ridges" on grain boundaries (Figs. 89, 93, and 94). Figures 93A and 94A are micrographs of vacuum sintered 71.8 IP samples. The polished surfaces in these micrographs were thermally etched in air at  $\sim 1550^\circ\text{C}$  for  $\sim 30$  min. The formation of ridges, a positive volume change, suggests that oxidation has occurred during air etching. The ridges are areas of high chemical potential and they should be reduced, probably by surface diffusion, during extended annealing. This is shown in Figs. 93B and 94B in which the "A" samples have been annealed in air at  $1600^\circ\text{C}$  for 100 h. The initial oxidation upon etching might be expected if the surface structure was initially oxygen deficient due to vacuum firing (in which partial decomposition of the mullite occurred). However, this decomposition could not be too extensive because no alumina layer is observed.

The sample in Fig. 94A was initially sintered in air to  $\sim 83\% \rho_{\text{th}}$  before vacuum sintering. At this density, a considerable amount of grain boundary formation and pore closure has occurred. Yet, ridges are observed on almost all grain boundaries. This suggests the possibility that oxygen may be sufficiently mobile to diffuse out of the partially

densified mullite structure during the subsequent vacuum sintering. The distance that the oxygen must diffuse through the solid depends on the open porosity and on the spacing between open pores. On the bulk surface (or on the particle surfaces before significant sintering has occurred),  $\text{SiO}_{(g)}$  and oxygen can readily escape after decomposition, leaving an  $\text{Al}_2\text{O}_3$  layer. We would not expect a residual  $\text{Al}_2\text{O}_3$  layer to undergo oxidation (which has been postulated as the cause of grain boundary ridges). However, in the interior of the specimen, we would expect diffusion of silicon monoxide through the solid to an open pore to be very slow compared to oxygen diffusion. Hence, only partial decomposition (oxygen loss) of mullite is postulated for the specimen interior after significant sintering has occurred. This is more consistent with the observed appearance of grain boundary ridges upon air etching.

### 3. Limiting Density and De-densification

#### (a) 60 wt% $\text{Al}_2\text{O}_3$ Composition

More evidence is provided for earlier conclusions regarding observations of a limiting density followed by de-densification (i.e. macroscopic expansion) due to entrapped gas. Table 9 lists the bulk density and % theoretical density values of 60 wt%  $\text{Al}_2\text{O}_3$  "gel" and "powder" samples sintered at 1700°C in various atmospheres.

The micrographs of 4 and 100 h, air sintered, "powder" and "gel" samples in Fig. 15 show that pore growth has occurred. As noted earlier (Fig. 16), the 60 IP ("powder" process) vacuum sintered microstructure is nearly pore-free because very little gas is entrapped when pores close. However, the bulk density values in Table 9 are higher than the theoretical value (3.01 g/cc). This is explained by a weight loss

Table 9. Density of 60 wt% Al<sub>2</sub>O<sub>3</sub> Samples Sintered in Various Atmospheres at 1700°C.

Atmosphere	Sintering Time(hrs)	"Powder"		"Gel"	
		Bulk Density (g/cc)	% $\rho_{th}$	Bulk Density (g/cc)	% $\rho_{th}$
Air	1	2.91	96.7		
	4	2.90	96.3	2.94	97.6
	100	2.88	95.7	2.90	96.3
Argon	4	2.85	94.7	2.89	96.0
	100	2.84	94.4	2.86	95.0
Vacuum	4	3.04	see text	3.01	see text
	100	3.05		3.00	

of silica before pores can close. After pores close, weight loss is primarily from the surface of the sample. The surface layer is removed prior to density determination. However, the weight loss before pore closure cannot be avoided and the composition shifts to a higher overall alumina content. Hence, the bulk densities measured are higher than the theoretical values for a 60 wt%  $\text{Al}_2\text{O}_3$  composition. The loss of silica is evident in the reduced amount of glass phase (compared to air sintering) in the vacuum sintered micrograph (see Fig. 95A, B).

With the fine particle size "gel" material, a higher silica weight loss might be expected and, therefore, higher bulk density values. The loss of silica is evident (Fig. 96A, B). Higher bulk densities are not observed, however, because pores still remain in the microstructure (Fig. 97). The reason for this behavior is uncertain. It is possible that the highly reactive "gel" material more strongly retains adsorbed films, moisture, etc. Since pore closure is expected to be extremely rapid due to the liquid phase and the fine particle size, these volatiles may be entrapped. A similar possibility is the entrapment of greater amounts of  $\text{SiO}_{(g)}$  which is present due to decomposition, under the low partial pressure of oxygen, of the siliceous glass phase.

A larger pore size is observed in argon sintered microstructures compared to those fired in air (Figs. 16 and 98). This could indicate: (1) an enhanced pore growth rate and/or (2) a larger "initial" pore size before pore growth occurs; i.e. when shrinkage stops the pore radius may be larger due to differences in the ambient pressure and/or the surface energy ( $P=2\gamma/R$ ). Pore growth may then occur at a similar rate for air and argon sintering, but would result in the larger pore size observed

in argon sintering.

It is not possible to provide a definitive explanation of the observed microstructures without a detailed quantitative kinetic study. However, a qualitative comparison of the various microstructures and a consideration of the possible mechanisms of pore growth (and grain growth) can be used to interpret the observed effect of atmosphere on microstructure development. The two explanations listed above are now discussed in more detail.

The second explanation for a larger pore size in argon sintering requires a consideration of pressure and surface energy effects. First, suppose the average pressure in the closed pores is the same in argon and air sintering. In order for shrinkage to stop at a larger average pore size in argon,  $\gamma_{SV}$  must be larger. It is anticipated, based on the results obtained in vacuum sintering, that an oxygen deficient mullite structure will develop during argon sintering. Such a structure would have a higher surface energy. Secondly, a higher average pressure is actually expected in the closed pores in argon sintering due to volatilization of silica (and entrapment of silicon monoxide gas). In addition, the pressure in the pores during air sintering may be lowered by oxygen diffusion to the surface, as oxygen is expected to be the most mobile of the four gas molecules (oxygen, nitrogen, argon, and SiO).

Consistent with the above interpretation are the microstructures in Figs. 16 and 98 labelled "sealed Mo." These samples were sintered in the Brew furnace in molybdenum crucibles which were sealed (by welding) under slightly less than 1 atm of argon. Upon heating, pressures significantly increase. In argon and air, the ambient pressure is ~1 atm

when pores first close. In the sealed crucible, the pressure is ~5 atm when pores first close. No density measurements could be made on these samples, but the microstructures indicate that they have the largest pores and lowest bulk densities.

The observed grain size (Figs. 95 and 96) is consistent with the above interpretation if grain growth occurs primarily by a solution-precipitation process in which larger particles grow at the expense of smaller particles (an Ostwald ripening process)<sup>70</sup>. It is expected that the pressure exerted by the gas filled pores will increase the solubility of the solid mullite in the liquid phase. Thus, the grain size would be expected to increase in the order of increasing pressure in the pores, i.e. vacuum < air < argon < "sealed Mo." Figures 95 and 96 indicate vacuum  $\approx$  air < argon < "sealed Mo" for the 100 h sintering time. The fact that the air and vacuum sintered grain sizes are roughly the same suggests that surface energy effects are important in determining the grain growth rates. The oxygen deficient mullite structures developed in vacuum, argon, and "sealed Mo" sintering will have higher surface energies (than in air sintered mullite) which provide a larger driving force for grain growth. It is interesting that the 4 h vacuum sintered sample has a much smaller grain size than the comparable air sintered sample (Fig. 99). An initially low grain growth rate in vacuum could be due to the loss of silica (i.e. less glass phase is present) that occurs before pores close. The enhanced rate (compared to air firing) after 4 h could indicate that the effect of increased surface energy has become dominant.

The possibility of an enhanced pore growth rate as the cause for the observed differences in pore size (with sintering in different atmospheres) is now considered in more detail. Pore growth may occur by three mechanisms: (1) Gas is created in the closed pores. The resultant increase in pressure may be relieved by expansion of the pores. (2) An Ostwald ripening process may occur in which gas and vacancies diffuse through the sample to eliminate small pores in favor of large pores (which have a lower interfacial energy). The driving force for gas diffusion exists due to the pressure gradient (i.e. there is a higher pressure in small pores, as indicated by  $P=2\gamma/R$ ). The vacancy concentration gradient is expected by the Thomson-Freundlich equation. (3) Mobile pores "attached" to grain boundaries may coalesce during grain growth.

Mechanism (1) is not considered likely in our system for several reasons. First, pore growth is observed in air sintering (Fig. 15). Both the mullite and glass phase are stable at 1700°C in air. Gas creation by decomposition (which forms  $\text{SiO}_{(g)}$  and  $\text{O}_{2(g)}$ ) only occurs under low partial pressures oxygen. Secondly, an equilibrium partial pressure of silicon monoxide gas will be quickly established in the closed pores during vacuum, argon, and "sealed Mo" sintering and further decomposition will be inhibited. The kinetic study with 60 IP (Fig. 14) indicates that pores will close by the time temperature is reached when sintering is at 1700°C. Therefore, no gas creation within pores is expected between 4 and 100 h sintering times.

Pore growth by mechanism (2) (Ostwald ripening) is not necessarily consistent with the explanation of different pore growth rates

in different sintering atmospheres. Gas migration



is necessary for pore growth and de-densification in mechanism (2). The solubility in mullite and the diffusion through mullite of nitrogen (air sintering) and argon, with their large molecular diameters ( $3.2\text{\AA}$  and  $3.4\text{\AA}$ , respectively), should be negligible. Glass phase, with its open structure, would provide the medium for solution and diffusion. Information on gas solubility in glasses is limited, but results indicate a rough correlation between gas molecular diameter and solubility. Consequently, very little difference is expected in solubility among oxygen (molecular diameter  $3.2\text{\AA}$ ), nitrogen, and argon. Studies on fused silica at  $\sim 1000^\circ\text{C}$  indicate the same solubility for oxygen and argon of  $\sim .01 C_i/C_g$ , where  $C_i$  is the concentration of gas dissolved in the glass and  $C_g$  is the concentration of molecules in the gas phase. No data was available on nitrogen solubility. Diffusion data in glasses are also limited. Data on fused silica at  $1000^\circ\text{C}$  are given in Table 10. Data on He and Ne were included in Table 10 to show the strong dependence of diffusion on the molecular size of the diffusing species. Considering the slightly larger size of nitrogen, the results indicate that gas migration rates should be roughly the same in air and argon sintering. Hence, if pore growth is controlled by gas diffusion, the rate of pore growth should be roughly the same for air, argon, and "sealed Mo" sintering. Considering the nearly pore-free microstructure for 60 IP in vacuum firing (Fig. 16), a gas diffusion controlled mechanism is reasonable.

The third mechanism of pore growth is coalescence by grain boundary migration. Since the initial grain size is the same in each case, the average grain growth rate increases in the order "sealed Mo" > argon > air. This implies an enhanced pore growth rate if mechanism (3) is

Table 10. Diffusion and Solubility Data for Various Molecules in Fused Silica at 1000°C.

Molecule	Diameter (Å)	Diffusion Coefficient (cm <sup>2</sup> /sec)	Activation Energy (kcal/mole)	Solubility (C <sub>i</sub> /C <sub>g</sub> )
O <sub>2</sub>	3.2	1.4 x 10 <sup>-9</sup>	26.6	~.01
Ar	3.2	6.6 x 10 <sup>-9</sup>	25	~.01
N <sub>2</sub>	3.4	not available	~26 <sup>*</sup>	not available
Ne	2.4	2.5 x 10 <sup>-6</sup>	8.8	~.019
He	2.0	5.5 x 10 <sup>-6</sup>	4.8	~.024

\* Estimated from permeation experiments.

operative. However, it is not clear that mechanism (3) is realistic for systems with large amounts of liquid phase.

A microstructure with solid crystalline grains, dispersed in a glassy matrix, develops when (1) large amounts of glass phase are present or (2) the solid-liquid dihedral angle approaches zero. In these cases of complete wetting of the solid crystals, grain growth must occur by a solution-precipitation mechanism. Figure 100 shows grain growth in a system with large amounts of glass phase. A 45.9 wt%  $\text{Al}_2\text{O}_3$  (A-14)/54.1 wt%  $\text{SiO}_2$  (silica flour) mixture was reaction sintered at 1700°C to form mullite and glass (Fig. 100A). Reaction is complete because only mullite, and no  $\alpha\text{-Al}_2\text{O}_3$ , is detected in the x-ray diffraction pattern. Upon additional heat treatment (Fig. 100B), mullite grains grow with an elongated morphology. The presence of mullite precipitation "rims" (with glass phase interiors) in Fig. 100B indicates that compositional fluctuations exist in the glass phase. Nucleation (and solution) of mullite grains in the glass phase is occurring as well as deposition (precipitation) of mullite on (and solution from) existing grains. When the overall  $\text{Al}_2\text{O}_3$  composition is increased up to 65 wt% (which decreases the amount of glassy phase), the same elongated morphology of the mullite grains persists (Fig. 101). This suggests that the solution-precipitation mechanism is still operative in our 60 wt%  $\text{Al}_2\text{O}_3$  samples. Grain growth kinetics studies by Buist, et al. provide support for the solution-precipitation mechanism in systems with only 15 vol % liquid phase. Furthermore, the angular mullite grains (i.e. lack of curvature) suggest that a low driving force exists for grain boundary migration. In addition, the anisotropic growth (i.e. elongated morphology) indicates that most of the

mullite surfaces consist of low energy crystallographic planes. Therefore, grain boundary migration due to highly anisotropic interfacial energies does not seem likely.

Although pore coalescence by grain boundary migration does not seem likely, coalescence can occur if two growing (by Ostwald ripening) pores impinge upon one another. Such a process is indicated by the micrographs in Fig.102. This process is more important in the systems with large amounts of entrapped gas.

In summary, the observed pore size appears to be dependent upon the entrapped gas pressure. Pore growth probably occurs by Ostwald ripening with some coalescence when growing pores impinge upon another. The observed mullite grain size is explained by the combined effects of the mullite surface energy and the entrapped gas pressure (which are both atmosphere dependent).

(b) 71.8 and 80 wt%  $\text{Al}_2\text{O}_3$  Compositions

Further evidence of pore growth and limiting density due to entrapped gas is seen in Figs. 103 and 104 in which 71.8 IP samples are fired from 4-100 h at  $\sim 1715^\circ\text{C}$  in air and in vacuum. Pore growth occurs between sintering times of 24 h and 100 h in air sintering (Fig.103D, E). This is consistent with the end of macroscopic densification at 24 h (Table 11). In vacuum firing (Figs. 104 and Table 11), no pore growth is observed and densities are higher.

Additional evidence is also provided by the results with 80 wt%  $\text{Al}_2\text{O}_3$  samples. Density values for air, vacuum, and argon sintered samples are given in Table 12 for "gel" and "powder" (IP) samples fired at  $1700^\circ\text{C}$  for 4 and 100 h.

Table 11. Density Values for 71.8 IP Samples Sintered in Air and Vacuum at 1715°C.

Atmosphere	Sintering Time (hrs)	Bulk Density (g/cc)	% Theoretical Density
Air	4	2.94	91.5
	4	3.01	94.7
	12	3.04	95.6
	24	3.05	95.9
	100	3.05	95.9
Vacuum	4	3.08	96.9
	8	3.13	98.4
	100	3.14	98.7

Table 12. Density Values for 80 wt%  $\text{Al}_2\text{O}_3$  Samples Sintered in Air, Vacuum, and Argon at 1700°C.

Atmosphere	Sintering Time (hrs)	80 IP		80 "Gel"	
		Bulk Density (g/cc)	% $\rho_{th}$	Bulk Density (g/cc)	% $\rho_{th}$
Air	4	2.73	81.1	3.27	97.1
	100	3.17	94.2	3.22	95.7
Argon	4	3.14	93.3	3.22	95.7
	100	3.13	93.0	3.18	94.5
Vacuum	4	3.04	90.3	3.33	98.9
	100	3.33	98.9	3.32	98.6

Table 12 shows that the "gel" samples all undergo de-densification. Pore growth is confirmed in Fig. 105. Growth of  $\text{Al}_2\text{O}_3$  particles (the white particles in Fig. 105) is also observed.

Pore growth due to gas creation is considered unlikely in these samples for the same reasons as in the 60 wt%  $\text{Al}_2\text{O}_3$  composition. In addition, it is noted that the decrease in bulk density (Tables 9 and 12) is nearly the same for both 60 and 80 wt%  $\text{Al}_2\text{O}_3$  "gel" samples. If gas creation was an important mechanism in pore growth, we would expect a much larger drop in bulk density in the glass-containing samples.

Ostwald ripening mechanisms were considered earlier to explain the observed pore growth in the 60 wt%  $\text{Al}_2\text{O}_3$  samples. These mechanisms are less likely in solid state sintering. Gas diffusion through the mullite matrix will be extremely slow. Pore growth by Ostwald ripening during solid state sintering has been proposed,<sup>43</sup> but experimental evidence has not been provided. Growth of  $\text{Al}_2\text{O}_3$  particles by diffusion through the mullite matrix is also considered unlikely due to low diffusivities.<sup>29</sup>

Second phase inclusions (such as pores and  $\text{Al}_2\text{O}_3$  particles) affect grain growth. Assuming that individual particles (grains) in a powder compact are dense (non-porous) and single phase, second phase inclusions are initially found on grain boundaries (as opposed to existing in the interior of the grains). In order for grain growth to occur, grain boundaries must either (1) migrate past the inclusions or (2) "drag" the inclusions along.<sup>57</sup>

Grain growth mechanism (1) requires that either (a) a large driving force for boundary migration exists or (b) inclusions are small in size and in number (i.e. total interfacial area is small). These requirements

are based on the fact that a straight, isotropic grain boundary cannot move past an inclusion because this would require an increase in grain boundary area (and, therefore, an increase in grain boundary energy). In order to move past an inclusion, the grain boundary must have sufficient curvature so that the net grain boundary area (and energy) is reduced.

Grain growth mechanism (2) occurs in systems where the driving force for grain boundary movement is small and inclusions are relatively mobile. Movement of inclusions may occur by vapor phase, surface, or bulk diffusion mechanisms. Mechanism (2) can account for the growth of pores and  $\text{Al}_2\text{O}_3$  particles in the present study. Two observations in the micrographs of 100 h sintered 80 wt%  $\text{Al}_2\text{O}_3$  samples support this mechanism: (1) Simultaneous pore growth (Fig.105),  $\text{Al}_2\text{O}_3$  particle growth (Fig.105), and grain growth (see Fig. 106 and recall the starting particle size was ~2 microns) has occurred. (2) The pores and  $\text{Al}_2\text{O}_3$  particles entrapped in grains tend to be small, while most of the larger inclusions are intergranular. If this mechanism is operative, we would also expect that the samples with the largest grain size would have the largest  $\text{Al}_2\text{O}_3$  particle size. This is most easily confirmed by comparing the low magnification 100 h, air sintered, "powder" microstructure (Fig.107A) which has a small grain size (Fig.106A) with the low magnification 100 h, "sealed Mo" sintered, "gel" microstructure (Fig.107G) which has a large grain size (Fig.106G).

In air sintering of 80 IP samples, no pore growth is observed from 4 to 100 h (Fig.108) despite considerable grain growth. At 100 h of sintering ( $\sim 94\% \rho_{th}$ ), the final stage has only just started (i.e. only a few exaggerated grains and entrapped pores are observed). If pore



coalescence does occur during grain growth prior to final stage densification, the absence of pore growth indicates that densification (reduction in total porosity) has compensated for any coalescence that occurs. The high magnification micrographs indicate that  $\text{Al}_2\text{O}_3$  particle growth has occurred. This is expected since the total volume of  $\text{Al}_2\text{O}_3$  particles is unchanging.

As observed with the 60 wt%  $\text{Al}_2\text{O}_3$  materials, vacuum sintering of the 80 wt%  $\text{Al}_2\text{O}_3$  "powder" sample yields a slightly higher final density than the "gel" material. More residual porosity and the occurrence of pore growth is observed in "gel" samples on vacuum sintering for 100 h (Figs. 105 and 107). In the 80 IP sample vacuum sintered for 100 h, the residual porosity consists only of small pores entrapped within grains (Fig. 109). It is again suggested that some volatile material (i.e. adsorbed films, mullite decomposition products, etc.) are more readily entrapped in closed pores during vacuum sintering of the more reactive (i.e. faster densifying) "gel" materials.

The large size of pores, grains and  $\text{Al}_2\text{O}_3$  particles in the argon and "sealed Mo" sintered samples is consistent with the mechanism of coalescence by grain boundary movement. The lower densities in these samples is also consistent with the presence of larger amounts of entrapped gas (in contrast to vacuum sintered samples which have very little entrapped gas and sinter nearly to theoretical density). One interesting observation from Table 12 (80 IP) is that samples in argon sinter to maximum density faster than in air and vacuum. This fact, along with the enhanced grain growth rate in argon, again suggests the importance of atmosphere on the surface energy of mullite. It is postulated that the partial

pressure of oxygen in argon sintering is lower than in vacuum because the former atmosphere is static. The tantalum furnace elements will be a getter for oxygen. The lower partial pressure of oxygen would lead to a higher mullite surface energy and, therefore, a greater driving force for densification and grain growth. An increased concentration of oxygen defects in the bulk structure could also result in increased diffusivities. Although no densification data were collected in "sealed Mo" sintering, we expect samples would also densify faster than in vacuum because the argon environment is static and the molybdenum crucible will be a getter for oxygen present.

#### IV. SUMMARY AND CONCLUSIONS

$\text{Al}_2\text{O}_3$  and  $\text{SiO}_2$  raw materials were processed by two methods - "powder" and "gel" processes - to form mullite-containing materials for sintering studies. The effects of phase composition, particle packing arrangement in the green compact, powder surface area, and sintering atmosphere on microstructural evolution and sintering kinetics (densification and grain growth) were investigated.

Rapid densification was observed when large amounts of liquid phase were present during sintering. Even trace amounts of glassy phase, which can only be resolved by transmission electron microscopy, can cause notable increases in densification rate. However, it is important to be cognizant of trade-offs between increased densification rate and possible adverse affects on properties (such as high temperature strength).

In "powder" process materials with compositions near or within the mullite solid solution range, a proportionality was observed between % theoretical density and the logarithm of time for the various sintering temperatures. This observation is consistent with the predictions of several intermediate stage sintering models. However, these models were found to be inadequate in the present study because of the failure to fulfill other associated predictions and to meet the various assumptions upon which the derivation of a  $\ln$  time dependence was based. The physically inhomogeneous nature of the materials in this study was a contradiction to the ideal pore-grain boundary geometries used in the various models. The nonuniformity in packing and in size of particles led to the

rapid formation of dense microregions (in which pores in closely packed regions were quickly eliminated), while large pores "opened up" in regions which were initially packed with a low density. This development requires the use of an "effective grain size" as a measure of the diffusion path length during sintering. This parameter is experimentally determined by measuring the spacing between pores. Pore spacing measurements are also used to show that inhomogeneity affects the rate of approach to theoretical density.

In "gel" materials, enhanced densification rates with increasing grinding times of the calcined powders is observed due to increasing surface area (decreasing particle size). Particle packing was important in determining the final density. Although the initial pore volume was kept nearly constant, lower final densities were observed when large pores were present in the green microstructure. Packing arrangements also caused the occurrence of densification substages. A qualitative model was presented to explain this behavior.

In the past, the method of testing a sintering model has involved the measurement of the time dependence of densification (and possibly the time dependence of grain growth). The present study indicates that a detailed microstructural analysis is also required in order to assess whether a sintering model is physically realistic.

Sintering atmosphere, in which the total pressure and the partial pressure of oxygen were the important variables, affected the microstructural development and the rates of grain growth and densification. The

partial pressure of oxygen can affect the diffusion coefficients and the interfacial energies. The total pressure is an important factor in determining the amount of gas that is entrapped in pores. Quantitative studies of densification rates, grain growth rates and pore growth rates are needed to provide more definitive explanations regarding the relative importance of the various driving forces and mass transport mechanisms.

#### ACKNOWLEDGMENT

It is a pleasure to express my appreciation to Professor Joseph A. Pask for his guidance and encouragement during the course of this work. My association with Professor Pask has been an extremely rewarding experience.

Interaction with colleagues and friends, particularly Victor F. Draper, Dr. David N.K. Wang, and Dr. Bob Powell, Jr., was helpful in the completion of this work. I would also like to thank Professors Dennis W. Hess and K. V. Sastry, for their time and effort in reading and commenting on the thesis.

The technical assistance of the support staff of the Materials and Molecular Research Division, Lawrence Berkeley Laboratory was greatly appreciated. Special thanks are extended to Gay Brazil (manuscript preparation), Gloria Pelatowski (technical drawings), and Jack Wodei (equipment maintenance).

Thanks are also due to Judith Ann Haxo for assistance in the typing of the thesis.

Finally, I would like to thank my family for their continuous encouragement of my efforts.

This work was supported by the National Science Foundation and the Division of Materials Sciences, Office of Basic Energy Sciences, U. S. Department of Energy under contract No. W-7405-Eng-48.

## REFERENCES

1. J.A. Pask, et al., p.246 in Ceramic Microstructures '76, edited by R.M. Fulrath and J.A. Pask, Westview Press, Colorado (1977).
2. F. Thummler and W. Thomma, Metallurgical Reviews, 12, 69 (1967).
3. J. Frenkel, J. Phys. (U.S.S.R.), 9, 385 (1945).
4. B. Pines, J. Tech. Phys. (U.S.S.R.), 16, 737 (1946).
5. G.C. Kuczynski, J. Appl. Phys., 21, 632 (1950).
6. G.C. Kuczynski, Trans. Amer. Inst. Min. Met. Eng., 185, 169 (1949).
7. W.D. Kingery and M. Berg, J. Appl. Phys., 26, 1205 (1955).
8. D.L. Johnson and I.B. Cutler, J. Am. Ceram. Soc., 46, 541 (1963).
9. D.L. Johnson, J. Appl. Phys., 40, 192 (1969).
10. F.V. Lenel and G.S. Ansell, p.281 in Modern Developments in Powder Metallurgy, Vol. 1, edited by H.H. Hausner, Plenum Press, New York (1966).
11. P.C. Dokko et al., J. Am. Ceram. Soc., 60, 150 (1977).
12. R.L. Coble and J.E. Burke, p.197 in Progress in Ceramic Science, Vol. III, edited by J.E. Burke, Pergamon Press, Oxford, (1963).
13. W.D. Kingery and B. Francois, p. 471 in Sintering and Related Phenomenon, edited by G.C. Kuczynski, N.A. Hooten, and C.F. Gibbon, Gordon Breach, New York (1967).
14. H.E. Exner et al., p.351 in Sintering and Related Phenomena, edited by G.C. Kuczynski, Plenum Press, New York (1973).
15. H. Fischmeister and H. Exner, Metall. 18, 392 (1964).
16. R. Penty, "Pressure-Sintering Kinetics and Mechanical Properties of High-Purity, Fine-Grained Mullite," (Ph.D. Thesis), Lehigh University

(1972).

17. K.S. Mazdiasni and L.M. Brown, J. Am. Ceram. Soc., 58, 149 (1975).
18. M.D. Sacks, "Correlation of Microstructure of Sintered Mullite Bodies with their Stress-Strain Behavior in Compression Loading at 1200°C," (M.S. Thesis), University of California, Berkeley, LBL-6205 (1977).
19. P.A. Lessing et al., J. Am. Ceram. Soc., 58, 149 (1975).
20. J.A. Pask et al., "Structure, Strength, and Corrosive Resistance of Aluminum Silicate Materials," Dept. of Materials Science and Mineral Engineering, University of California, Berkeley (1977).
21. J.A. Pask et al., *ibid.*, (1978).
22. G.S. Perry, Trans. and J. Brit. Ceram. Soc., 72, 279 (1973).
23. J. Grofcsik, Mullite, Its Structure, Formation and Significance, Publishing House of the Hungarian Academy of Sciences, Budapest (1961).
24. R.F. Davis and J.A. Pask, p.37 in High Temperature Oxides, Vol. IV, edited by A.M. Alper, Academic Press, New York (1971).
25. B. Ghate, "synthesis and Pressure Sintering Kinetics of High-Purity, Fine-Grained Mullite," (Ph.D. Thesis), Lehigh University, (1973).
26. J.C. Wurst and J.A. Nelson, J. Am. Ceram. Soc., 55, 109 (1972).
27. E.E. Underwood, Quantitative Stereology, Addison Wesley Publishing Co., Reading, MA, (1970).
28. V.F. Draper, "Mullite Phase Equilibria in the System  $\text{CaO-Al}_2\text{O}_3\text{-SiO}_2$ ," (M.S. Thesis), University of California, Berkeley, LBL-5706 (1976).
29. I.A. Aksay, "Diffusion and Phase Relationship Studies in the Alumina-Silica System," (Ph.D. Thesis), University of California, Berkeley, LBL-1403 (1972).



30. R.L. Coble, J. Am. Ceram. Soc., 45, 124 (1962).
31. J. White, Proc. Brit. Ceram. Soc., 13, 155 (1965).
32. R.L. Coble, J. Appl. Phys., 32, 793 (1961).
33. R.L. Coble and T.K. Gupta, p.423 in Sintering and Related Phenomena, edited by G.C. Kuczynski, N.A. Hooten, and C.F. Gibbon, Gordon Breach, New York (1967).
34. T.E. Clare, J. Am. Ceram. Soc., 48, 159 (1966).
35. R.L. Coble, J. Appl. Phys., 32, 787 (1961).
36. J.H. Rosolowski and C. Grescovich, J. Am. Ceram. Soc., 58, 177 (1975).
37. B. Wong, "Kinetics and Mechanisms of Single Phase Solid State Sintering," (Ph.D. Thesis), University of California, Berkeley, LBL-3957 (1975).
38. W. Beere, Acta. Met., 23, 139 (1975).
39. C.E. Hoge and J.A. Pask, p.109 in Physics of Sintering, edited by M.M. Ristic, Boris Kidric Institute of Nuclear Sciences, Yugoslavia (1973).
40. J.A. Pask, "Thermodynamics and Mechanisms of Sintering," LBL-8419 (1978).
41. C. Grescovich and K.W. Lay, J. Am. Ceram. Soc., 55, 142 (1972).
42. C. Grescovich and J.H. Rosolowski, J. Am. Ceram. Soc., 59, 336 (1972).
43. G.C. Kuczynski, p. 217 in Sintering and Related Phenomena, edited by G.C. Kuczynski, Plenum Press, New York (1973).
44. J.E. Burke, J. Am. Ceram. Soc., 40, 80 (1957).
45. J.E. Burke, p. 120 in Ceramic Fabrication Procedures, edited by W.D. Kingery, Technology Press and John Wiley, New York (1958).
46. C.S. Smith, Trans. AIME, 175, 15 (1949).

47. D. Turnbull, Trans. AIME, 191, 661 (1951).
48. J.E. Burke, Trans. AIME, 180, 73 (1949).
49. J.E. Burke, "Grain Growth," General Electric Report No. 67-C-046 (1967).
50. K. Lucke and K. Dietert, Acta. Met., 5, 628 (1957).
51. J. Cahn, Acta. Met., 10, 789 (1962).
52. P. Niessen and W.C. Winegard, J. Inst. Metals, 94, 31 (1966).
53. F.A. Nichols, J. Appl. Phys., 37, 4599 (1966).
54. F.A. Nichols, J. Am. Ceram. Soc., 51, 468 (1968).
55. W.D. Kingery and B. Francois, J. Am. Ceram. Soc., 48, 546 (1965).
56. C. Zener, Trans. AIME, 175, 15, (1948).
57. R.J. Brook, p.331 in Ceramic Fabrication Processes, edited by F. Wang, Academic Press, New York (1976).
58. J. White, p. 81 in Sintering and Related Phenomena, edited by G.C. Kuczynski, Plenum Press, New York (1976).
59. P. Feltham, Acta. Met., 5, 97 (1957).
60. M. Hillert, Acta. Met., 13, 227 (1965).
61. P.J. Jorgensen, J. Am. Ceram. Soc., 48, 207 (1965).
62. T. Ikegami et al., J. Appl. Phys., 50, (1979).
63. R.F. Walker, J. Am. Ceram. Soc., 38, 187 (1955).
64. P.J. Anderson and P.L. Morgan, Trans. Faraday Soc., 60, 930 (1964).
65. P.F. Eastman and I.B. Cutler, J. Am. Ceram. Soc., 49, 526 (1966).
66. C.E. Hoge, "Thermodynamics and Kinetics of Sintering," (Ph.D. Thesis), University of California, Berkeley, LBL-3116 (1975).

67. T.K. Gupta and R.L. Coble, J. Am. Ceram. Soc., 51, 521 (1968).
68. R.F. Davis et al., J. Am. Ceram. Soc., 55, 98 (1972).
69. V. Skola, Keram. Rundsch. Kunst.-Keram., 45, 188 (1951).
70. G.W. Greenwood, p.103 in The Mechanism of Phase Transformations in Crystalline Solids, Inst. Metals Monograph 33, London (1969).
71. R. Doremus, Glass Science, John Wiley, New York, (1973).
72. Buist et al., Trans. Brit. Ceram. Soc., 64, 173 (1965).

FIGURE CAPTIONS

1. Processing scheme for Alcoa A-14 alumina/Ottawa silica flour raw materials ("powder" process).
2. Processing scheme for Atomergic  $\gamma$ -alumina/DuPont Ludox silica raw materials ("gel" process).
3. Equilibrium  $\text{SiO}_2$ - $\text{Al}_2\text{O}_3$  phase diagram according to Aksay and Pask.<sup>29</sup>
4. Schematic diagram of quench-type furnace.
5. Microstructures of "IP" compositions ranging from 60 to 80 wt%  $\text{Al}_2\text{O}_3$  which were sintered at 1700°C in air for 12 hrs.
6. A: Microstructure of 71.8 IP showing small amounts of glassy phase.  
B: Microstructure of 75 IP in which glass phase is not detected.
7. Microstructures of "IP" compositions ranging from 71.8 to 75 wt%  $\text{Al}_2\text{O}_3$  which were sintered at 1700°C in air for 12 hrs.
8. Transmission electron micrographs of 73 IP microstructure indicating the presence of small amounts of glassy phase.
9. Stress-strain behavior in compression at 1200°C for 71.8 IP, 73 IP, 74 IP, and 75 IP samples.
10. Stress-strain behavior in compression at 1400°C for 71.8 IP and 74 IP samples.
11. Microstructure for 73 IP sintered for 1 hr at 1580°C which shows an  $\text{Al}_2\text{O}_3$  particle (hexagonal shaped particle in the center) that was detected by EDAX.
12. Microstructure of 71.8 IP sintered for 100 hrs at 1700°C showing large glass "pockets" (top). Bottom: "A" after heavy etch.
13. Scanning electron micrographs of the pressed surfaces of the green compacts for the indicated compositions.

14. % theoretical density vs. time plots for temperatures in the range 1540°C-1730°C for 60 IP.
15. Microstructures illustrating pore growth from 4 to 100 hrs sintering at 1700°C for 60 IP (top) and 60 wt%  $\text{Al}_2\text{O}_3$  "gel" material (bottom).
16. Effect of atmosphere on the microstructure of 60 IP sintered at 1700°C for 100 hrs. The absence of pores in vacuum sintering ("B") is consistent with the gas entrapment argument.
17. % theoretical density vs. time plots at 1660°C for 60 IP, 73 IP, 73 PP, and 75 IP.
18. % theoretical density vs. time plots (1540°C-1730°C) for 73 IP.
19. % theoretical density vs. time plots (1540°C-1730°C) for 73 PP.
20. % theoretical density vs. time plots (1540°C-1730°C) for 75 IP.
21. % theor. density vs.  $\ln$  time plots (1540°C-1730°C) for 73 IP.
22. % theor. density vs.  $\ln$  time plots (1540°C-1730°C) for 73 PP.
23. % theor. density vs.  $\ln$  time plots (1540°C-1730°C) for 75 IP.
24. Plot of grain size vs. porosity (data from 1540°C-1730°C) for 73 IP.
25. Plots of mean pore intercept length,  $\bar{I}_{PL}$ ,  $\bar{I}_{PLA}$ , vs. porosity (data from 1540°C-1730°C) for 73 IP.
26. Illustration of the method by which  $\bar{I}_{PL}$ ,  $\bar{I}_{PLA}$ , and  $P_L$  are determined.
27. Plot of number of pore interceptions per unit area,  $N_A$ , vs. porosity (data from 1540°C-1730°C) for 73 IP.
28. Plots of estimated number of pores per unit volume ( $N_{VIPL}$  and  $N_{VIPLA}$ ) vs. porosity (data from 1540°C-1730°C) for 73 IP.
29. Micrograph of 73 IP sample with a density of 61.9 % $\rho_{th}$ .
30. Higher magnification of sample in Fig. 29 illustrating the polycrystalline nature of the dense microregions.

31. Two spherical particles of equal size which form a straight grain boundary.
32. Two spherical particles of unequal size which form a curved grain boundary.
33. Mechanism of grain growth by (1) neck formation followed by (2) boundary movement, (after Grescovich and Lay<sup>41</sup> with slight modifications).
34. Plot of pore surface (interface) area per unit volume,  $S_V$ , vs. porosity (data from 1540°C-1730°C) for 73 IP.
35. Schematic plot illustrating the continuation of the  $\% \rho_{th}$  vs.  $\ln$  time plot from the first measured point to the point where the  $\ln$  time proportionality begins.
36. Micrograph of 73 IP sample in which connections between dense microregions are illustrated.
37. Micrographs of 73 IP samples with densities from 61.9-71.1  $\% \rho_{th}$ . Note the smoothing and rounding ("C", "D") of sharp edges ("A") on particles/clusters.
38. Pore intercept histograms for samples "A", "B", and "D" of Fig. 37. The values of  $\bar{I}_{PL}$  are  $.91\mu$  (61.9 $\% \rho_{th}$ ),  $1.00\mu$  (65-6 $\% \rho_{th}$ ), and  $.91\mu$  (71.1 $\% \rho_{th}$ ), respectively.
39. Micrograph of 73 IP sample in which two winding "tentacled" pores have been outlined.
40. Pore intercept histograms for 73 IP samples with densities from 73.6-84.5 $\% \rho_{th}$ . The values of  $\bar{I}_{PL}$  are  $.88\mu$  (73.6 $\% \rho_{th}$ ),  $.74\mu$  (77.4 $\% \rho_{th}$ ),  $.68\mu$  (80.5 $\% \rho_{th}$ ), and  $.61\mu$  (84.5 $\% \rho_{th}$ ).

41. Micrographs for 73 IP samples in densification Region IV in which pores become more convex with increasing density.
42. Pore intercept histograms for 73 IP samples with densities from 84.5-90.5% $\rho_{th}$ . The values of  $\bar{I}_{PL}$  are .61 $\mu$  (84.5% $\rho_{th}$ ), .63 $\mu$  (86.5% $\rho_{th}$ ), and .79 $\mu$  (90.5% $\rho_{th}$ ).
43. Pore intercept histograms for 73 IP samples sintered to approximately the same density with different temperature-time schedules. The values of  $\bar{I}_{PL}$  are .74 $\mu$  (89.3% $\rho_{th}$ ), .75 $\mu$  (89.5% $\rho_{th}$ ), and .79 $\mu$  (90.5% $\rho_{th}$ ).
44. Plot of % open porosity vs. total porosity (data from 1540°C-1730°C) for 73 IP.
45. Micrographs of 73 IP samples illustrating two common observations of final stage microstructures: (1) pores located within grains and (2) exaggerated grain growth.
46. Micrographs of 73 IP samples with densities from 89.5-97.2% $\rho_{th}$ . The observed increase in  $\bar{I}_{PL}$  (Fig. 25) and decrease in  $N_V$  (Fig. 28) during densification Region VI can be explained by the diffusional elimination of smaller pores (from "A" to "B").
47. Pore intercept histograms for 73 IP samples. The values of  $\bar{I}_{PL}$  are .89 $\mu$  (95.4% $\rho_{th}$ ) and .94 $\mu$  (96.9% $\rho_{th}$ ).
48. Plots of  $\ln$  grain size vs.  $\ln$  time for various temperatures (1540°C-1730°C). Included are (1) experimentally measured data points, (2) points generated by using the smooth curves of Figs. 21 and 24, and (3) points generated by using the smooth curve of Fig. 24 with values obtained by extrapolation of the curves in Fig. 21.

49. Unfired 73 IP compacts showing very small particles clustered on larger particles.
50. Grain size histograms of 73 IP samples. The average grain size is  $.76\mu$  ( $58\%\rho_{th}$ , green compact),  $1.00\mu$  ( $63.6\%\rho_{th}$ ) and  $1.57\mu$  ( $71.1\%\rho_{th}$ ).
51. Grain size histograms of 73 IP samples. The average grain size is  $1.57\mu$  ( $71.1\%\rho_{th}$ ),  $2.11\mu$  ( $89.5\%\rho_{th}$ ), and  $2.60\mu$  ( $95.3\%\rho_{th}$ ).
52. Grain size histograms of 73 IP samples. The average grain size is  $2.60\mu$  ( $95.3\%\rho_{th}$ ) and  $5.62\mu$  ( $97.2\%\rho_{th}$ ).
53. Plots of  $\ln\left(\frac{d\rho}{d\ln t} \cdot T\right)$  vs.  $1/T$  for 73 IP, 73 PP, and 75 IP.  $\frac{d\rho}{d\ln t}$  is the slope obtained from the straight lines in Figs. 21, 22, and 23.
54. Plots of  $\ln\left(\frac{d\rho}{dt} \cdot T\right)$  vs.  $1/T$  at various densities ( $65-92.5\%\rho_{th}$ ) for 73 IP. Included are points obtained by extrapolating the curves in Fig. 21 to higher densities. Both the models of Coble and of Wong predict straight lines with constant slope for the various densities.
55. Plots of  $Q$ , the apparent activation energy which were obtained from the plots in Fig. 54, vs. density for 73 IP, 73 PP, and 75 IP. The values of  $Q$  were obtained using the extrapolated values.
56. Plot of  $N$ , the estimated number of interconnected pores per unit volume, vs. porosity for 73 IP.  $N$  is estimated by multiplying  $N_{VIPL}$ , the estimated number of pores per unit volume, by the fractional open porosity.
57. Top: Plots of  $\ln(1-P)$  vs.  $\int_{t_0}^t \frac{dt}{(d_{ave})^3}$  for various temperatures ( $1540^\circ\text{C}-1730^\circ\text{C}$ ) for 73 IP.



Bottom: Plots of  $\ln(1-P)$  vs.  $\int_{t_0}^t \frac{dt}{(d_{ave})^4}$  for various temperatures (1540°C-1730°C) for 73 IP.

58. (1) Plots of  $\ln$  grain size vs.  $\ln$  porosity (data from 1540°C-1730°C and green compact) for 73 IP and (2) plot of  $\ln N_{VIPL}$ , the estimated number of pores per unit volume, vs.  $\ln$  porosity (data from 1540°C-1730°C) for 73 IP. The dotted line represents 10% porosity.

59. Top: Plots of the mean distance between first neighbors of pore intercept segments,  $\lambda_1$ , vs. porosity (data from 1540°C-1730°C) for 73 IP.

Bottom: Plot of the mean free distance between pores,  $\lambda$ , vs. porosity (data from 1540°C-1730°C) for 73 IP.

60. Plot of the ratio  $\lambda/\lambda_1$  vs. porosity (data from 1540°C-1730°C) for 73 IP.

61. Plots of (1)  $\ln(\lambda^3 - \lambda_0^3)$  vs.  $\ln$  time and (2)  $\ln(\lambda_1^3 - \lambda_{10}^3)$  vs.  $\ln$  time at various temperatures (1540°C-1730°C) using the data from Figs. 21 and 59 for the 73 IP material.

62. Micrographs of agglomerates that form upon drying of gelled mixed oxides.

63. Top: Micrographs of pressed surfaces of green compacts of "gel" materials ground for various times (0-12 hr). Large aggregates are rapidly broken down upon grinding. Interaggregates pores decrease in size with increased grinding.

Bottom: Higher magnification illustrating that the individual crystallite size is the same for all grind times.

64. Micrograph of large aggregate (zero hour ground material) illustrating inhomogeneity.

65. Plots of % theoretical density vs. time at 1660°C for "gel" materials ground for various times (0-12 hr).
66. Micrographs of "gel" materials ground for various times (0-12 hr) which were sintered at 1660°C for 18 hr.
67. % theoretical density vs. time plots (1540°C-1700°C) for 12 hr ground "gel" material.
68. % theoretical density vs. time plots (1540°C-1700°C) for 5 hr ground "gel" material.
69. % theoretical density vs. time plots (1540°C-1700°C) for 1 hr ground "gel" material.
70. % theoretical density vs. time plots (1540°C-1700°C) for 0.5 hr ground "gel" material.
71. % theoretical density vs. time plots (1540°C-1700°C) for 0 hr ground "gel" material.
72. % theoretical density vs.  $\ln$  time plots (1540°C-1700°C) for 12 hr ground "gel" material.
73. % theoretical density vs.  $\ln$  time plots (1540°C-1700°C) for 5 hr ground "gel" material.
74. % theoretical density vs.  $\ln$  time plots (1540°C-1700°C) for 1 hr ground "gel" material.
75. % theoretical density vs.  $\ln$  time plots (1540°C-1700°C) for 0.5 hr ground "gel" material.
76. % theoretical density vs.  $\ln$  time plots (1540°C-1700°C) for 0 hr ground "gel" material.
77. Simple cubic packing arrangement of three different particle sizes.

78. Construction of a schematic plot of % theoretical density vs. time for the arrangement in Fig. 77 assuming a linear densification rate.
79. Schematic illustration of a particle size distribution with three modes.
80. A and B: Construction of a schematic plot of % theoretical density vs.  $\ln$  time for a packing arrangement with three particle size modes in which a proportionality between  $\% \rho_{th}$  and  $\ln$  time is assumed.  
C: Plot of % theoretical density vs. time from the values used in Fig. 80B.
81. A and B: Construction of a schematic plot of % theoretical density vs.  $\ln$  time for a packing arrangement with three particle size modes in which (1) a proportionality between  $\% \rho_{th}$  and  $\ln$  time is assumed and (2) densification of a particle size regime does not begin until densification of the preceding region is nearly complete. C: Plot of % theoretical density vs. time from the values used in Fig. 81B.
82. Schematic plots of the form in Fig. 80 illustrating the effect of temperature.
83. Schematic plots of the form in Fig. 81 illustrating the effect of temperature.
84. Micrographs of 12 hr ground "gel" samples sintered at 1580°C for 1, 6, and 18 hr. By 1580°C-1 h ( $64.3\% \rho_{th}$ ), some aggregates are almost completely dense due to the elimination of very small intra-aggregate pores (Region I). Between 1580°C-1 h and 1580°C-6 h ( $76.1\% \rho_{th}$ ), larger intra-aggregate and small inter-aggregate pores are eliminated (Region II).

85. Lower magnification of samples in figures illustrating that the elimination of larger pores (Region III) occurs primarily between 1580°C-6 h ( $76.1\% \rho_{th}$ ) and 1580°C-18 h ( $83.5\% \rho_{th}$ )
86. High magnification micrograph of 1580°C-6 h sample in figures 84, 85 illustrating microinhomogeneity of "gel" materials.
87. % theoretical density vs.  $\ln$  time plots at 1580°C for "gel" materials ground for various times (0-12 hrs) which show that a Region II-Region III transition density is observed in each plot.
88. Plots of % theoretical density vs. composition (overall wt%  $Al_2O_3$ ) for "IP" materials sintered in air and vacuum at 1700°C for 12 hrs. Uncertainty in the values for vacuum-fired, low  $Al_2O_3$  content samples (indicated by the dashed line and dotted data points) arises from the loss of silica in vacuum sintering.
89. Micrographs of "IP" samples (60-80 wt%  $Al_2O_3$ ) which were vacuum-sintered at 1700°C for 12 hrs.
90. Plots of % weight loss vs. composition (overall wt%  $Al_2O_3$ ) for "IP" materials sintered in air and vacuum at 1700°C for 12 hrs. The vacuum data is consistent with the earlier observations (section III.A.1.) that small amounts of glass phase persist up to the two phase region of mullite and alumina (Fig. 3).
91. Top: Plots of % weight loss vs. sintering time for air and vacuum fired 71.8 IP samples at ~1715°C.  
Bottom: A: Microstructure of vacuum sintered 71.8 IP sample illustrating the effect of mullite decomposition which results in a porous  $Al_2O_3$  layer (top). B: EDAX spectra for "A", dotted spectrum is from the mullite matrix; lined spectrum is from the

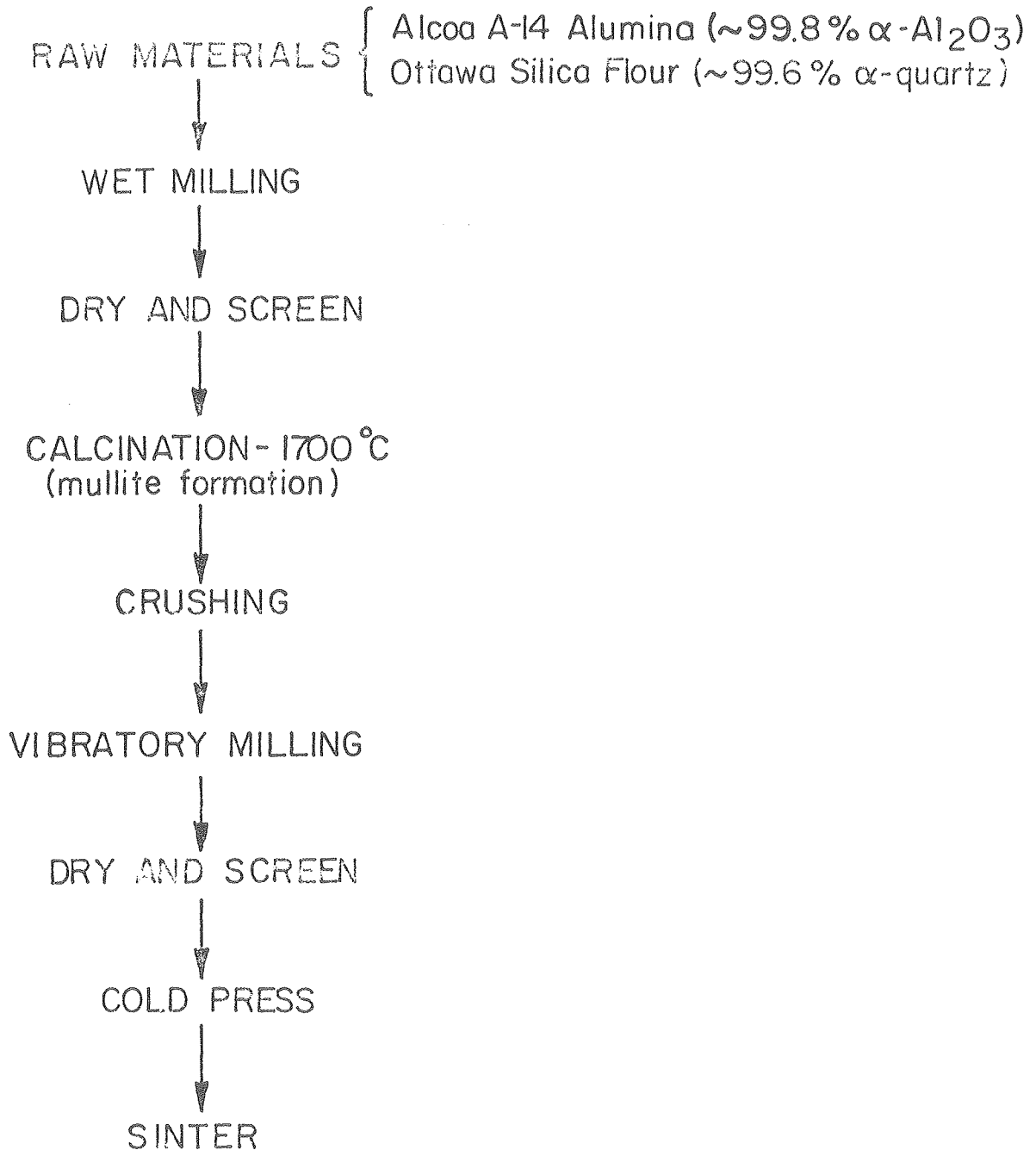
porous  $\text{Al}_2\text{O}_3$  layer.

92. A: Micrograph of 71.8 IP sample sintered ~140 hrs in vacuum at ~1715°C which indicates the occurrence of sintering of the porous  $\text{Al}_2\text{O}_3$  layer. B: Higher magnification of "A" showing large  $\text{Al}_2\text{O}_3$  grains. C: Sintering of the porous  $\text{Al}_2\text{O}_3$  layer also occurs in vacuum sintering of "gel" materials.
93. A: Micrograph of vacuum sintered 71.8 IP sample which, after polishing, was thermally etched for ~1/2 hr at 1550°C in air. B: Micrograph of vacuum sintered 71.8 IP sample in "A" which, after polishing, was annealed for 100 hrs at 1600°C in air.
94. A: Micrograph of 71.8 IP sample which was (1) sintered in air to ~83% $\rho_{th}$ , (2) subsequently vacuum sintered to ~95% $\rho_{th}$ , and, after polishing, (3) thermally etched in air for ~1/2 hr at 1550°C. B: Micrograph of 71.8 IP sample which was (1) sintered in air to ~83% $\rho_{th}$ , (2) subsequently vacuum sintered to ~95% $\rho_{th}$ , and, after polishing, (3) annealed for 100 hrs at 1660°C in air.
95. Micrographs of 60 IP samples which were sintered in various atmospheres for 100 hrs at 1700°C.
96. Micrographs of 60 wt%  $\text{Al}_2\text{O}_3$  "gel" samples which were sintered in various atmospheres for 100 hrs at 1700°C.
97. Micrographs of 60 wt%  $\text{Al}_2\text{O}_3$  "gel" samples which were sintered in vacuum at 1700°C for 4 and 100 hrs.
98. Micrographs of 60 wt%  $\text{Al}_2\text{O}_3$  "gel" samples which were sintered in various atmospheres for 100 hrs at 1700°C.

99. Micrographs of 60 IP samples which were sintered in (1) air (Top) for 4 hrs ("A") and 100 hrs ("C") and (2) vacuum (Bottom) for 4 hrs ("B") and 100 hrs ("D").
100. A: Micrograph with mullite (light phase) and glass (dark phase) formed by reaction sintering a 45.9 wt%  $\text{Al}_2\text{O}_3$ /54.1 wt%  $\text{SiO}_2$  mixture at 1700°C. B: Micrograph of sample in "A" with extended heat treatment. Mullite grains grow with an elongated morphology. Numerous mullite precipitation "rims" are noted.
101. Two phase (mullite and glass) microstructures which indicate that the elongated morphology of mullite persists as the overall  $\text{Al}_2\text{O}_3$  content is increased: 55 wt% ("A"), 60 wt% ("B"), and 65 wt% ("C").
102. Two phase (mullite and glass) microstructures which indicate that growing pores may impinge upon one another and coalesce.
103. Micrographs of 71.8 IP samples sintered in air at 1715°C for various times (4-100 hrs). Pore growth is observed between 24 and 100 hrs.
104. Micrographs of 71.8 IP samples sintered in vacuum at ~1715°C for various times (4-100 hrs). No pore growth is observed.
105. Micrographs of 80 wt%  $\text{Al}_2\text{O}_3$  "gel" samples sintered in various atmospheres at 1700°C for 4 hrs (Top) and 100 hrs (Bottom). Growth of pores and alumina particles is observed.
106. Micrographs of 80 wt%  $\text{Al}_2\text{O}_3$  "gel" and "powder" (IP) samples sintered in various atmospheres at 1700°C for 100 hrs. Note that the pores and  $\text{Al}_2\text{O}_3$  particles which are entrapped within grains tend to be small while the larger inclusions are intergranular.

107. Micrographs of 80 wt%  $\text{Al}_2\text{O}_3$  "gel" and "powder" (IP) samples sintered in various atmospheres at 1700°C for 100 hrs.
108. Micrographs of 80 IP samples sintered in air for 4 hrs (Top) and 100 hrs (Bottom) illustrating that (1) no pore growth has occurred and (2)  $\text{Al}_2\text{O}_3$  particle growth has occurred.
109. Micrographs of 80 IP samples sintered in vacuum at 1700°C for 4 hrs (Top) and 100 hrs (Bottom). Residual porosity consists only of small pores entrapped within grains.

## PROCESSING SCHEME

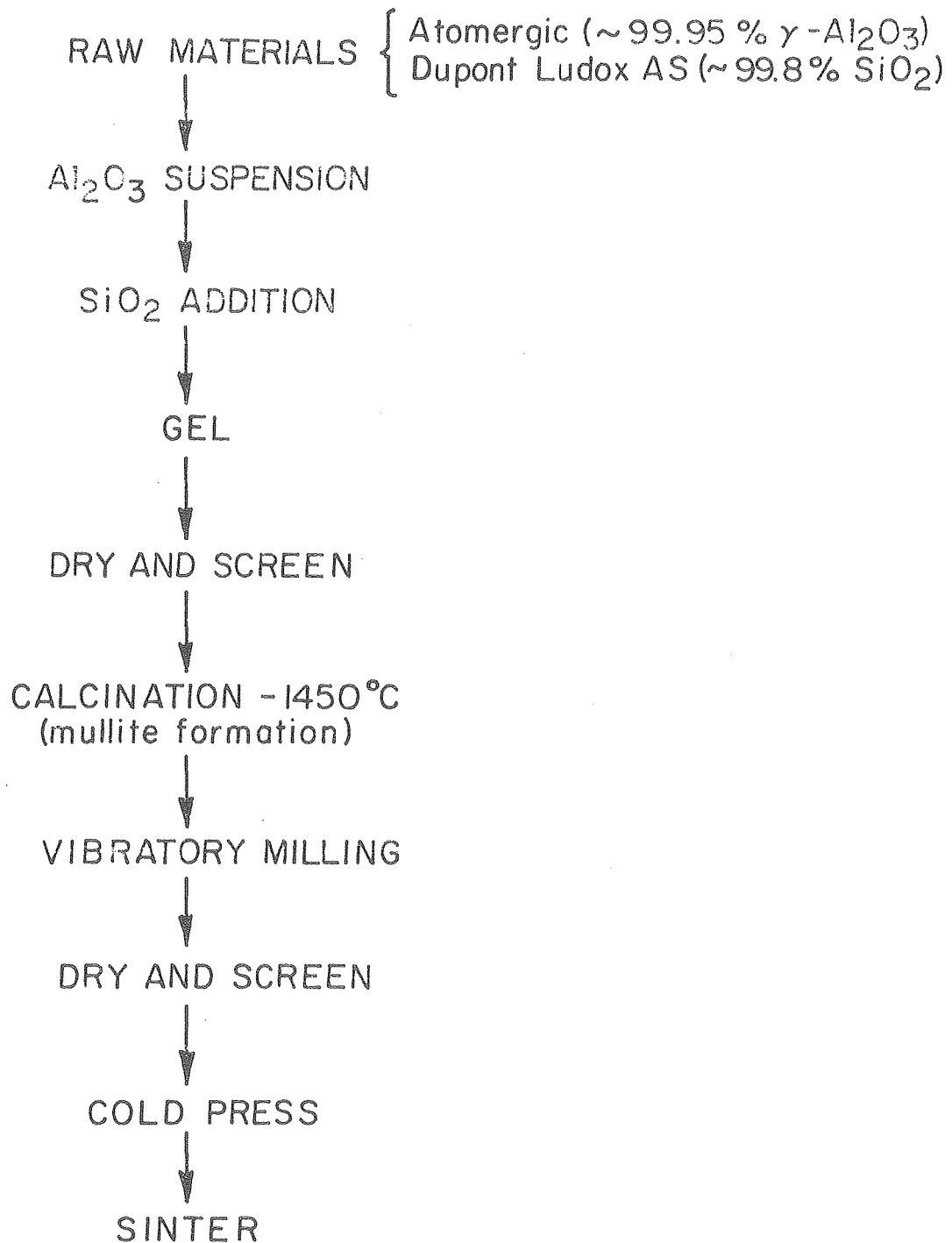


XBL 785-4932

Fig. 1

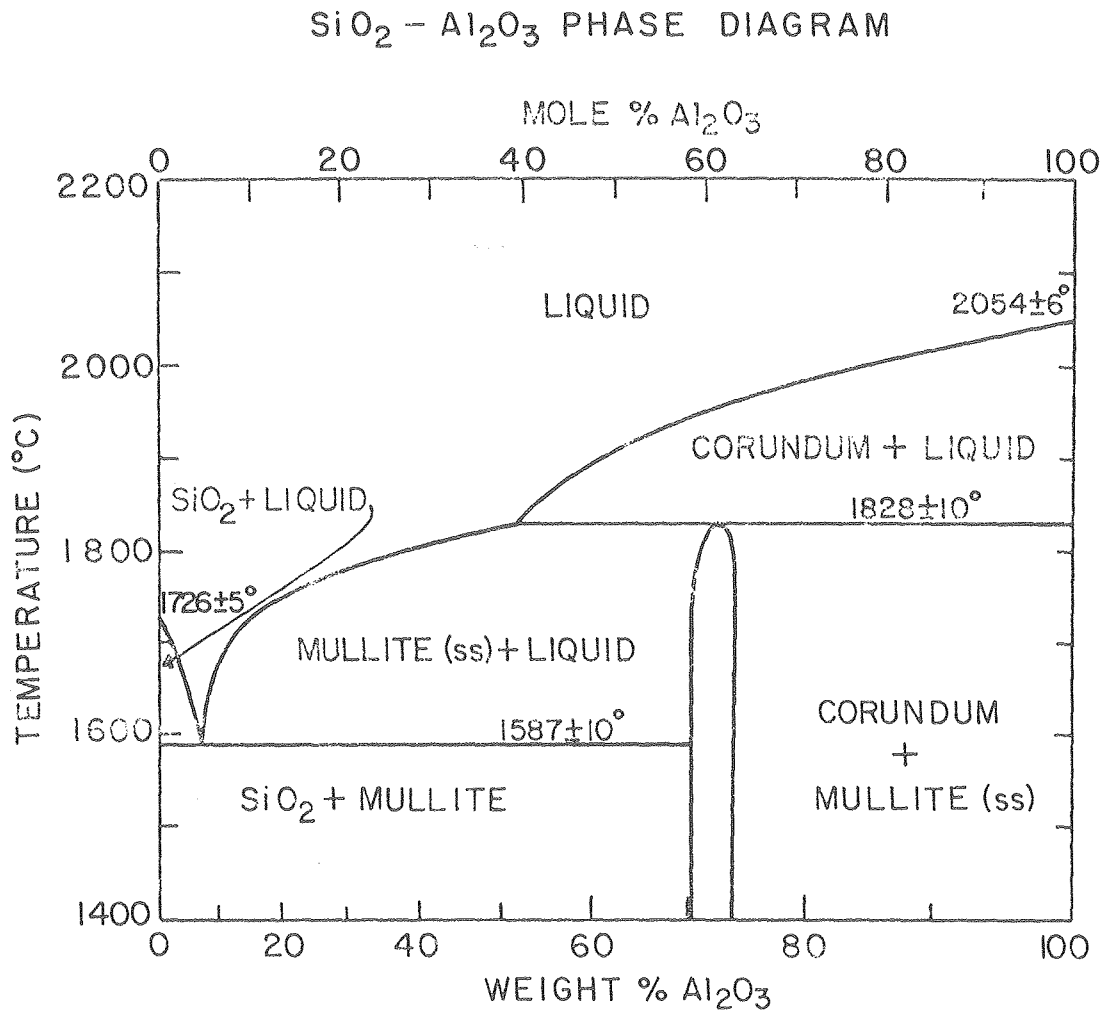


## PROCESSING SCHEME



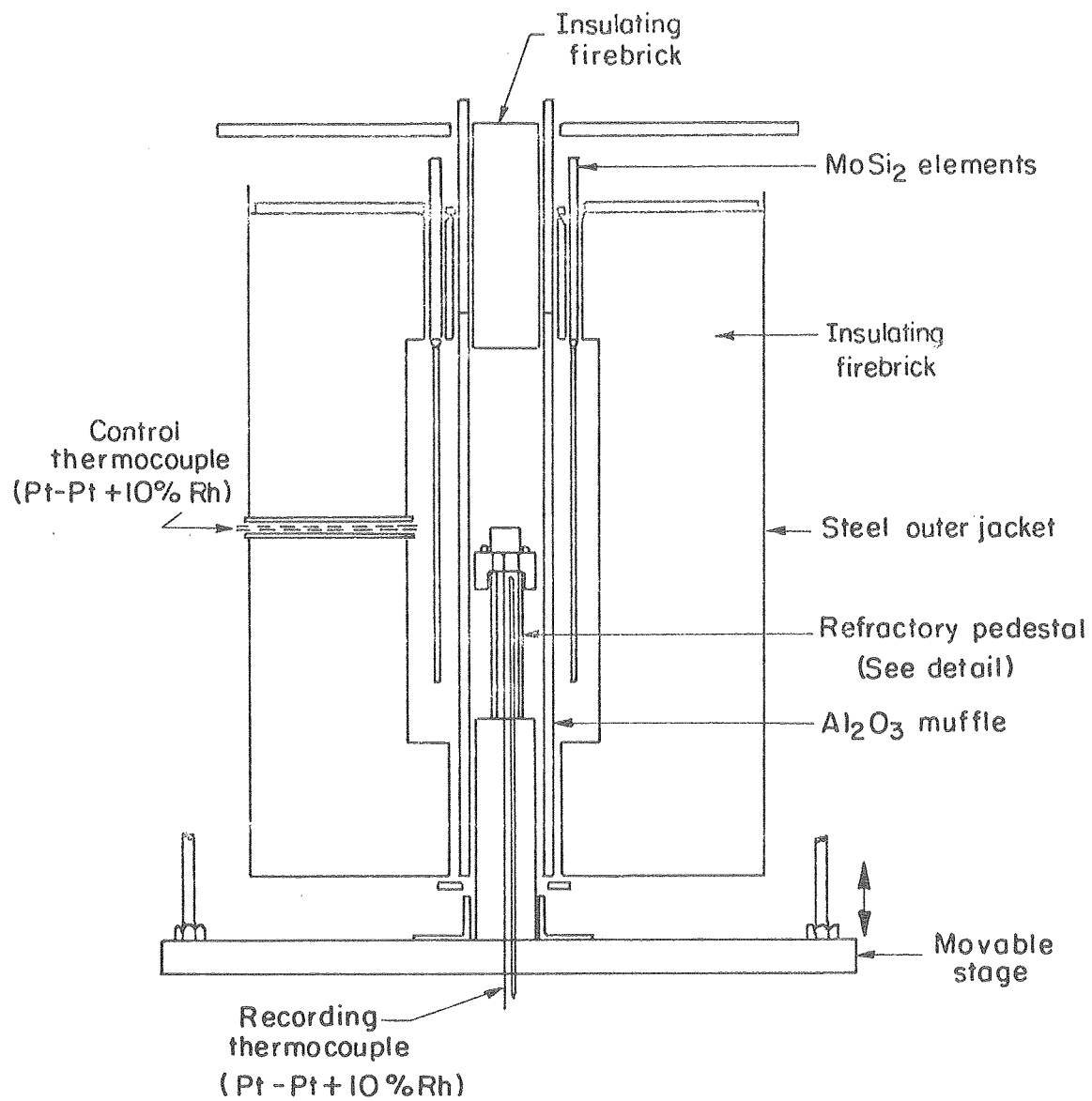
X BL 785 - 4933

Fig. 2



XBL 7810-5879

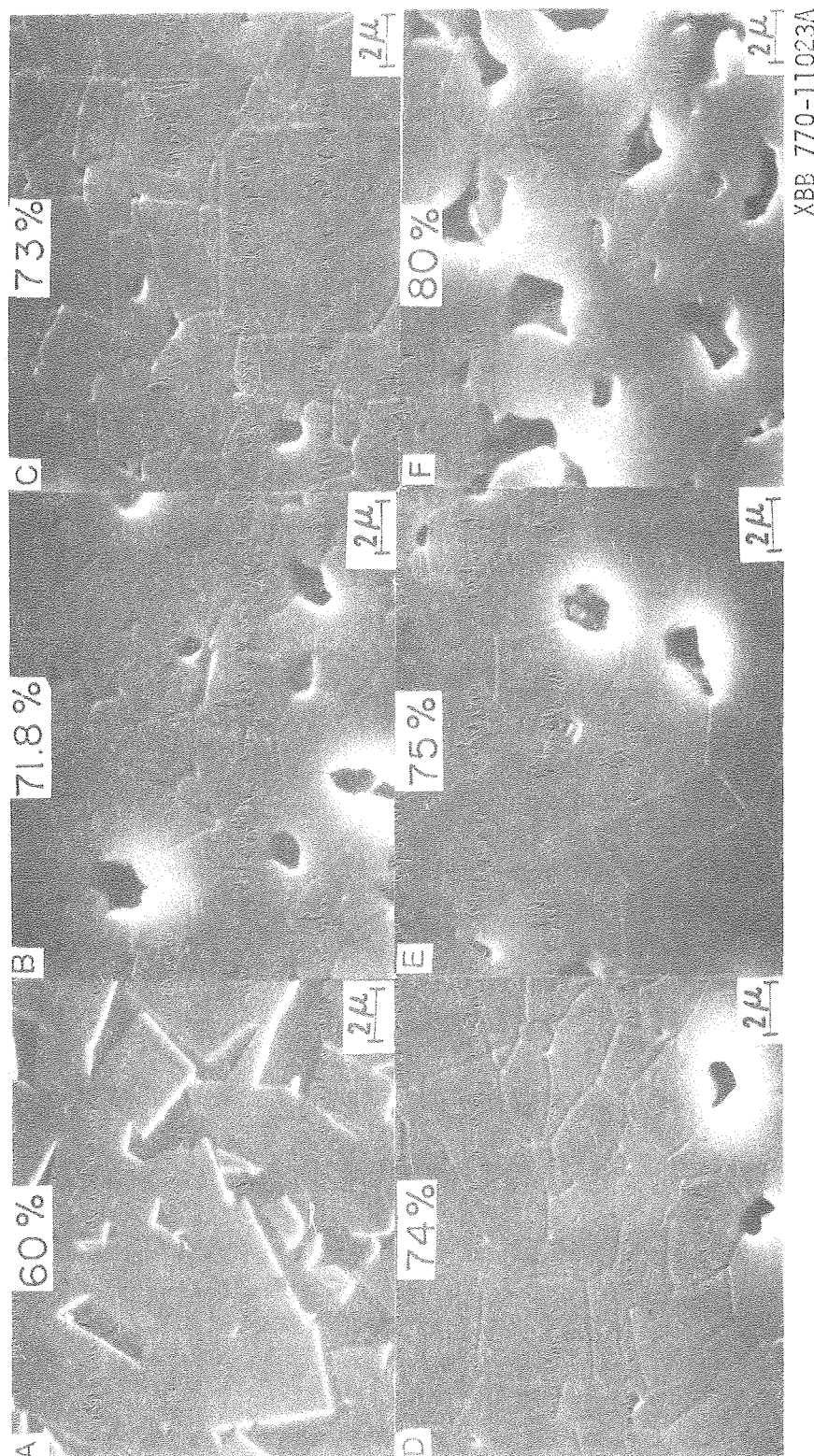
Fig. 3



XBL 754-6162

Fig. 4

# AIR



XBB 770-11023A

Fig. 5

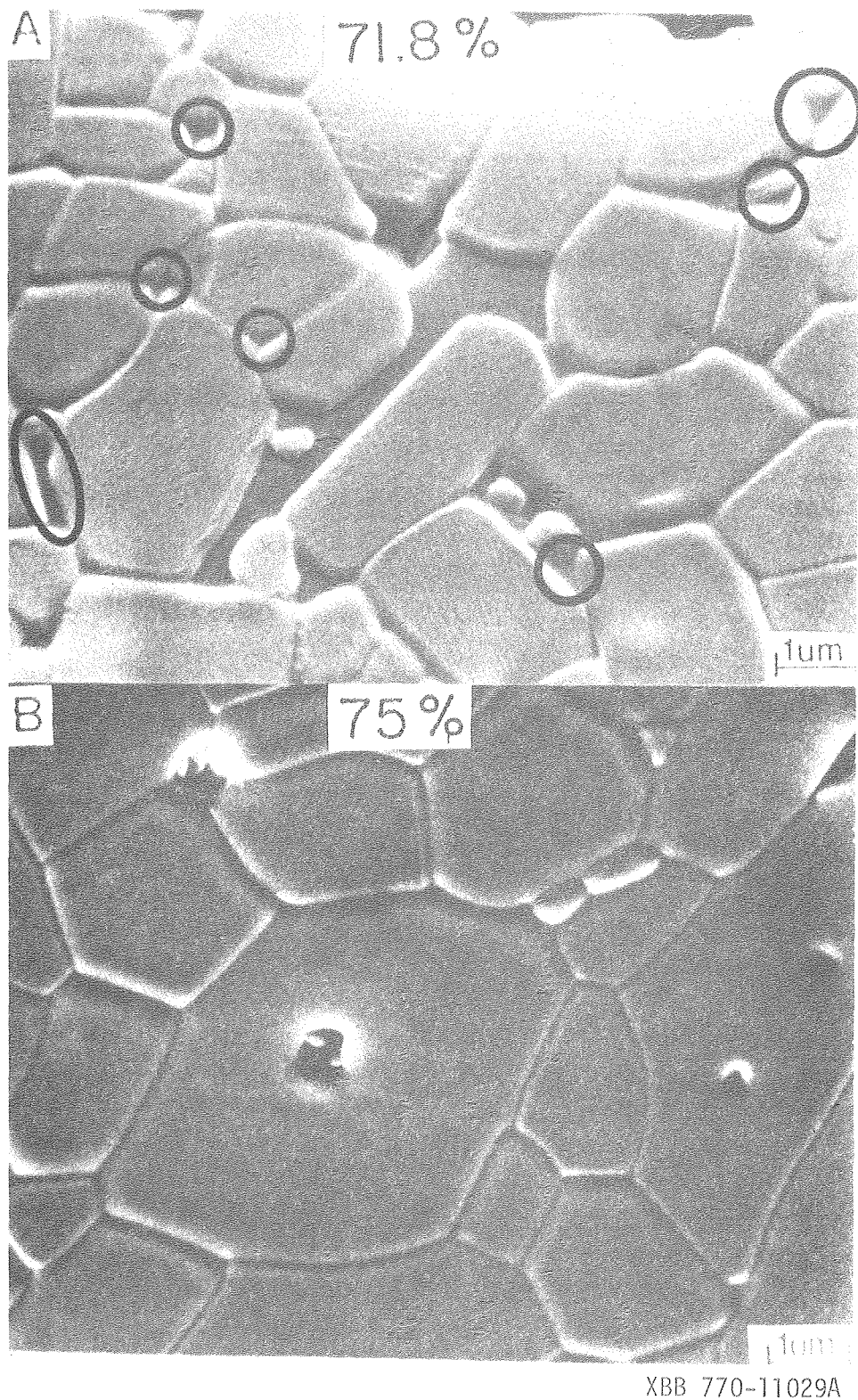


Fig. 6

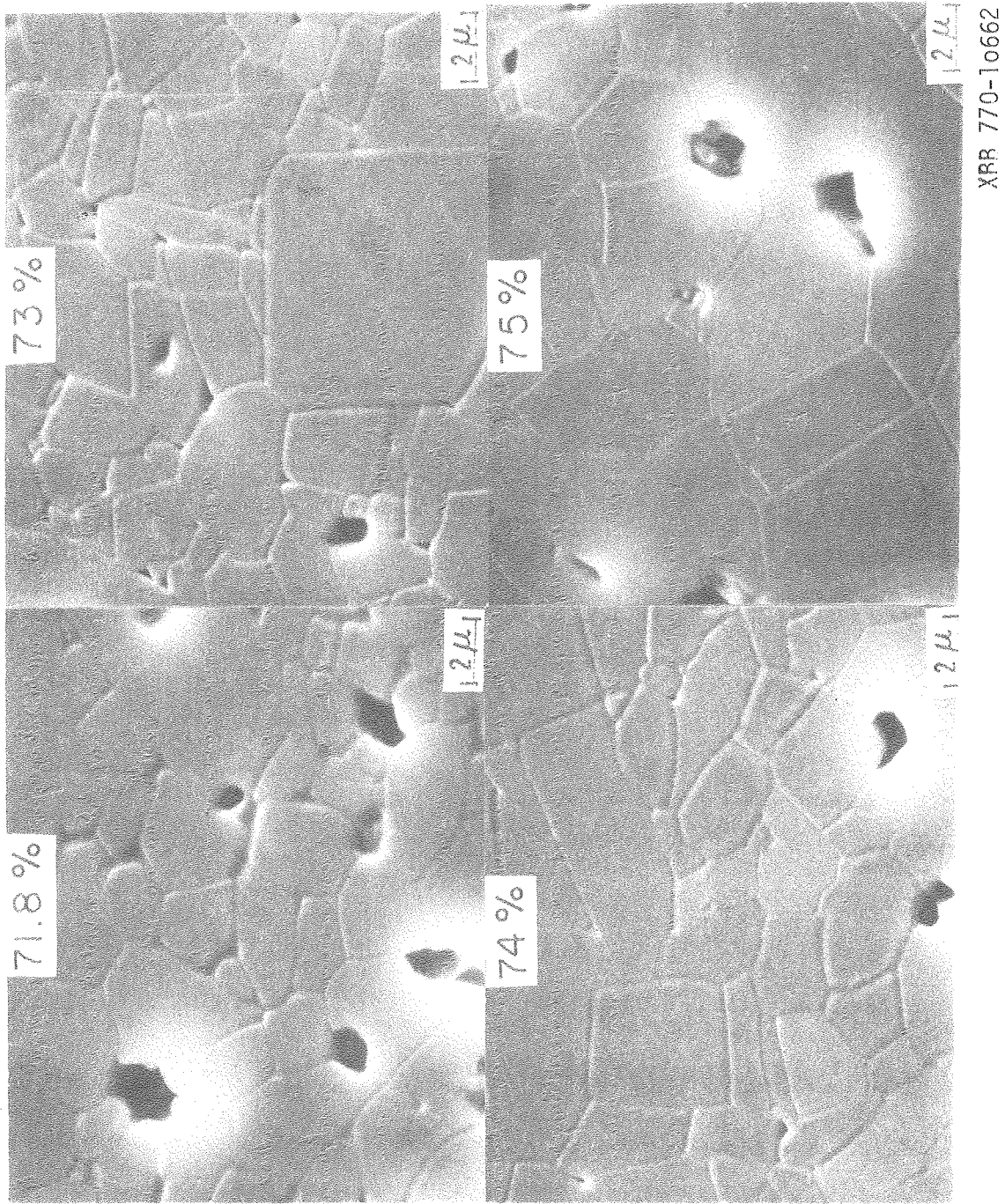


Fig. 7



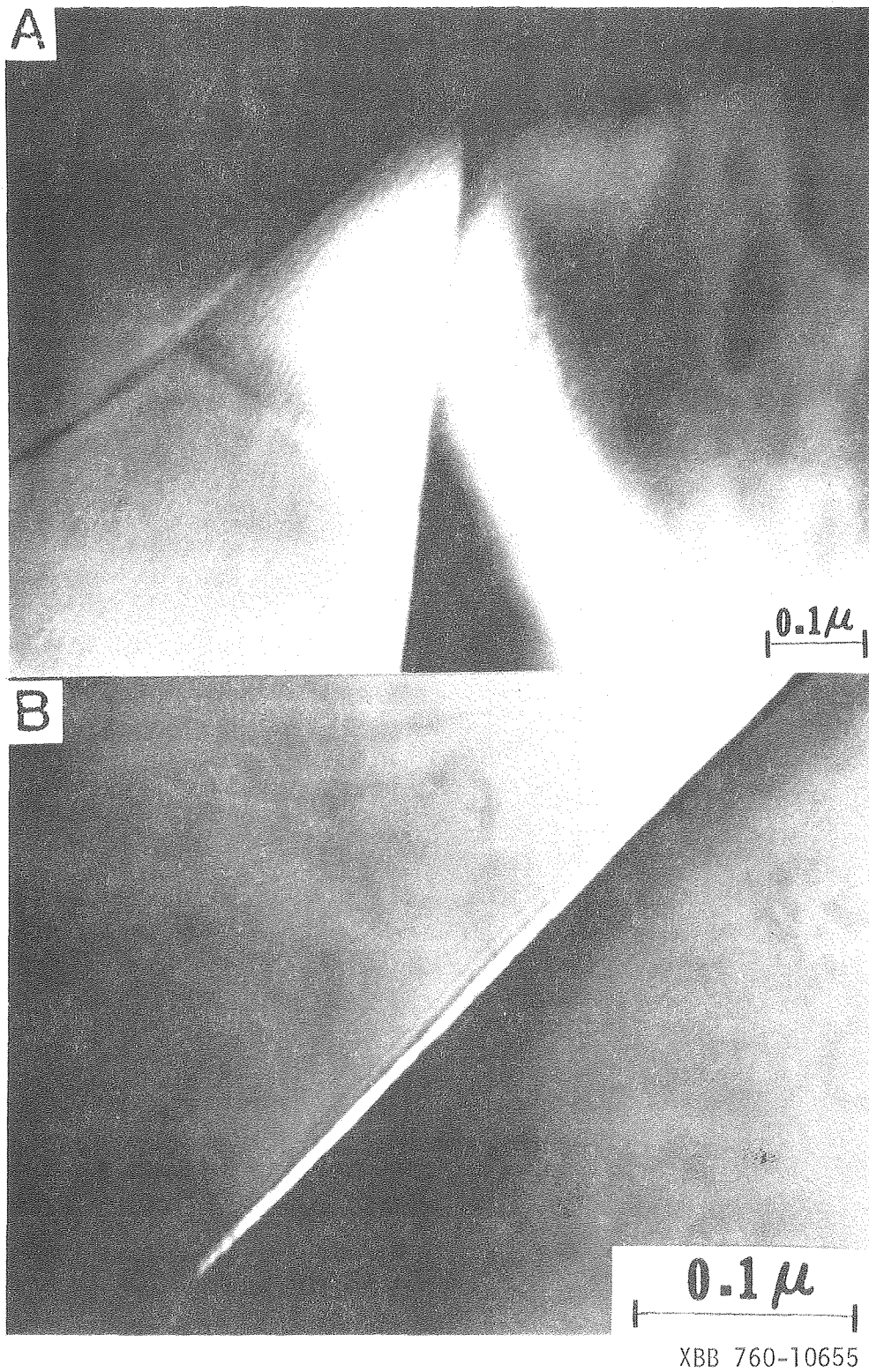
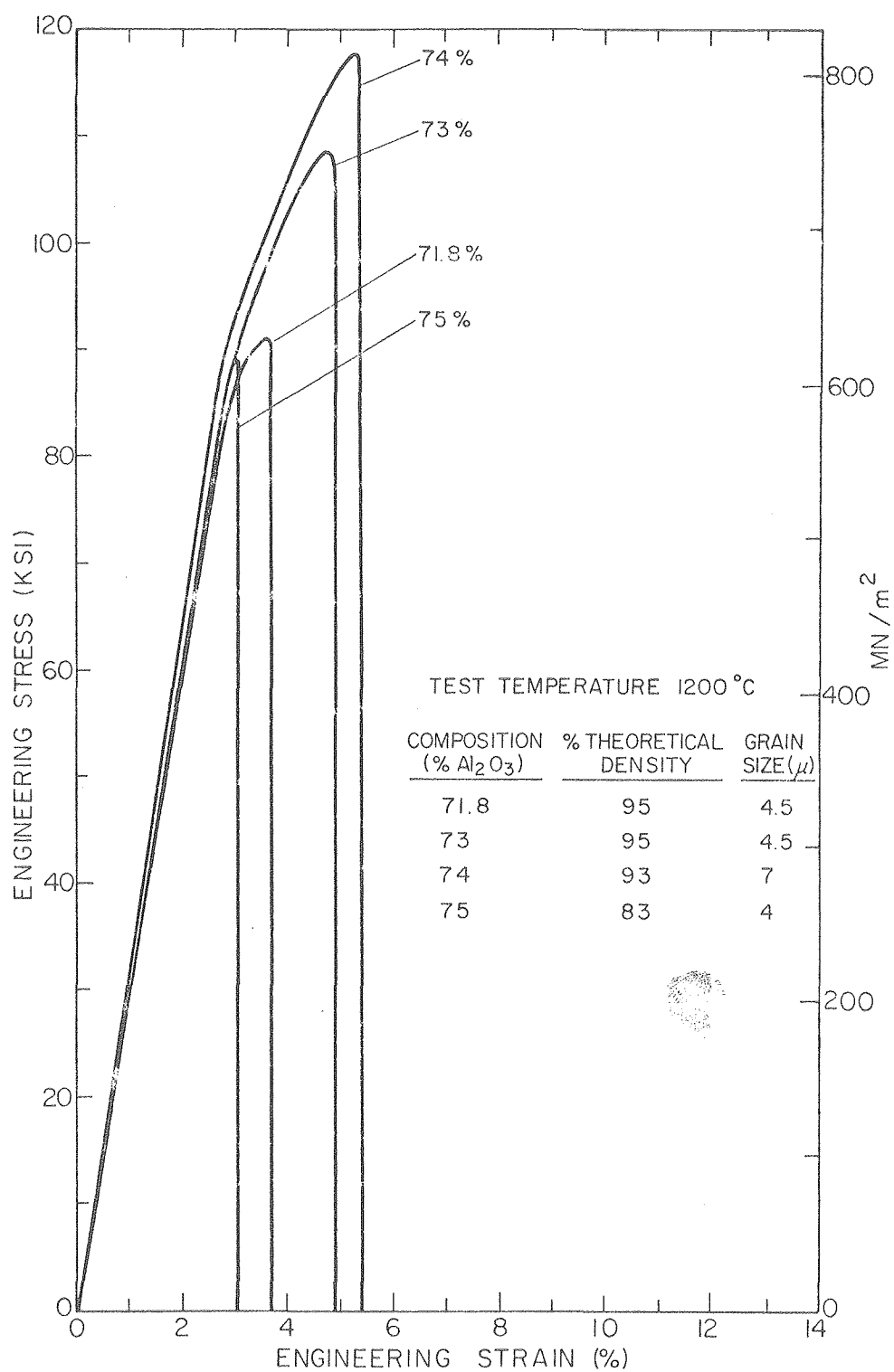


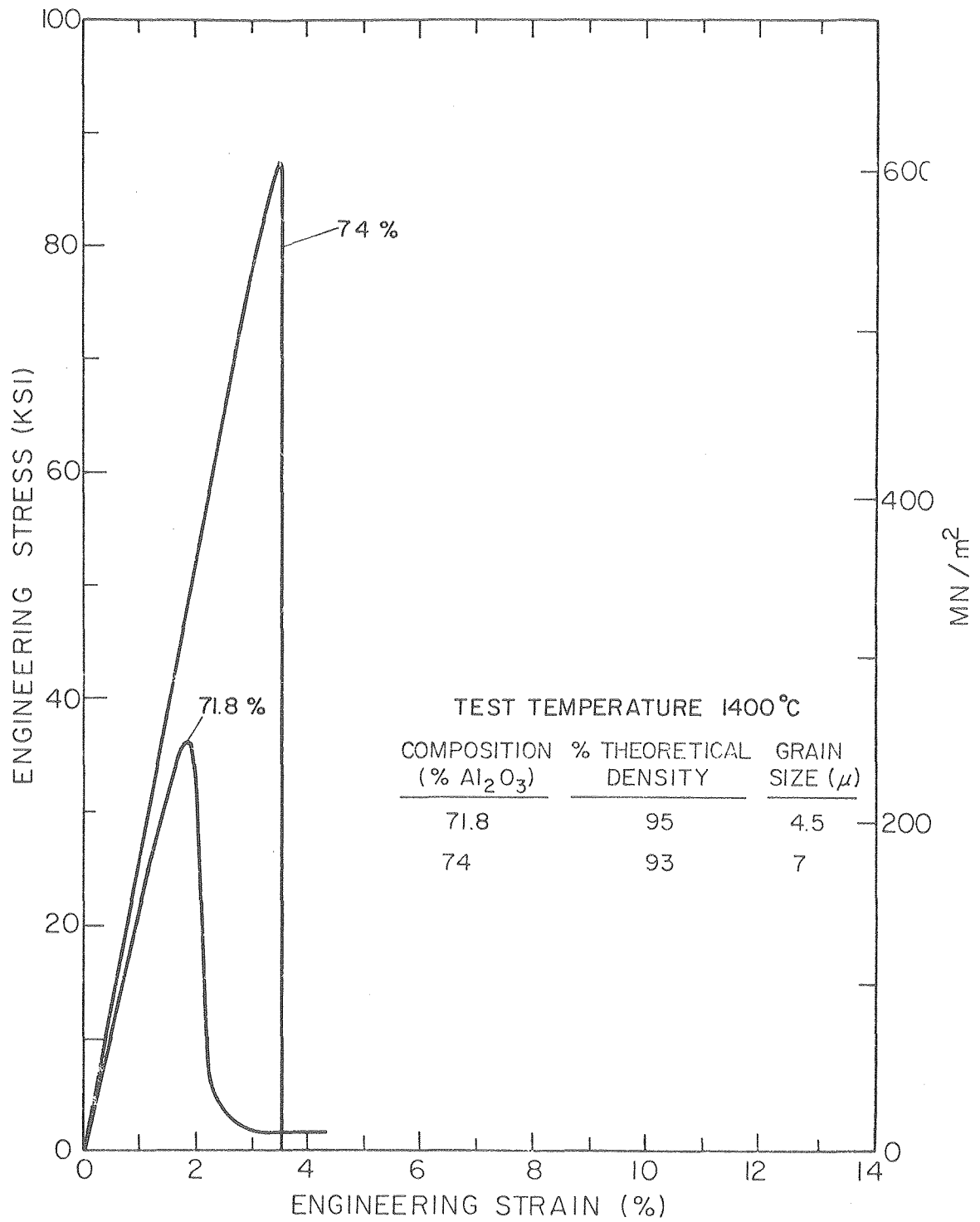
Fig. 3



XBL 7710-6237

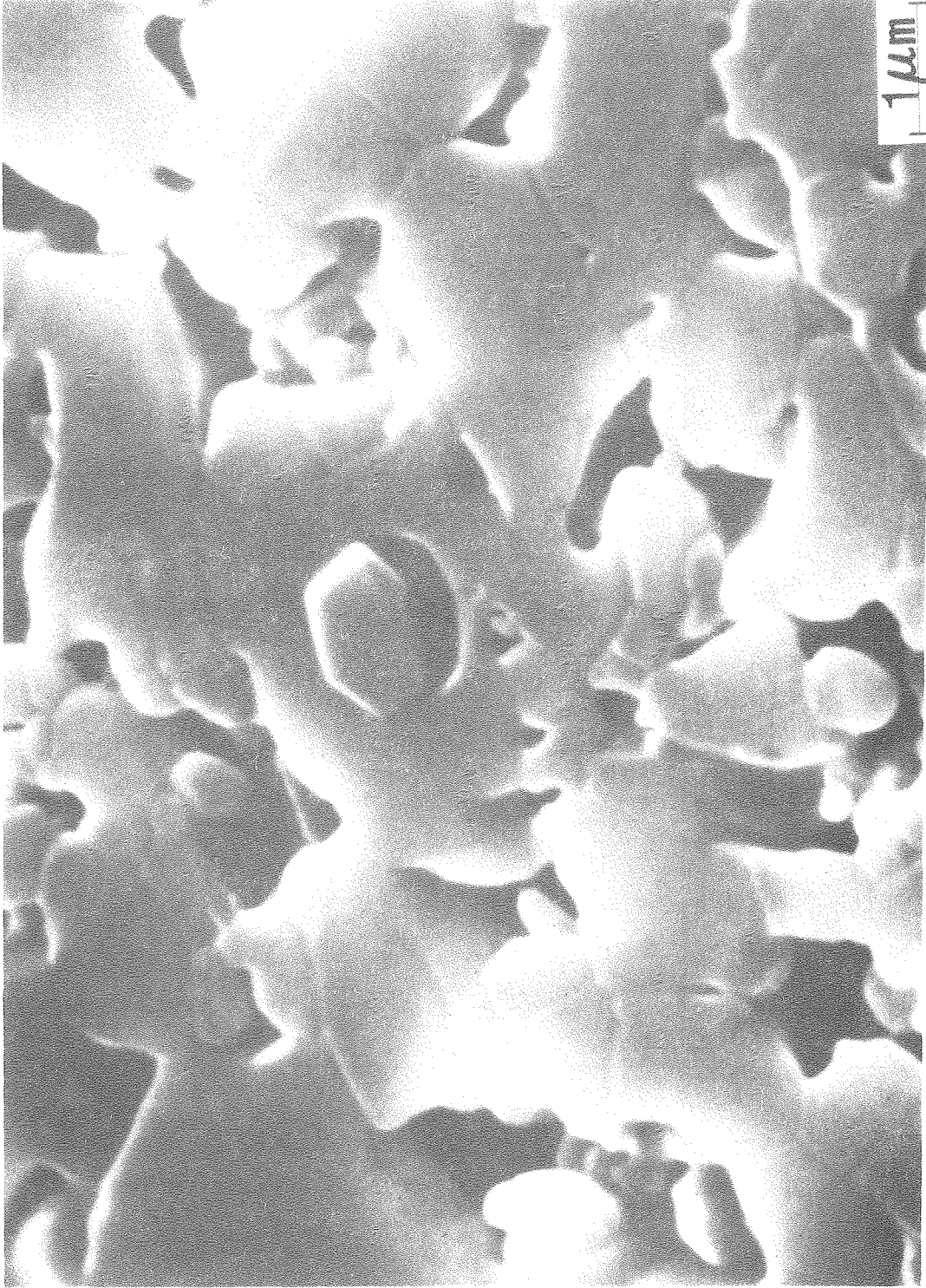
Fig. 9





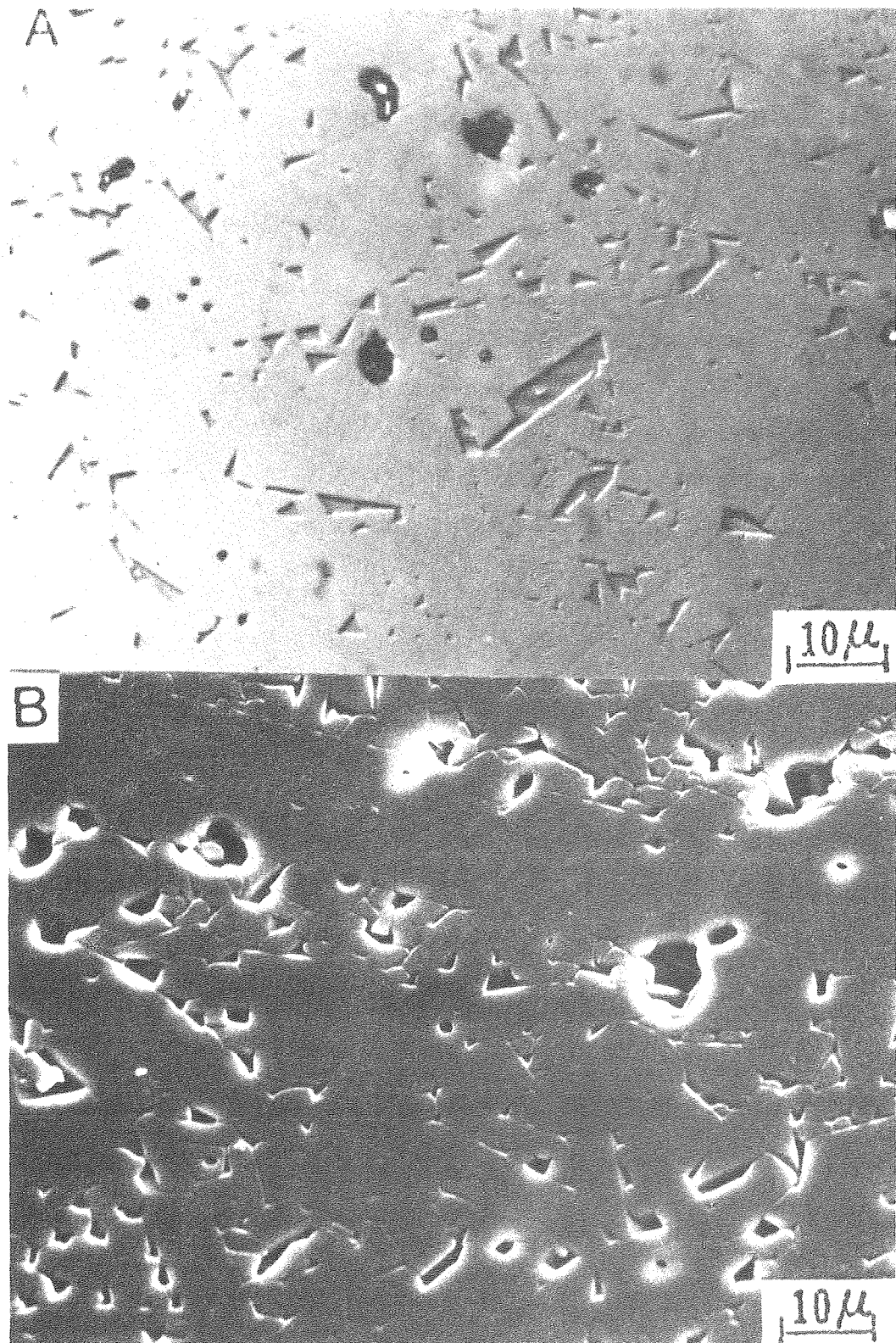
XBL 7710-6238

Fig. 10



XBB 790-15979

Fig. 11



XBB 771-82

Fig. 12

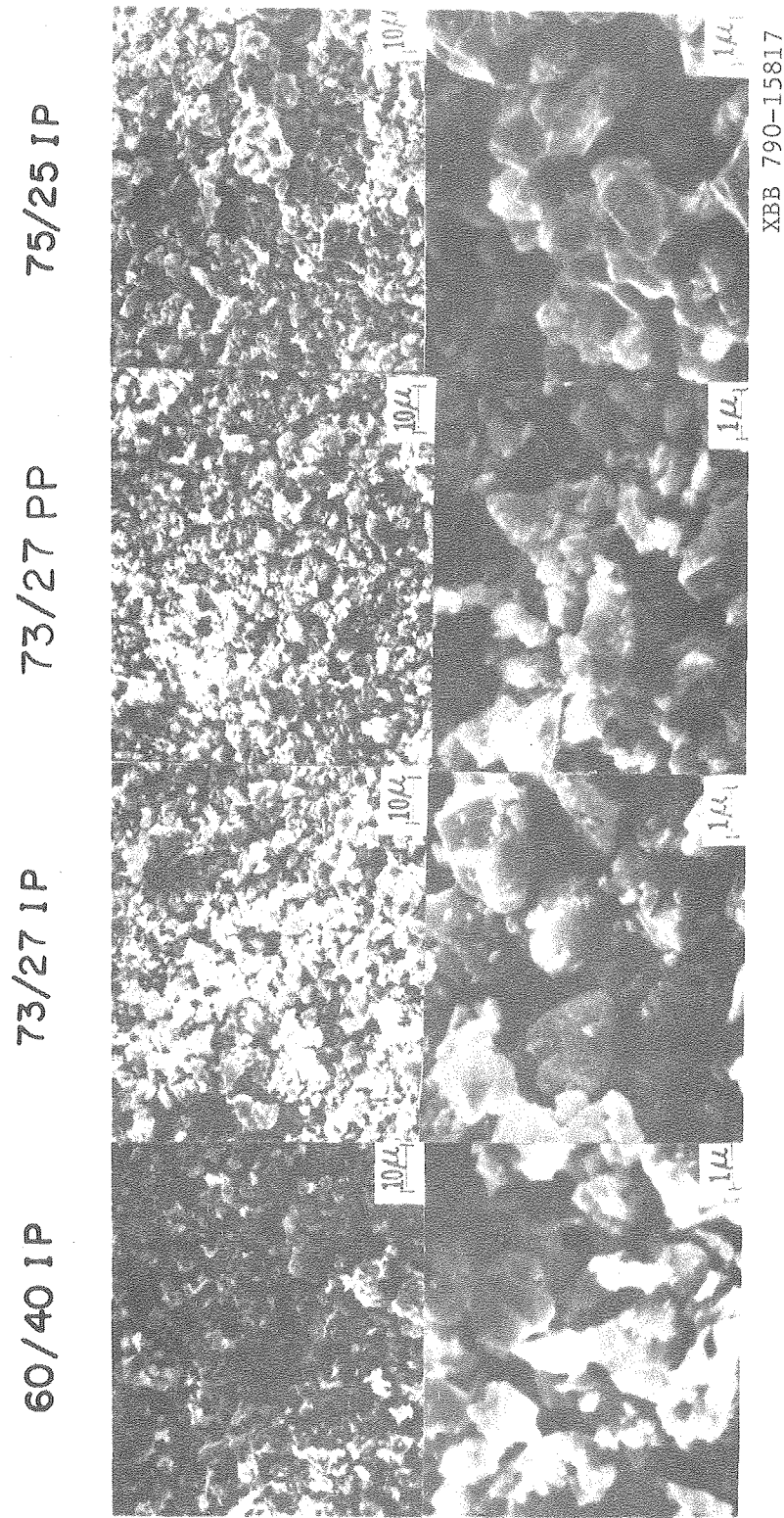
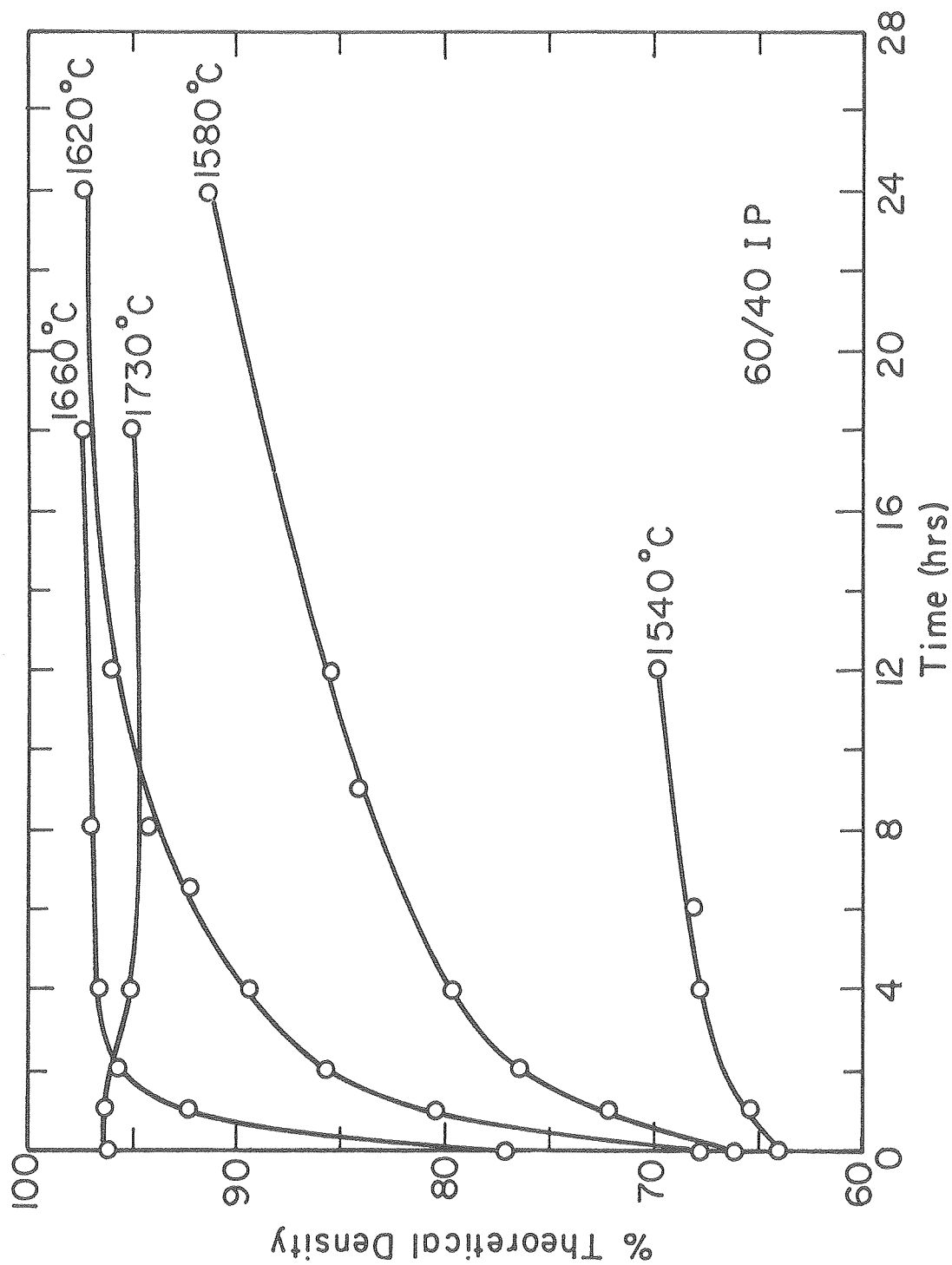


Fig. 13



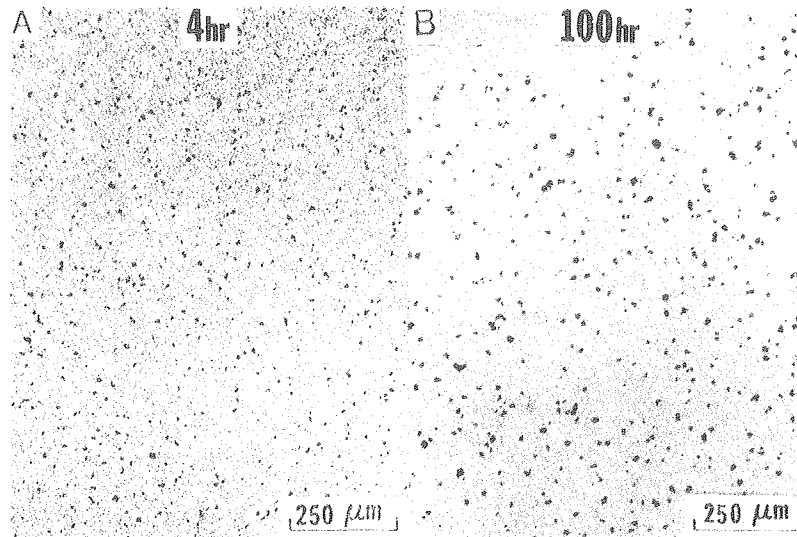
XBL785-4930

Fig. 14

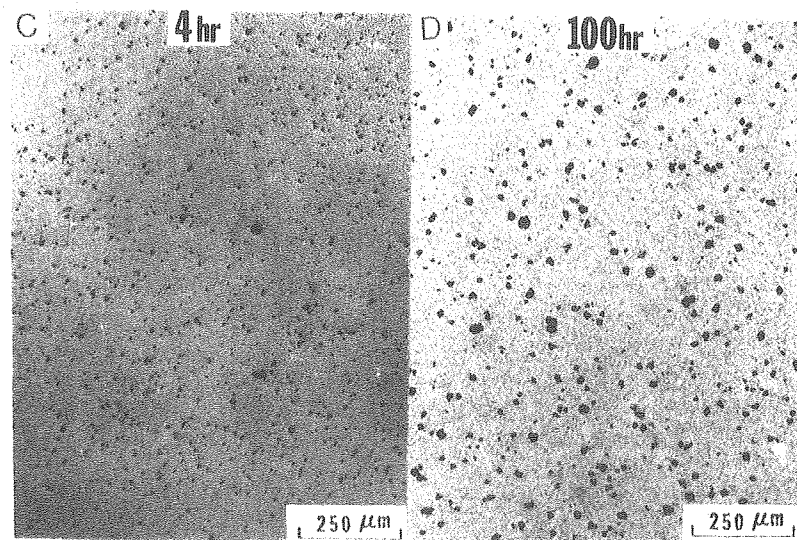


COMPOSITION: 60/40

POWDER



GEL



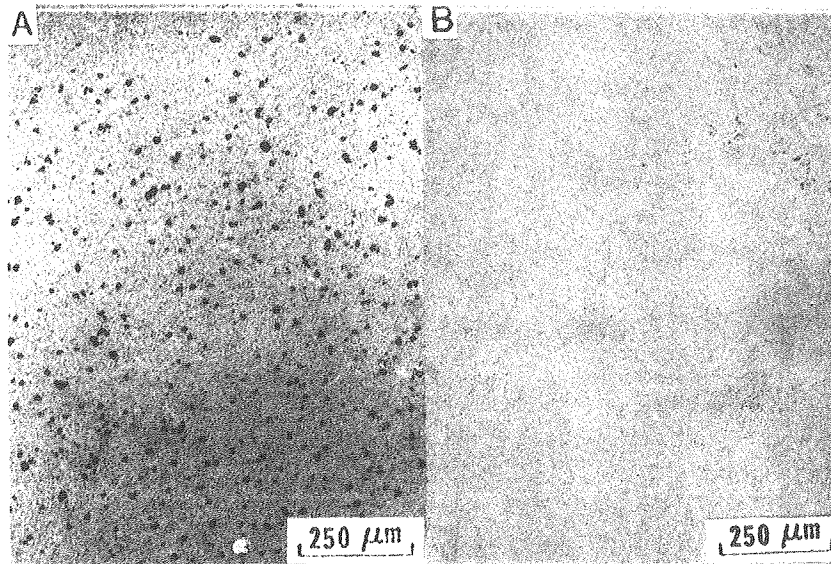
XBB 790-15935

Fig. 15

# COMPOSITION: 60/40

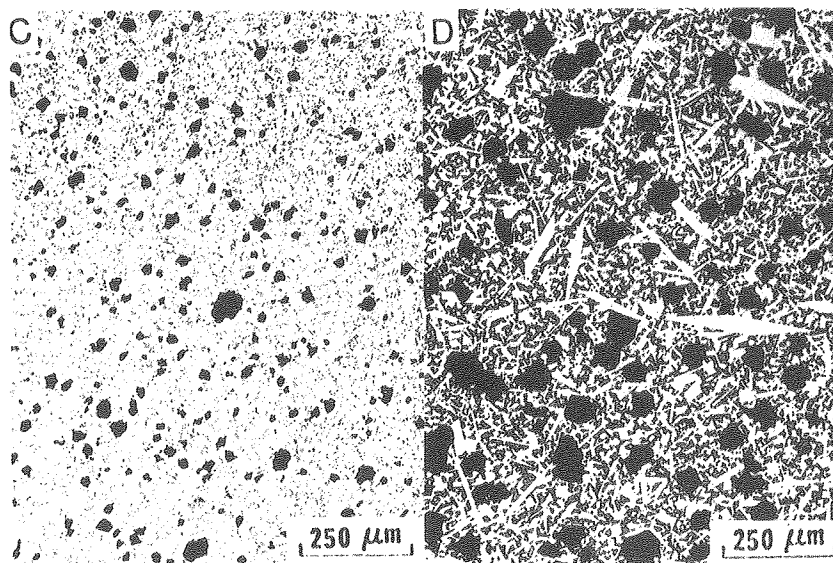
AIR

VACUUM



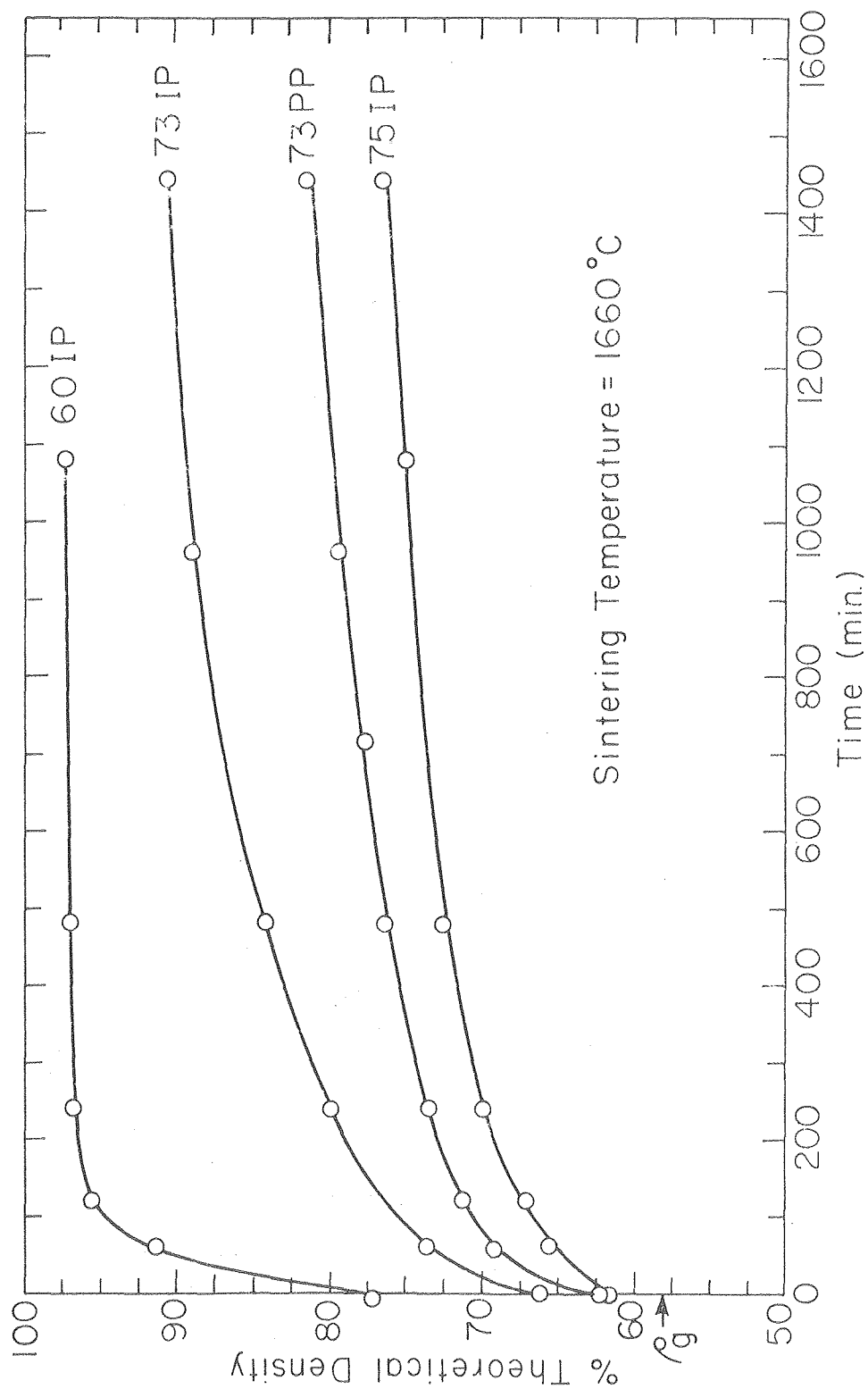
ARGON

SEALED Mo



XBB 790-15078

Fig. 16



XBL 7911-14503

Fig. 17



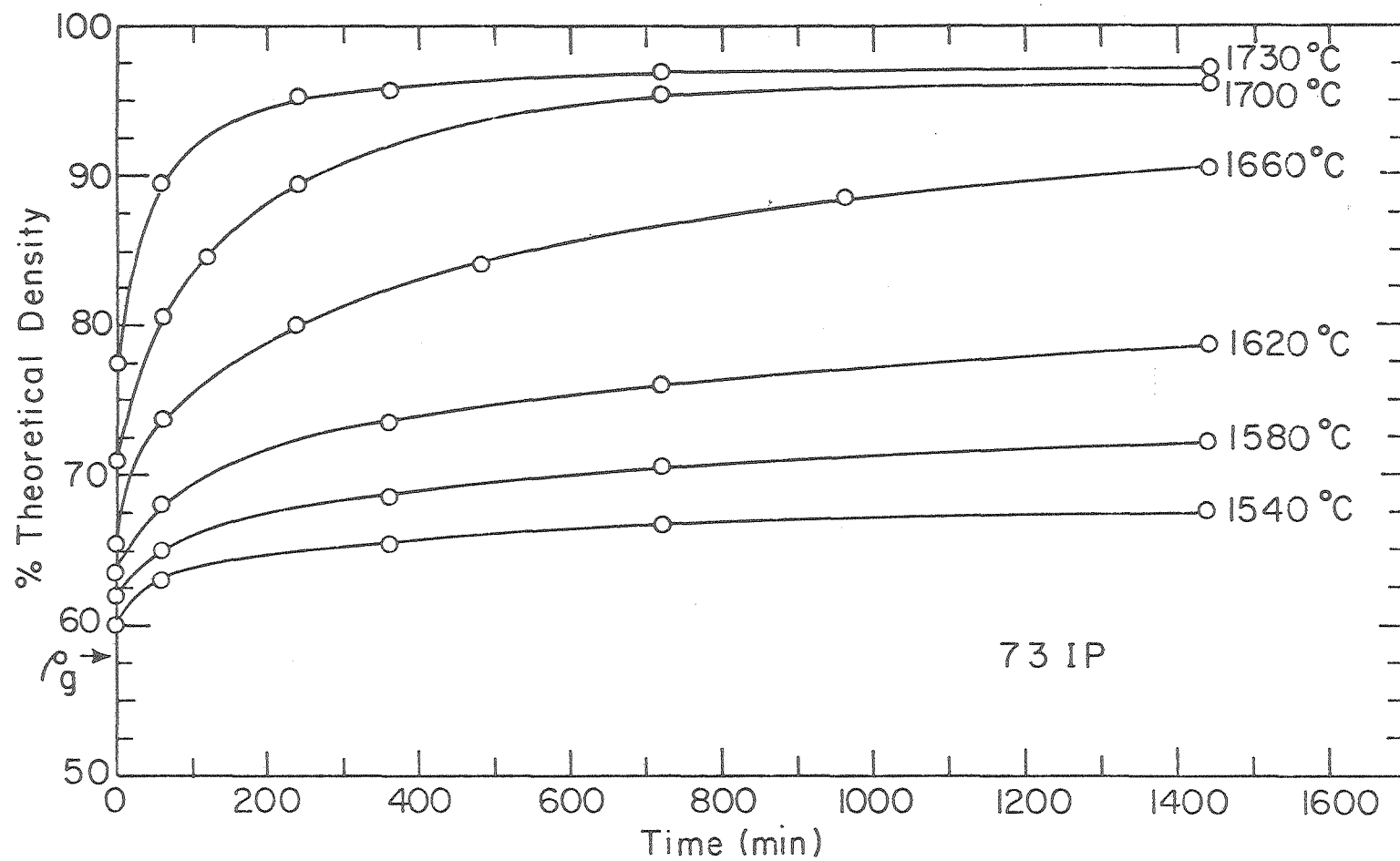
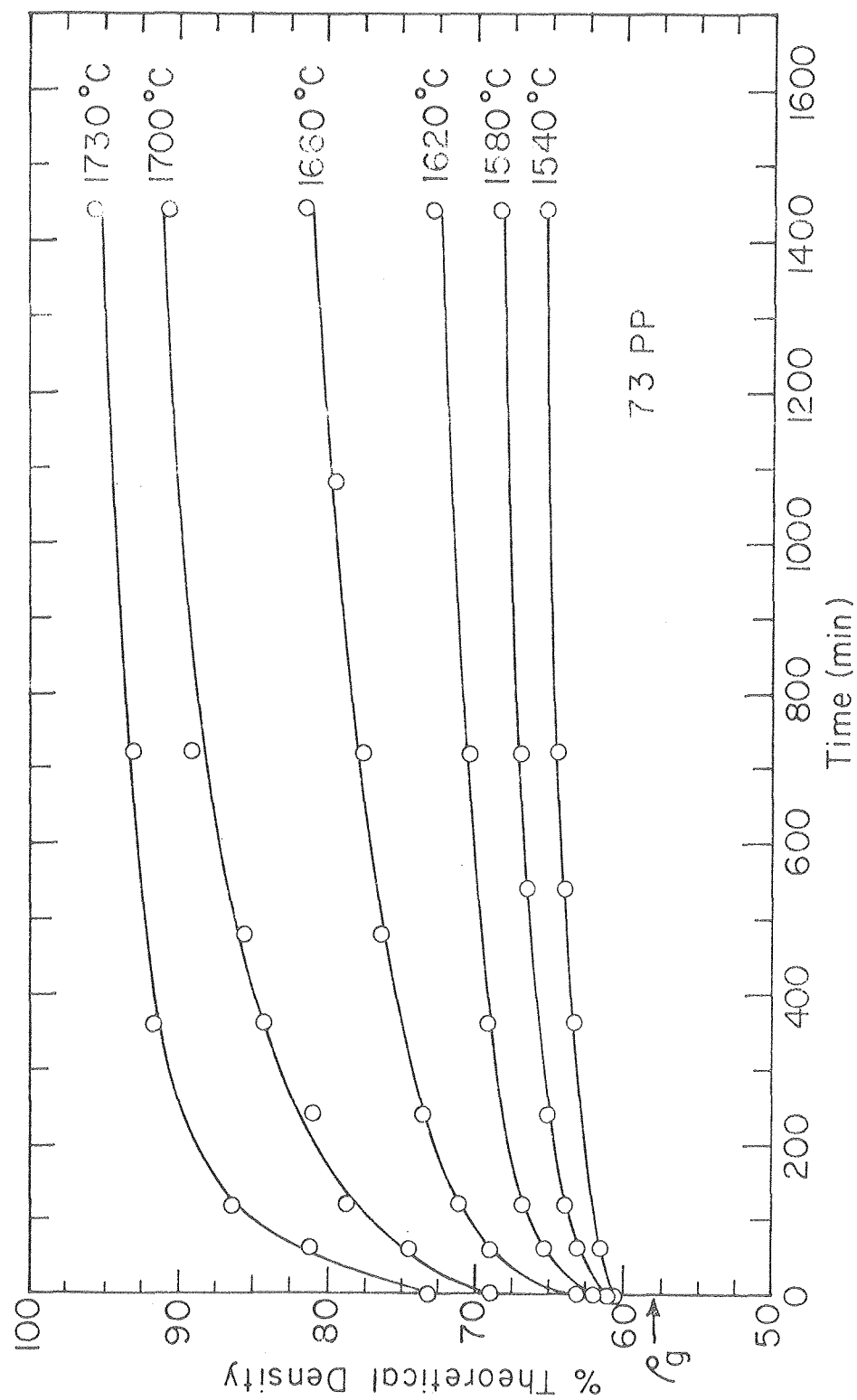


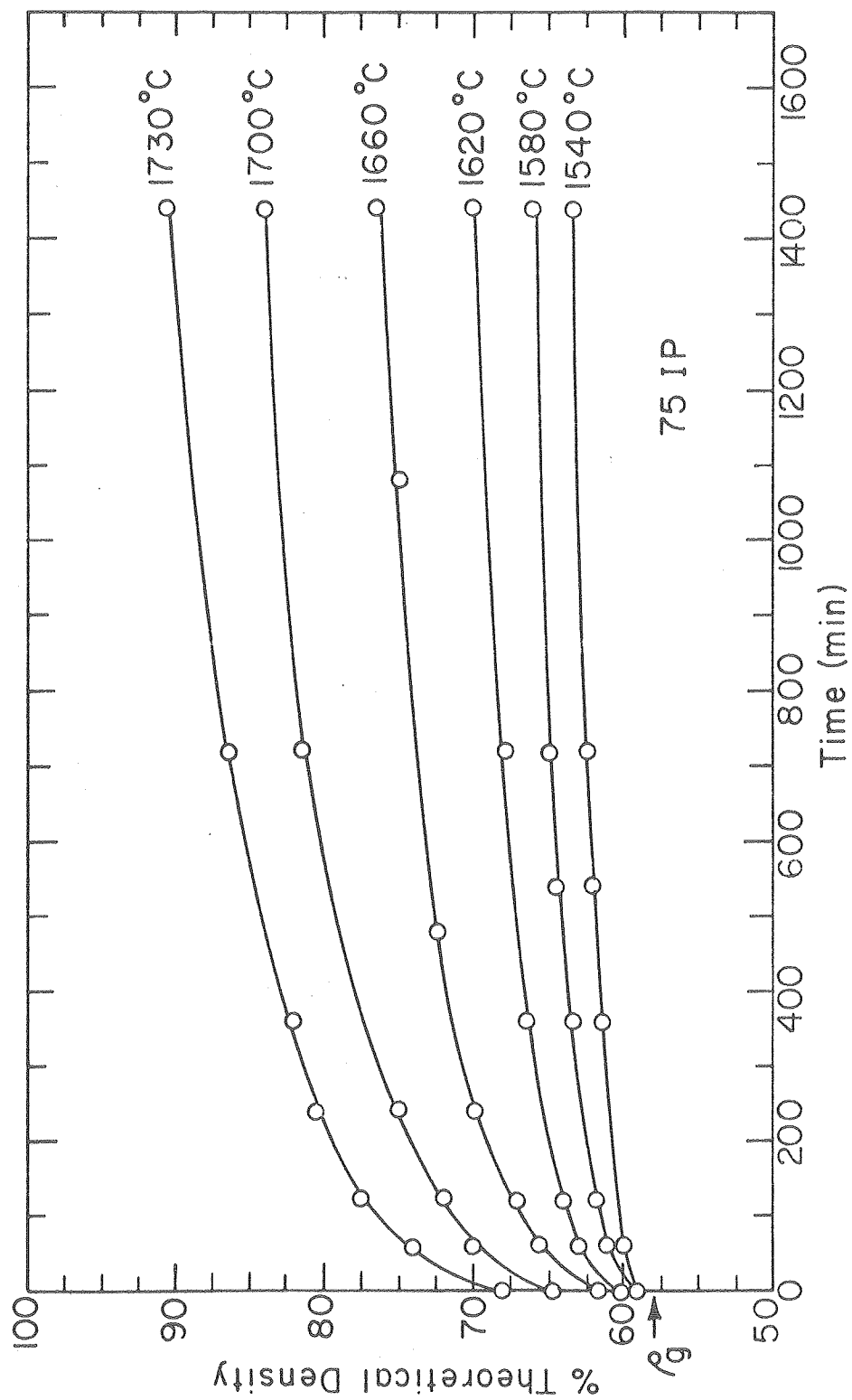
Fig. 18

XBL 7911-14510



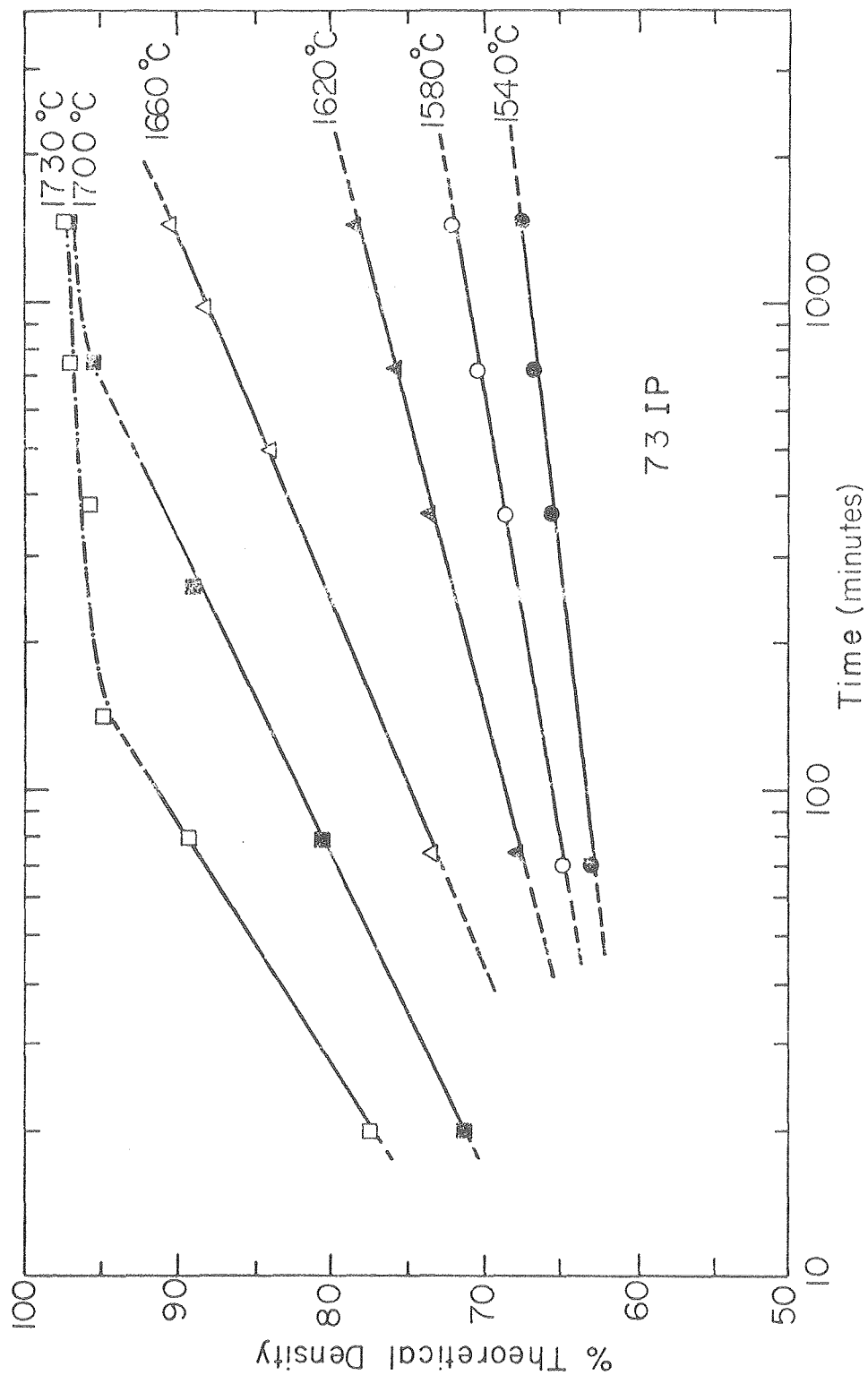
XBL 7911-14509

Fig. 19



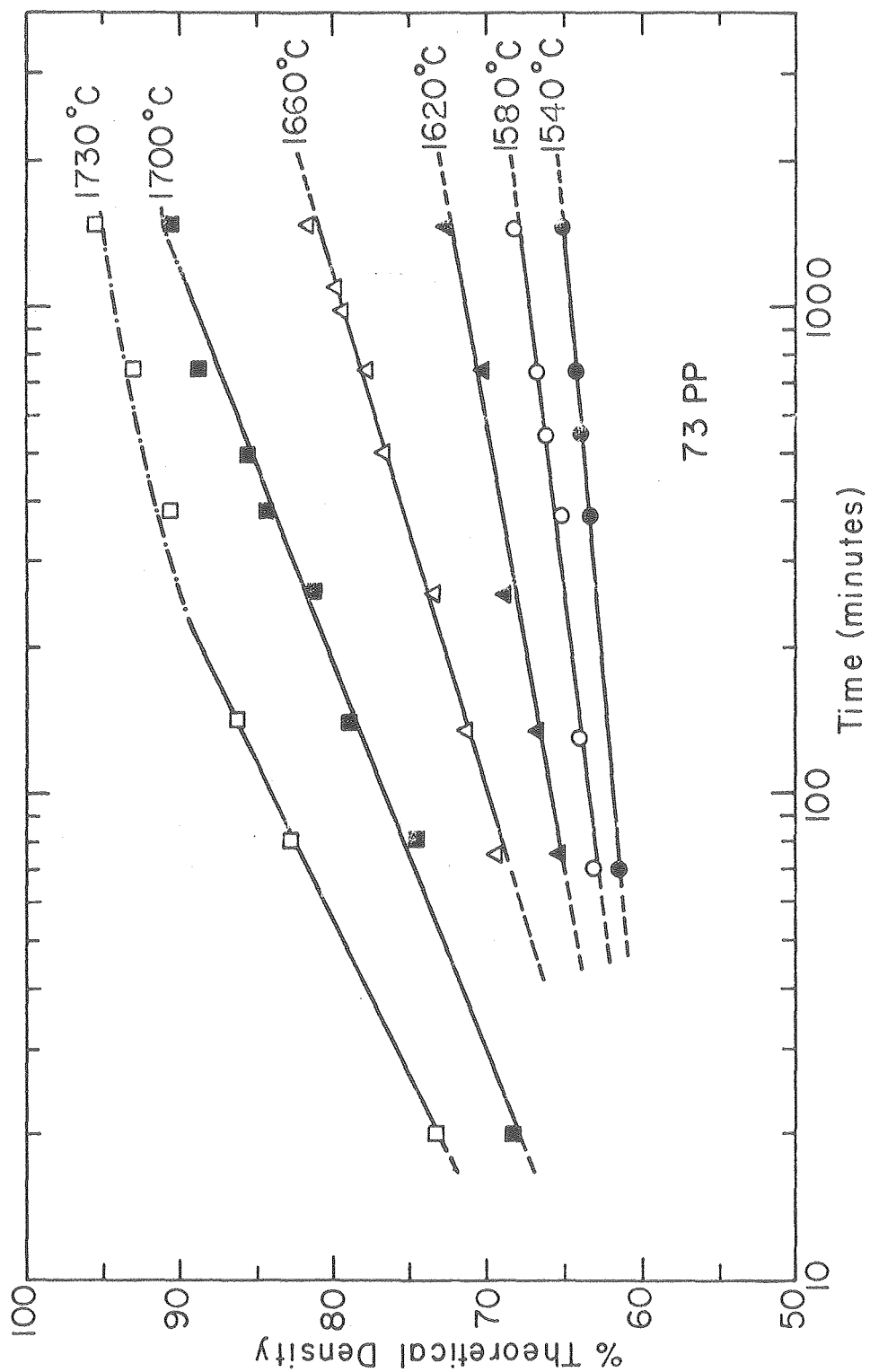
XBL 7911-14511

Fig. 20



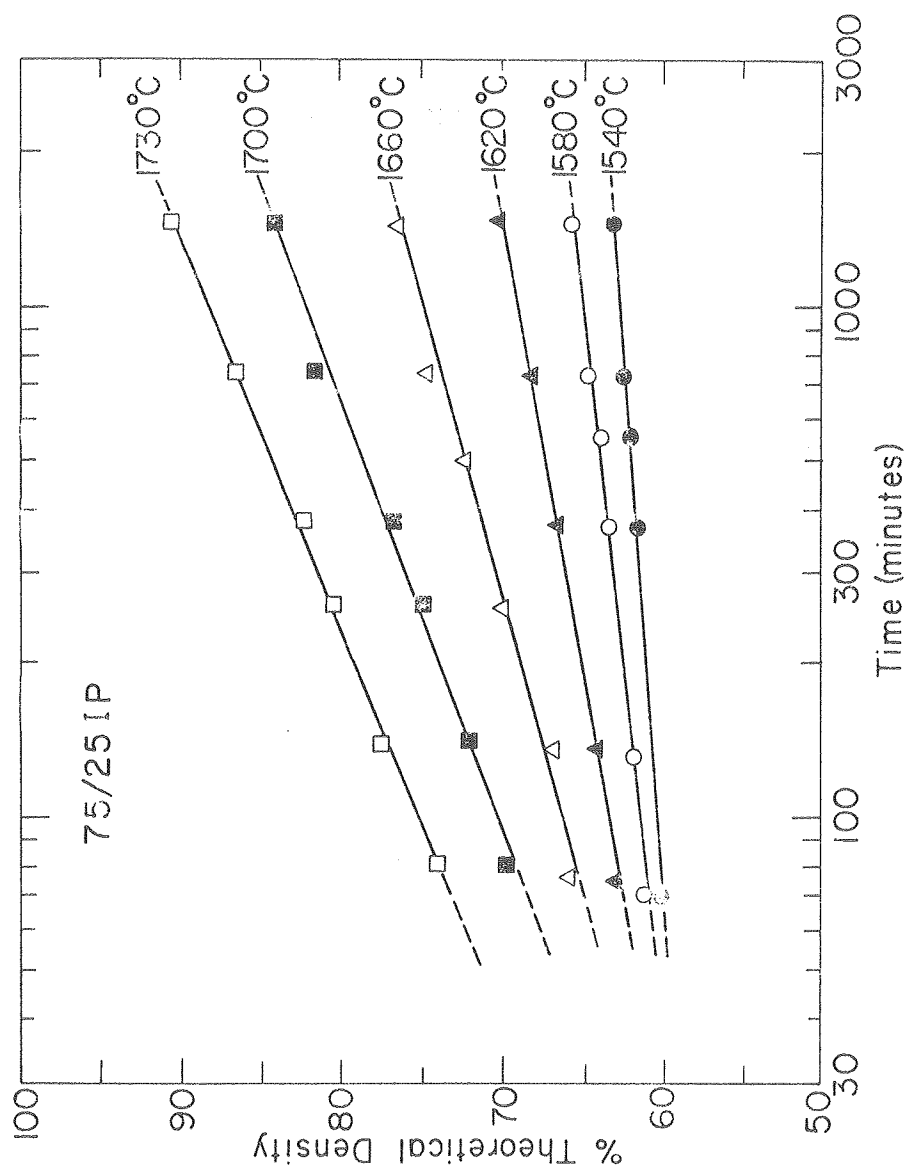
XBL 7810-5889

Fig. 21



XBL 7810-5890

Fig. 22



XBL 7810-5894

Fig. 23

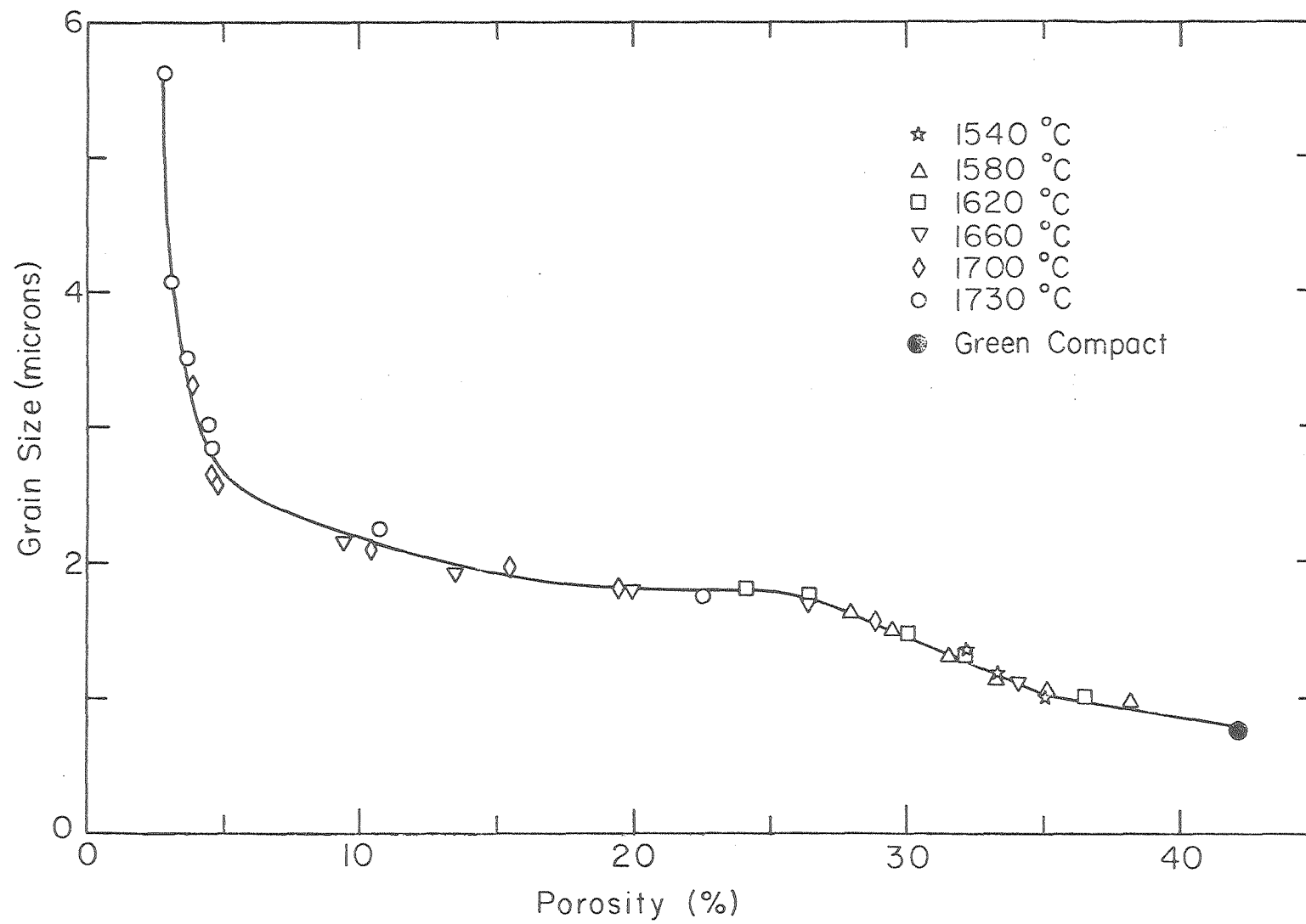
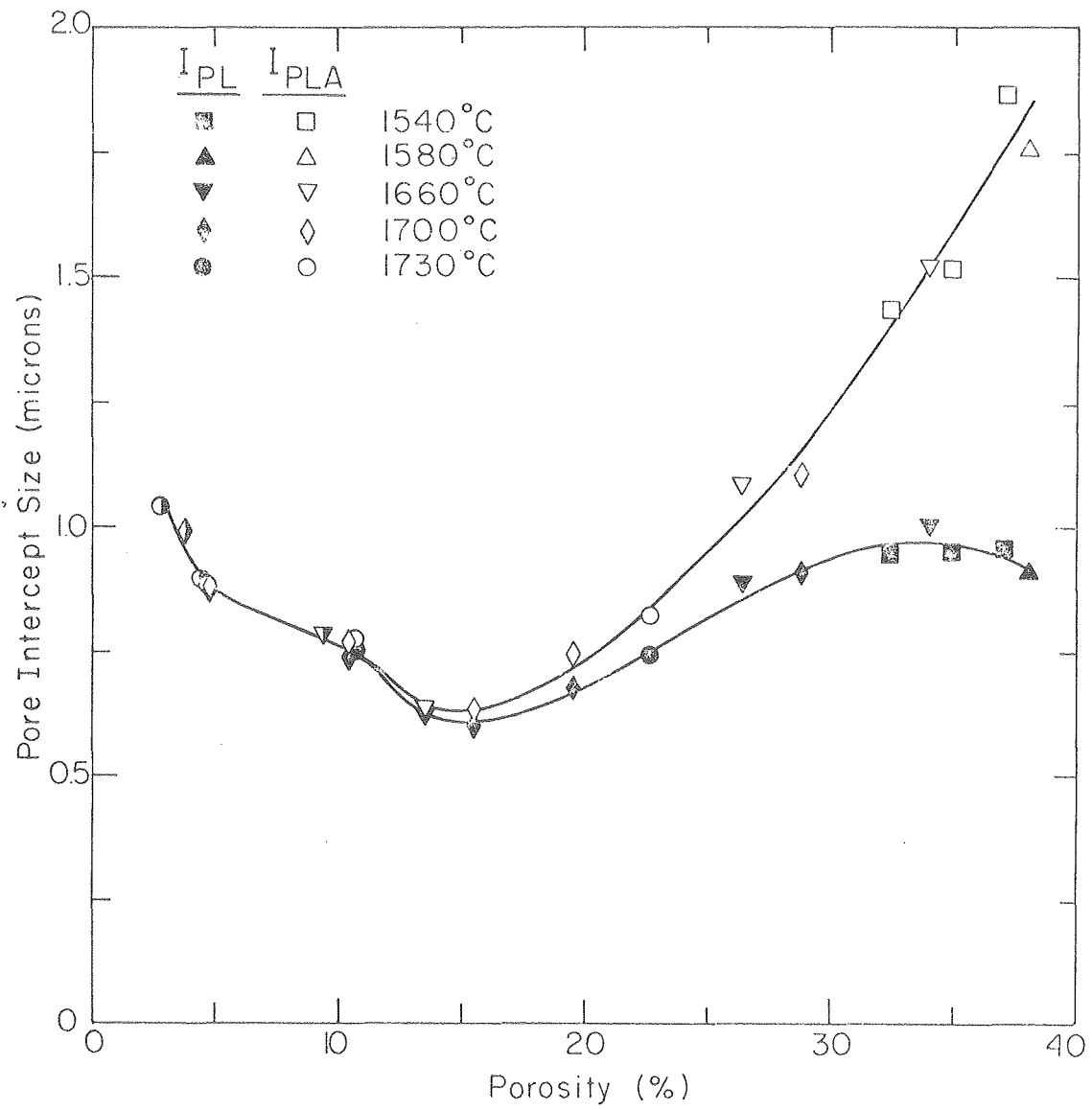


Fig. 24

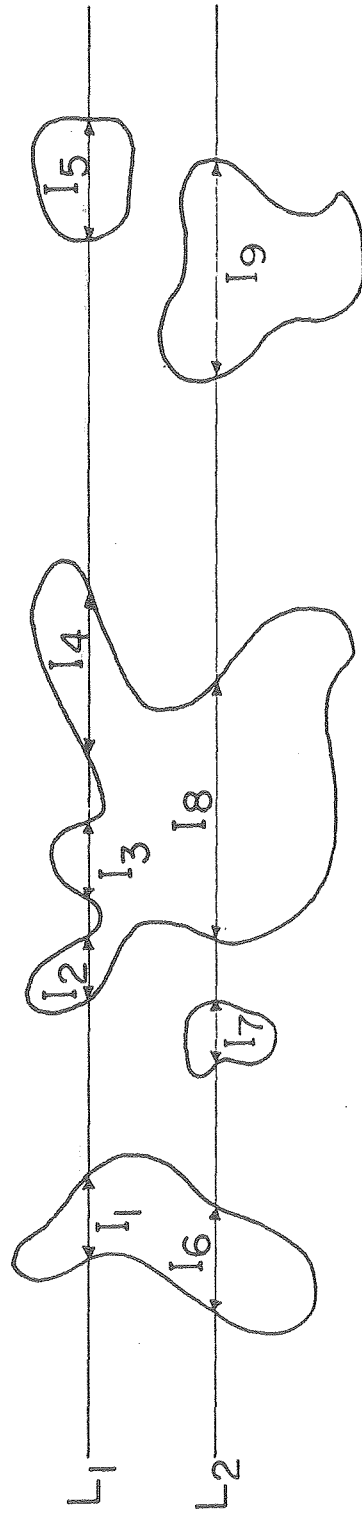
XBL 7912- 5402



XBL 7912-5405

Fig. 25





$L_1$  and  $L_2$  are lines of length  $L$

$$\text{For } L_1: \quad \bar{I}_{PL} = \frac{\sum_{i=1}^5 I_i}{5}$$

$$\bar{I}_{PLA} = \frac{\sum_{i=1}^5 I_i}{3}$$

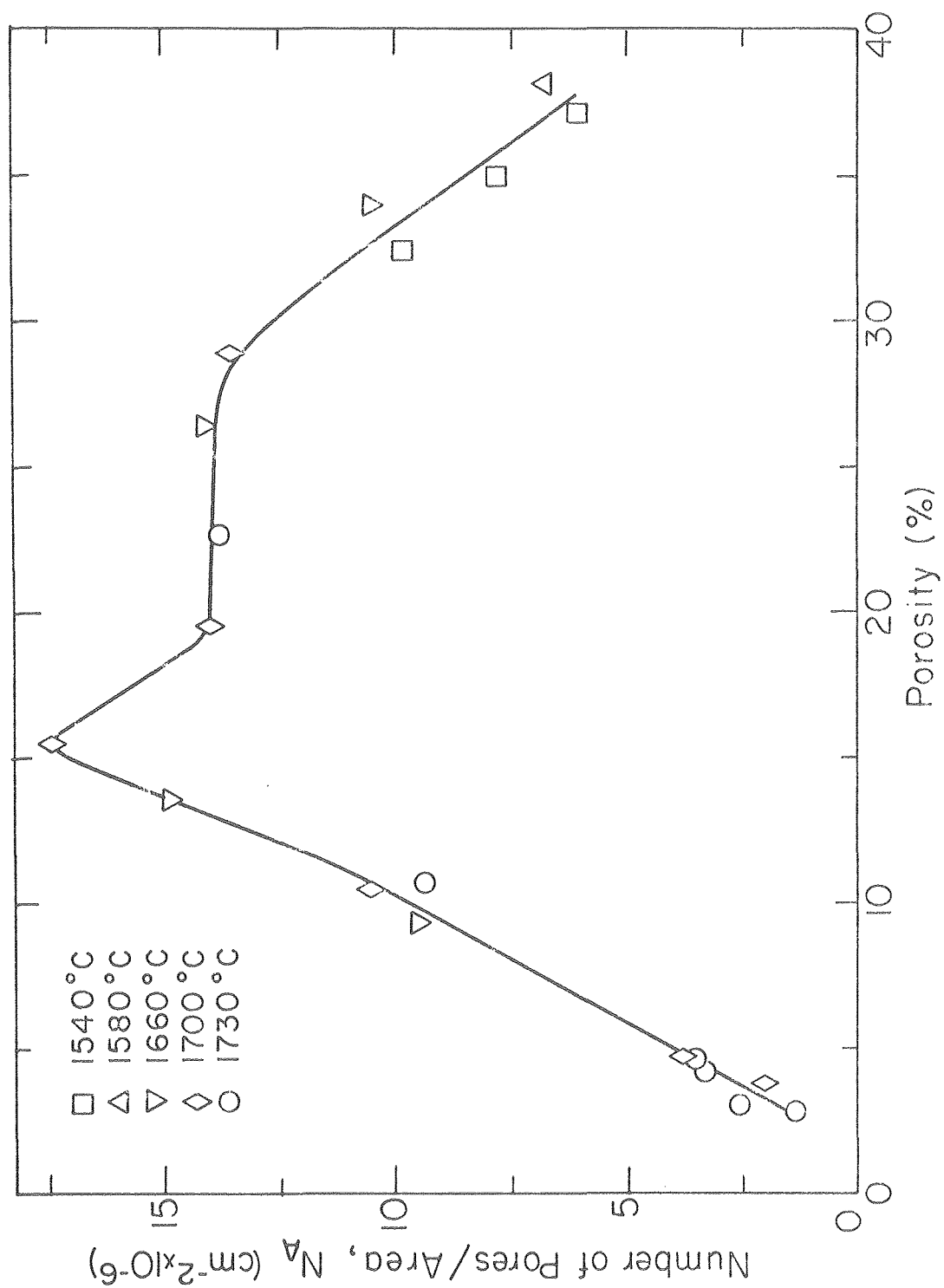
$$P_L = \frac{10}{L}$$

$$\text{For } L_2: \quad \bar{I}_{PL} = \bar{I}_{PLA} = \frac{\sum_{i=6}^9 I_i}{4}$$

$$P_L = \frac{8}{L}$$

XBL79I-14516

Fig. 26



XBL 7912-5458

Fig. 27

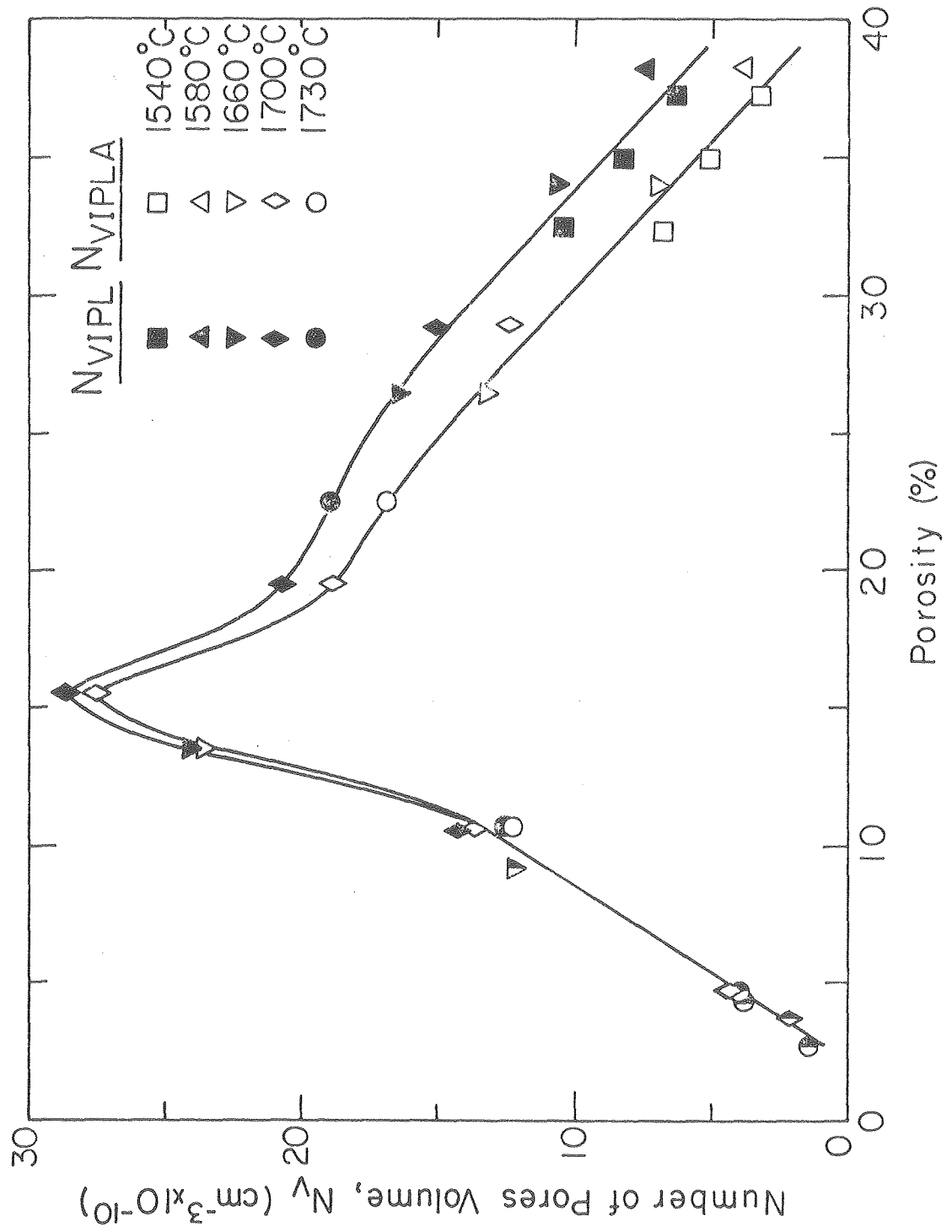


Fig. 28

XBL7912-5406

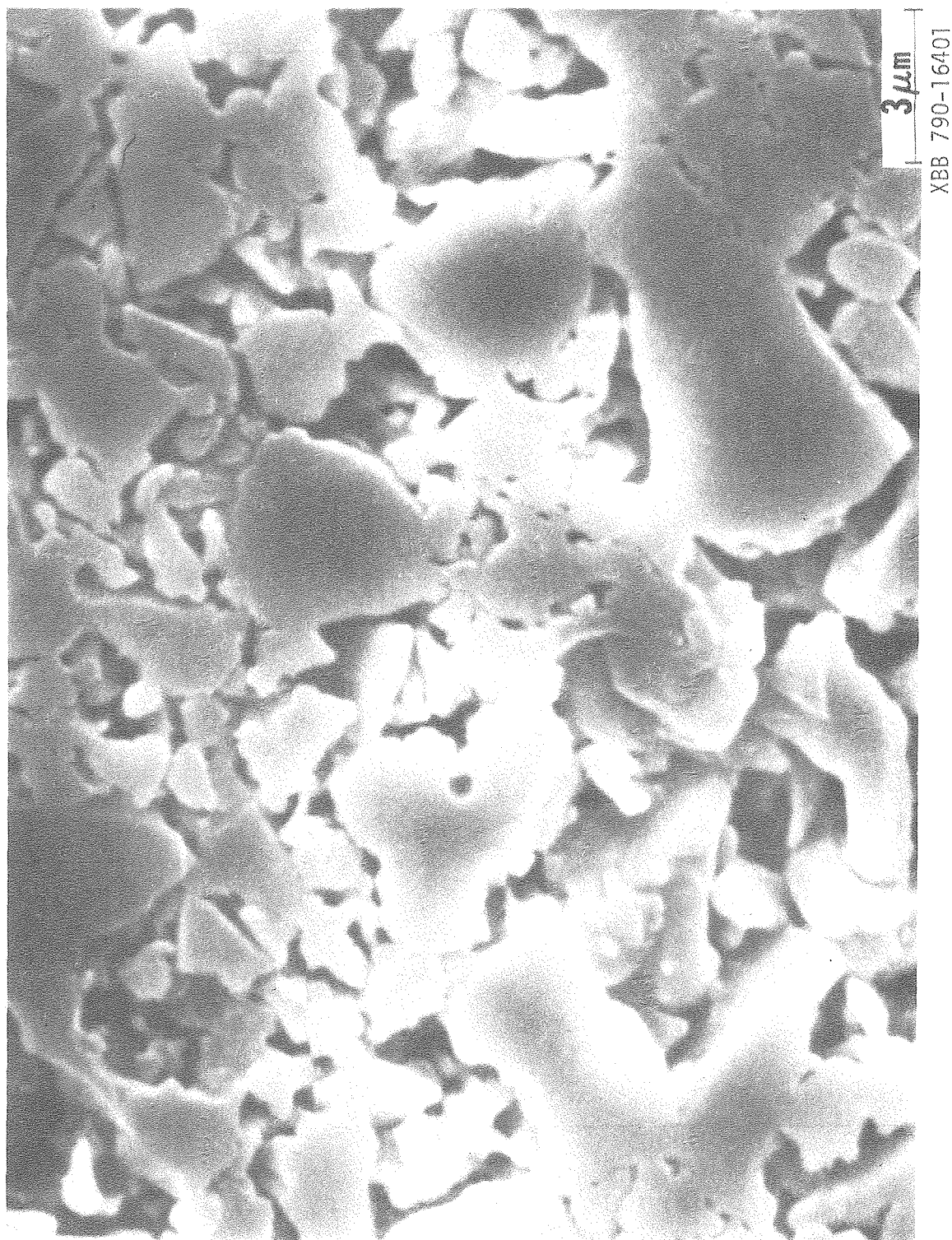
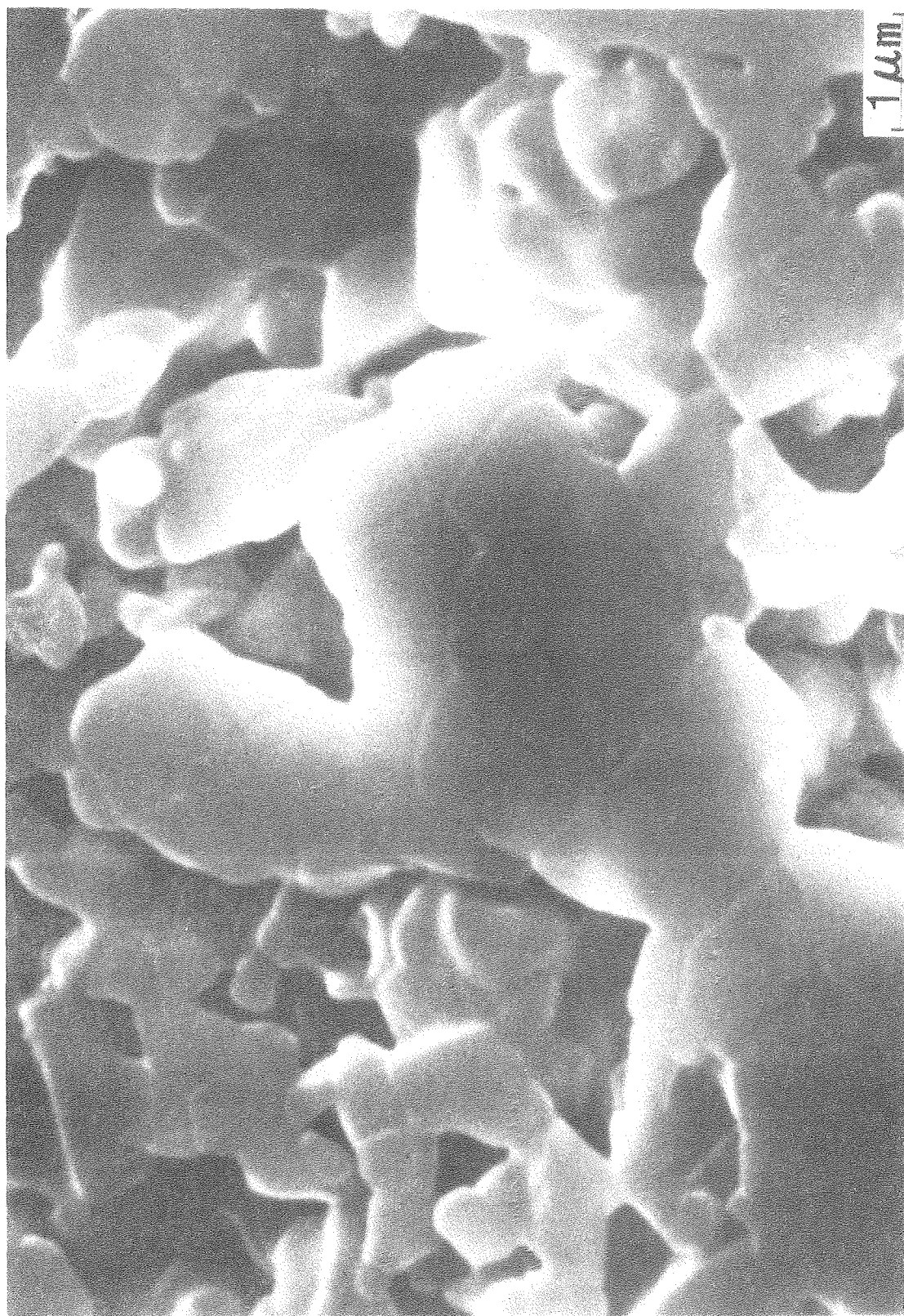
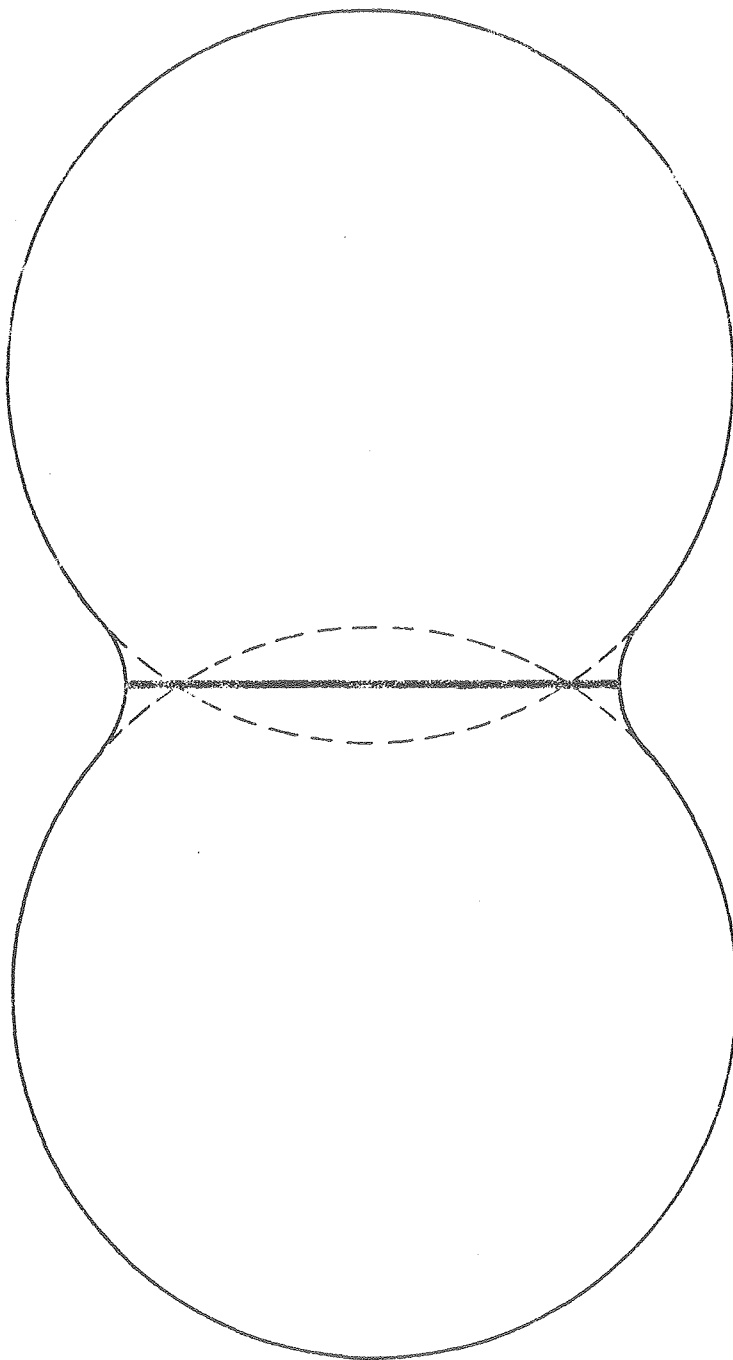


Fig. 29



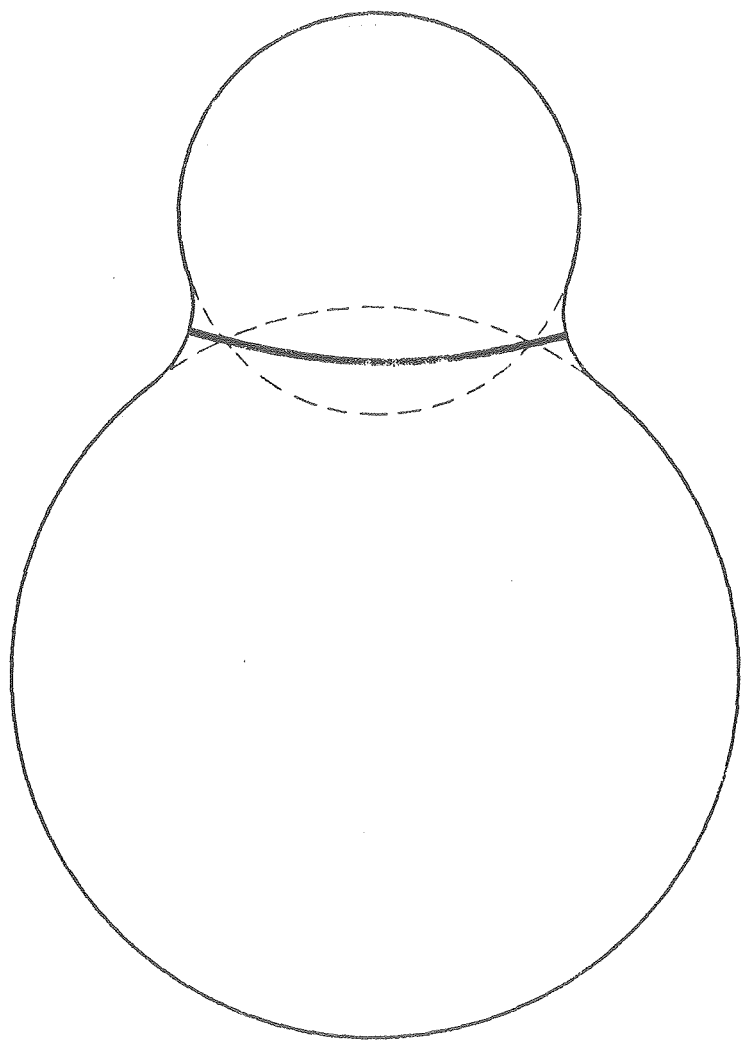
XBB 790-15930

Fig. 30



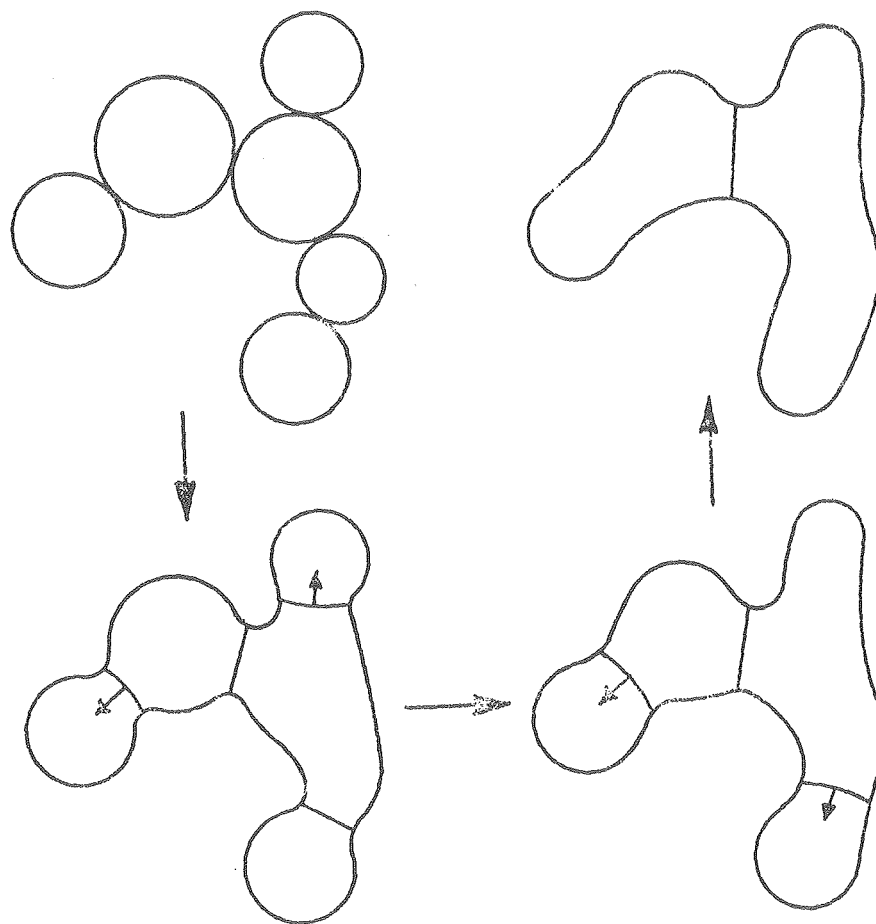
XBL 7912-13526

Fig. 31



XBL 7912-13525

Fig. 32



XBL 7911-13520

Fig. 33



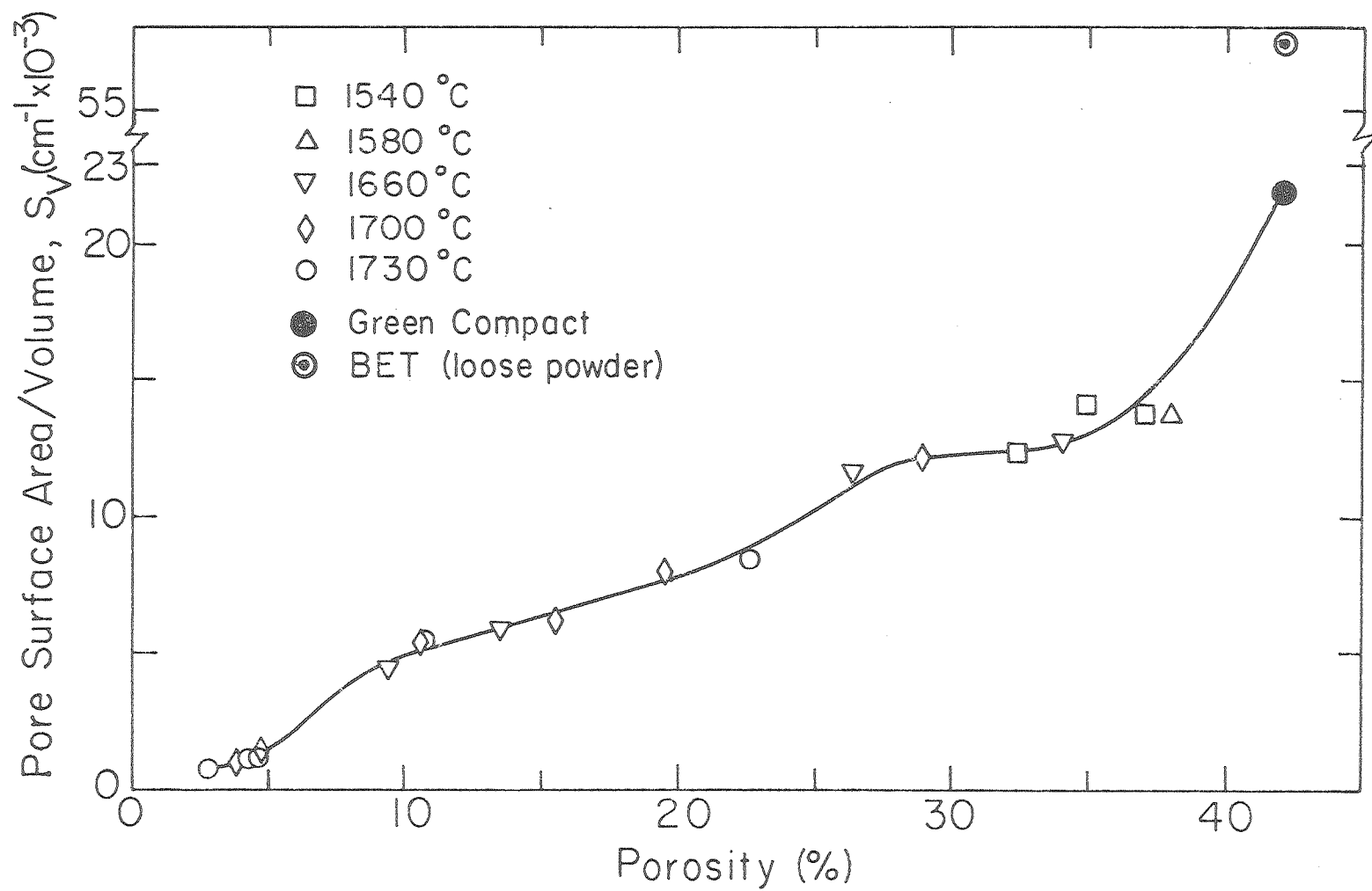
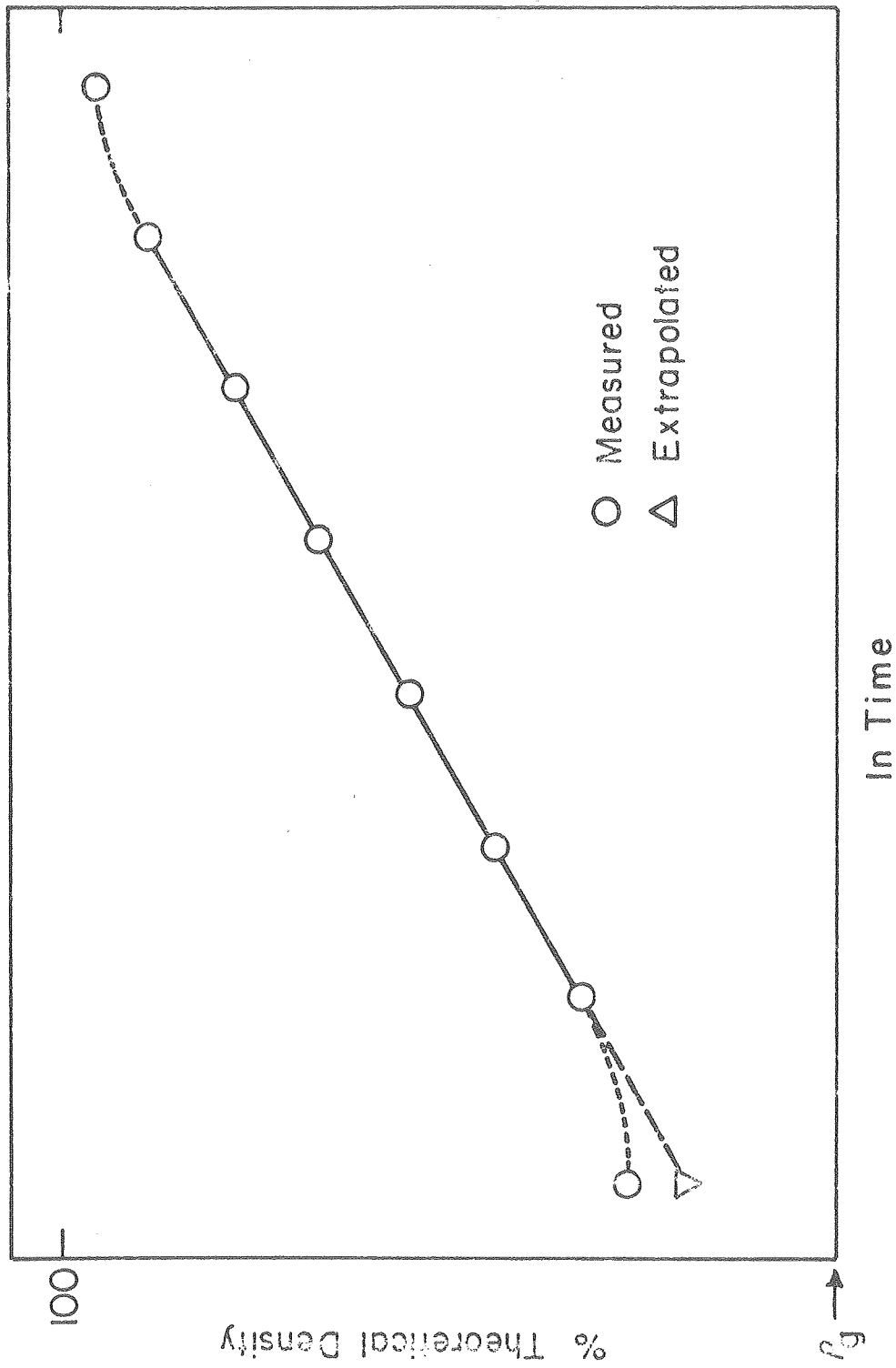
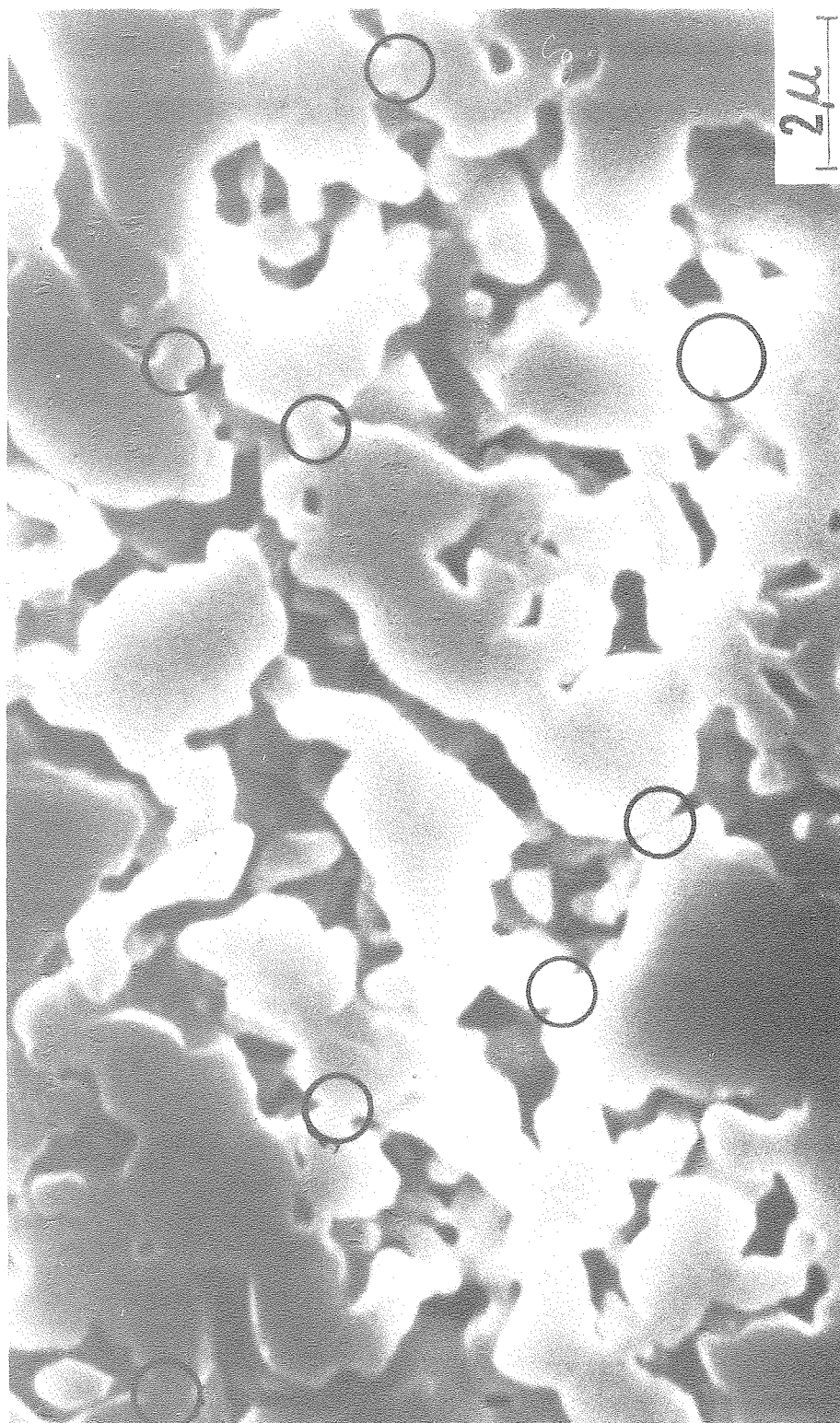


Fig. 34

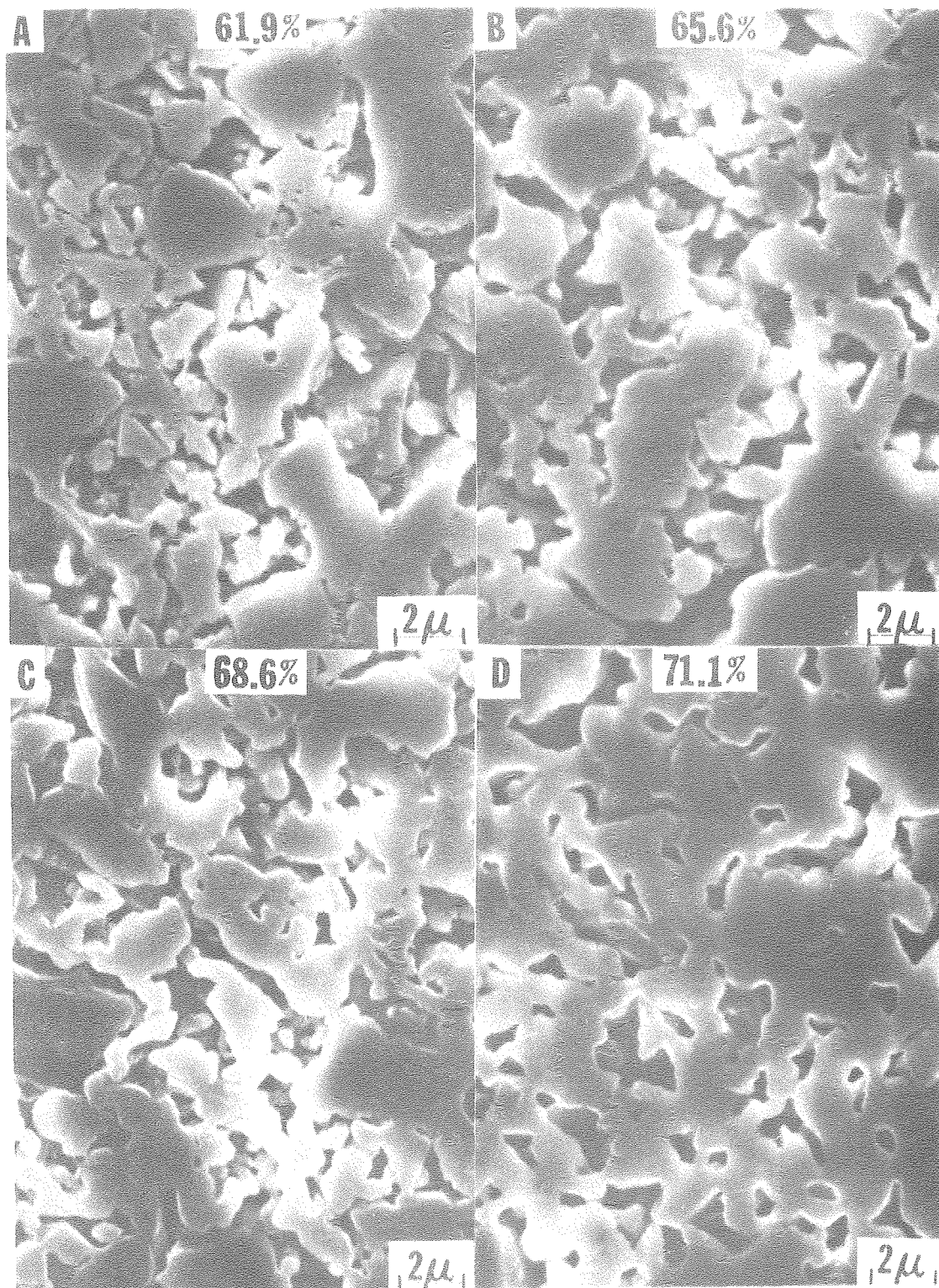
XBL 7912-5457





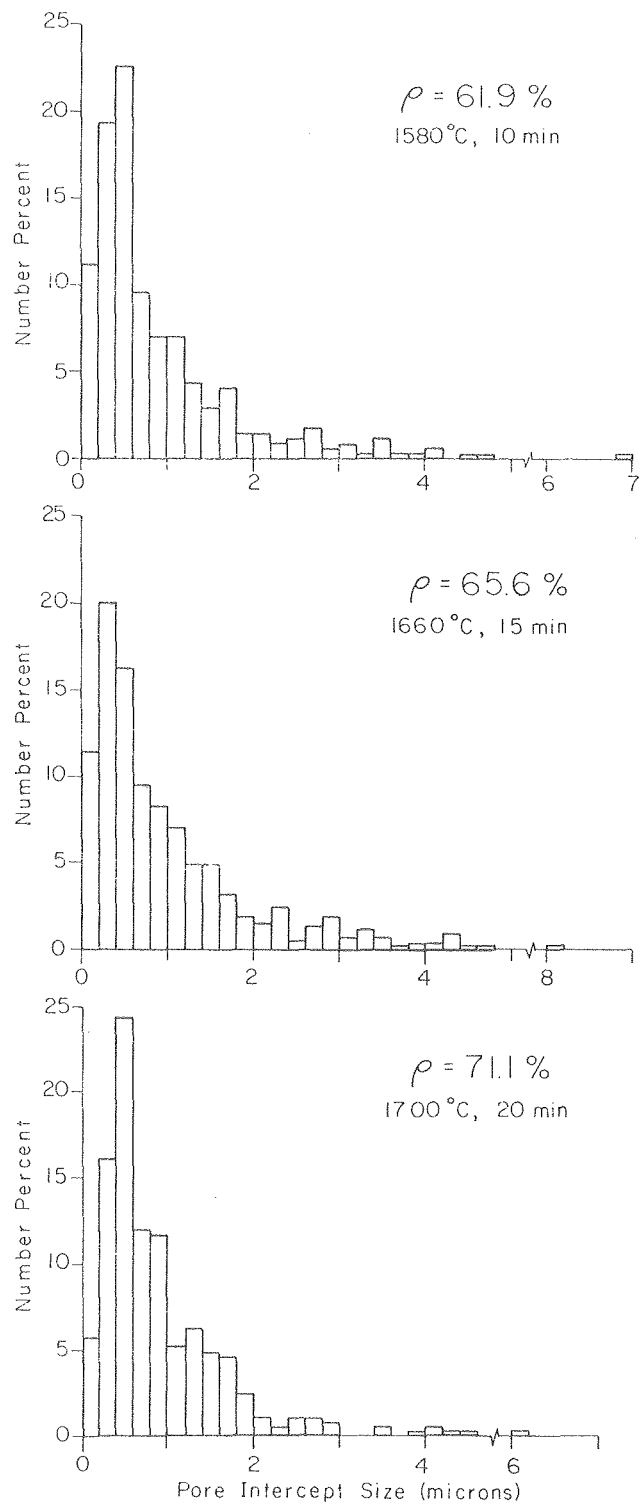
XBB 790-15625

Fig. 36



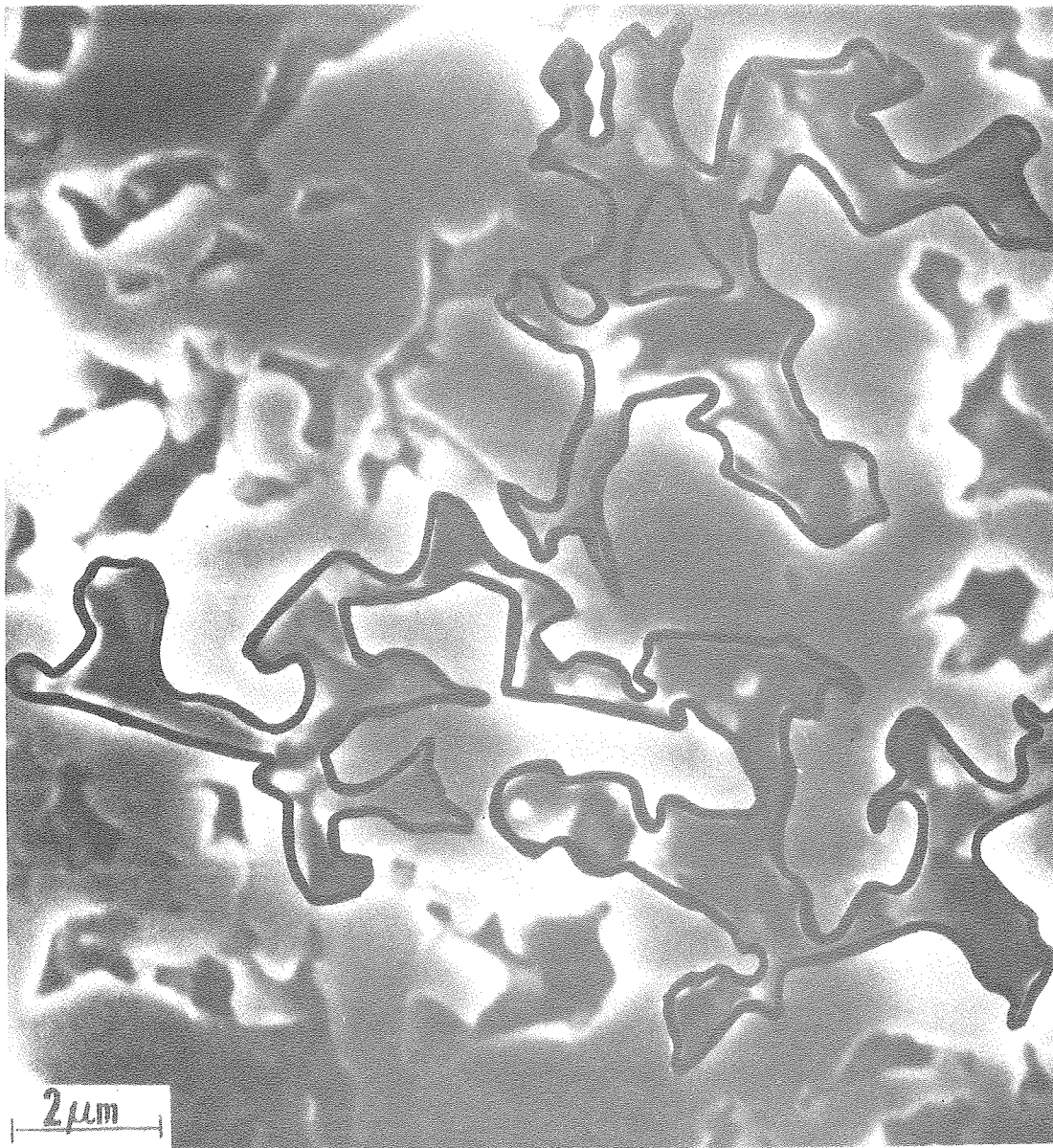
XBB 790-16636

Fig. 37



XBL 7912-5403

Fig. 38



XBB 790-16634

Fig. 39

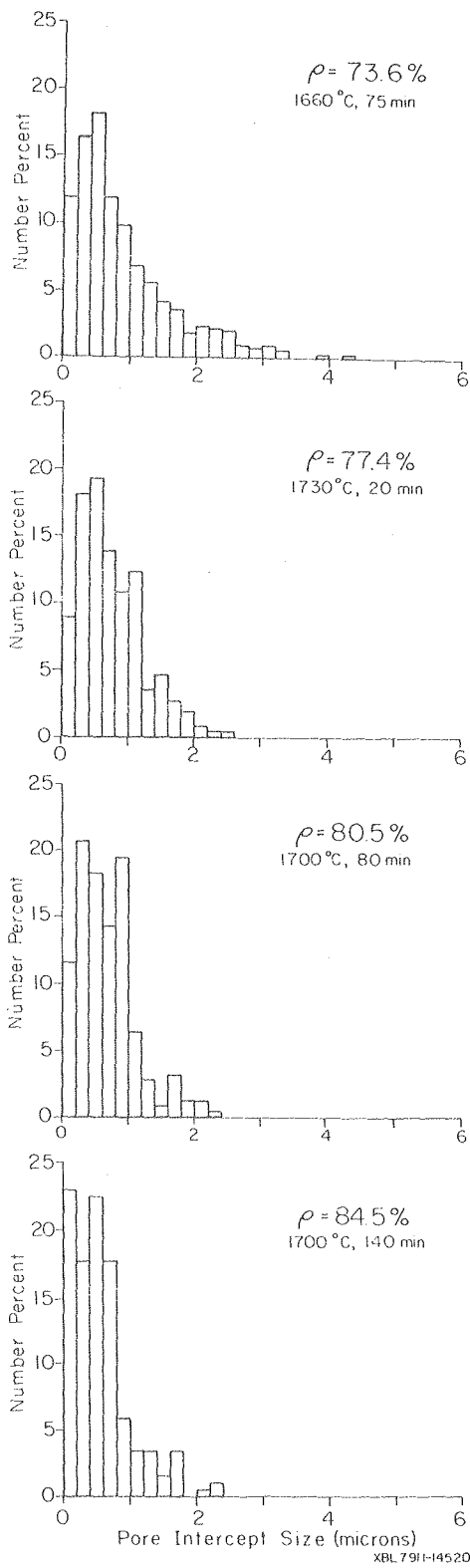
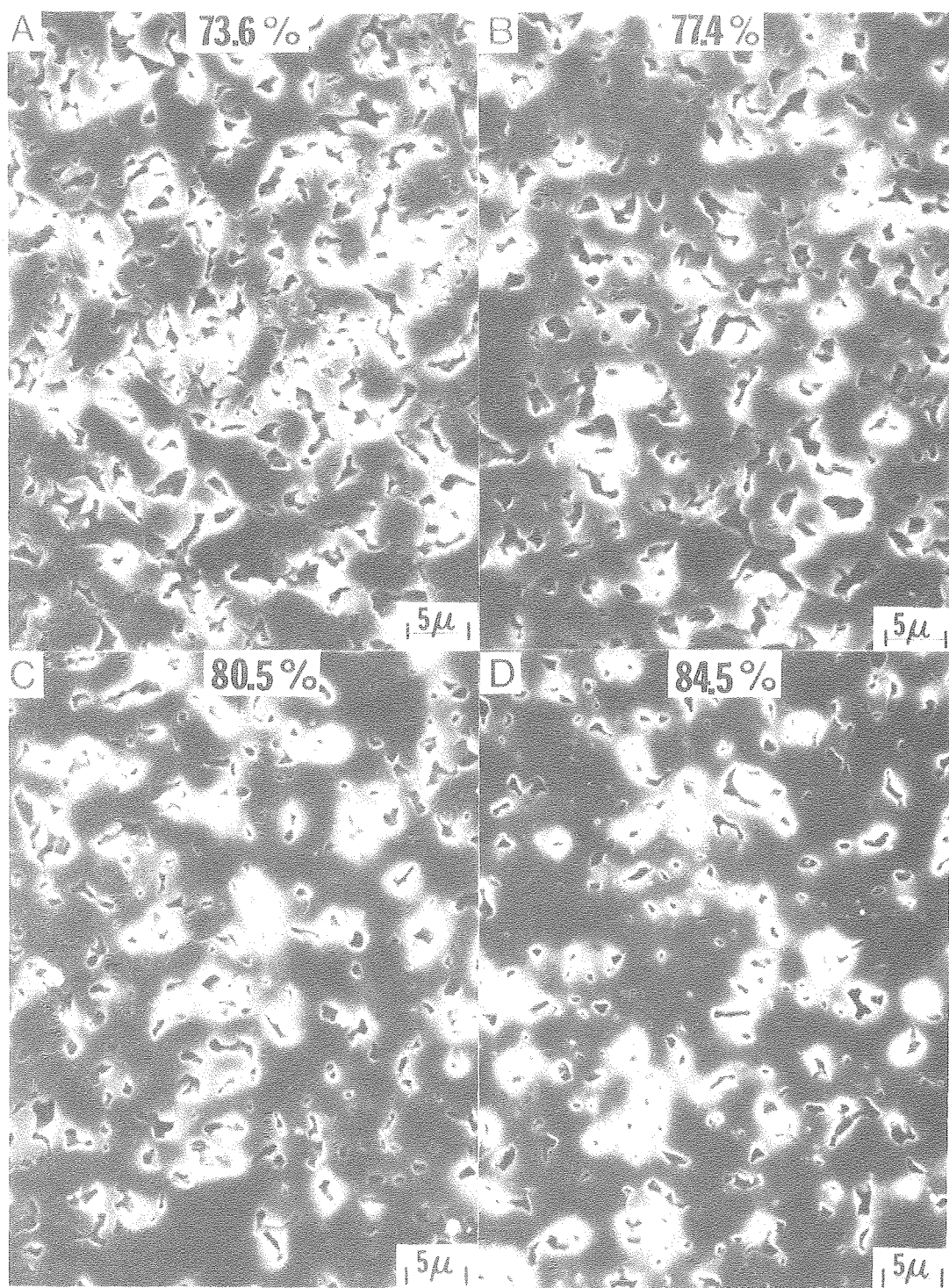


Fig. 40





XBB 790-16012

Fig. 41



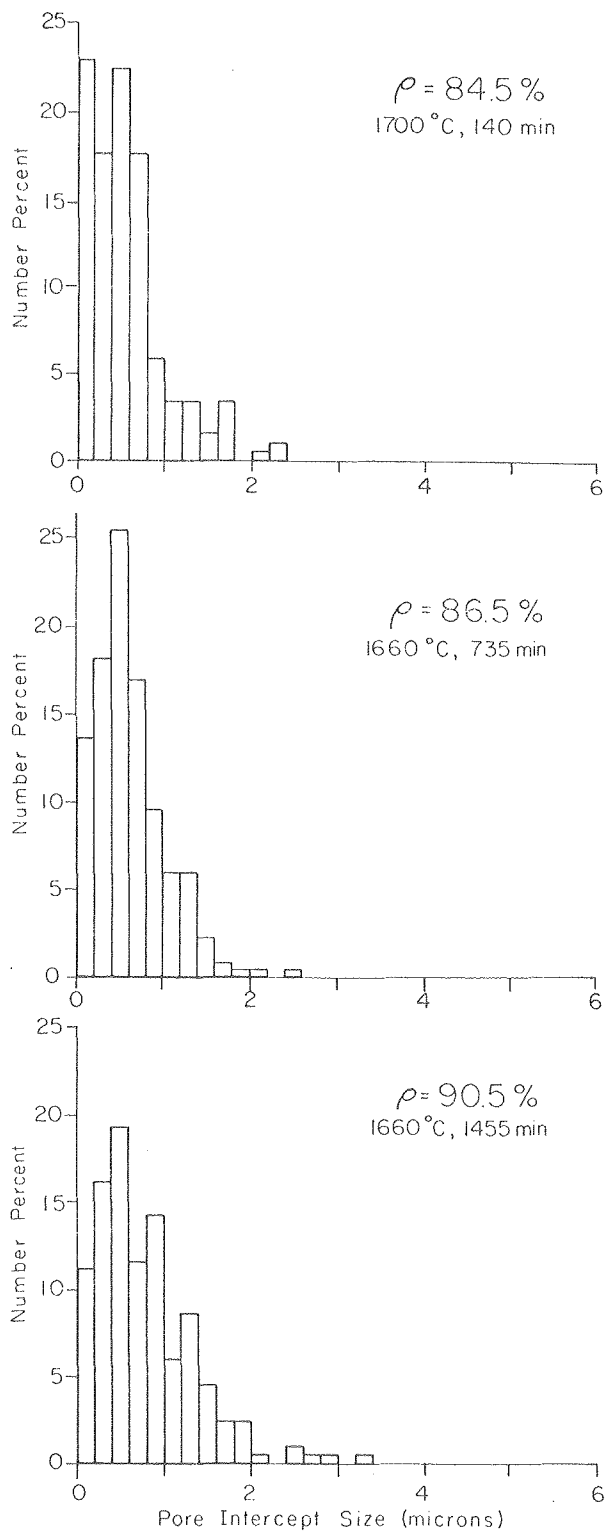


Fig. 42

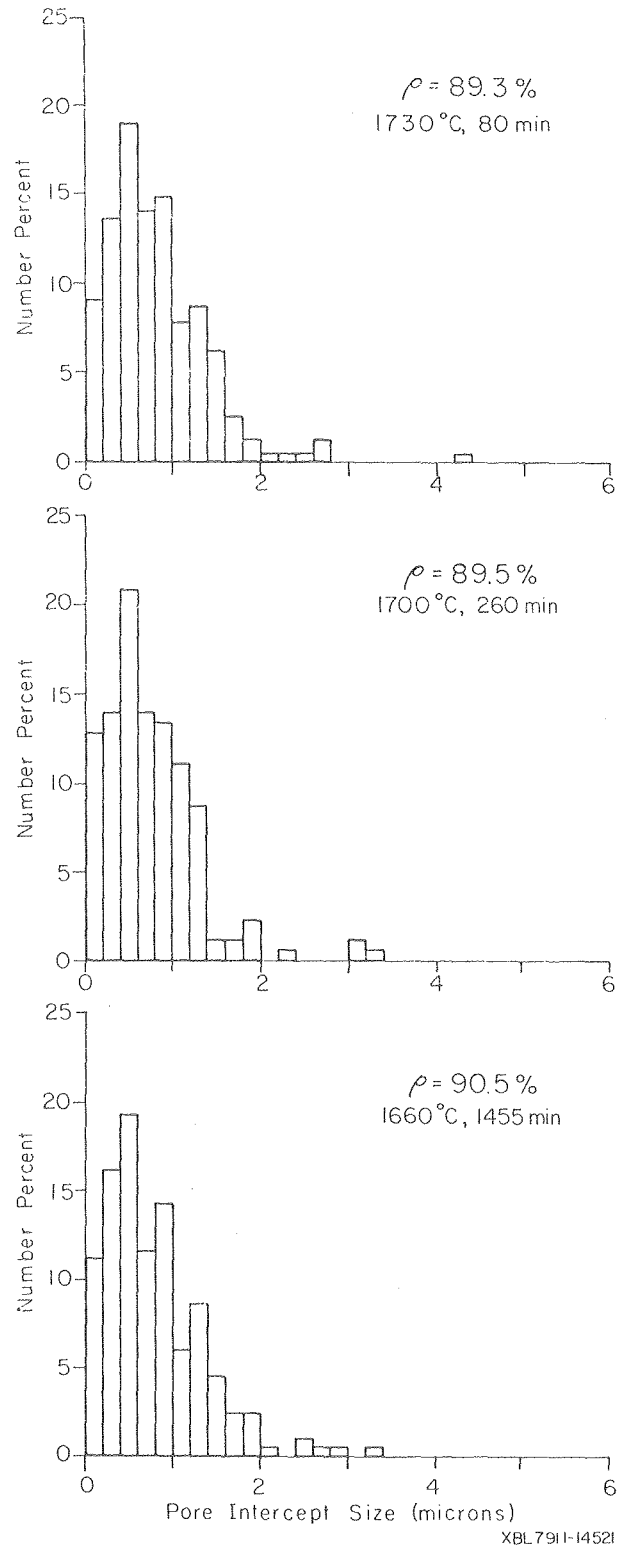


Fig. 43

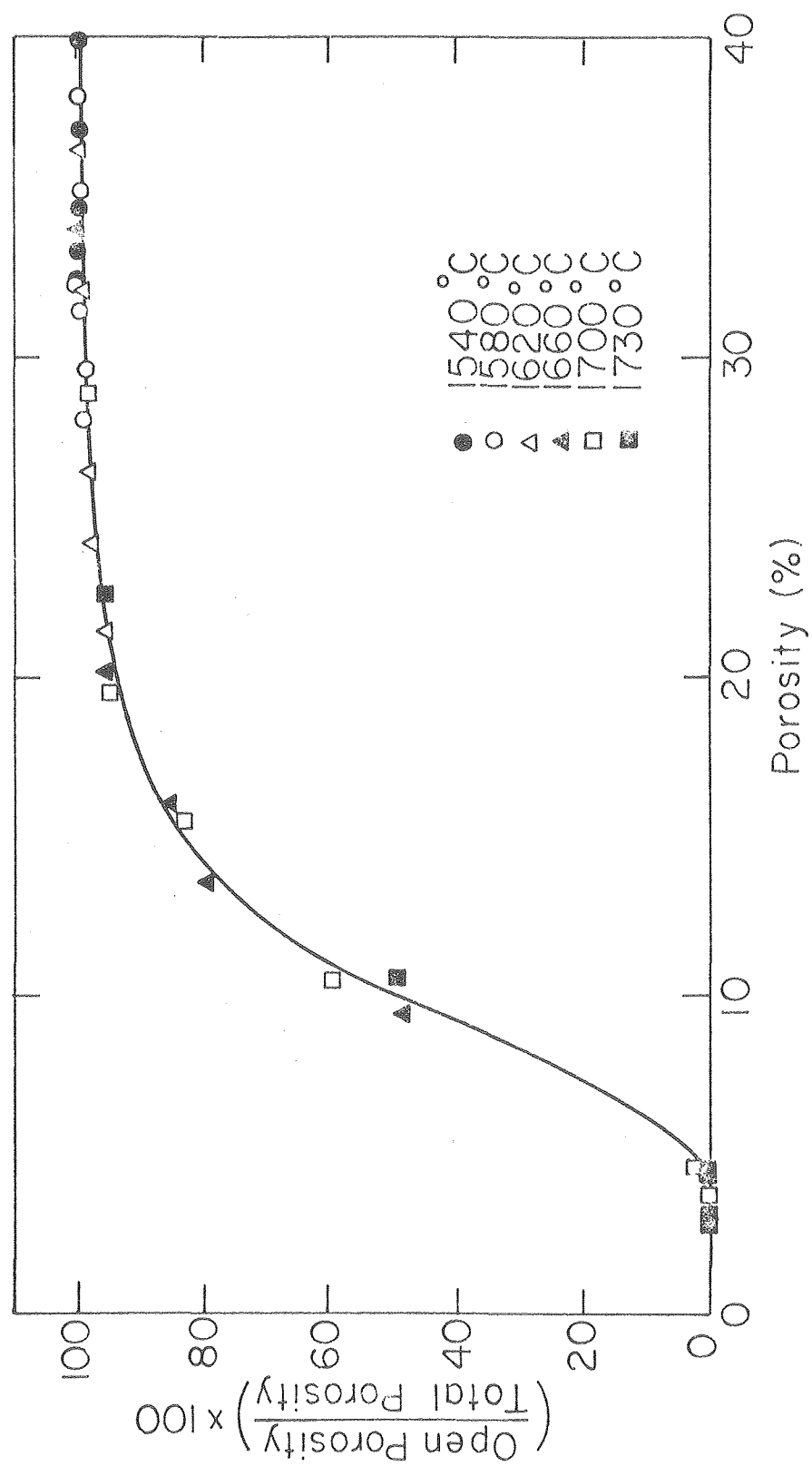
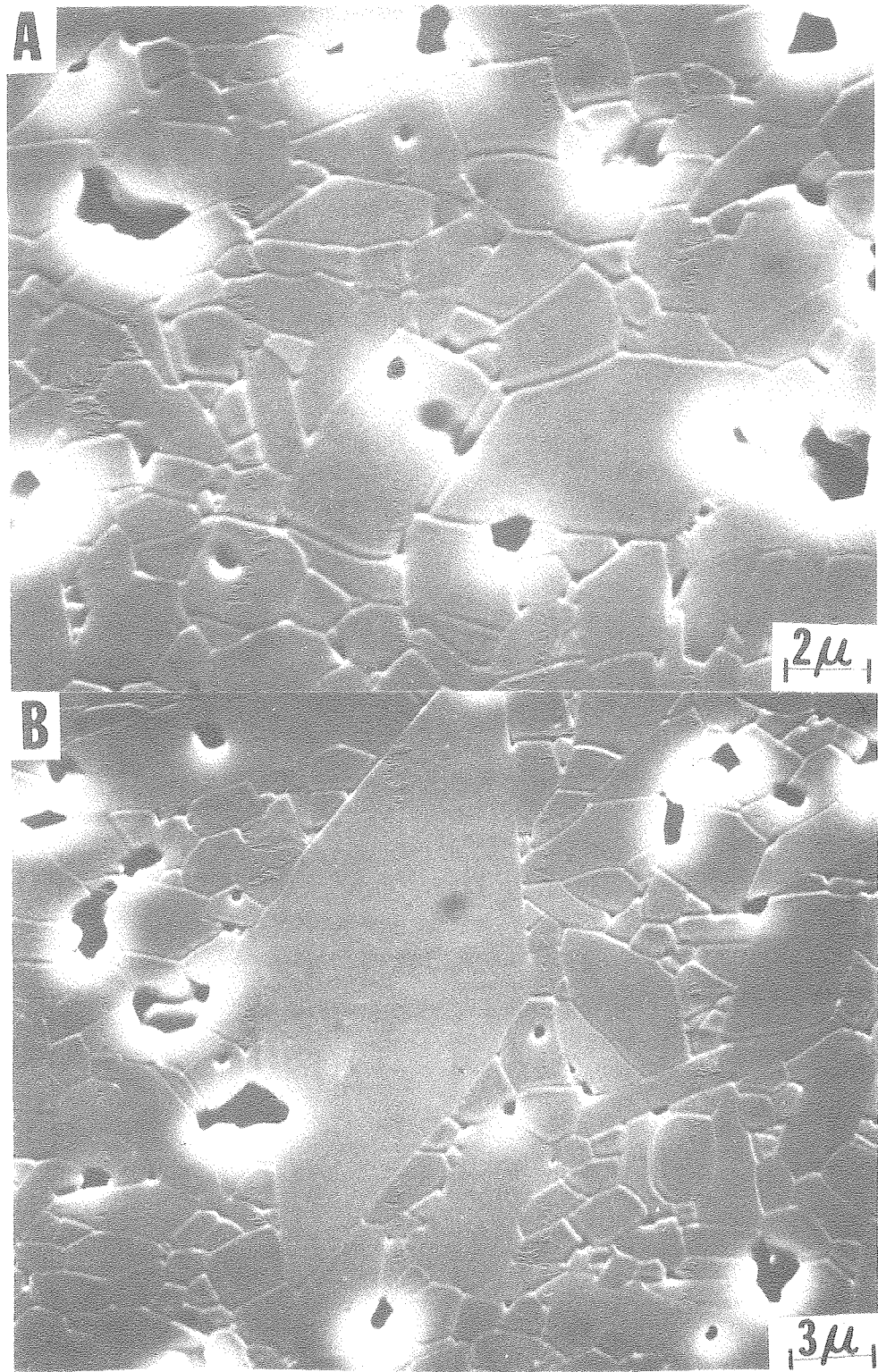


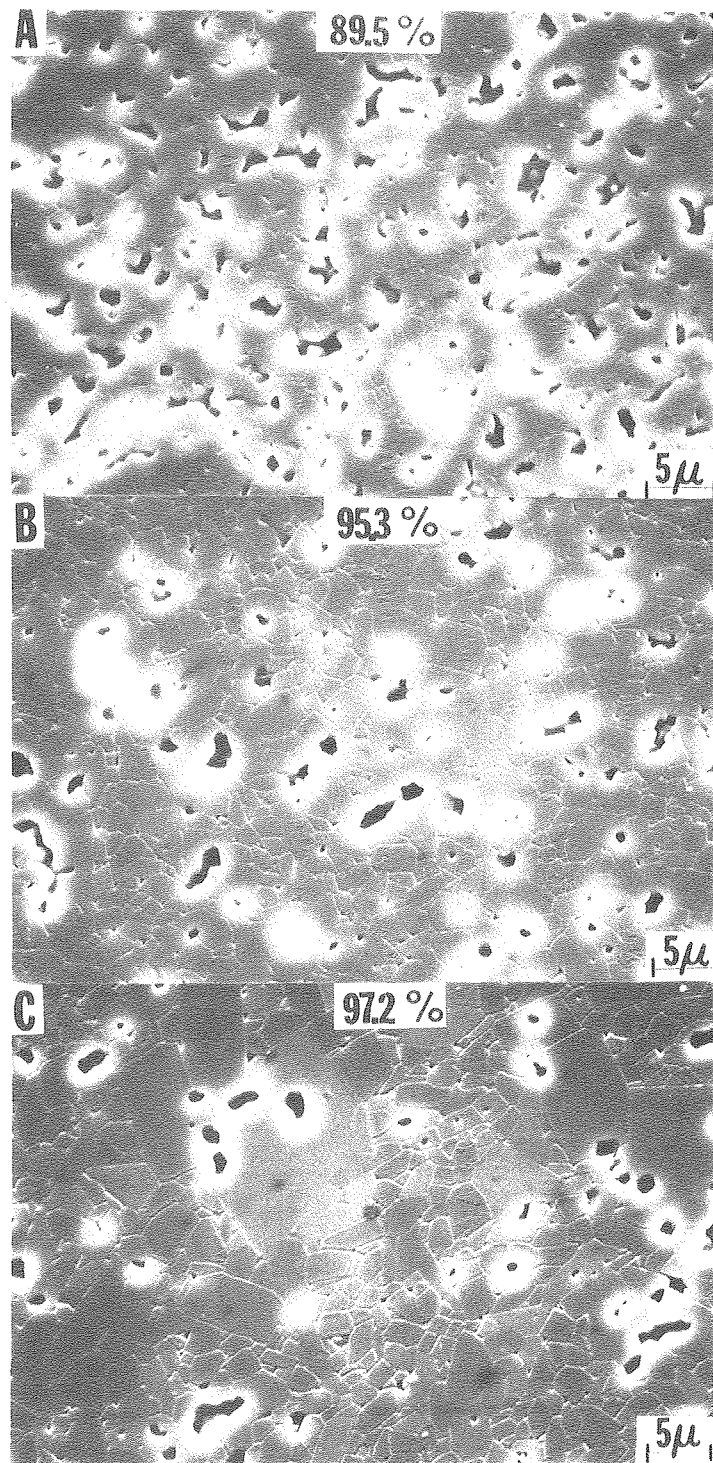
Fig. 44

XBL 7911-14518



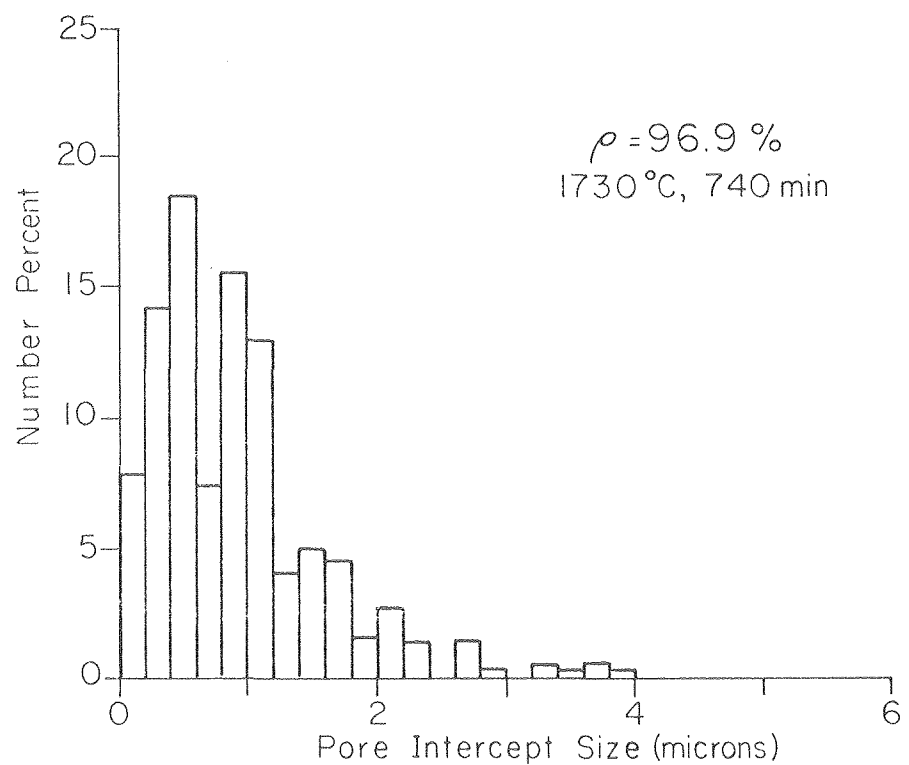
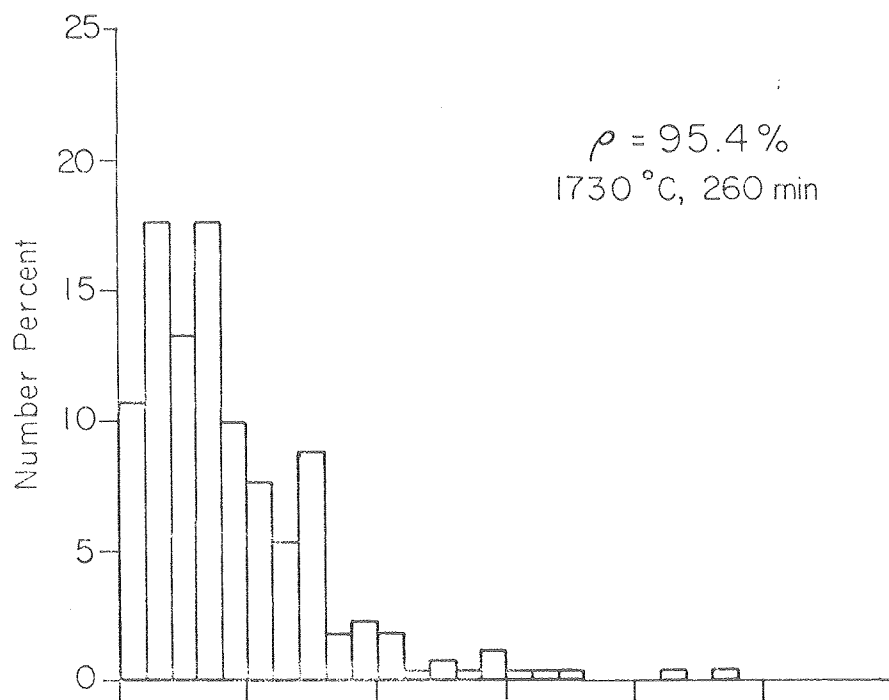
XBB 790-16011

Fig. 45



XBB 790-16013

Fig. 46



XBL7911-14519

Fig. 47

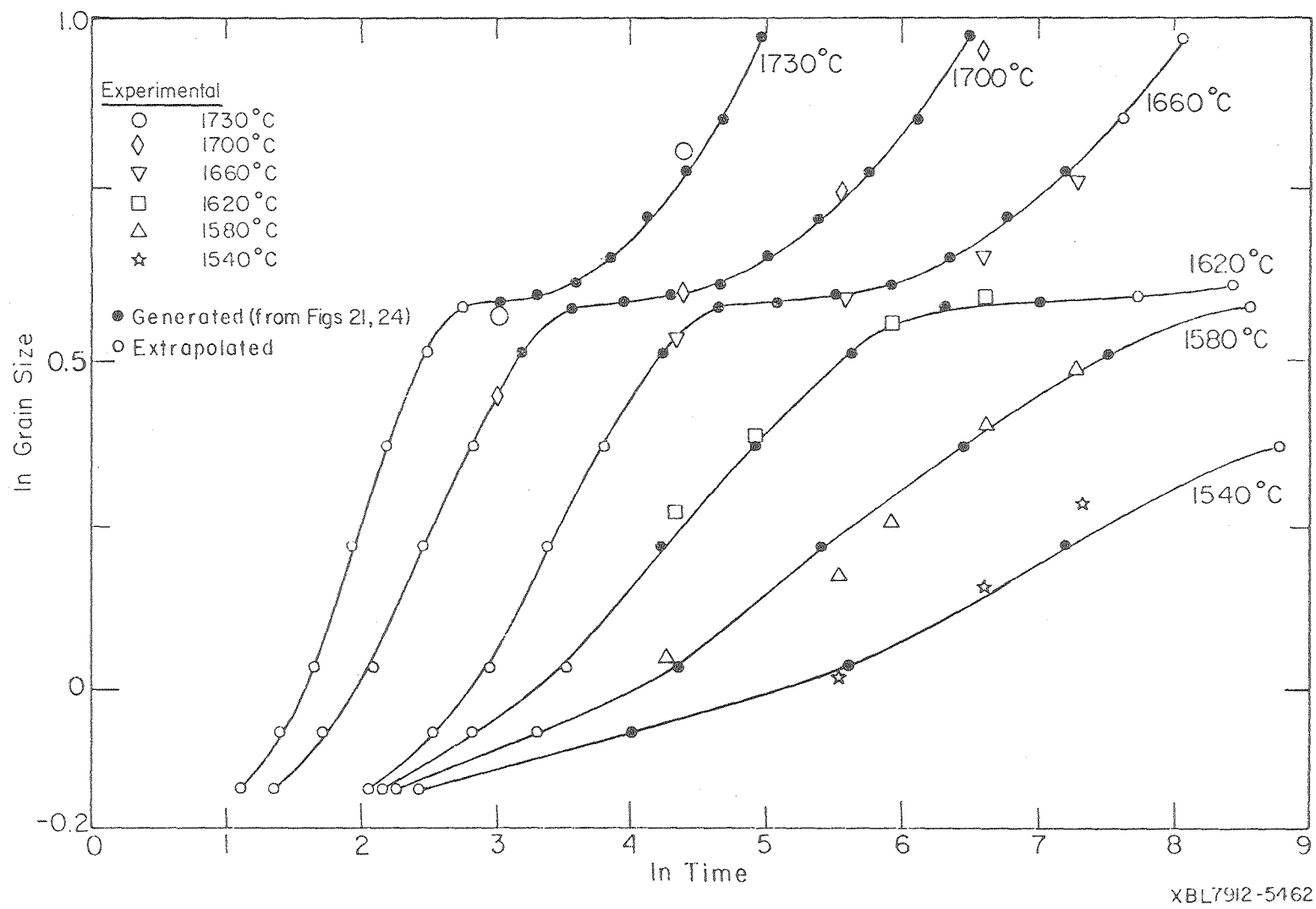


Fig. 48

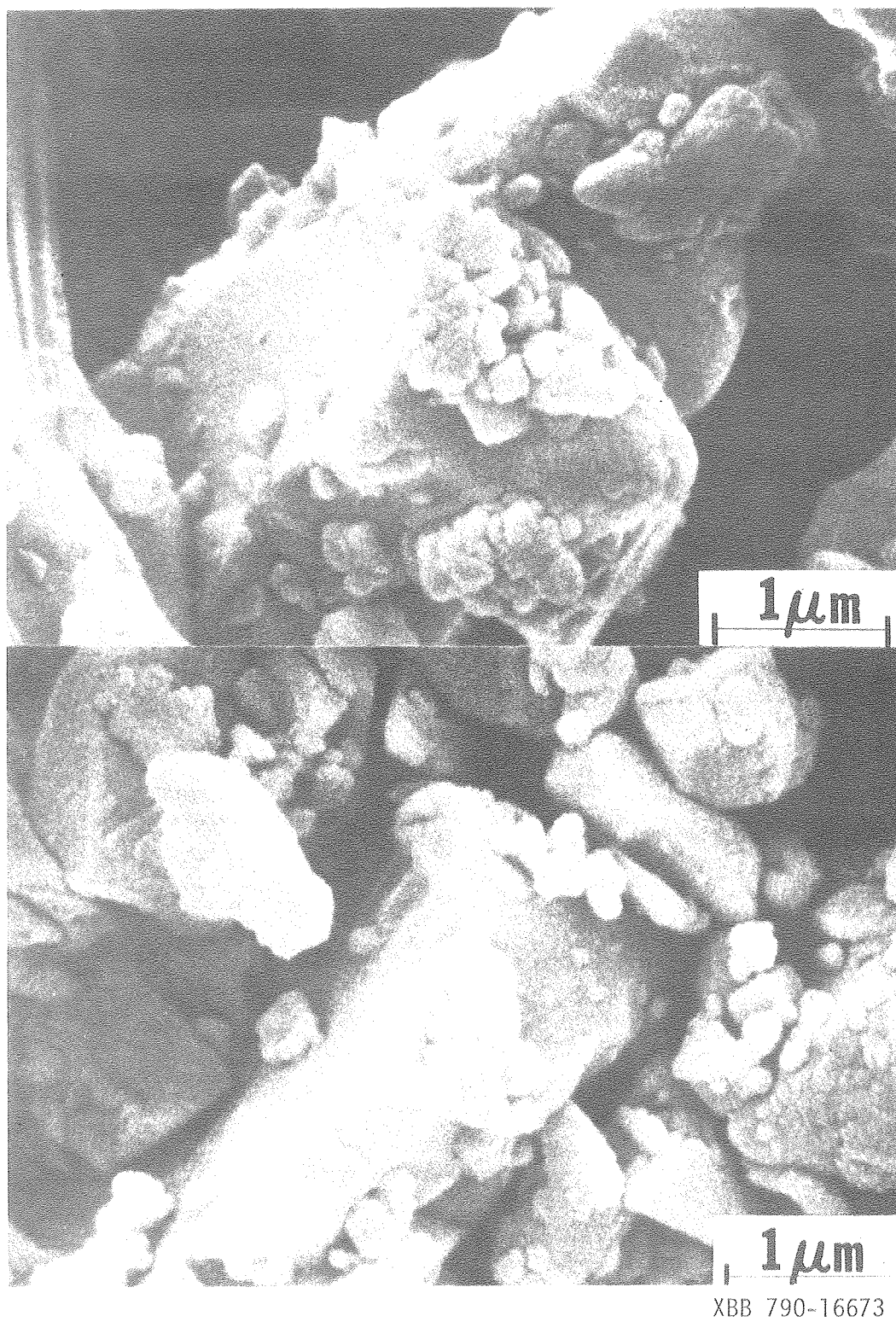


Fig. 49



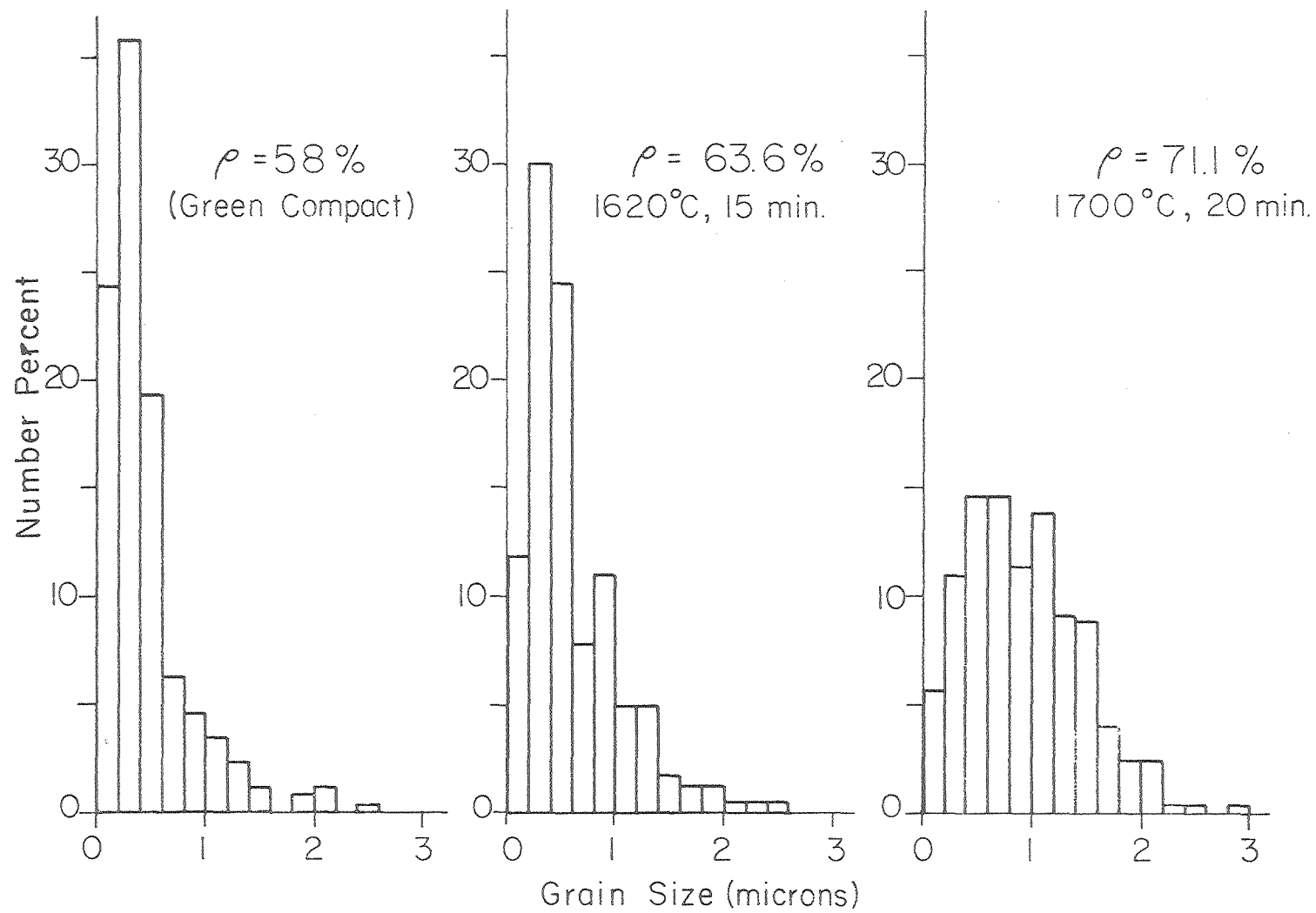
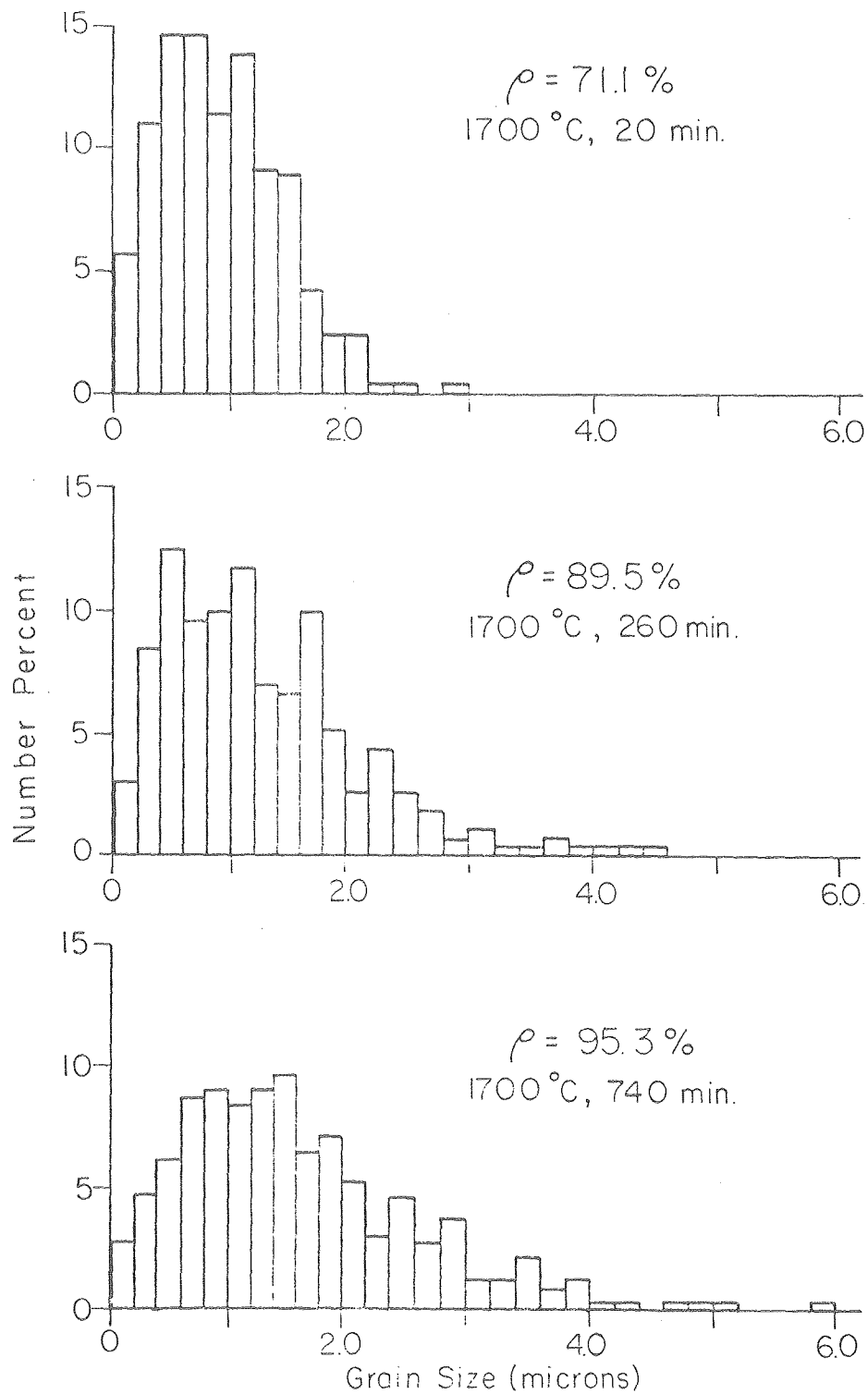


Fig. 50

XBL7912-14593



XBL 7912-14596

Fig. 51

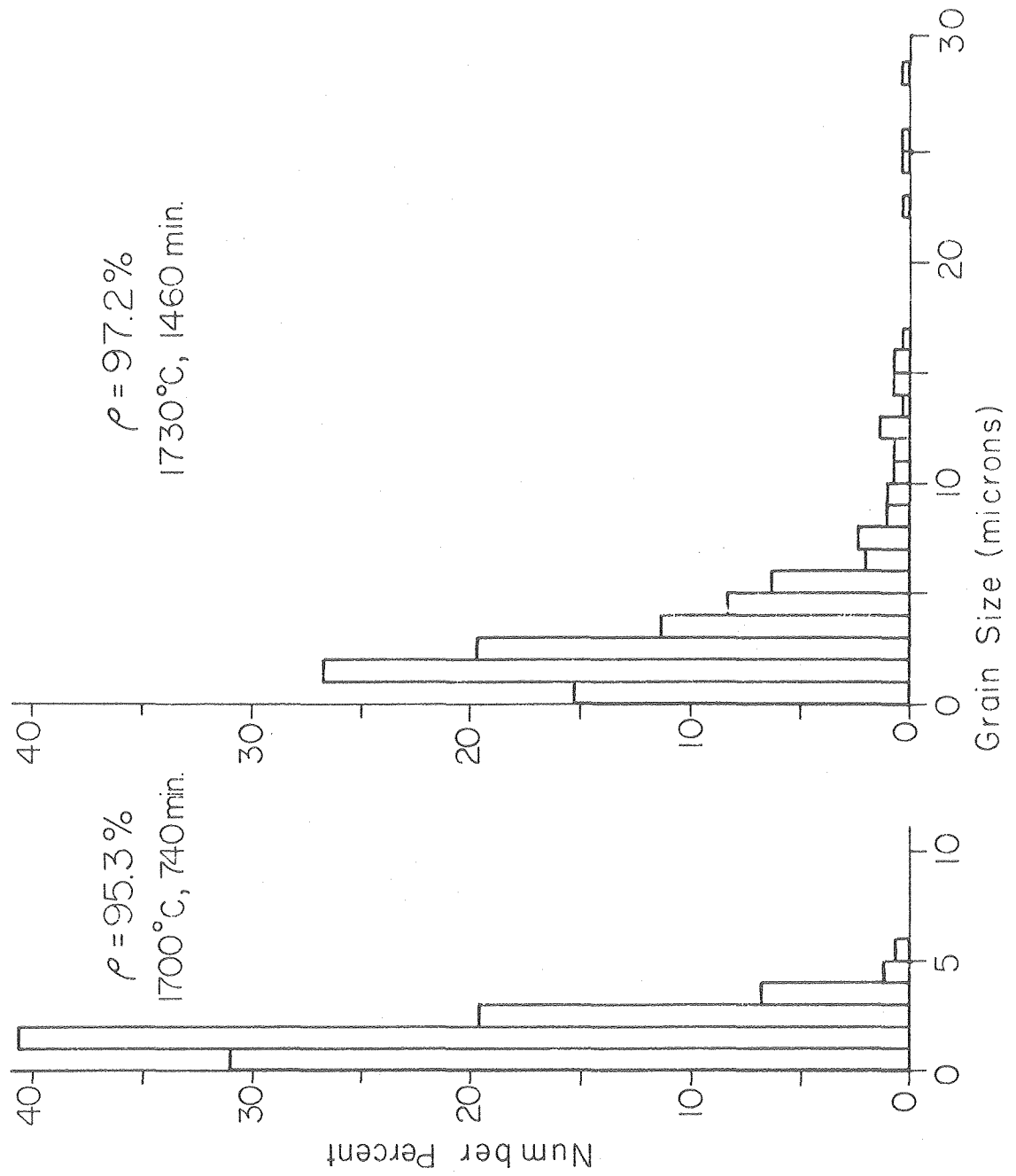
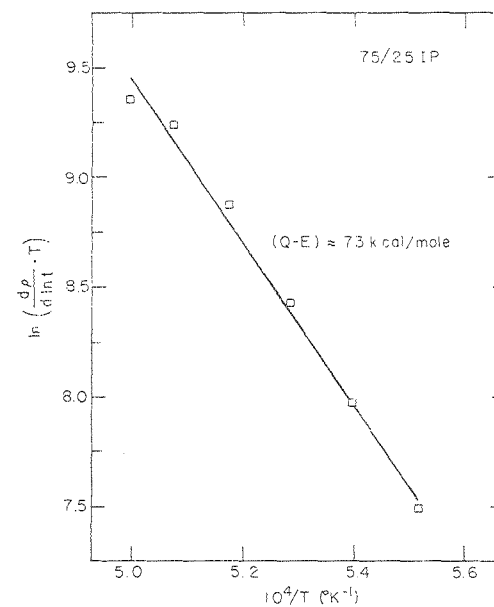
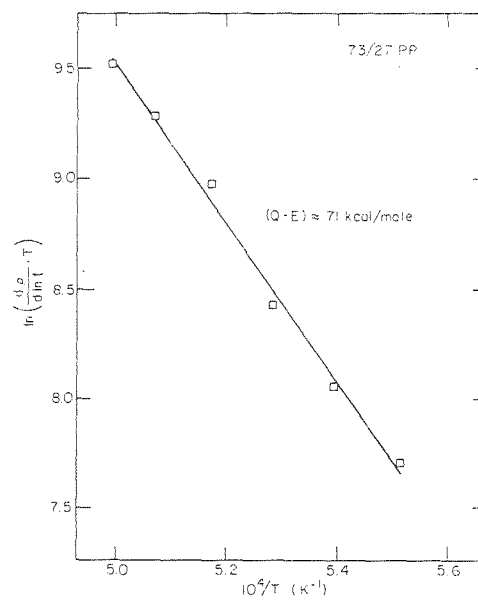
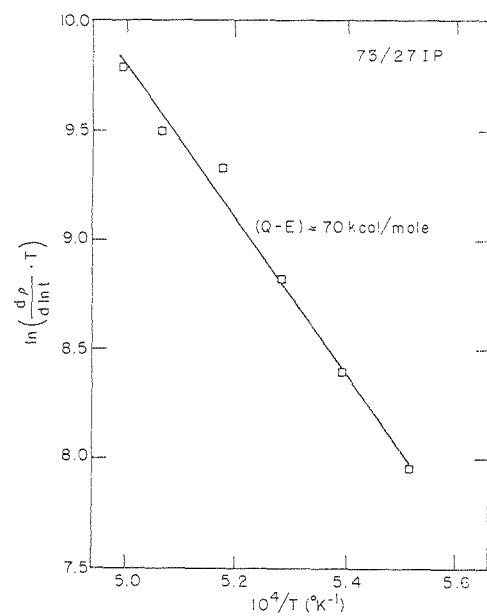


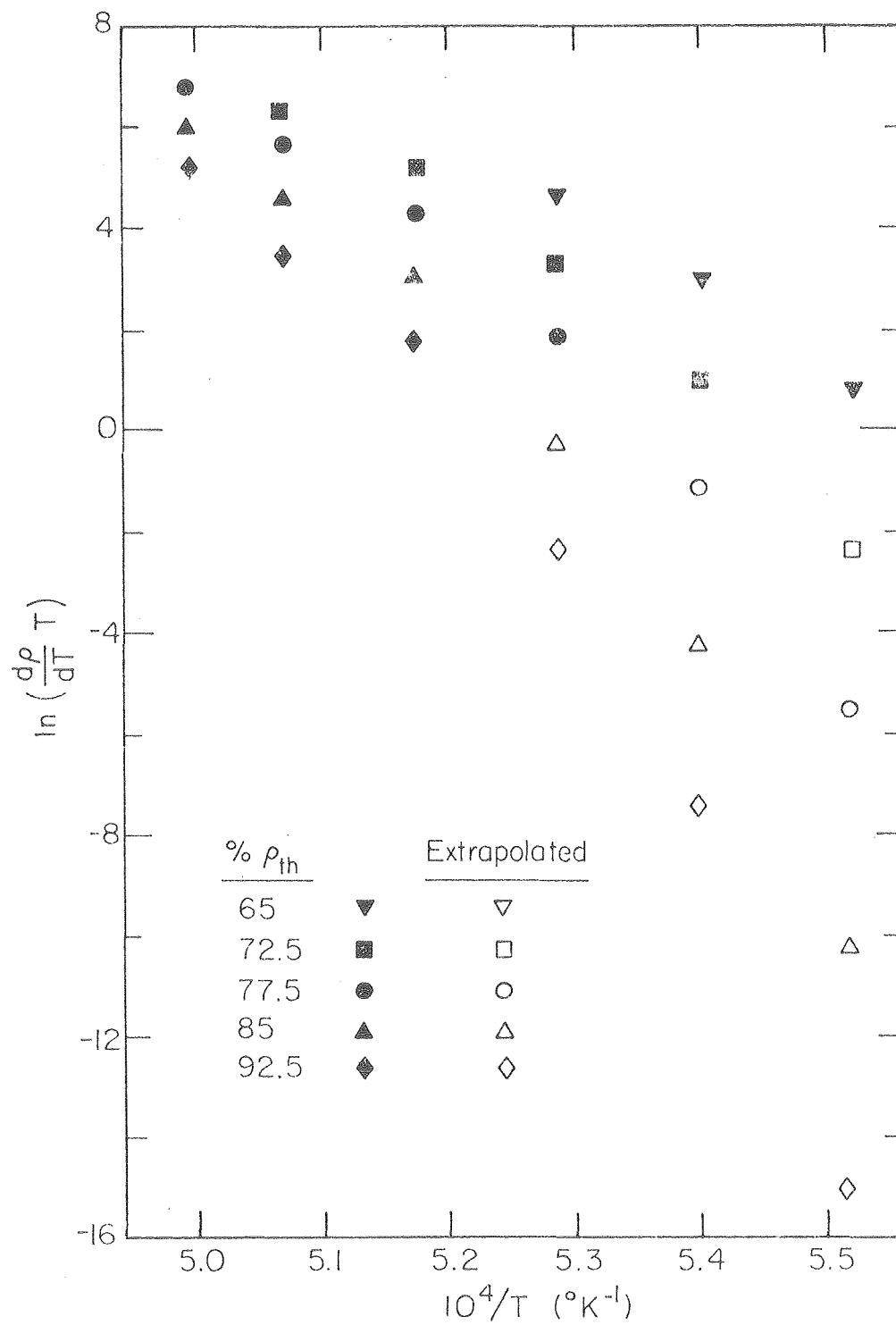
Fig. 52

XBL7912-14599



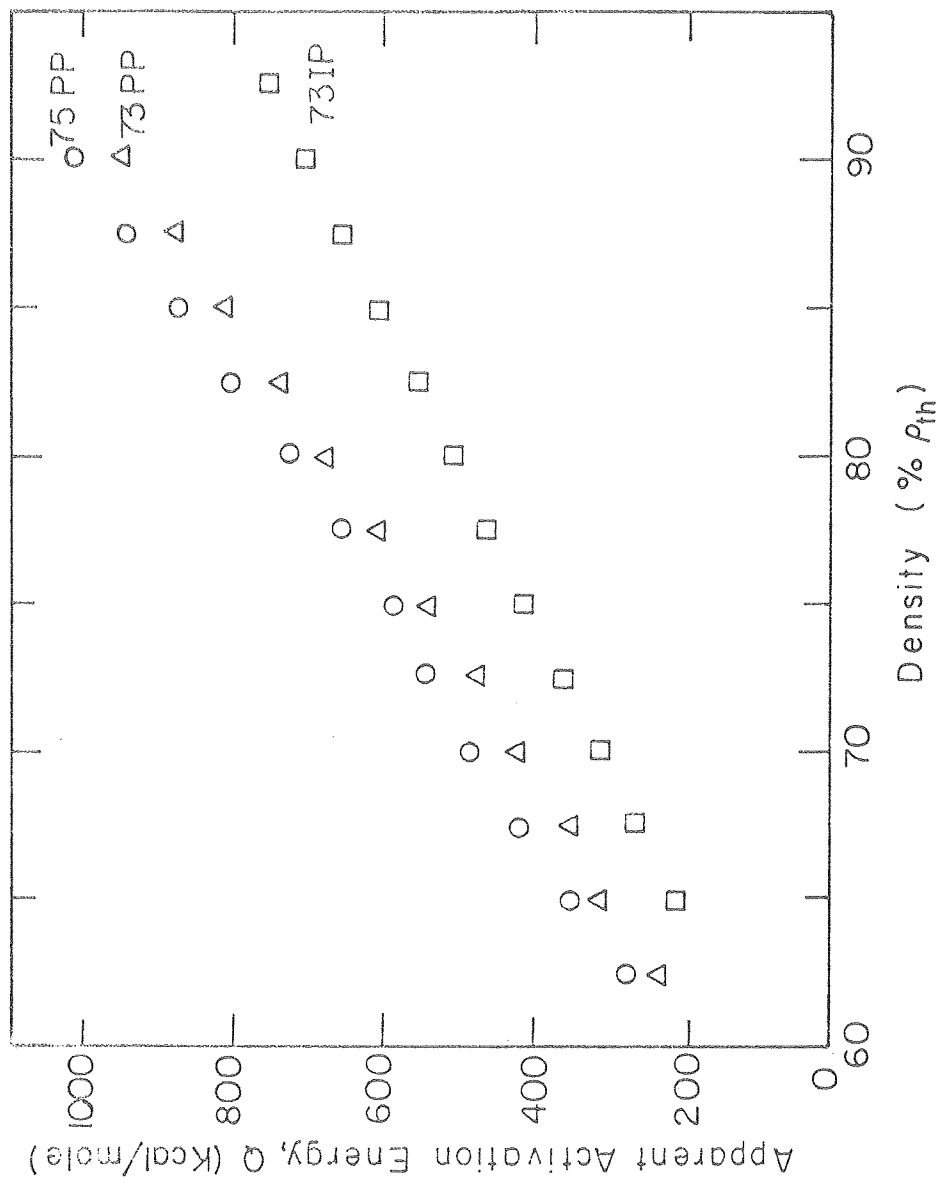
XBL 7911-14513A

Fig. 53



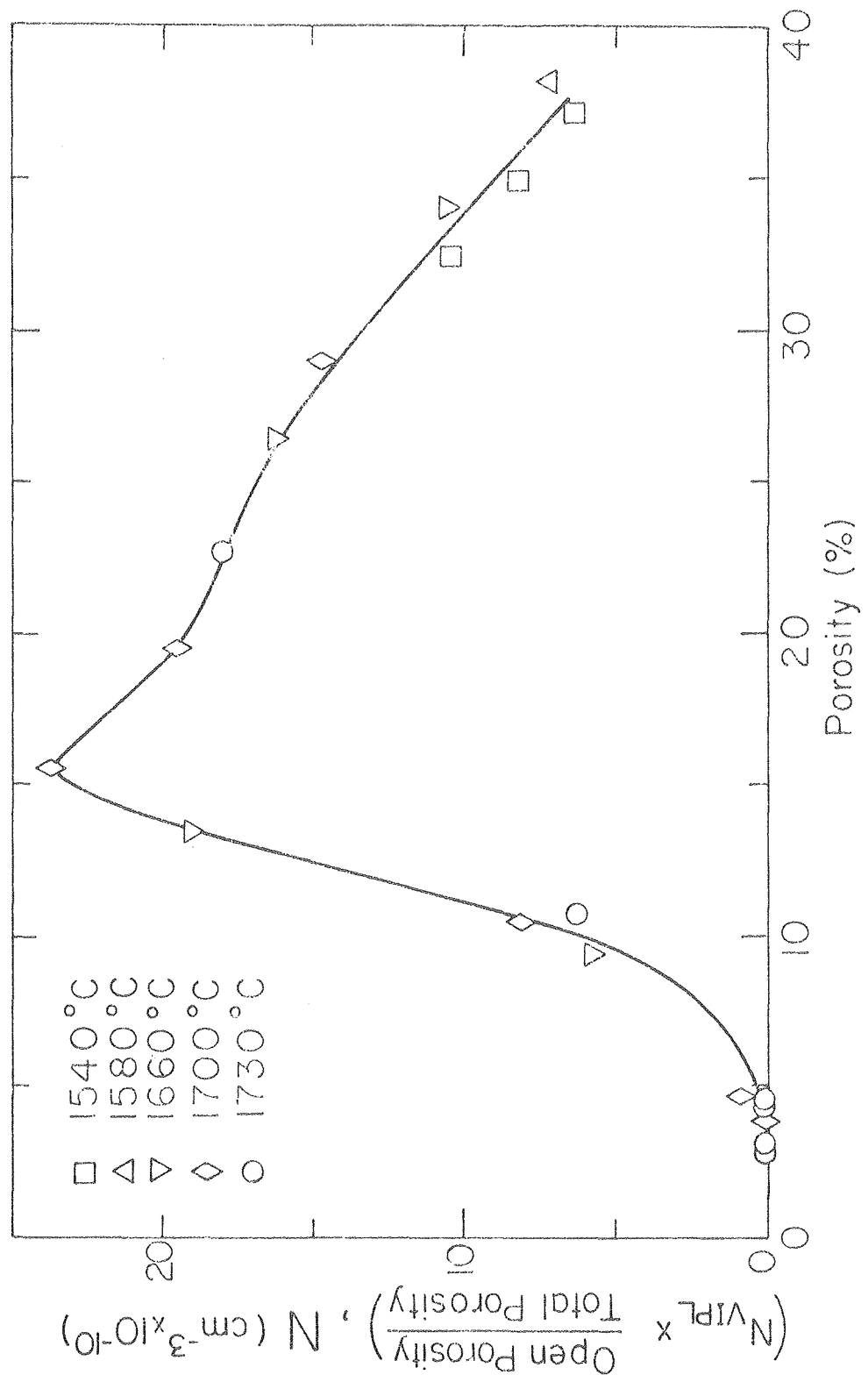
XBL 7912-14597

Fig. 54



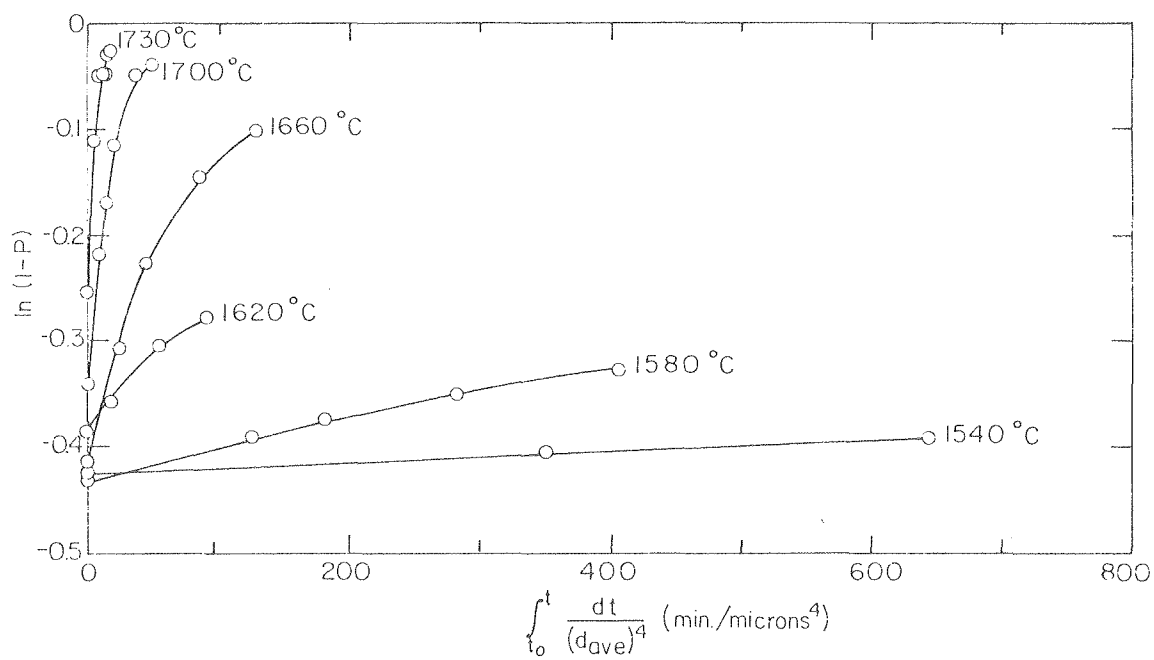
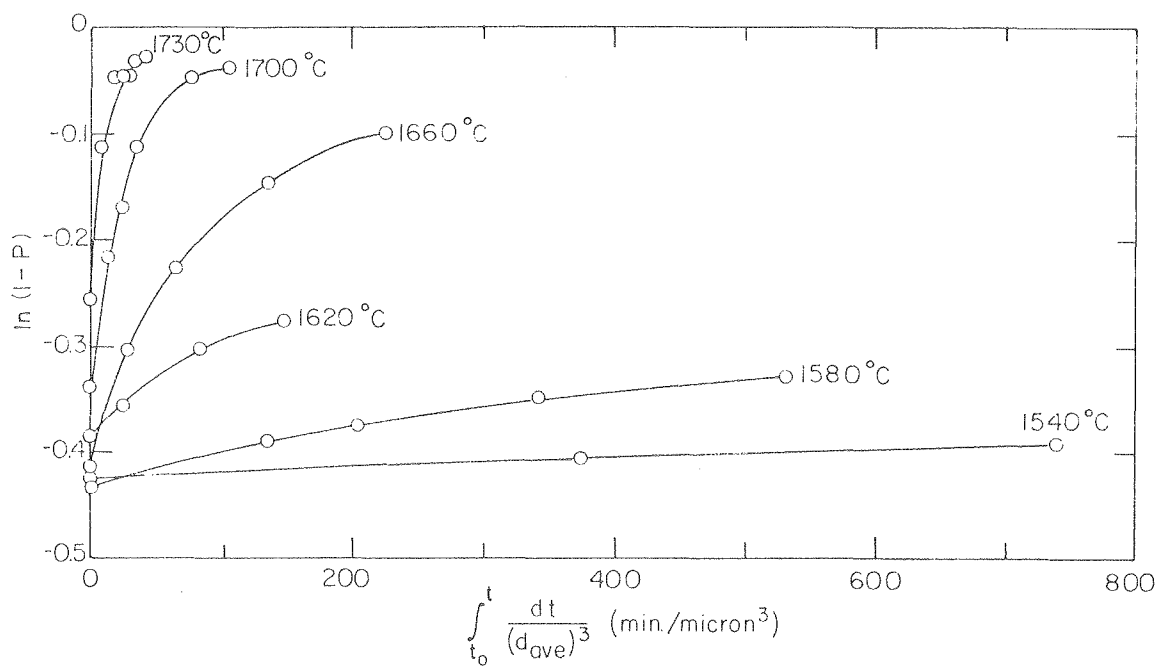
XBL 7912-5461

Fig. 55



XBL 7912-5460

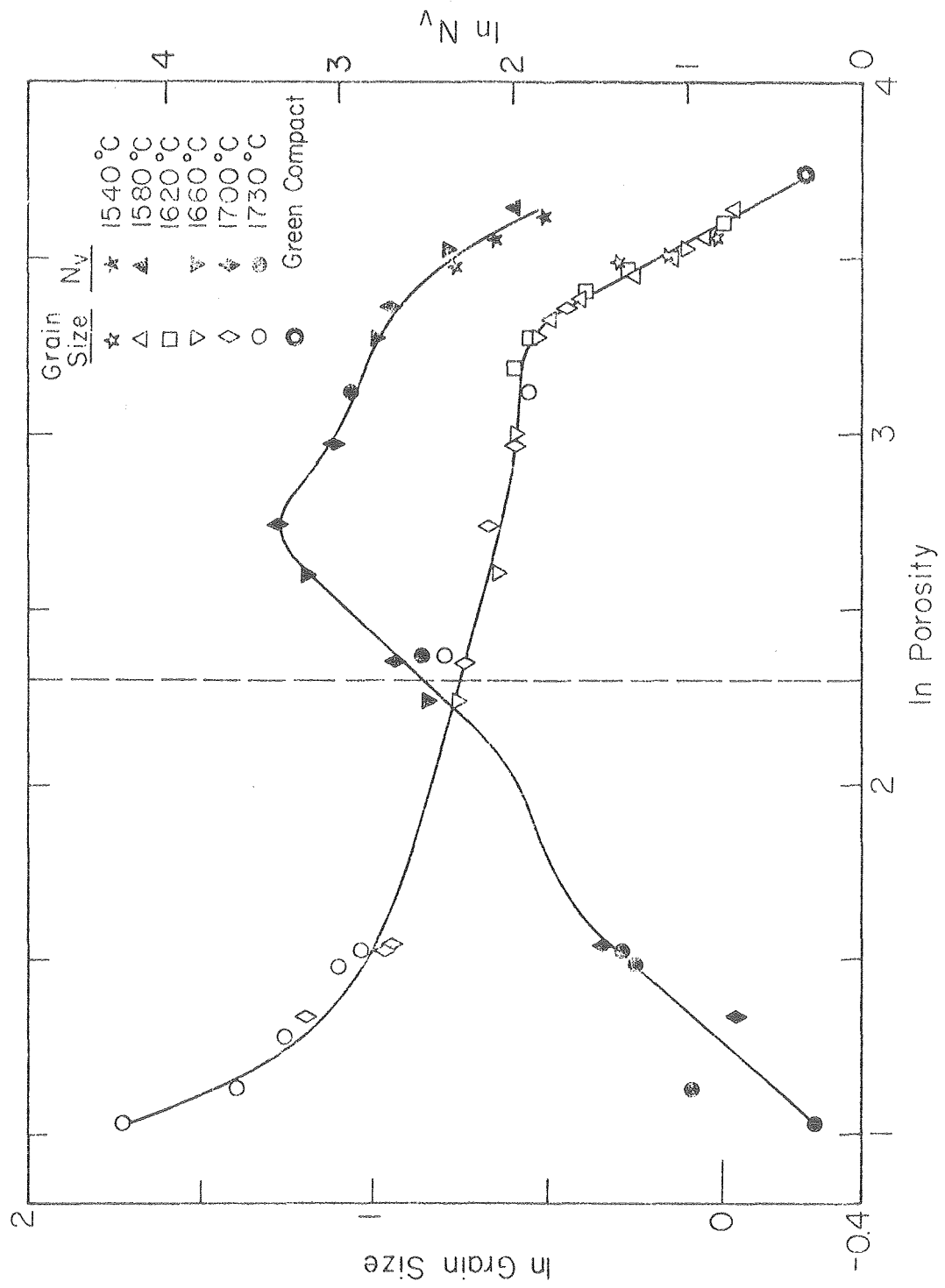
Fig. 56



XBL79i2-14595

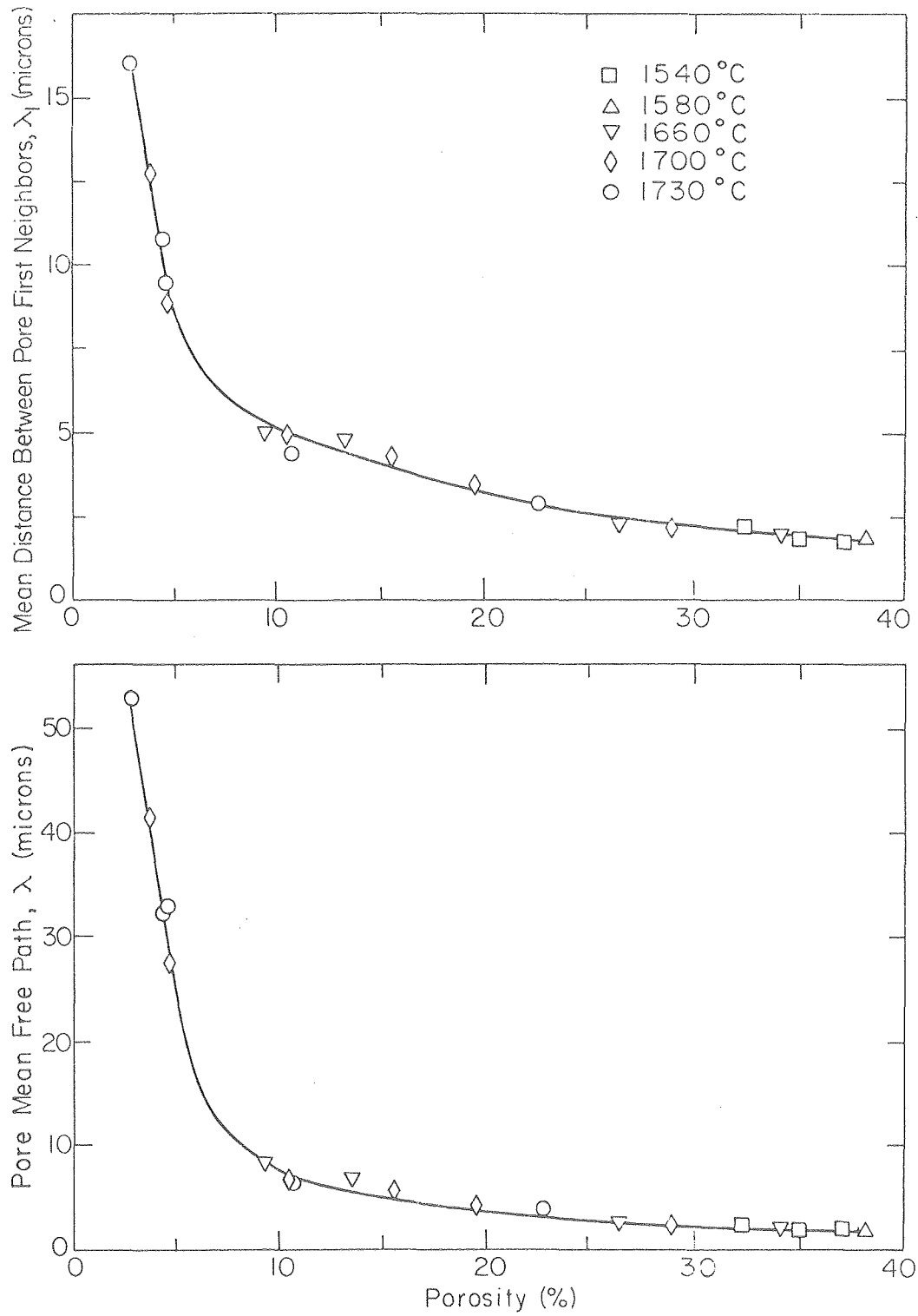
Fig. 57





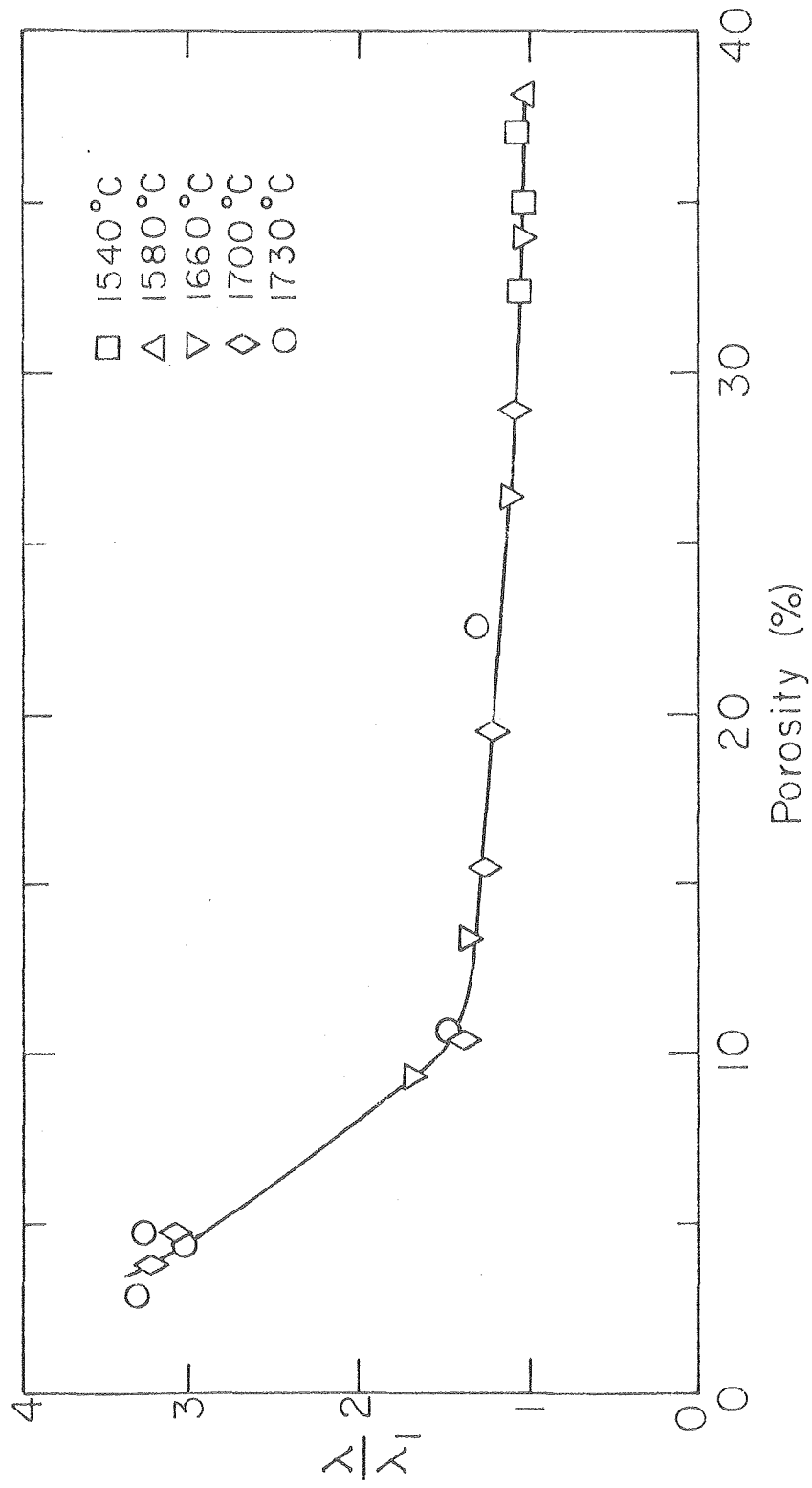
XBL 7912-5404

Fig. 58



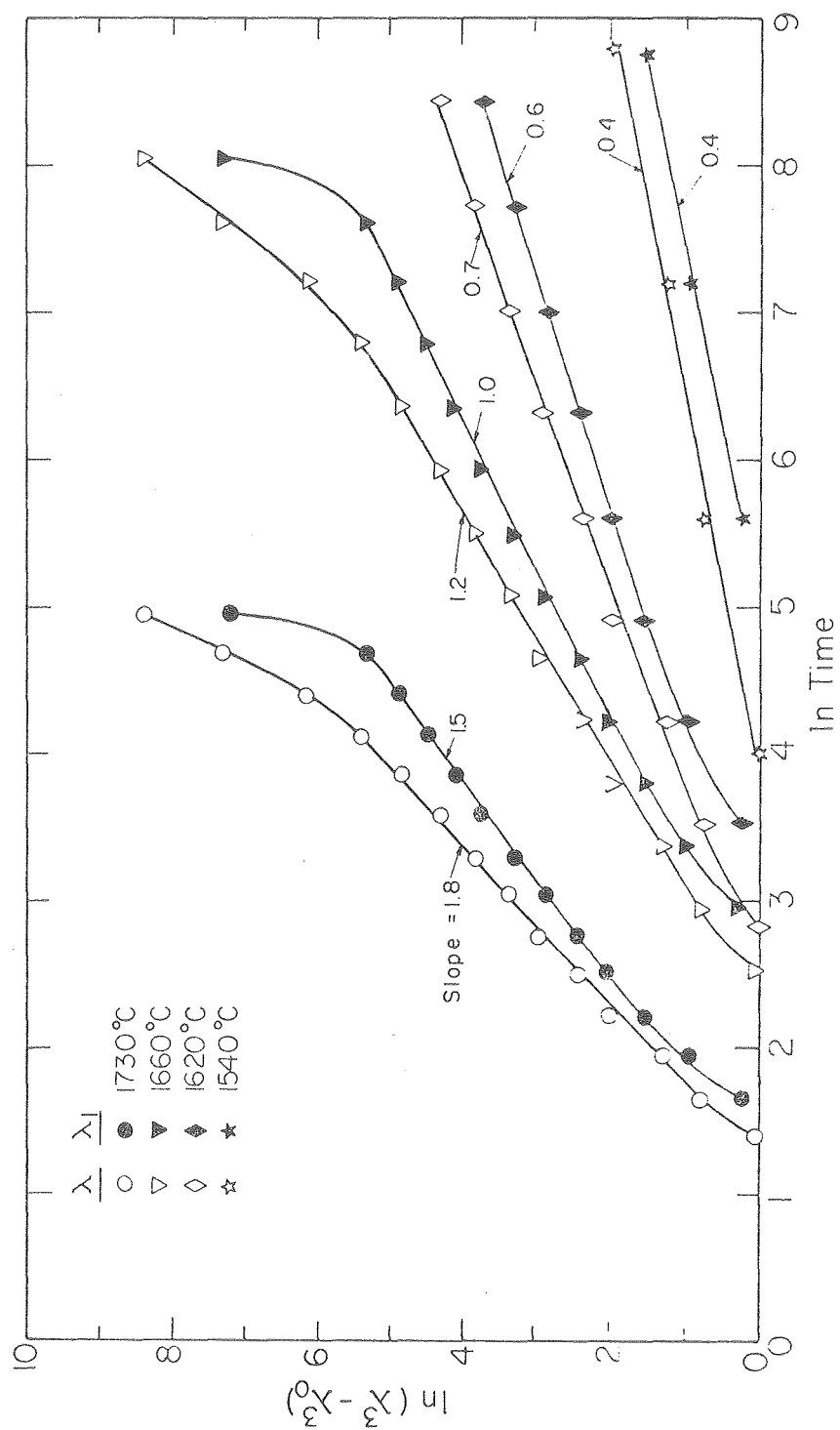
XBL7912-5407

Fig. 59



XBL 7912-5459

Fig. 60



XBL 7912-5463

Fig. 61

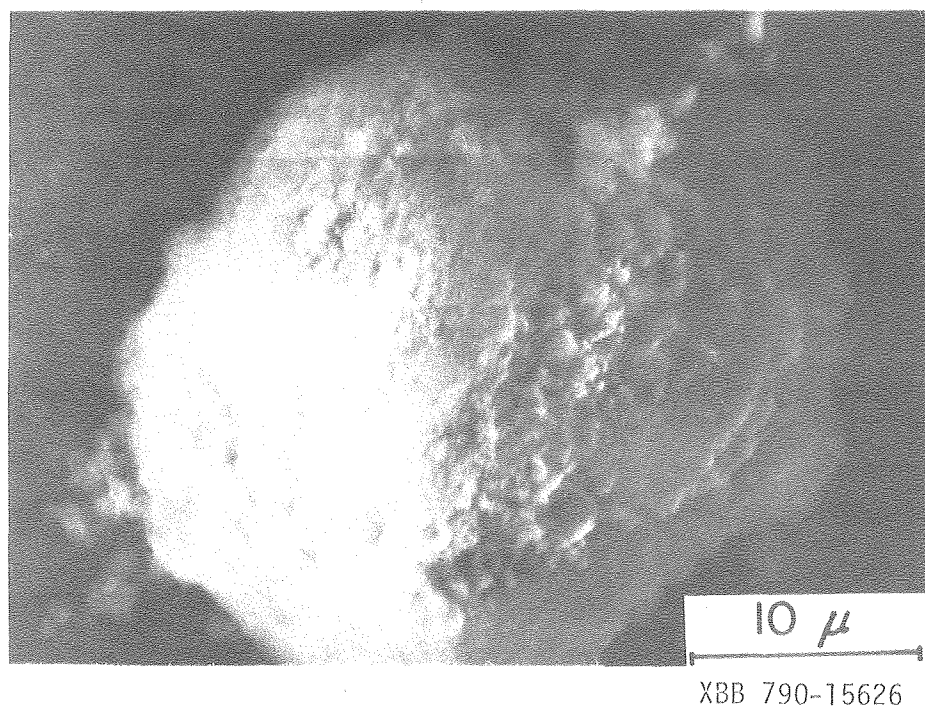
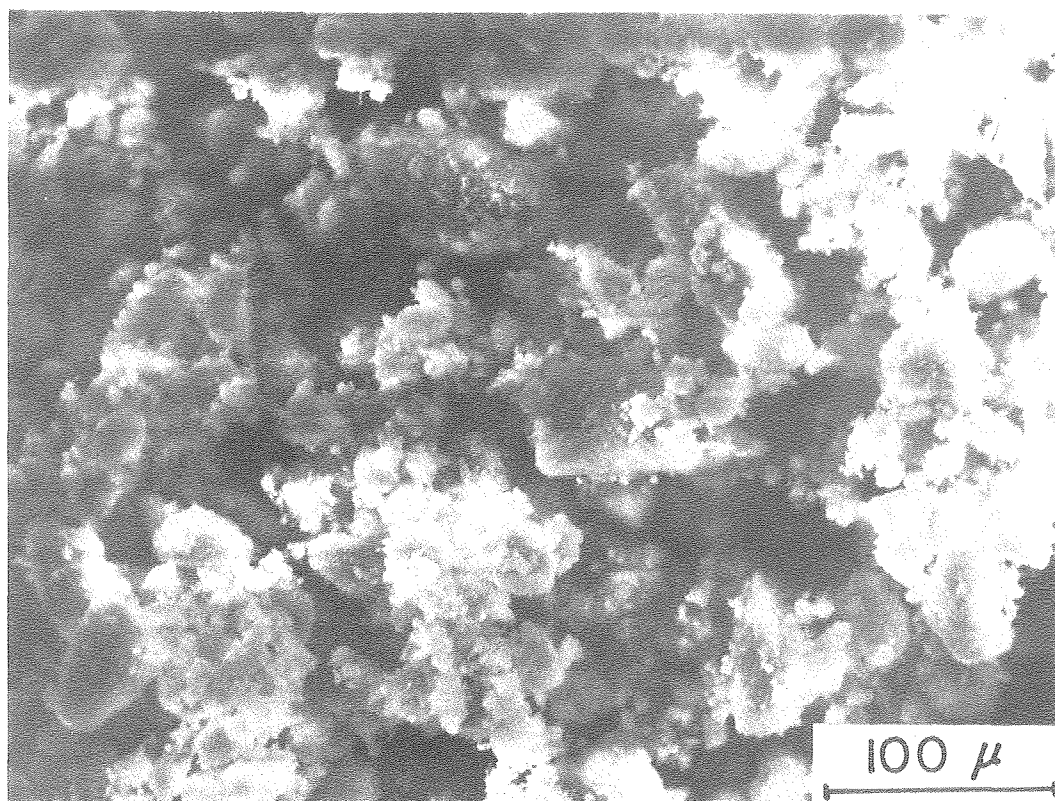


Fig. 62

73/27 "GEL": GREEN STATE

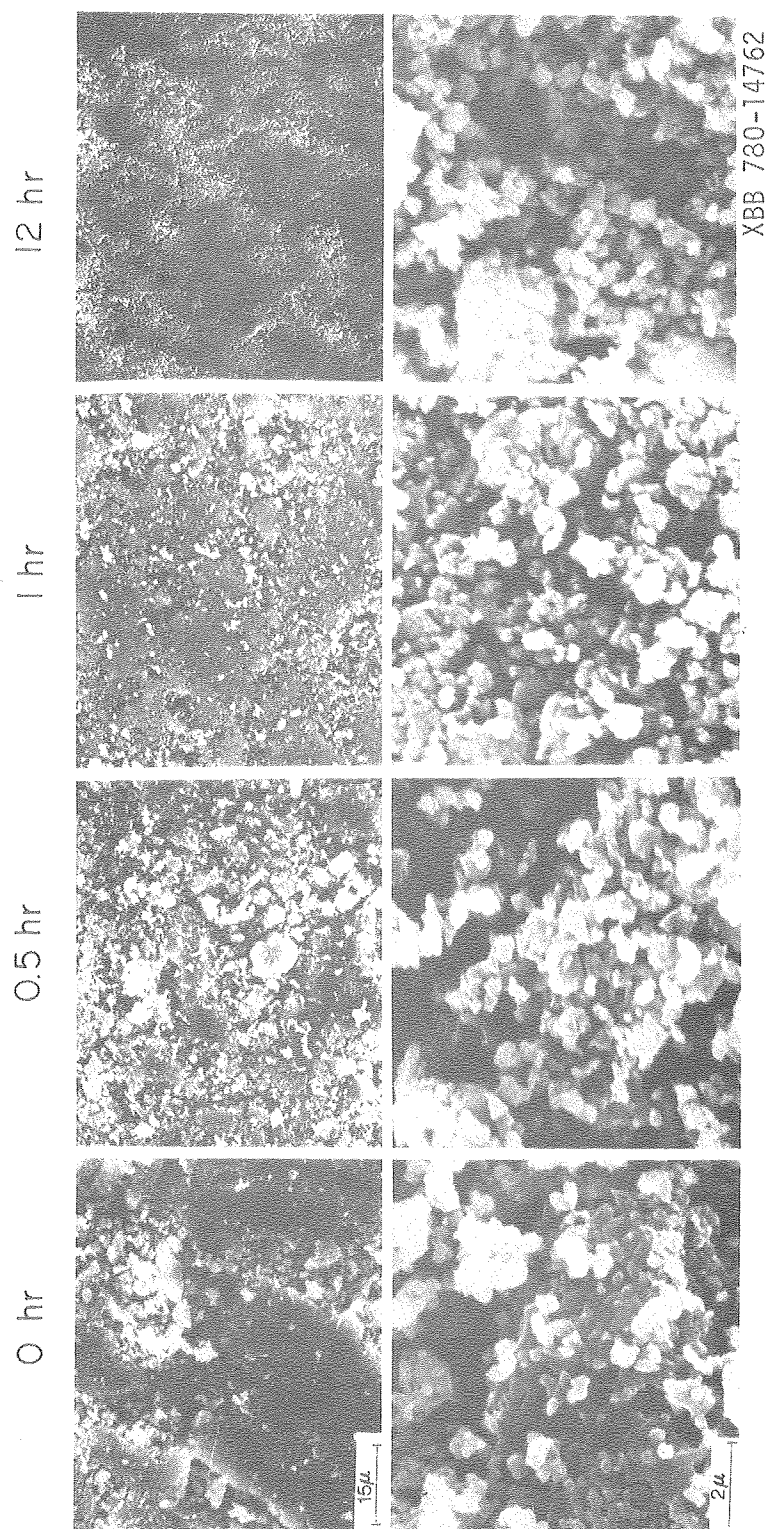
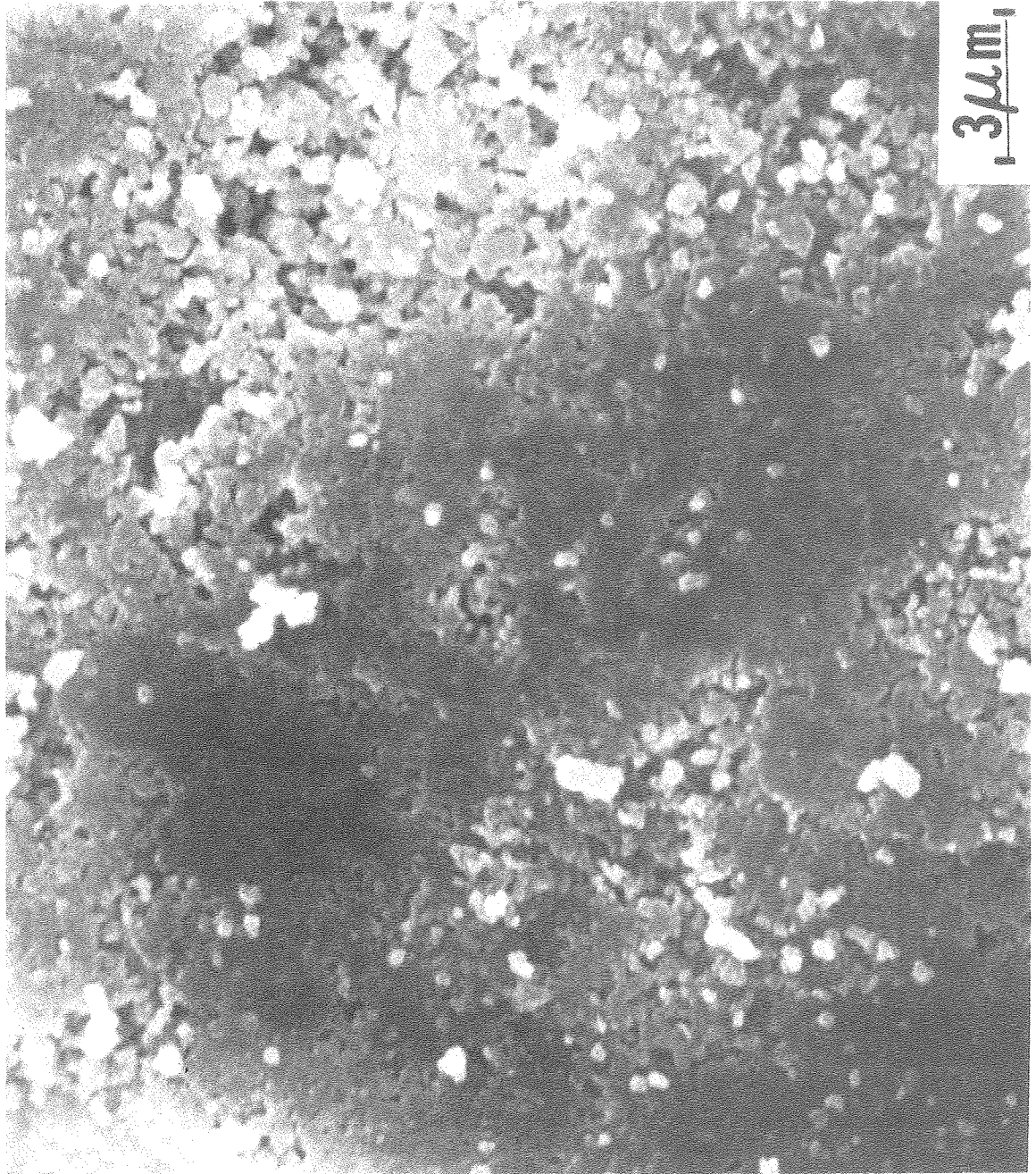
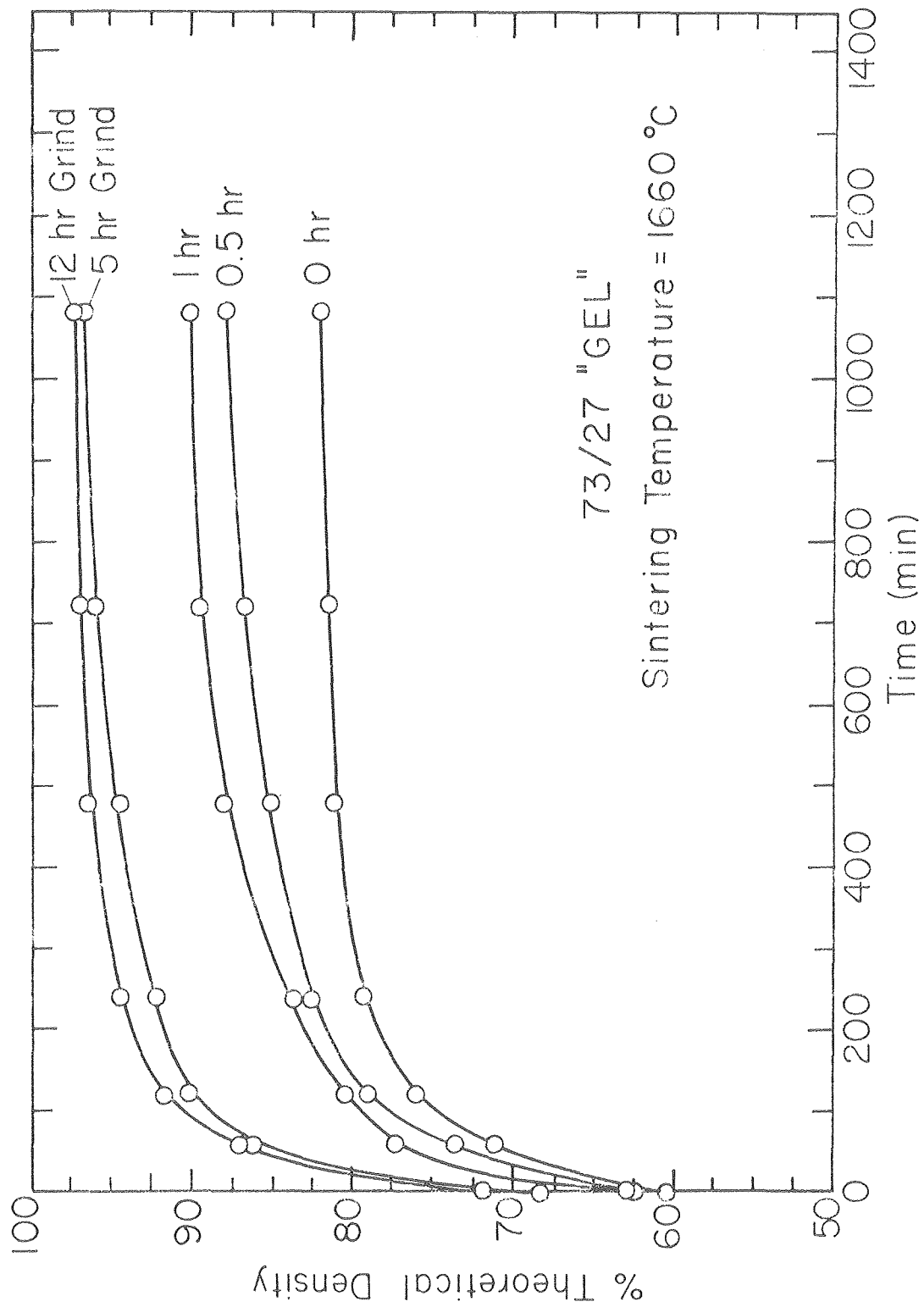


Fig. 63



XBB 790-15978

Fig. 64



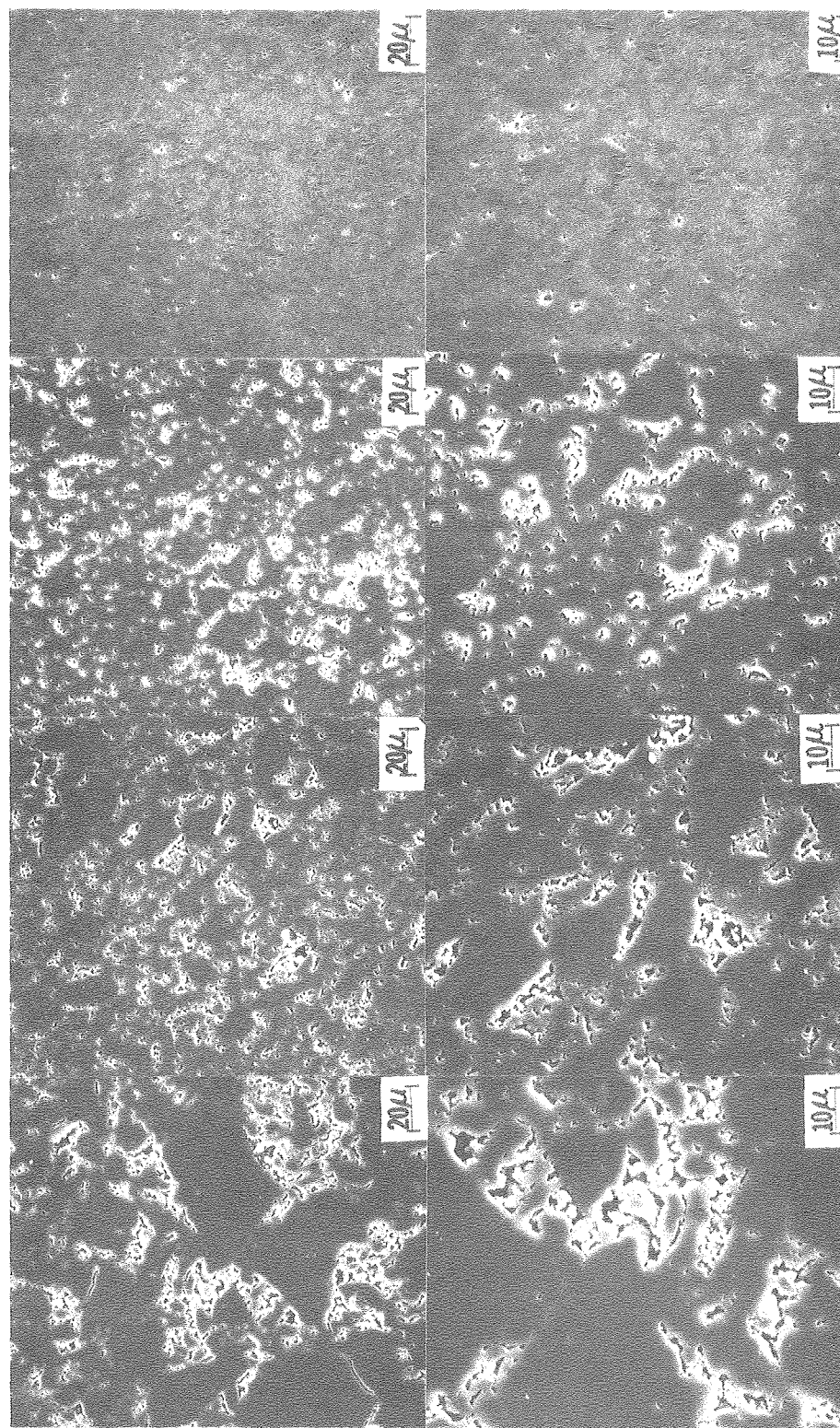
XBL 7912-5401

Fig. 65



73/27 "GEL": 1660 °C for 18 hr

0 hr      0.5 hr      1 hr      12 hr



XBB 785-5269A

Fig. 66

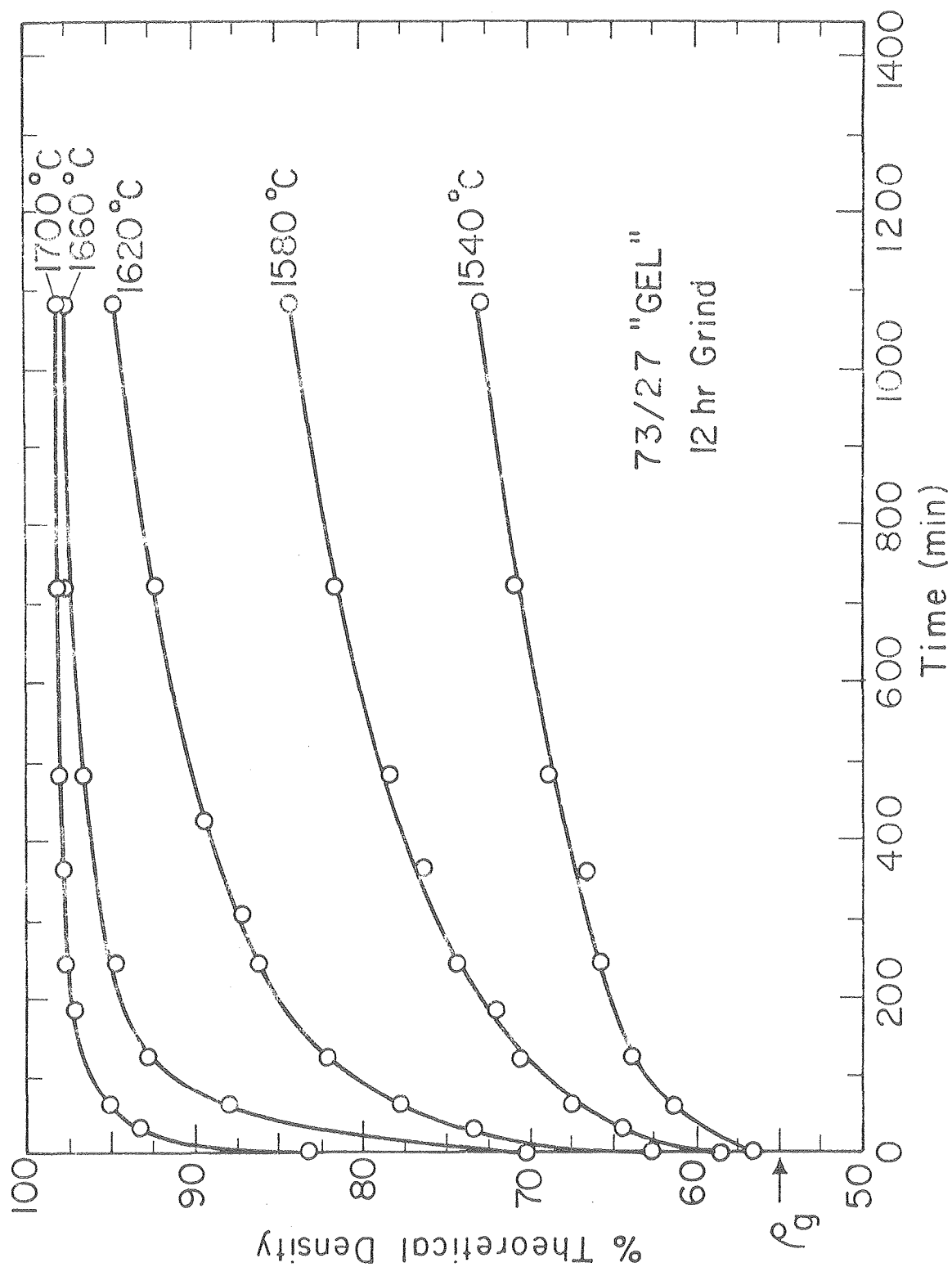
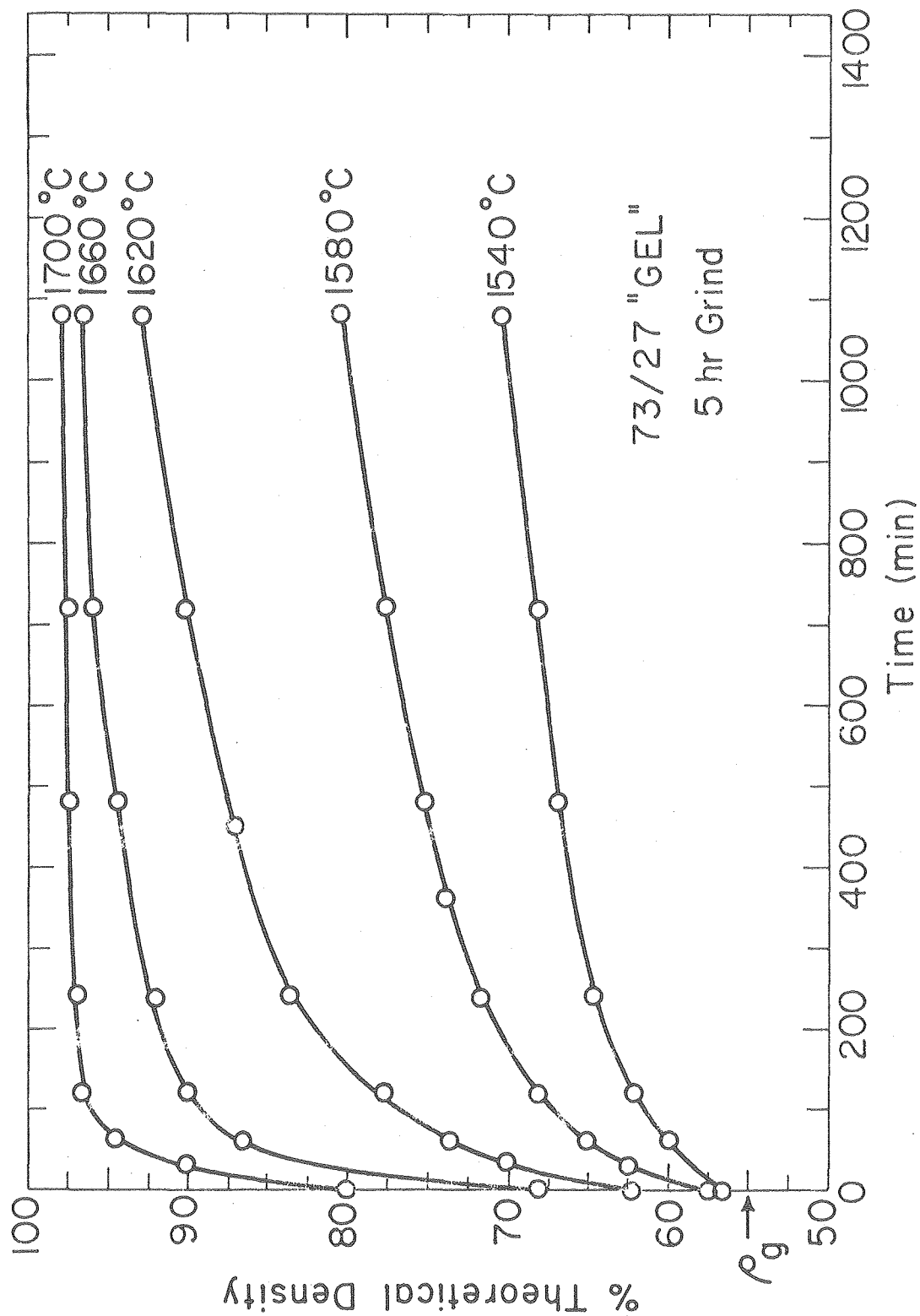
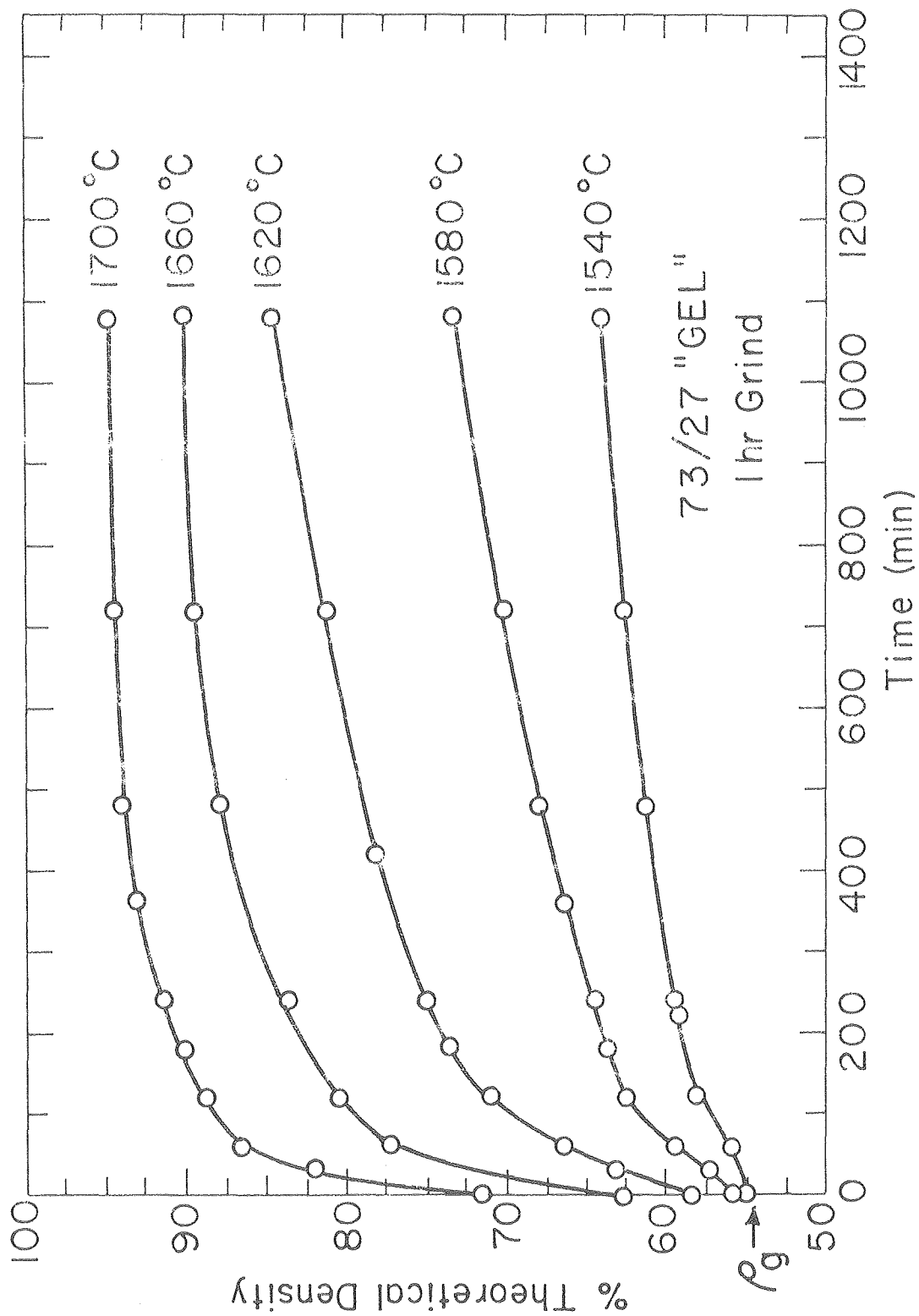


Fig. 67 XBL 785-4927A



XBL 7911-13523

Fig. 68



XBL 7912-13524

Fig. 69

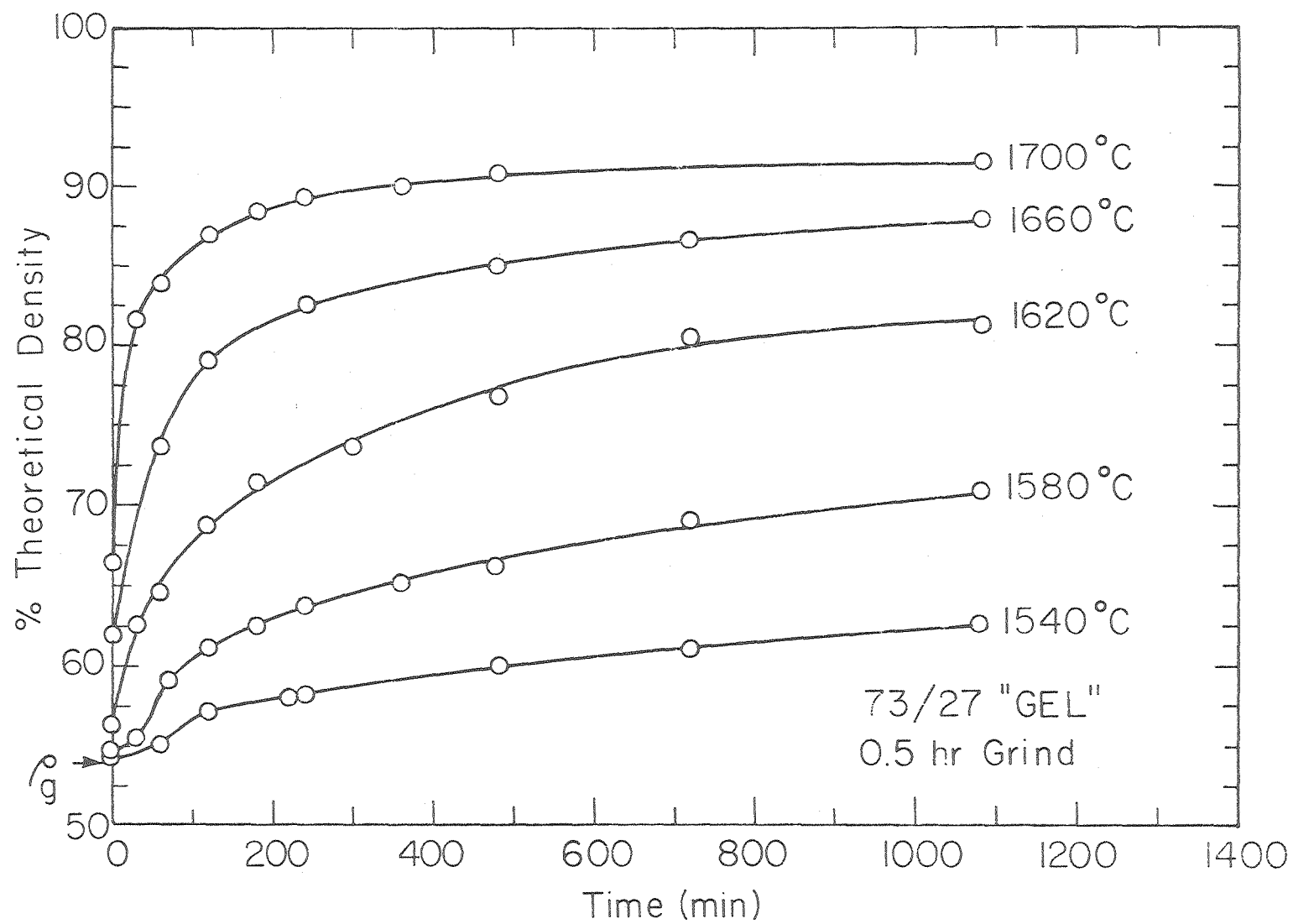
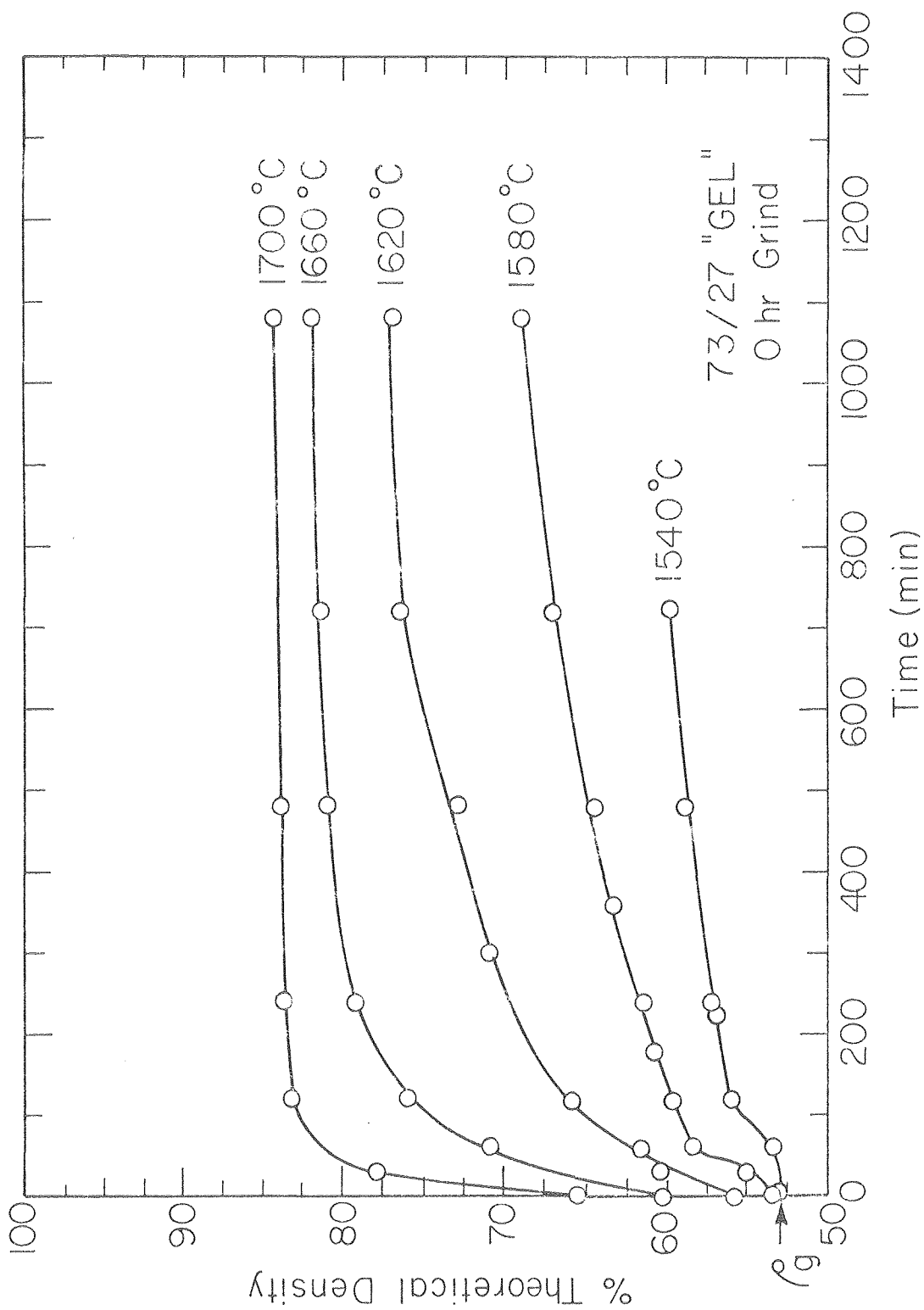


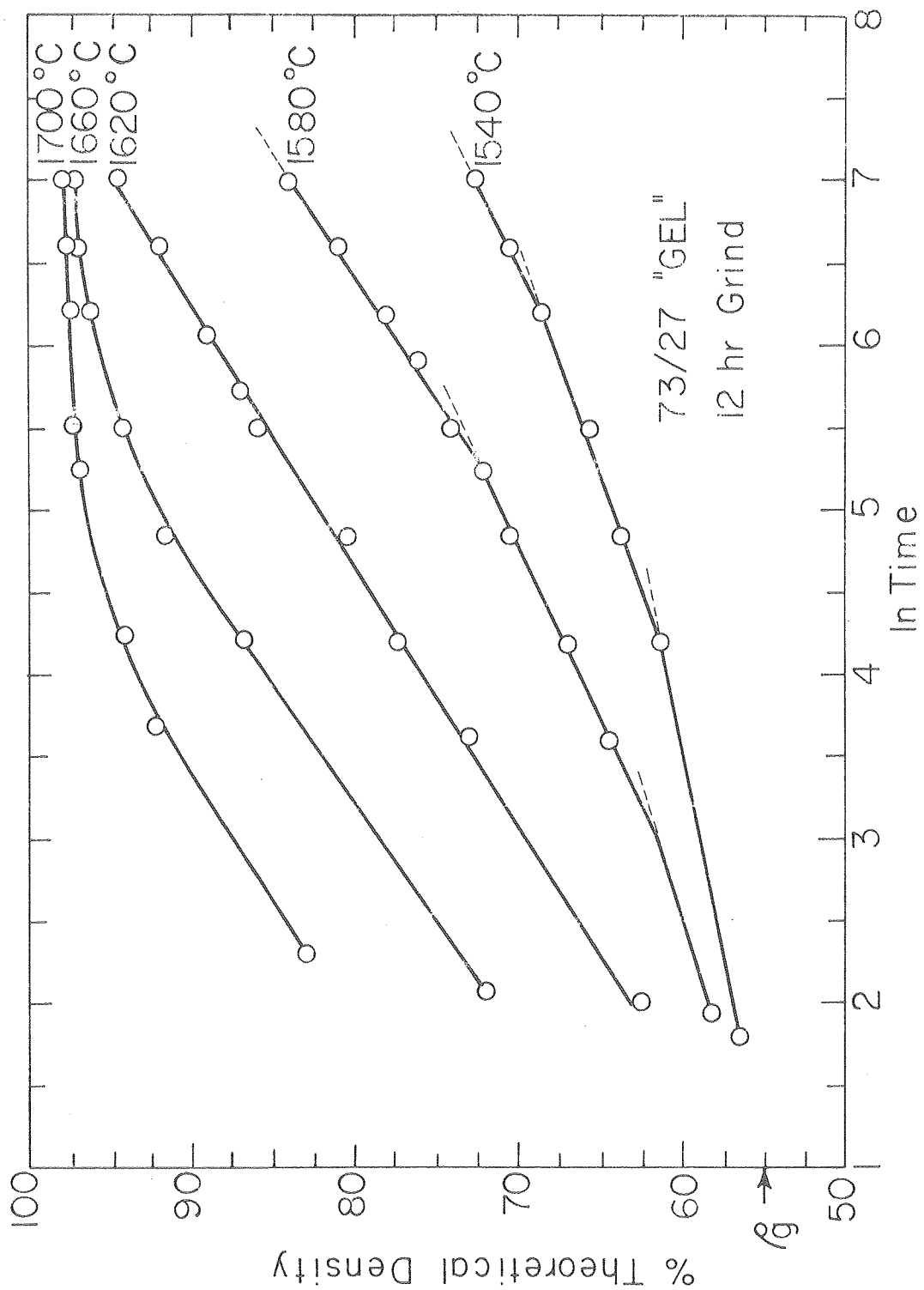
Fig. 70

XBL7911-14507



XBL 7911-14508

Fig. 71



XBL 7911-14500

Fig. 72

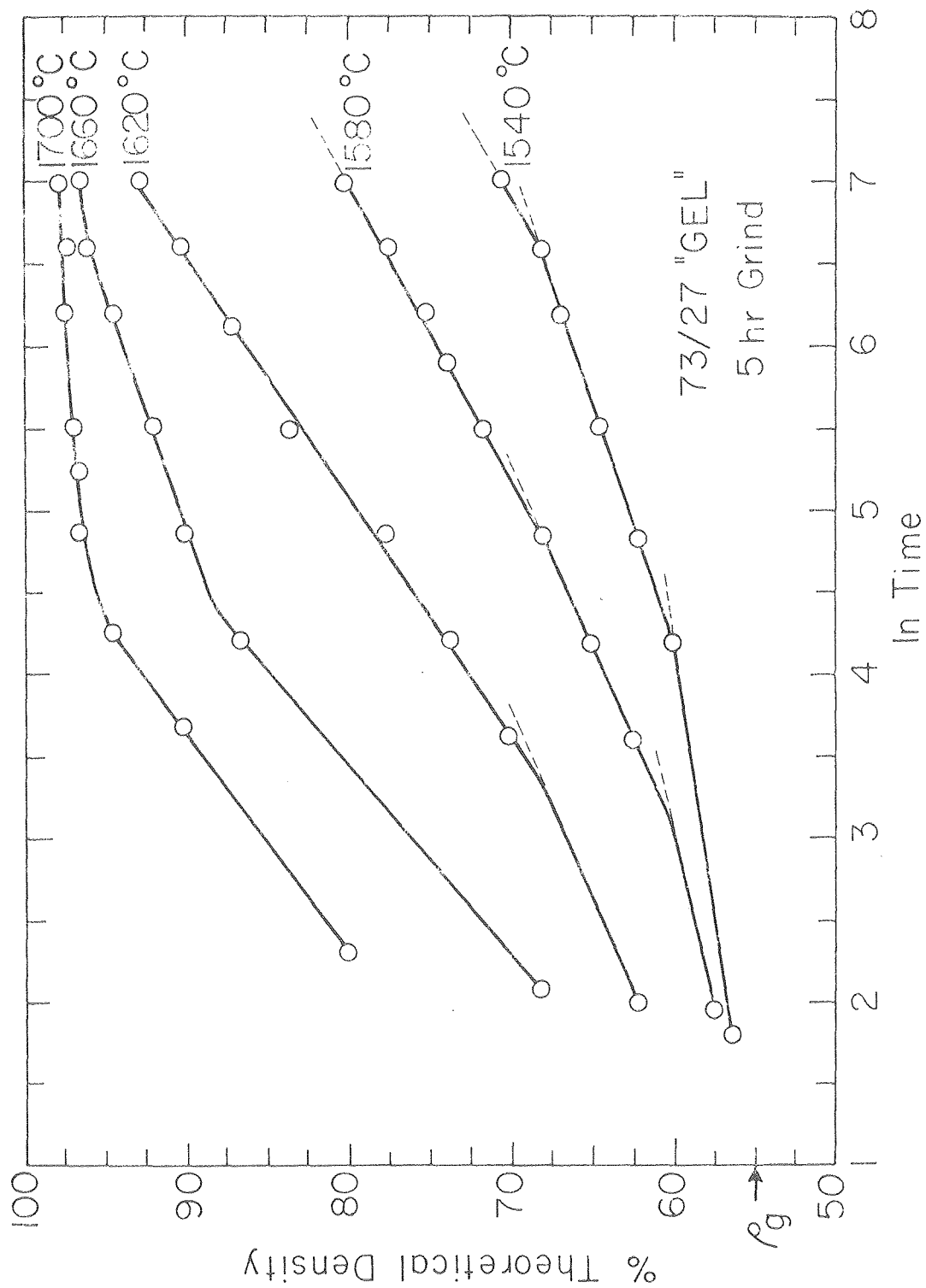


Fig. 73

XBL 7911-14501



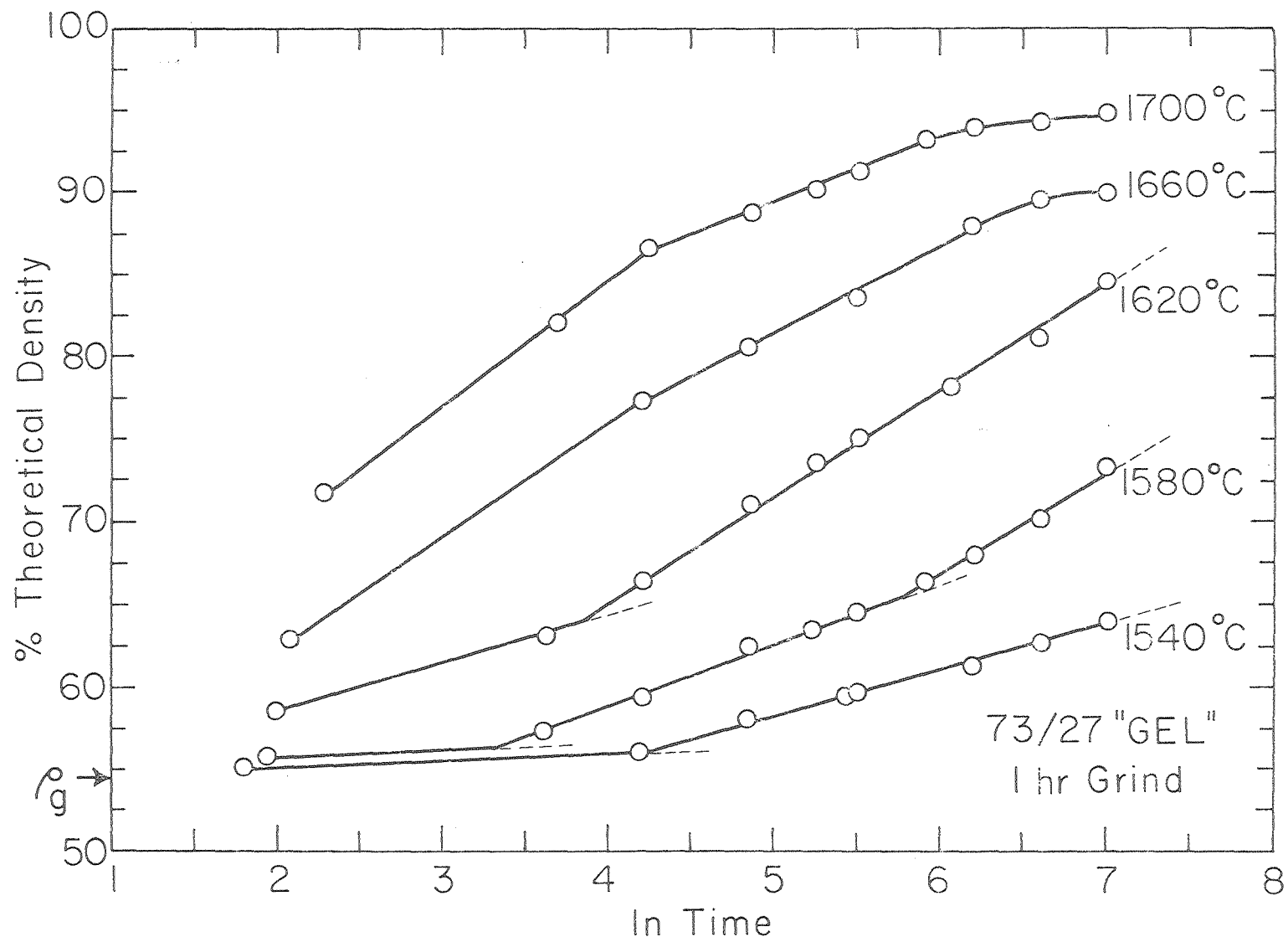


Fig. 74

XBL 7911-14502

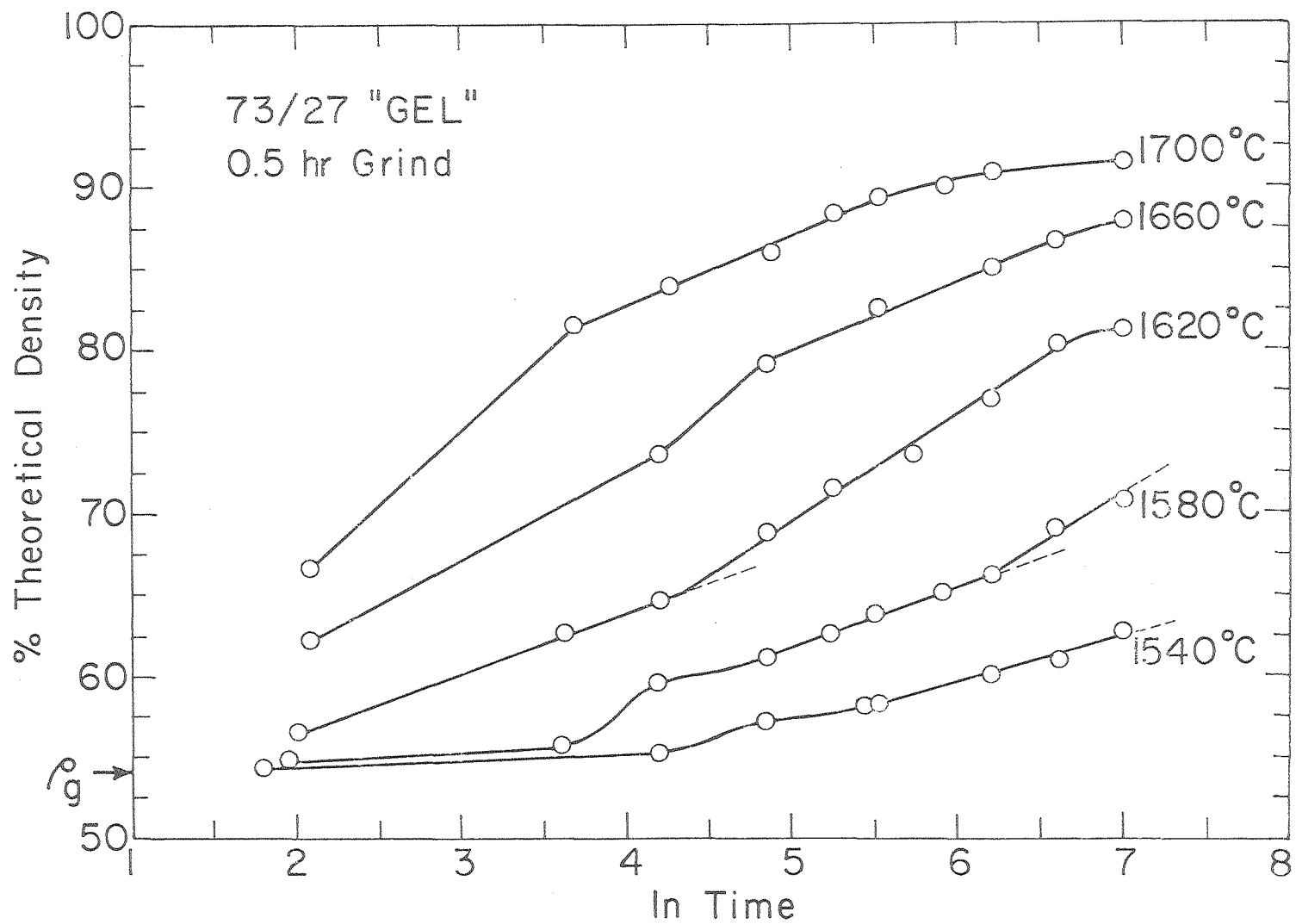
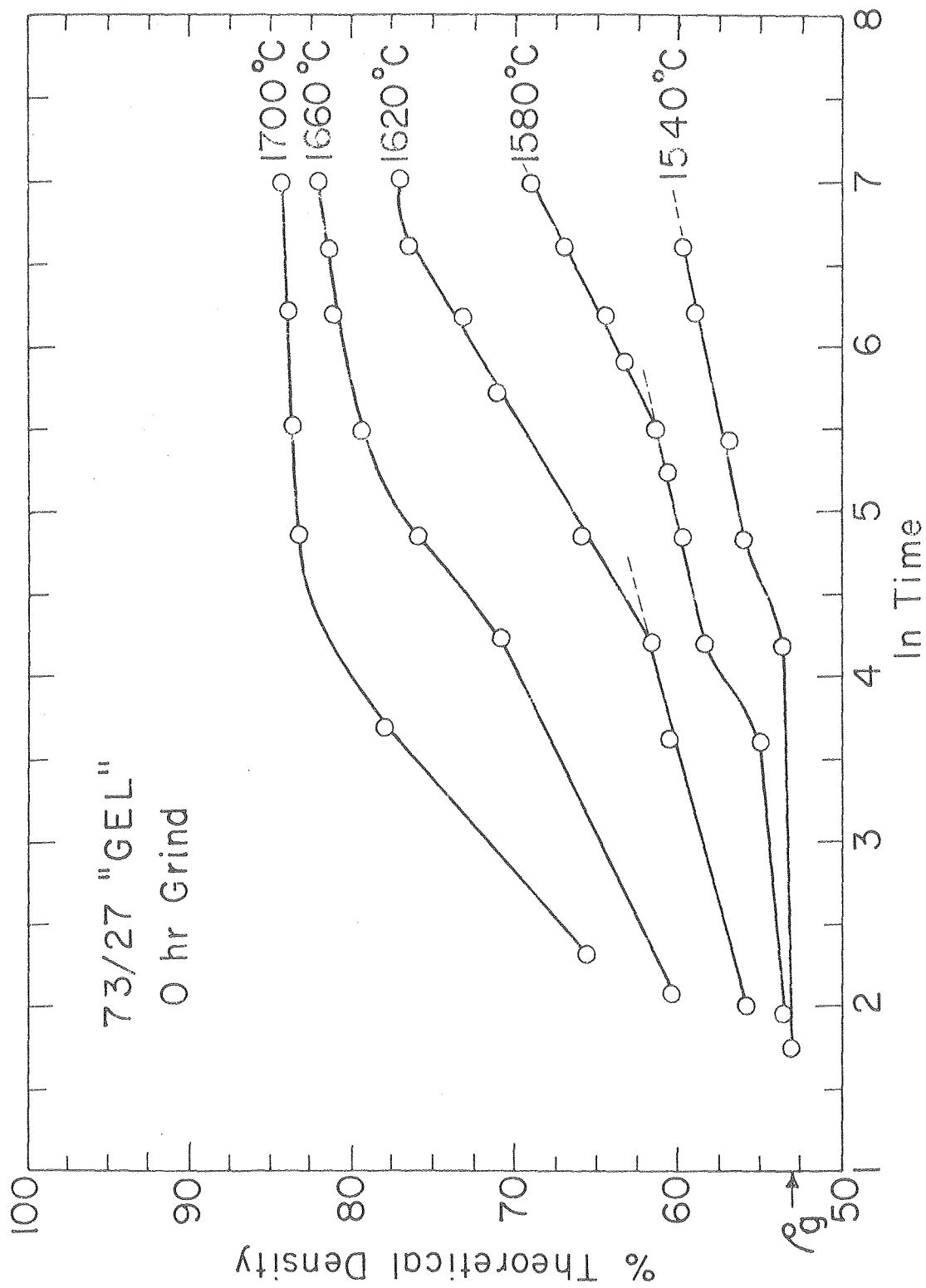


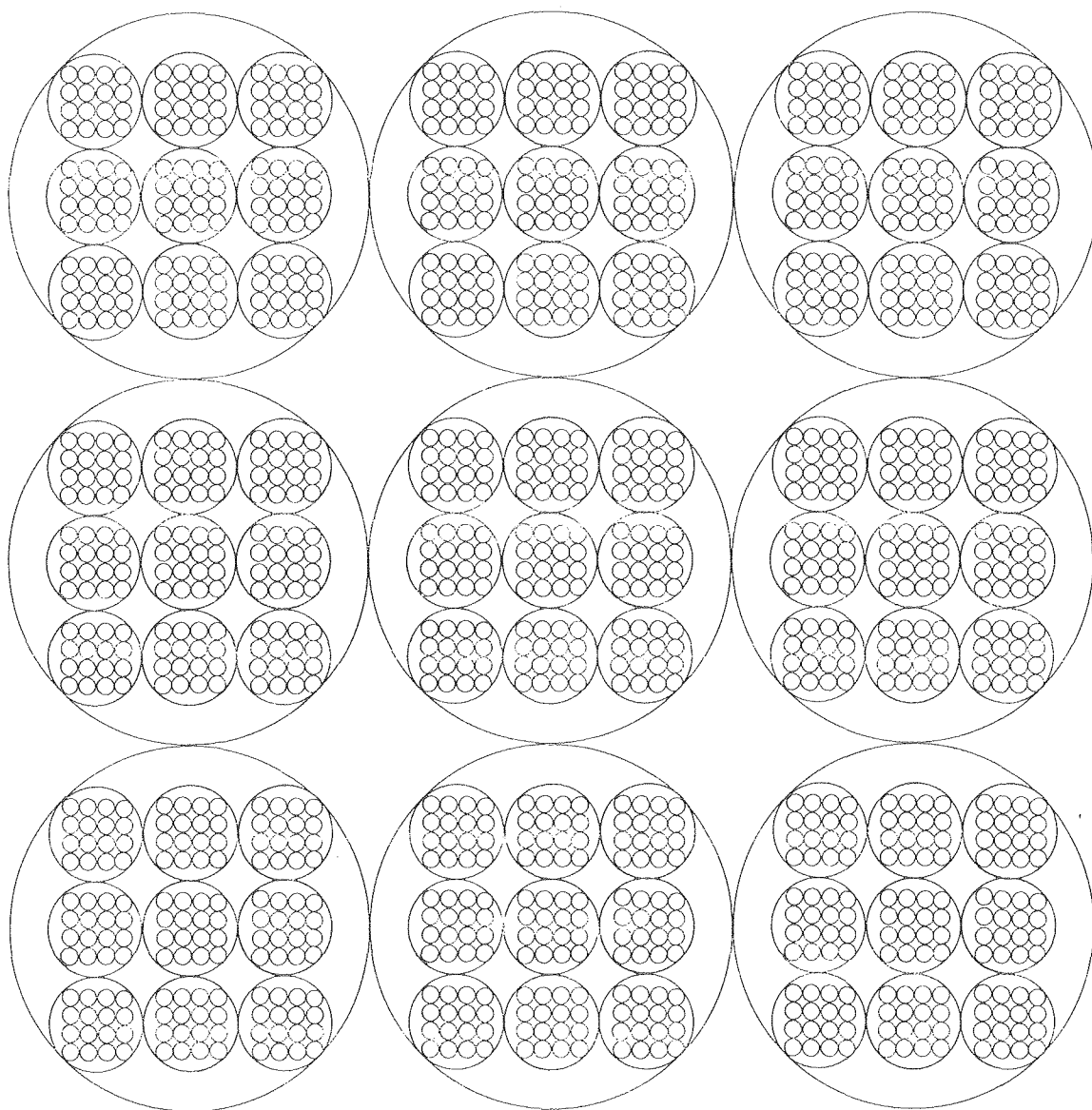
Fig. 75

XBL 79II-14504



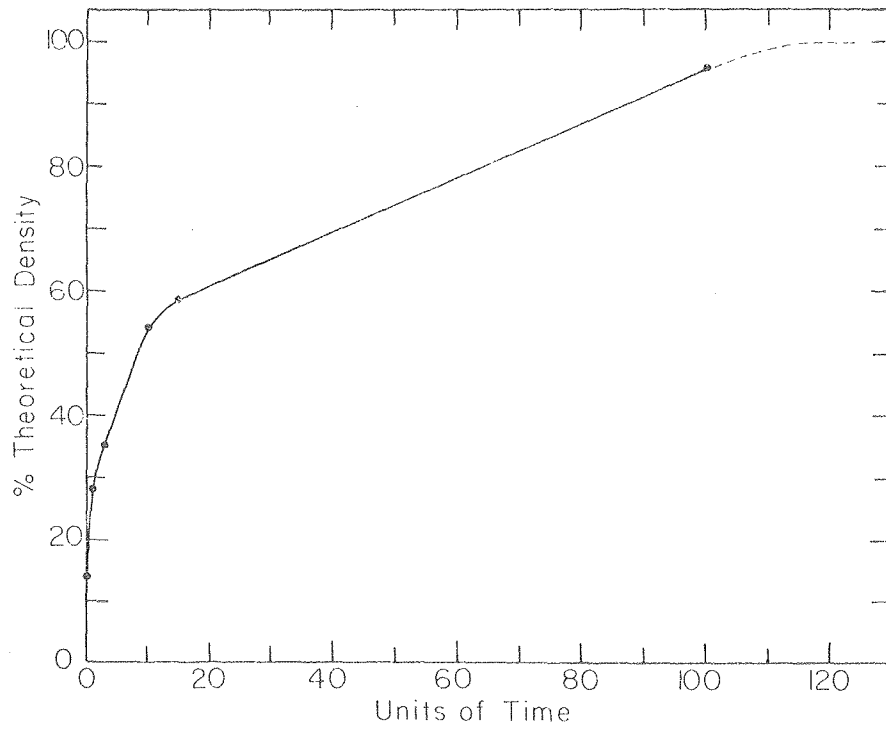
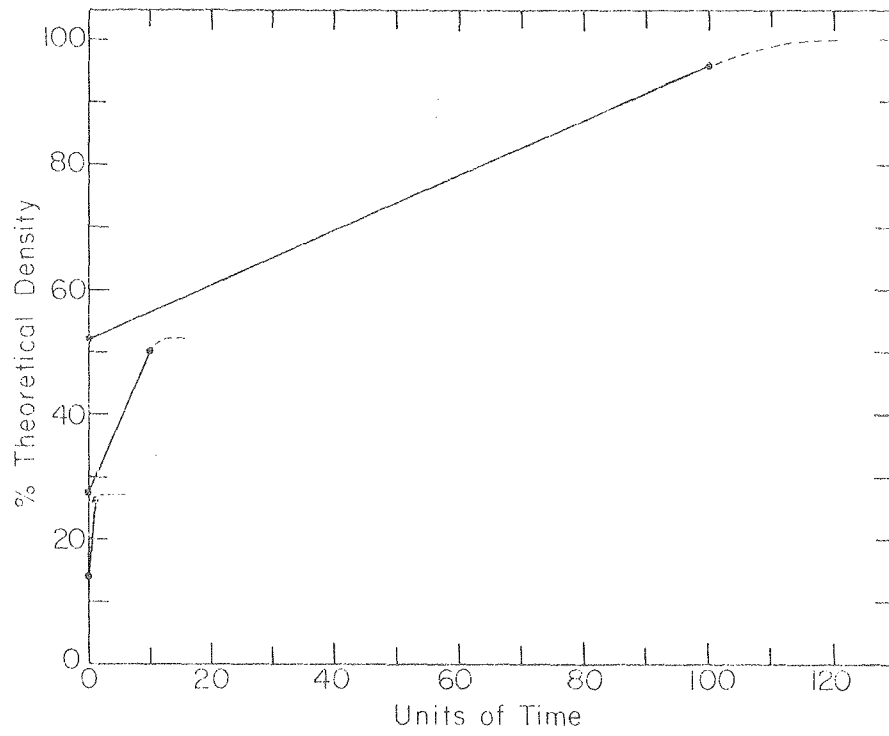
XBL 7911-14505

Fig. 76



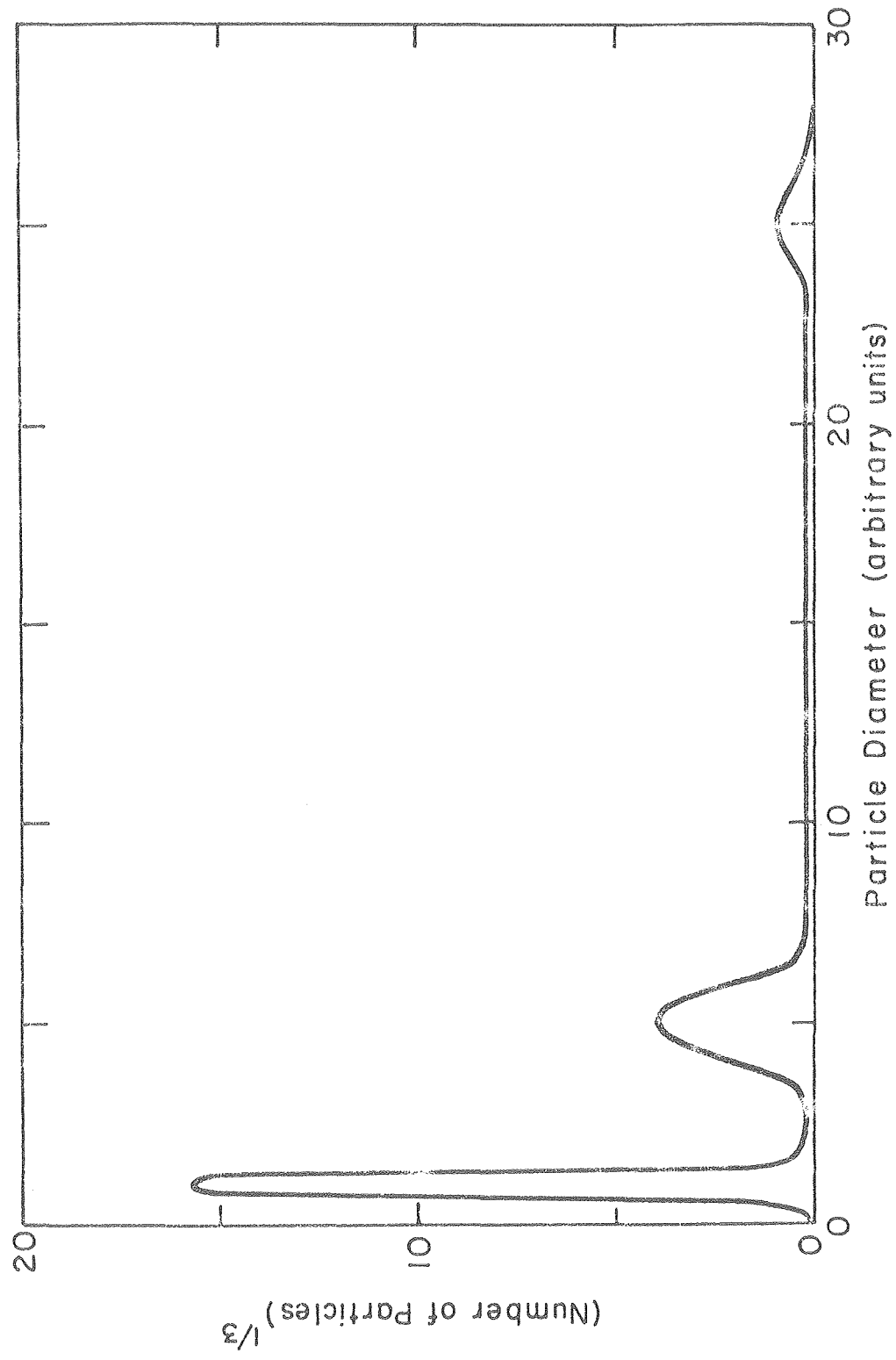
XBL 7912-13699

Fig. 77



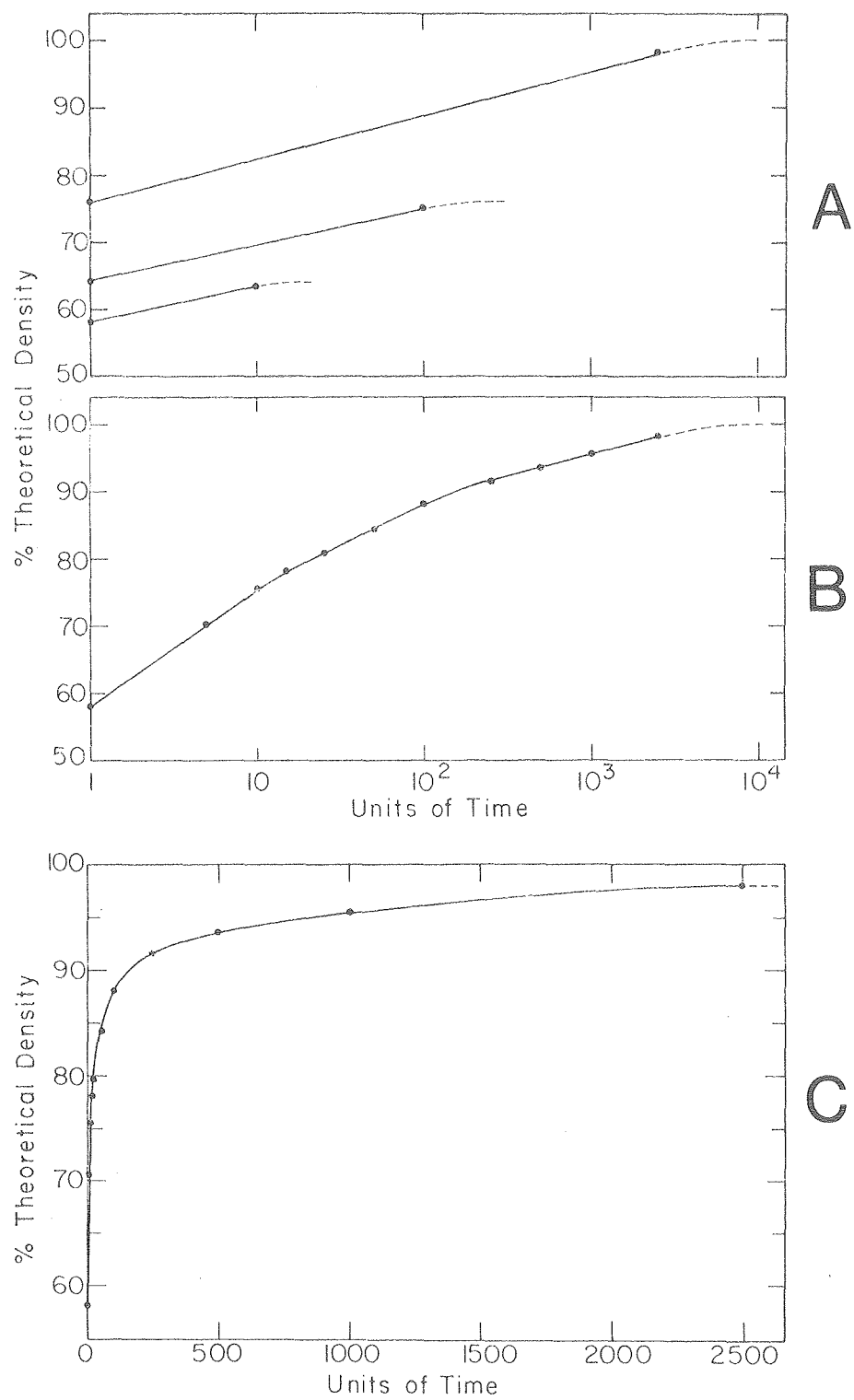
XBL 7911-I4512

Fig. 78



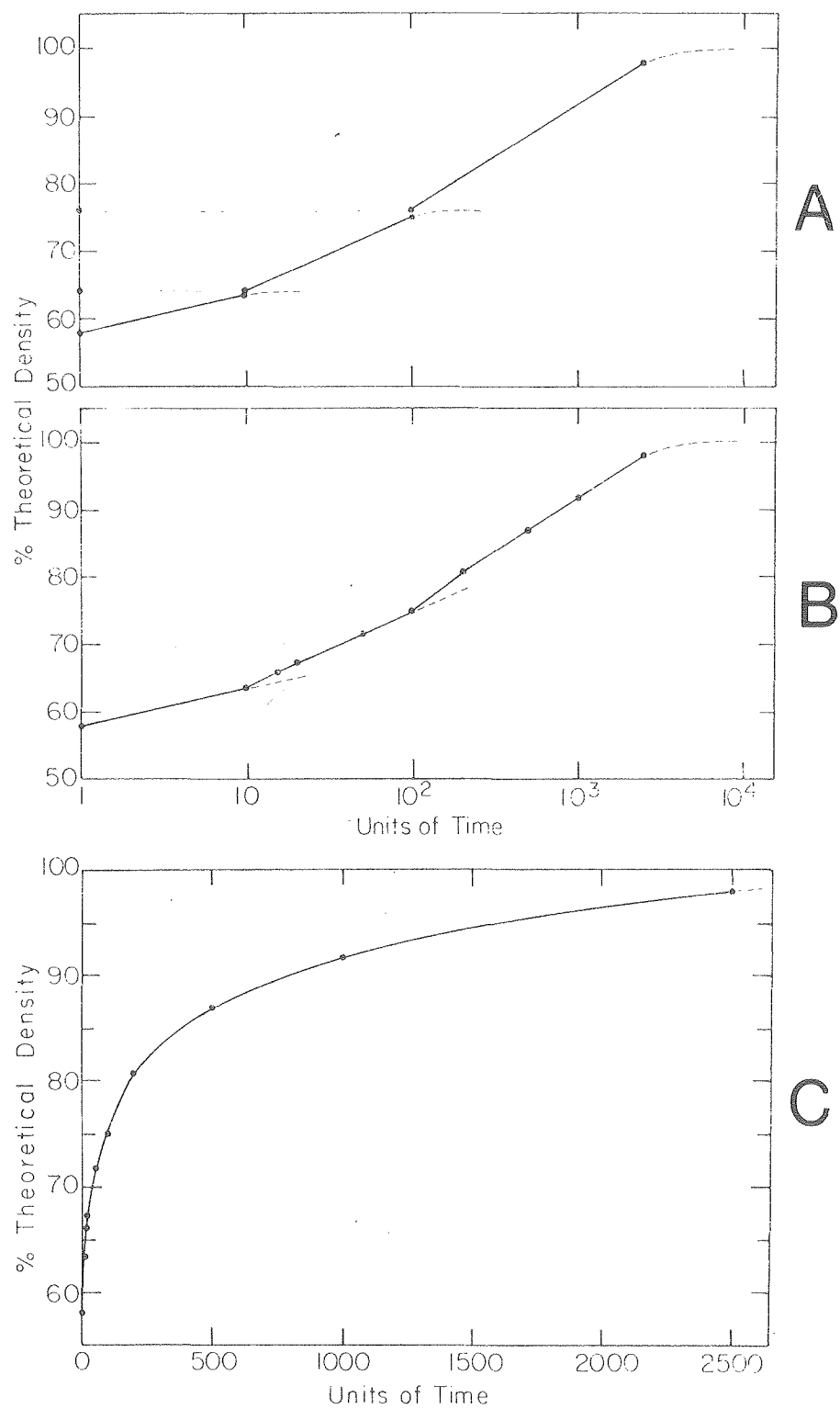
XBL 7911-13522

Fig. 79



XBL 7912-14593

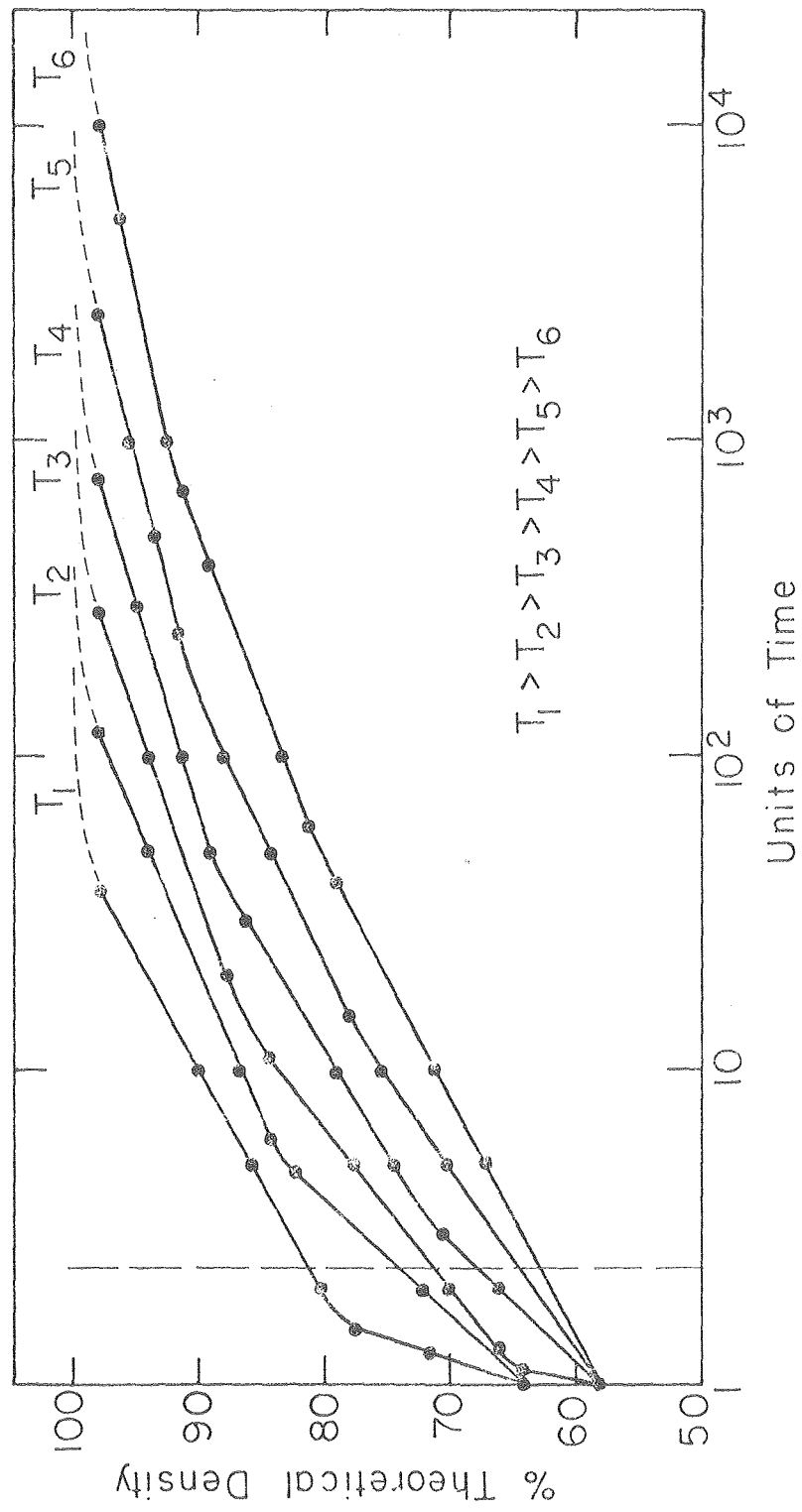
Fig. 30



XBL 7912-14 594

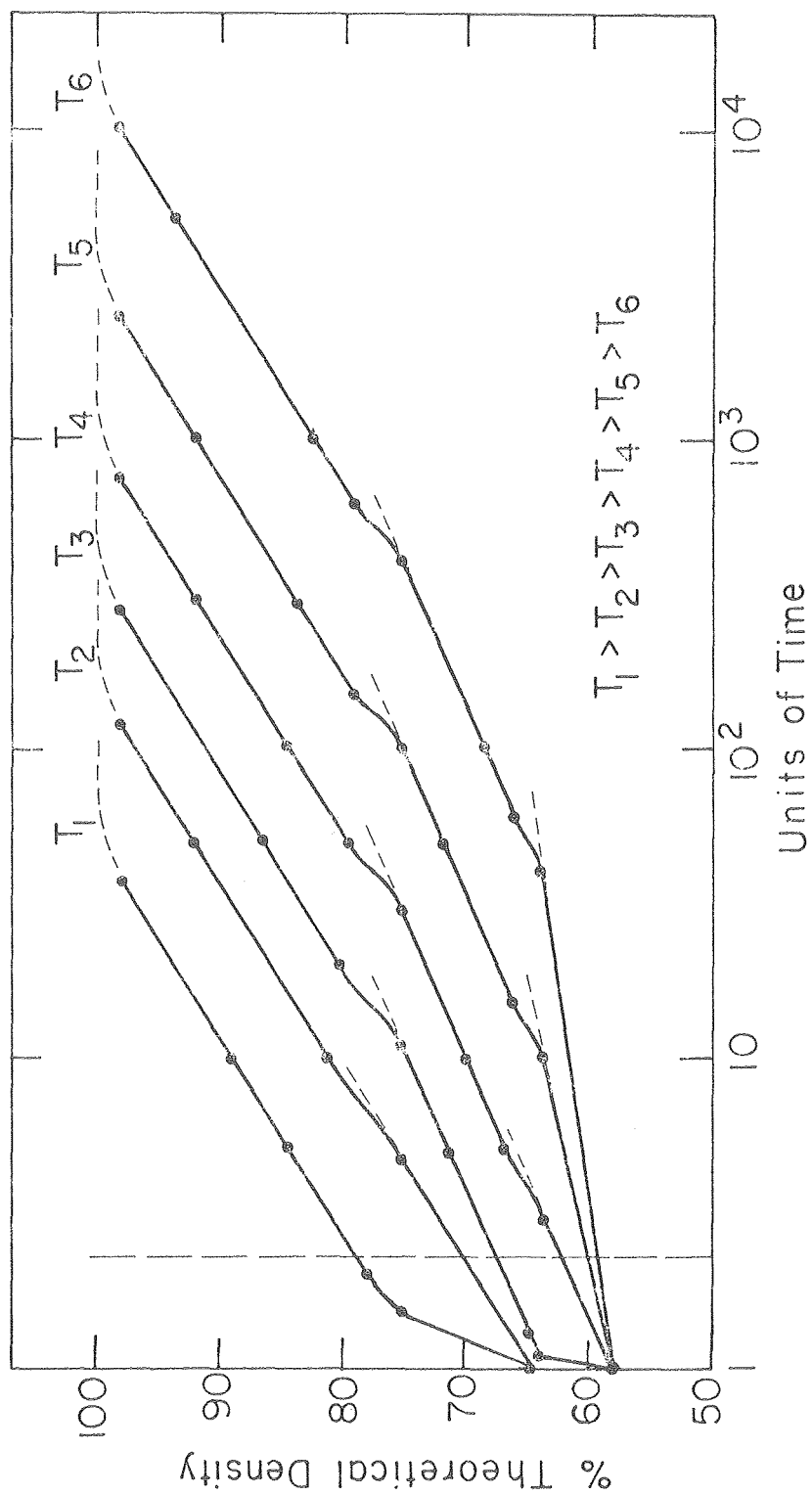
Fig. 81





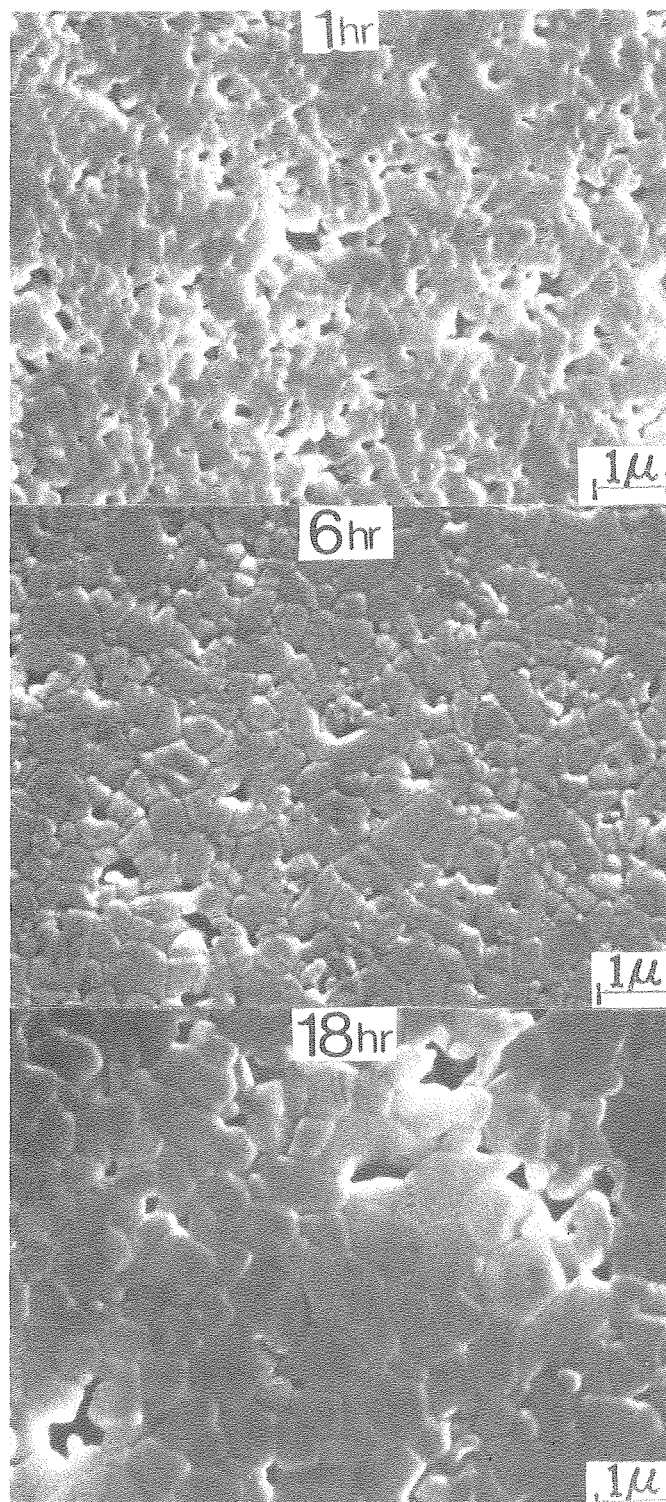
XBL 7911-14514

Fig. 82



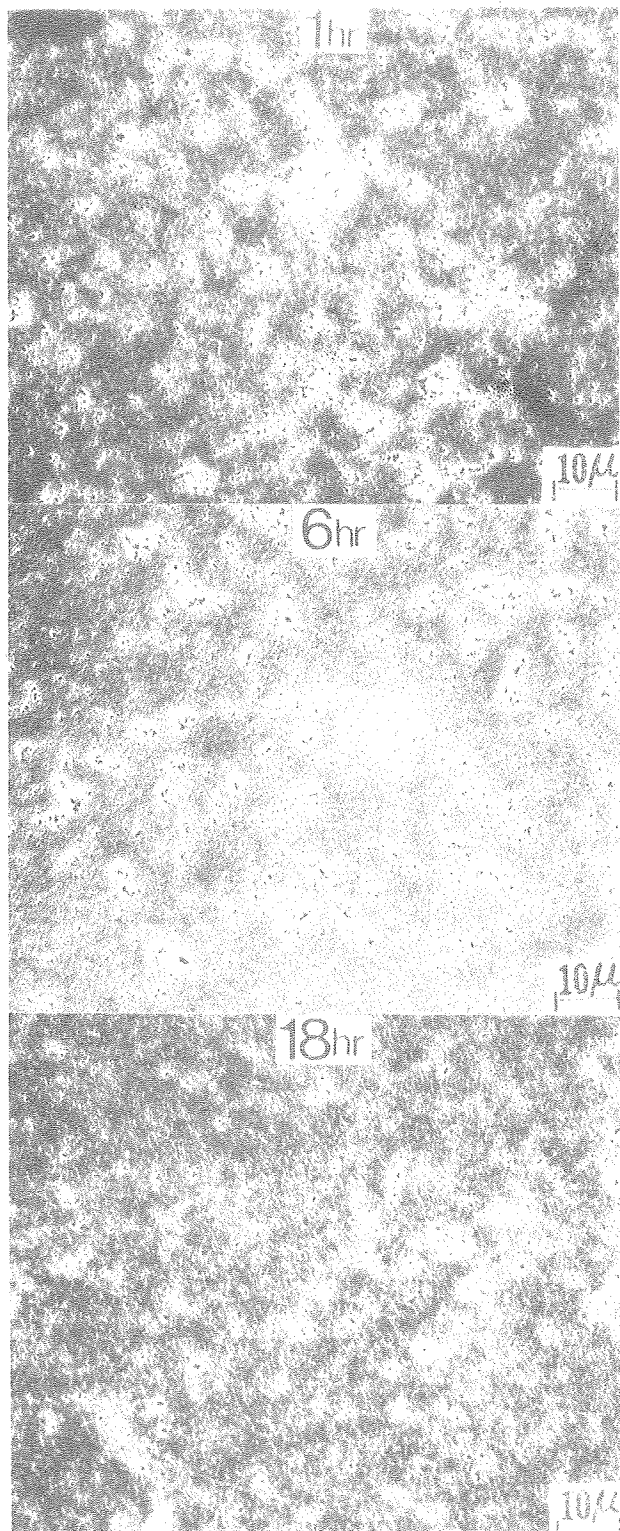
XBL 7911-14506

Fig. 83



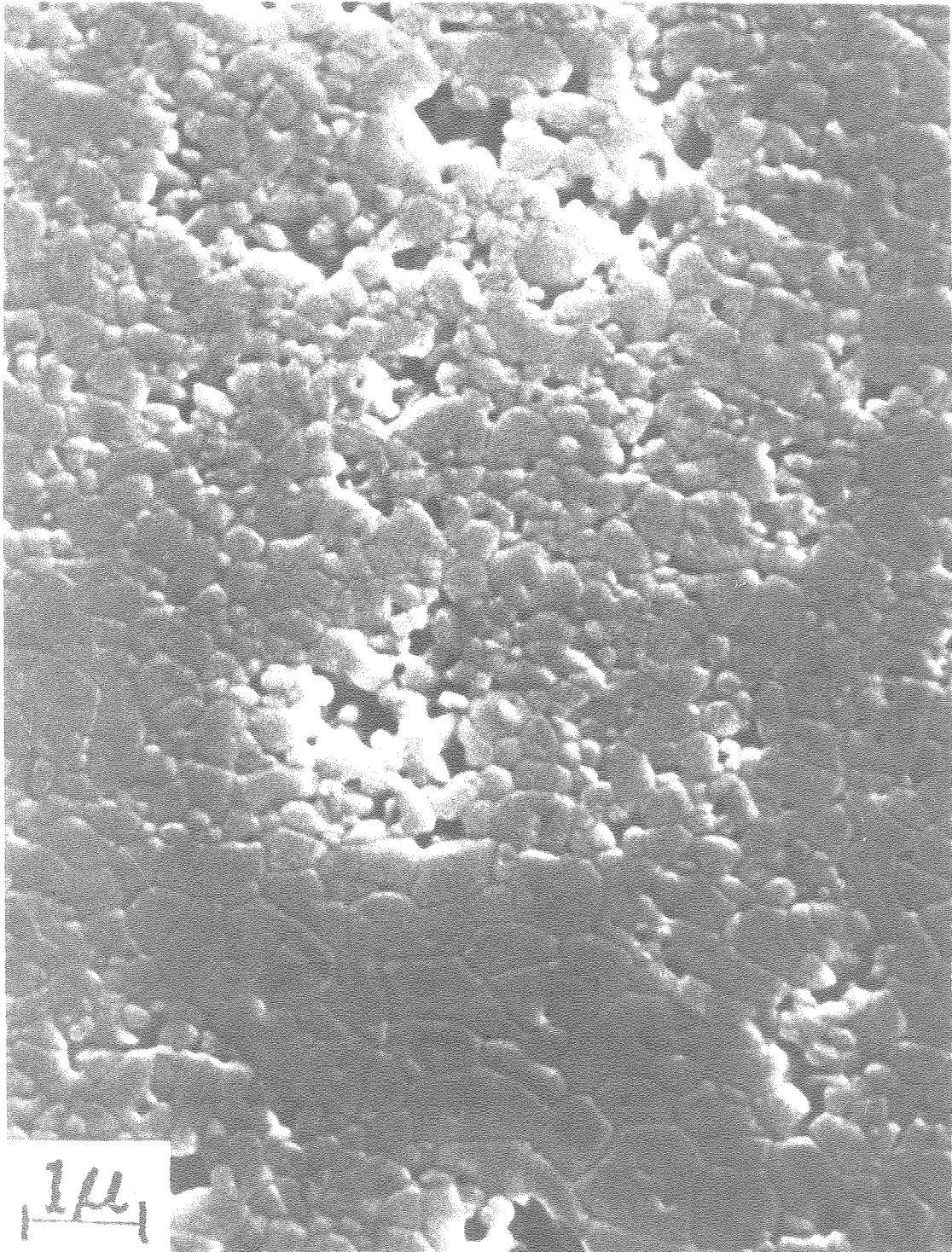
XCB 790-16248

Fig. 84



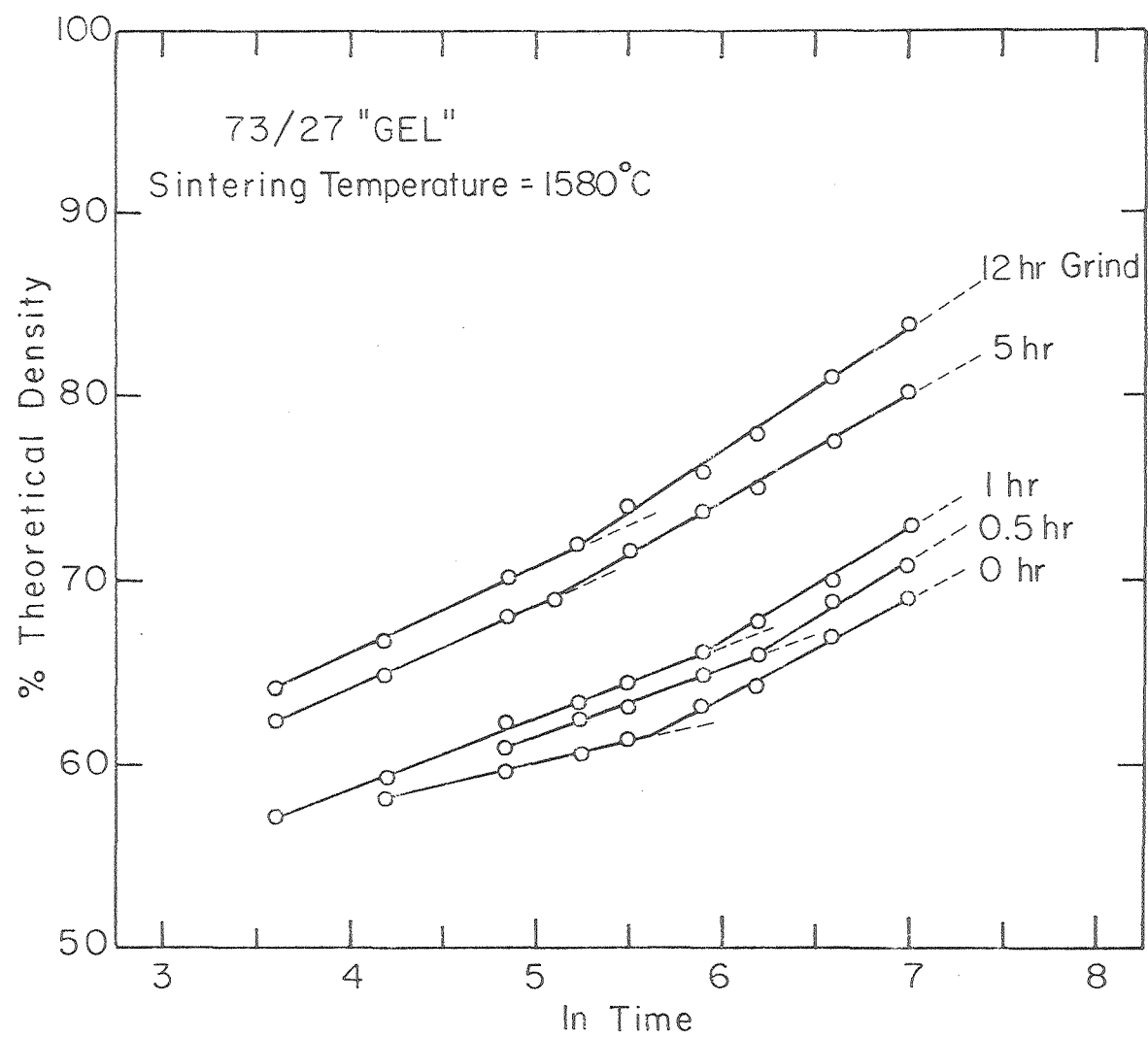
XBB 790-16247

Fig. 85



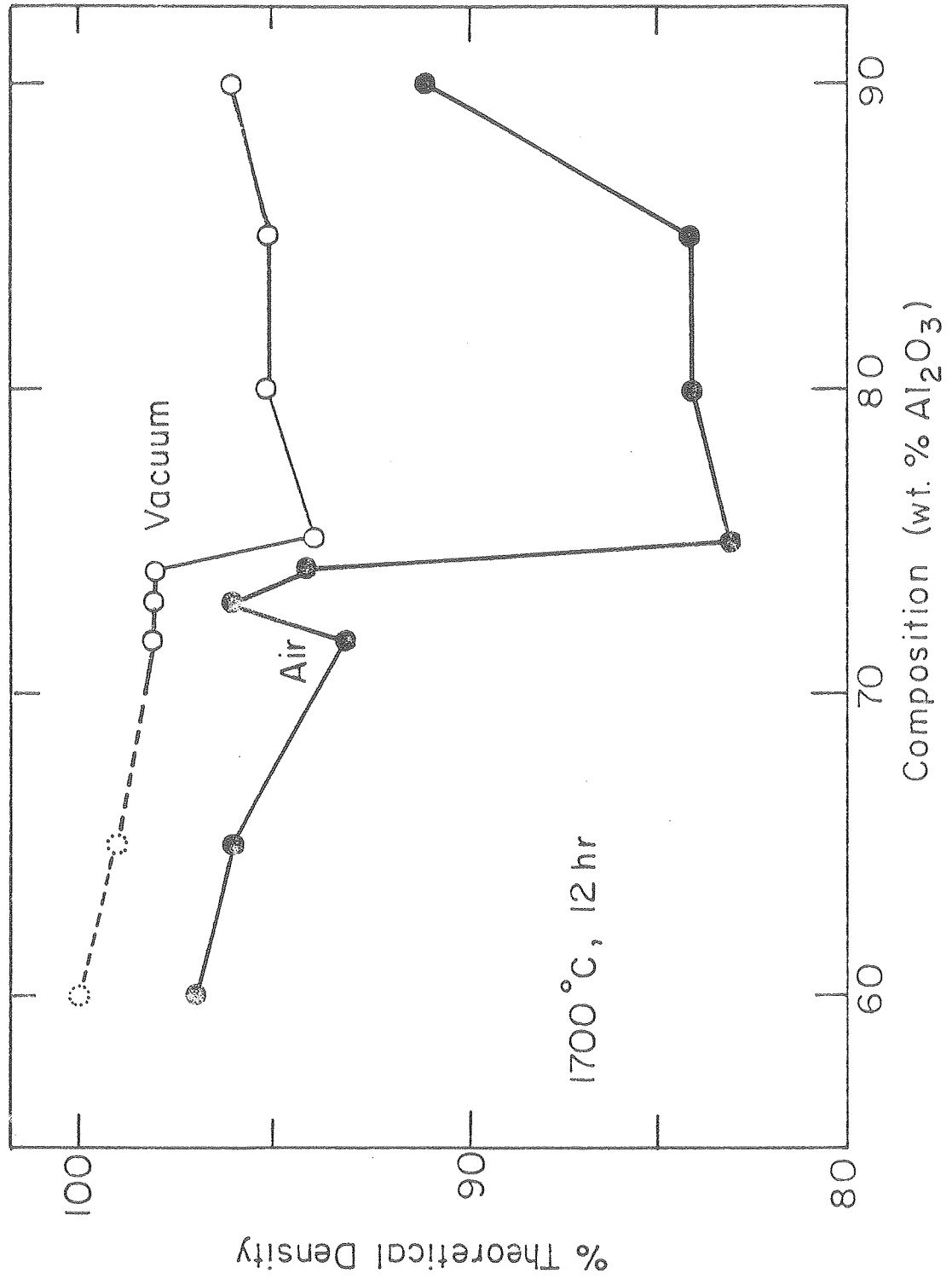
XBB 785-5306

Fig. 86



XBL7911-I4515

Fig. 87

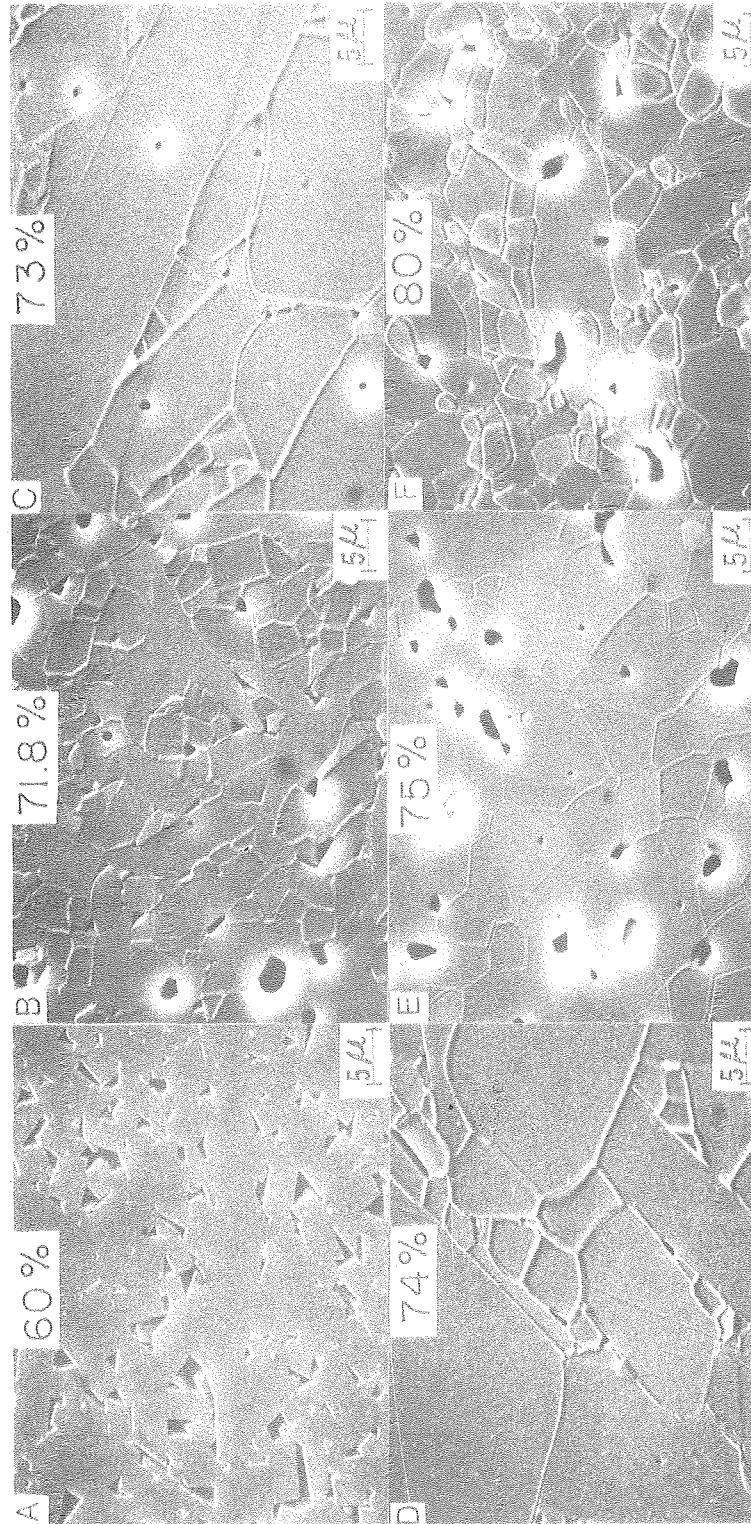


XBL 7912 - 5400

Fig. 88



# VACUUM



XBB 770-11024

Fig. 89



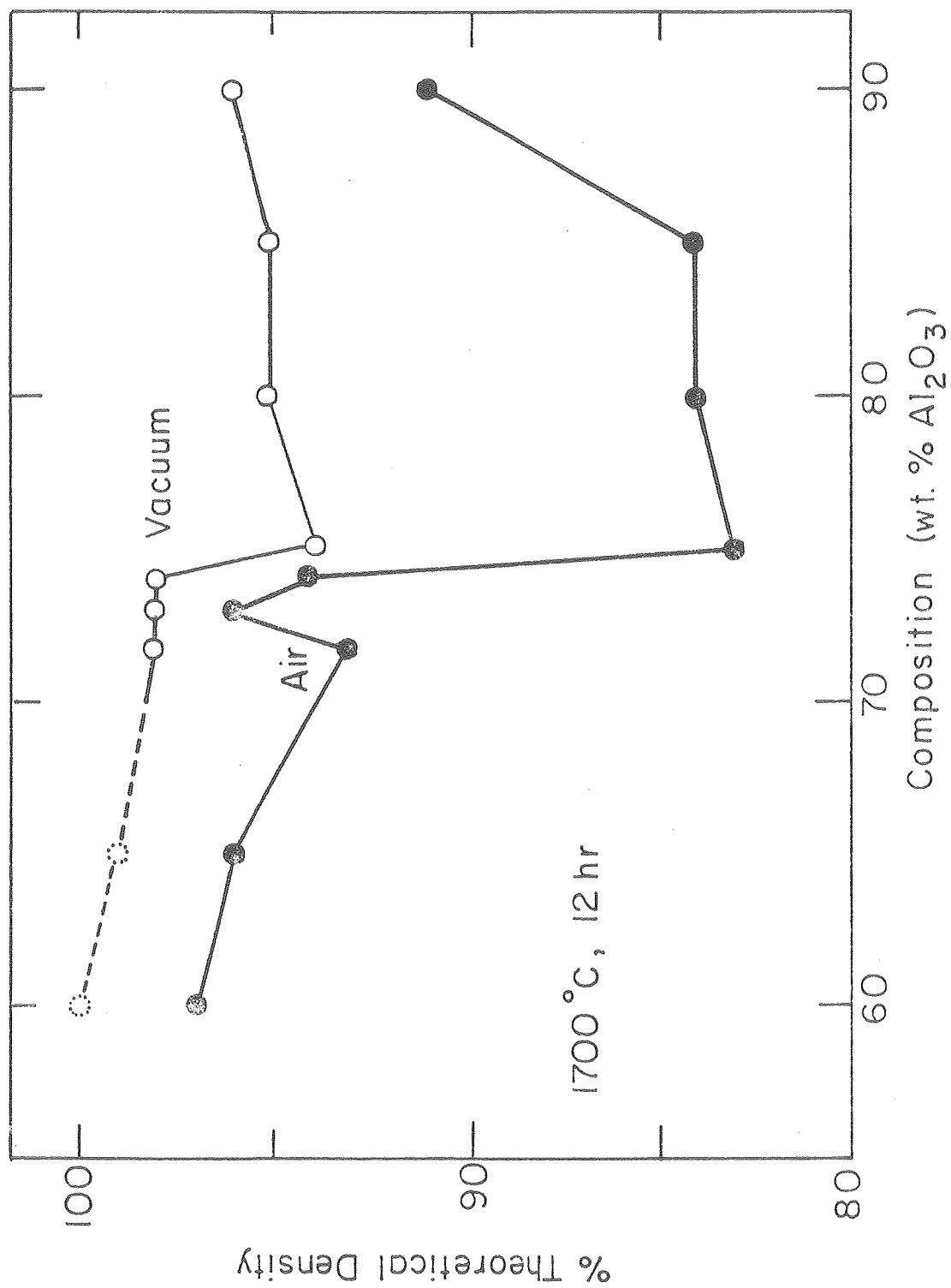
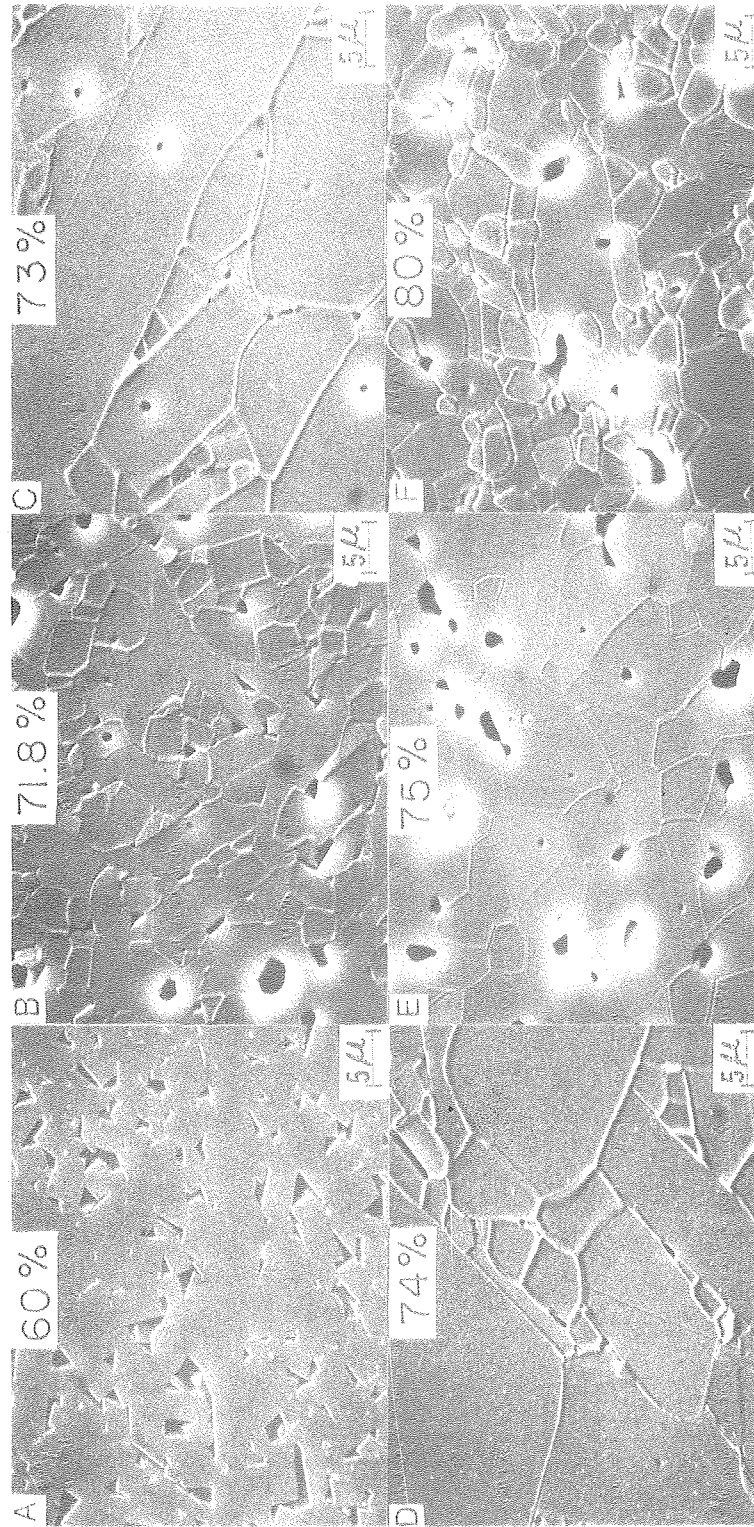


Fig. 88

XBL 7912 - 5400

# VACUUM



XBB 770-11024

Fig. 89

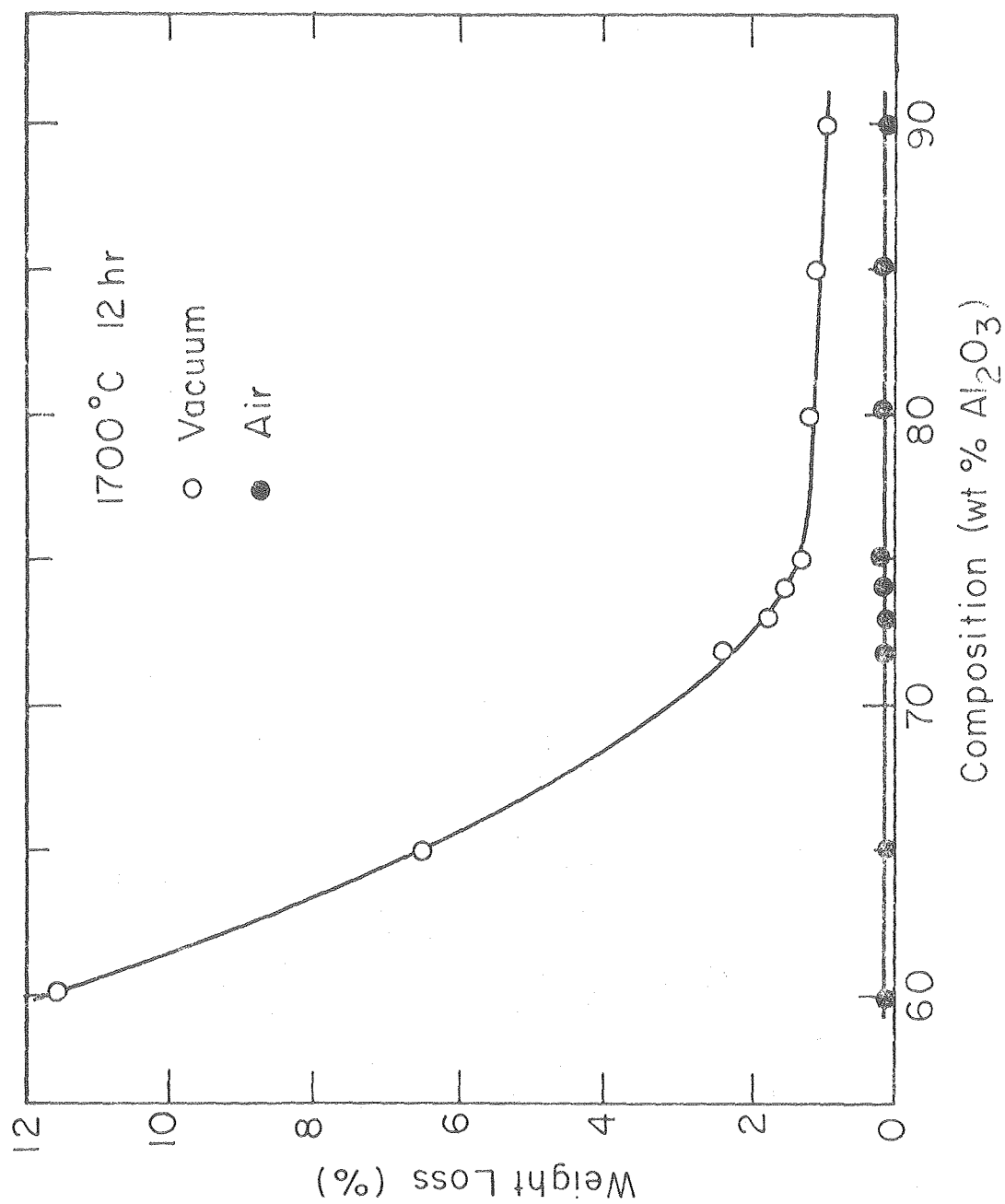


Fig. 90

XBL7911-14517

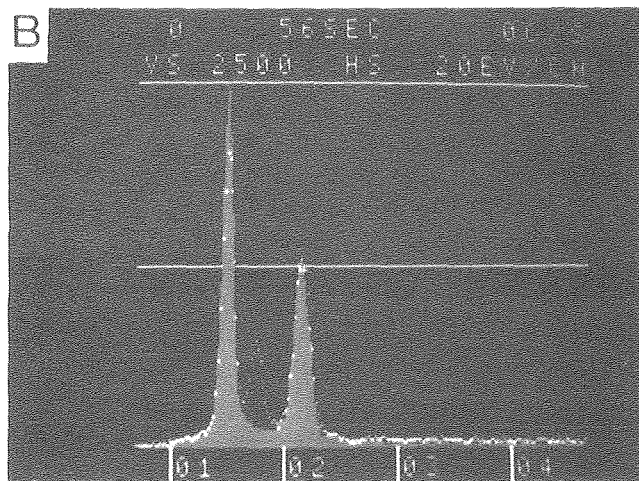
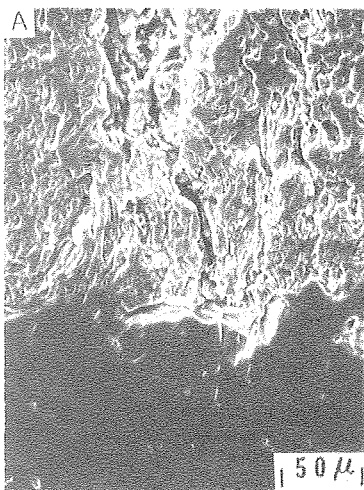
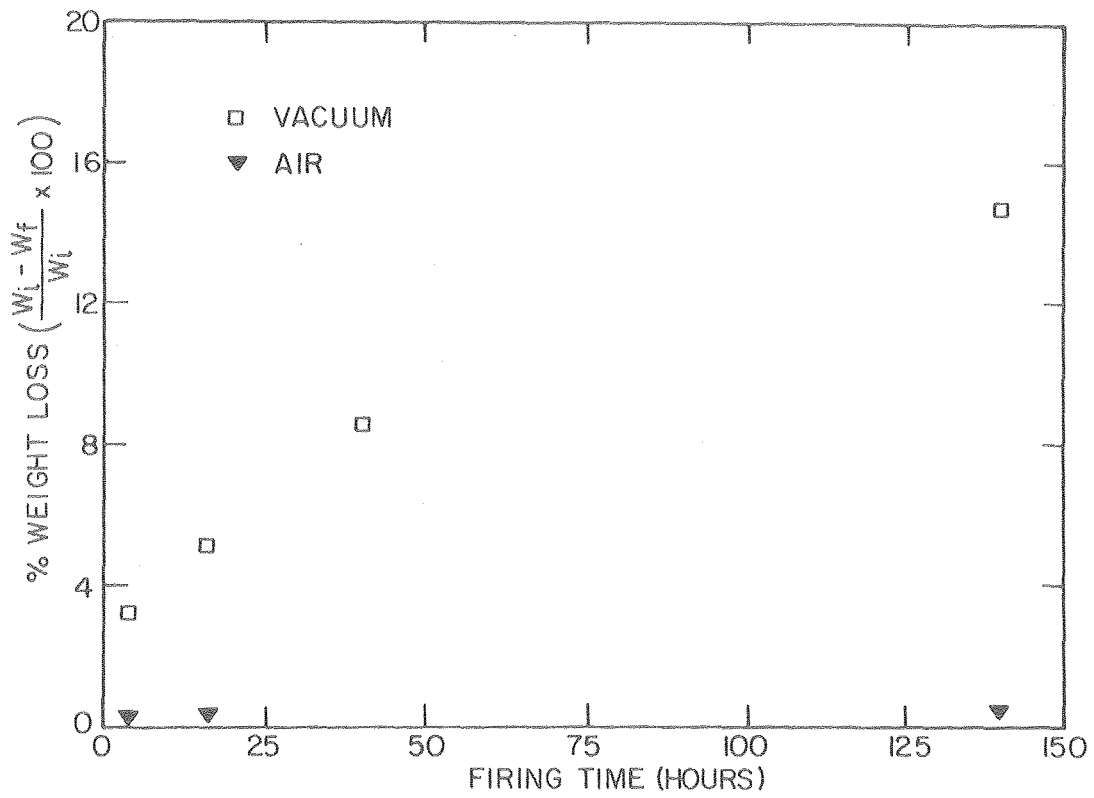
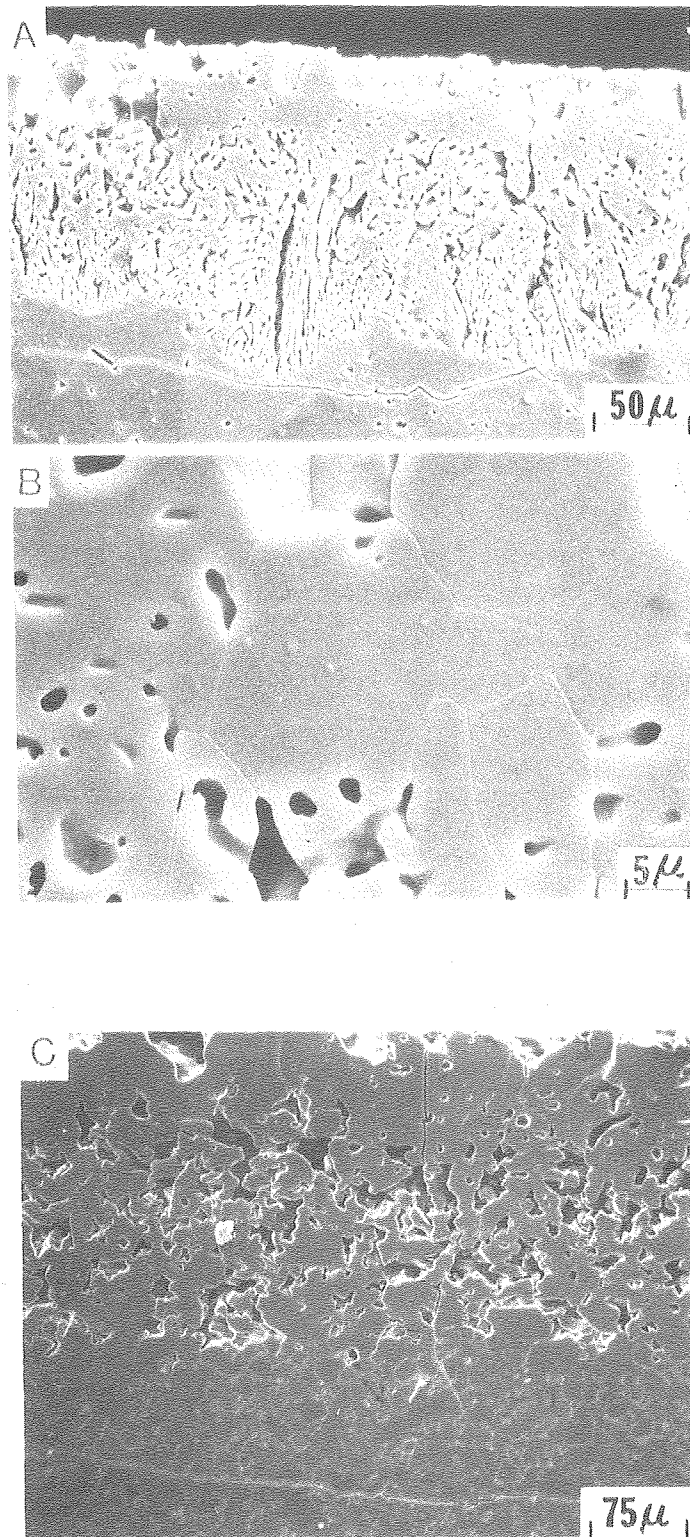
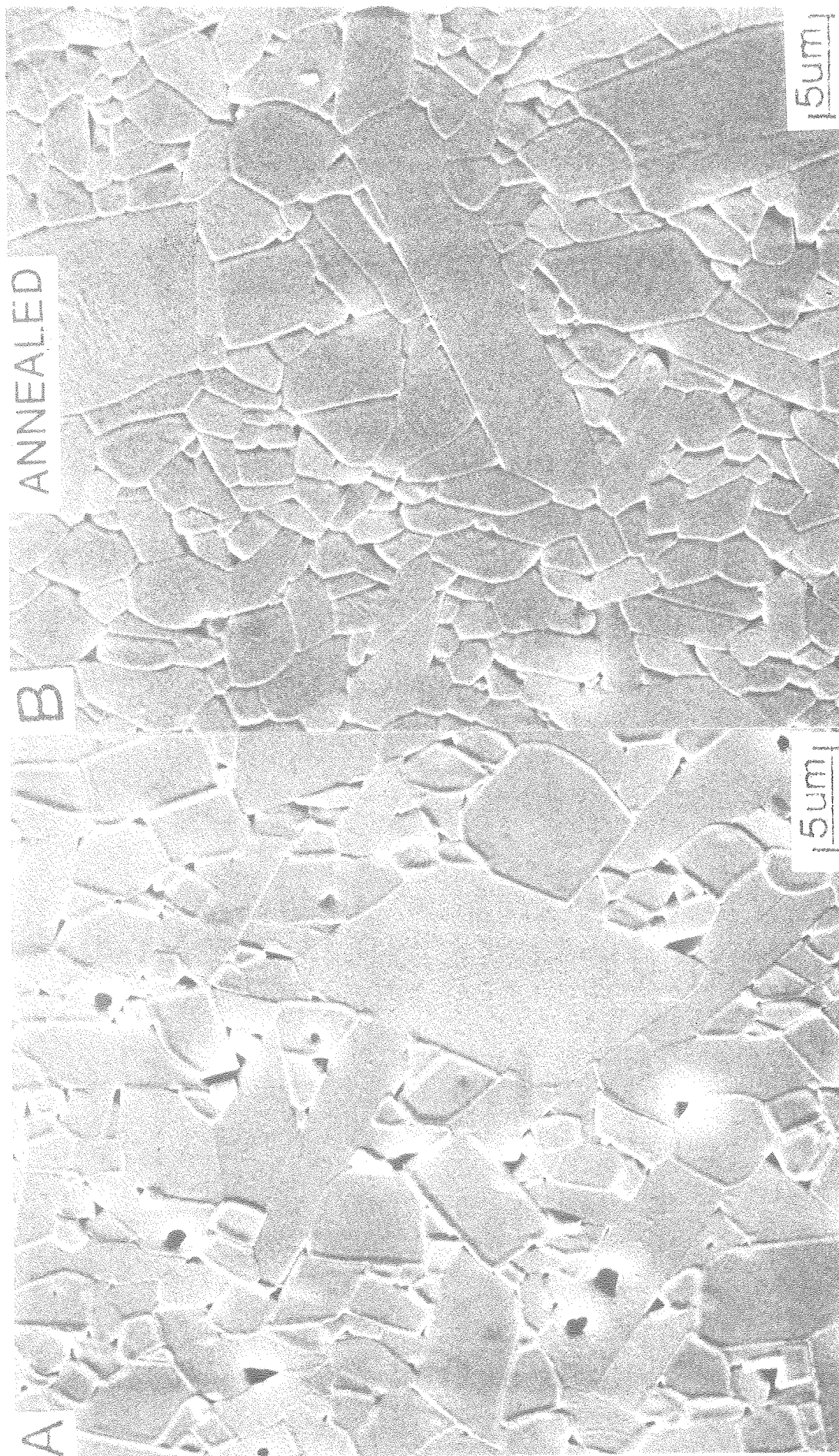


Fig. 91



XBB 790-15933

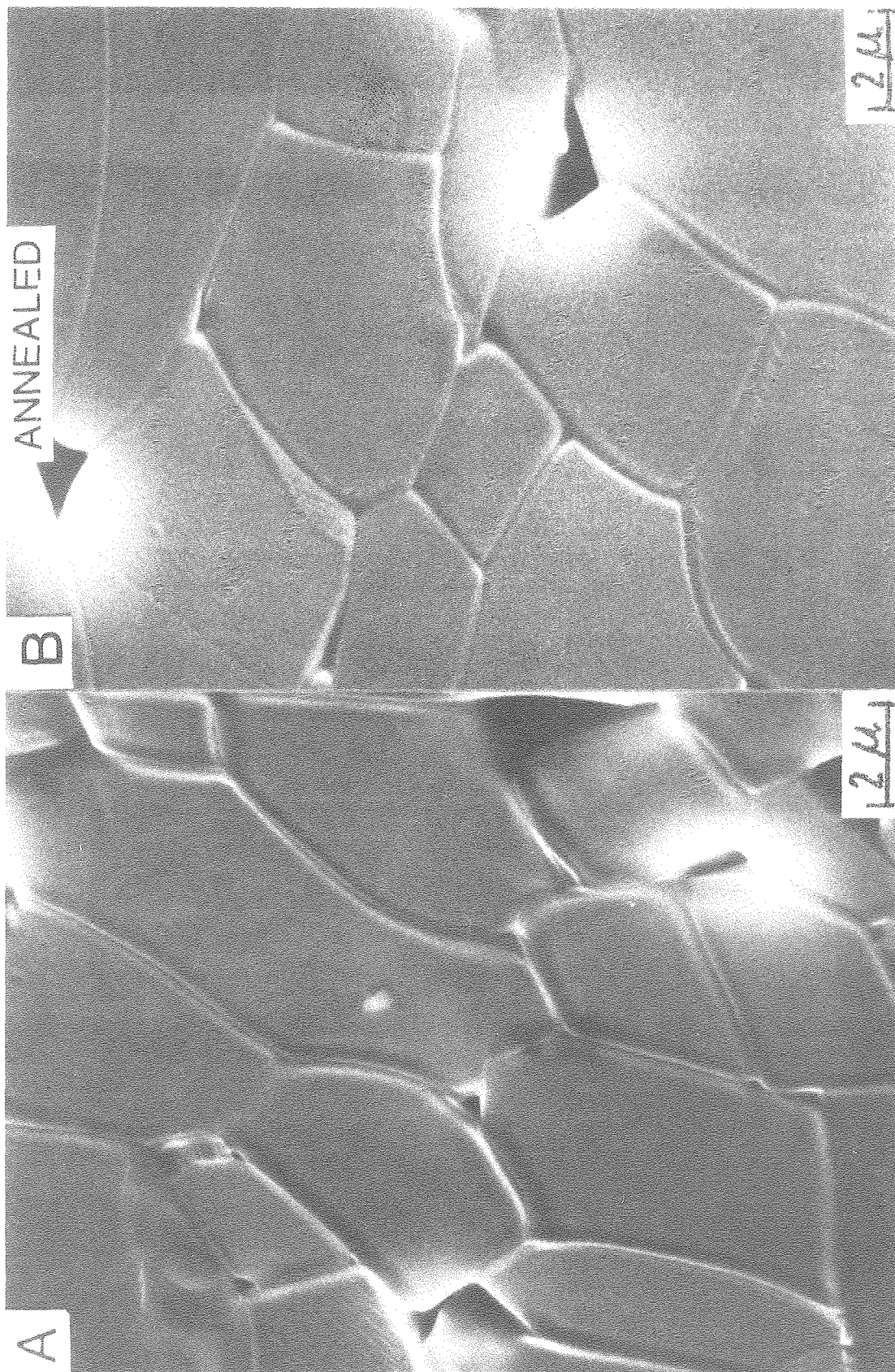
Fig. 92



XBB 790-15917

Fig. 93





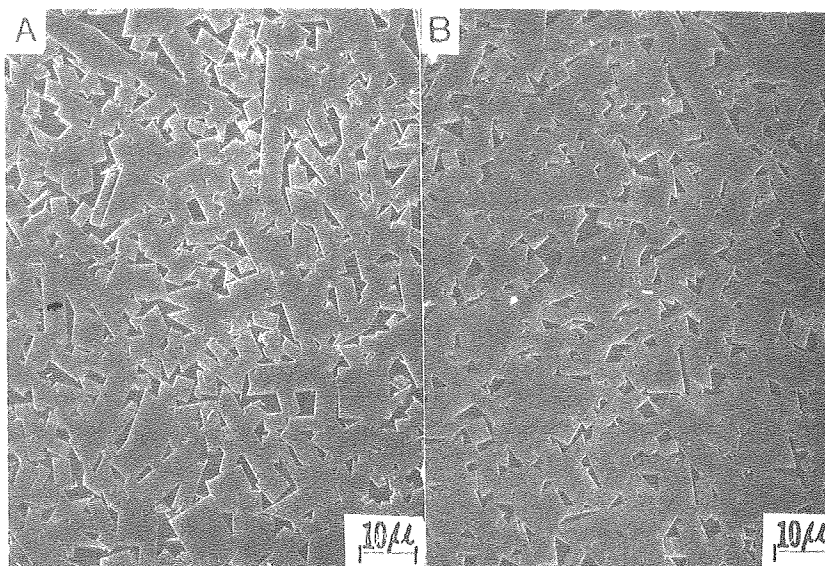
XBB 790-15912

Fig. 94

# COMPOSITION: 60/40

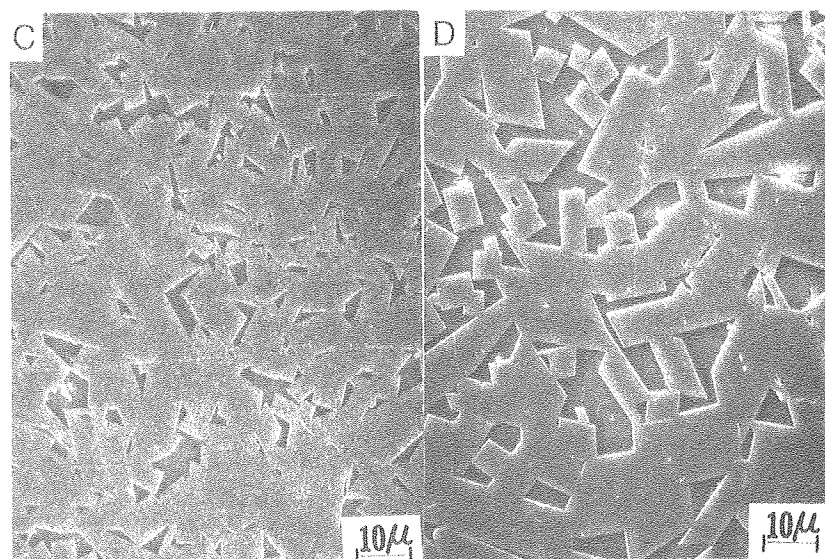
AIR

VACUUM



ARGON

SEALED Mo



XBB 790-15079

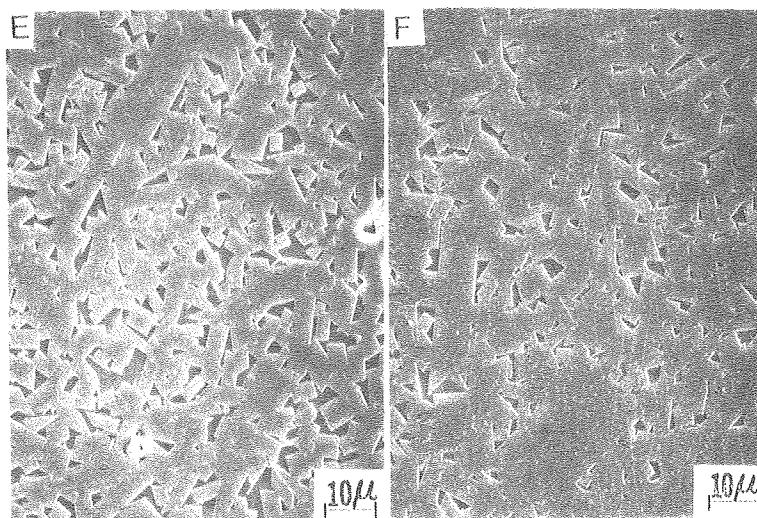
Fig. 95



COMPOSITION: 60/40

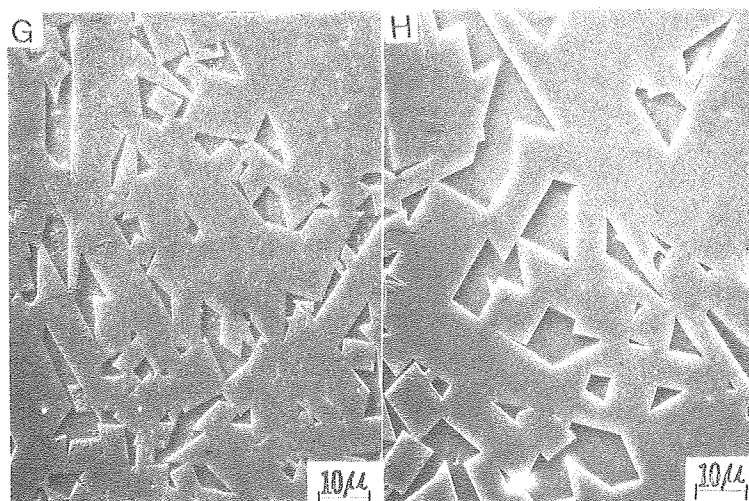
AIR

VACUUM



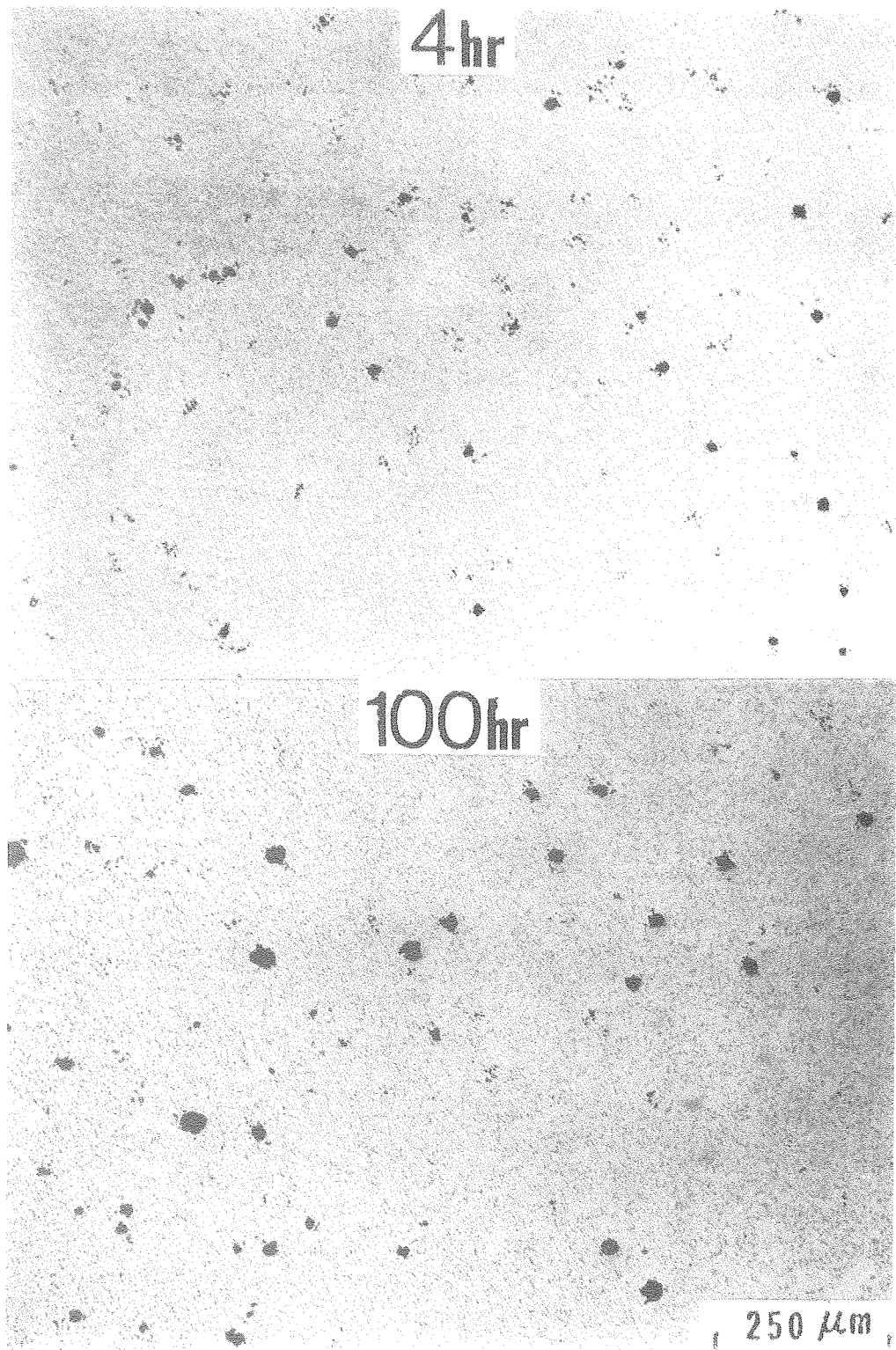
ARGON

SEALED Mo



XBB 790-15934

Fig. 96



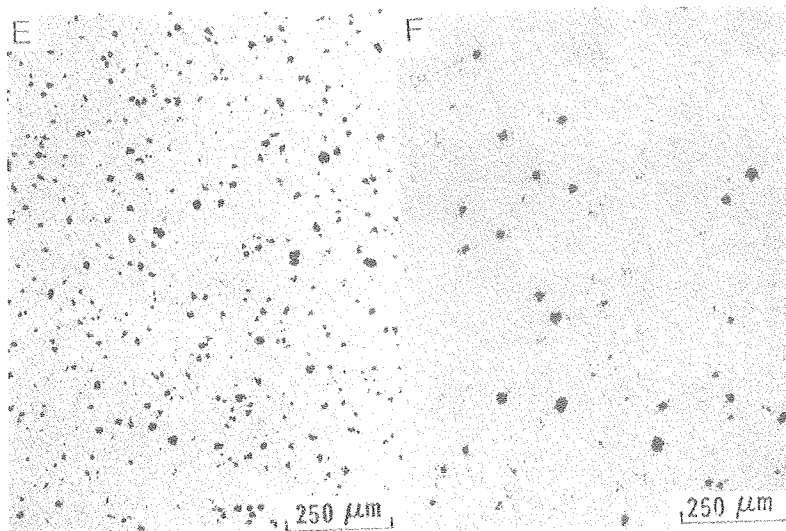
XBB 790-15913

Fig. 97

# COMPOSITION: 60/40 "GEL"

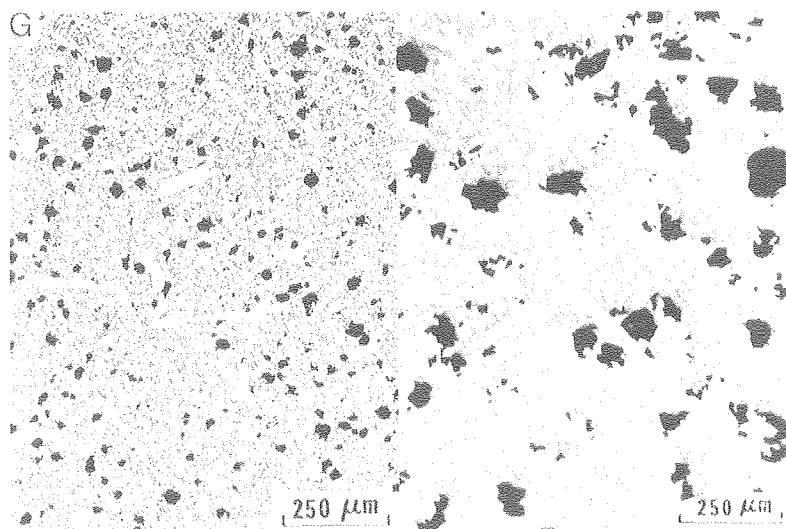
AIR

VACUUM



ARGON

SEALED MO

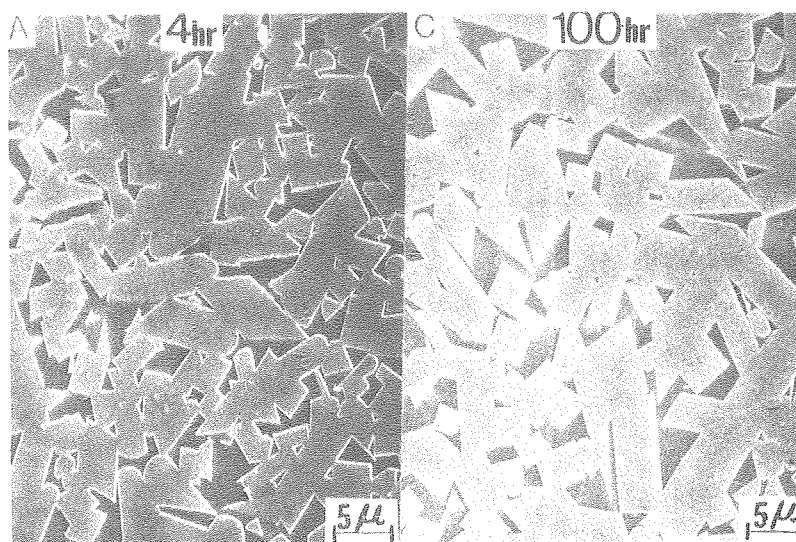


XBB 790-15917

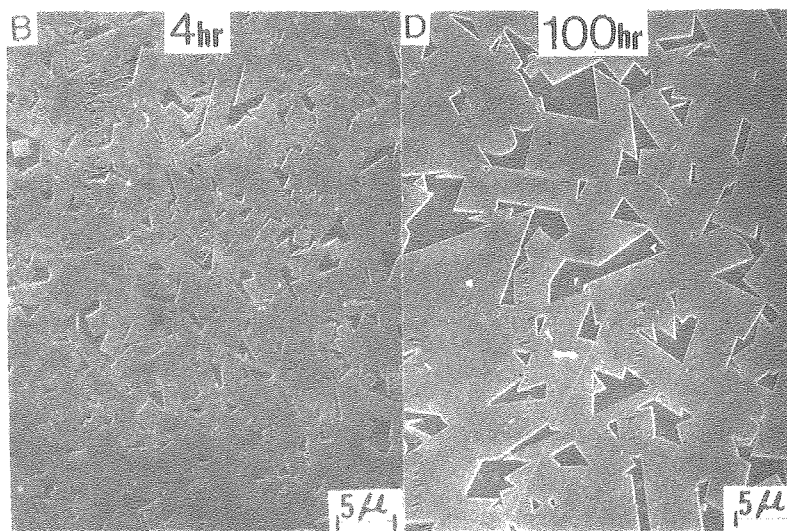
Fig. 98

COMPOSITION: 60/40

AIR

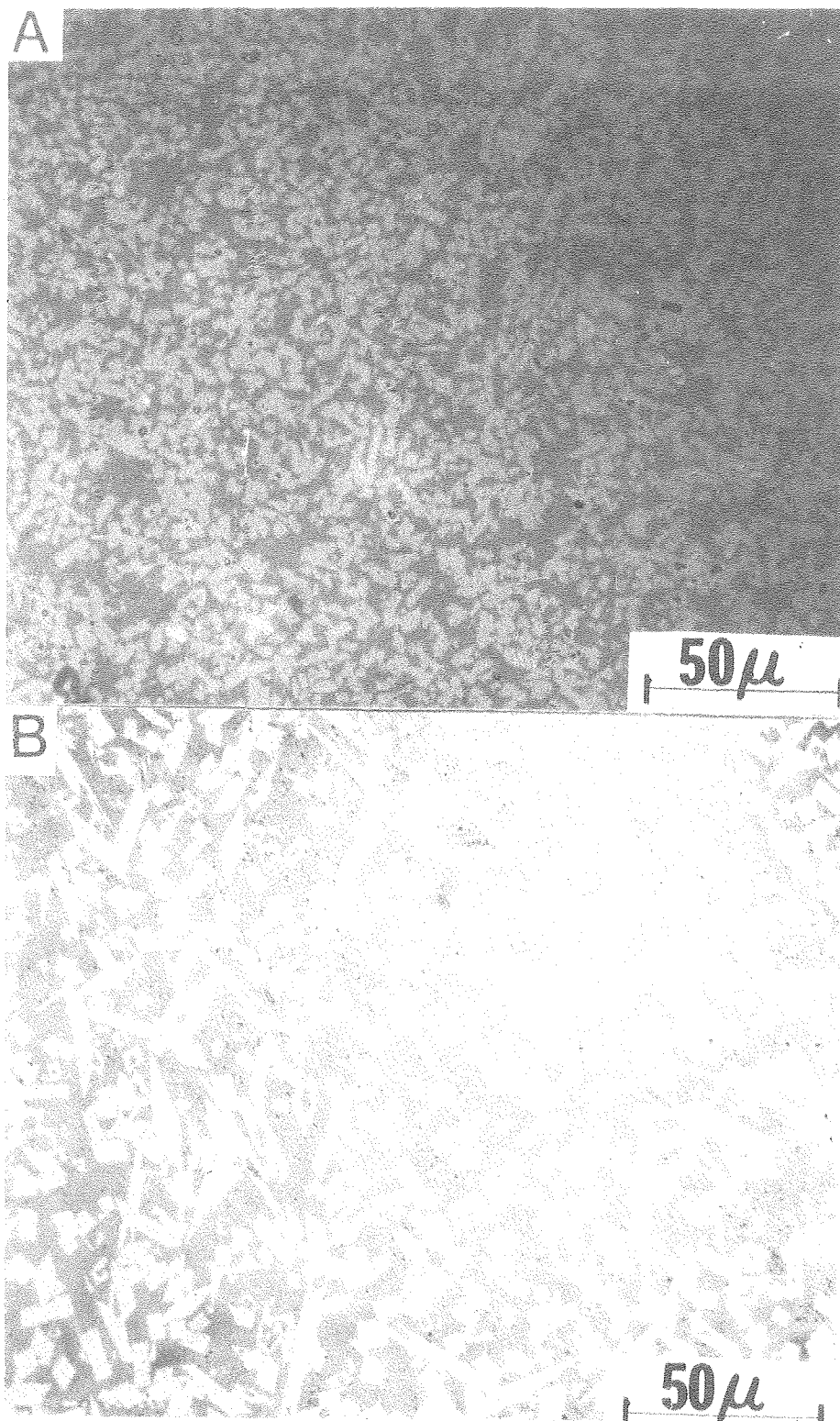


VACUUM



XBB 790-15818

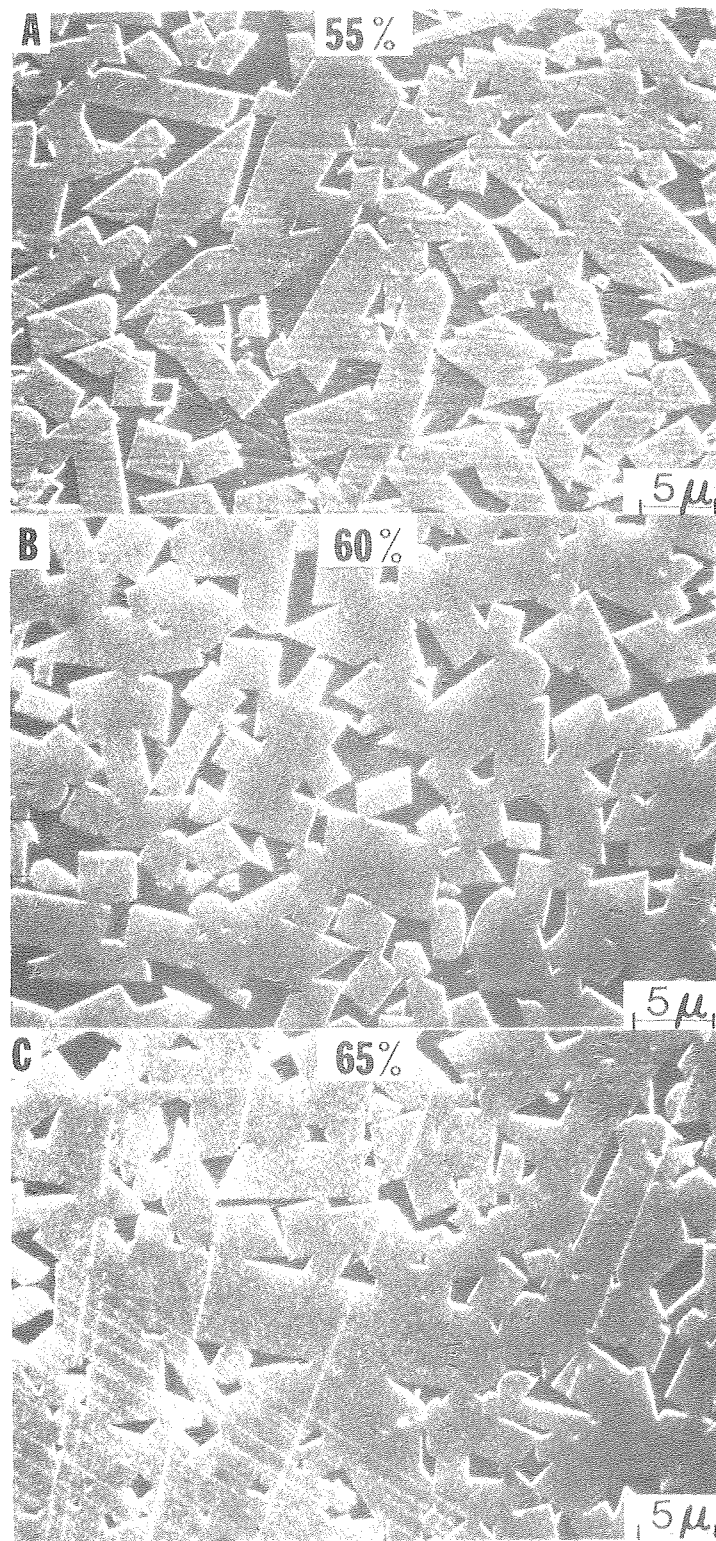
Fig. 99



XBB 790-16246

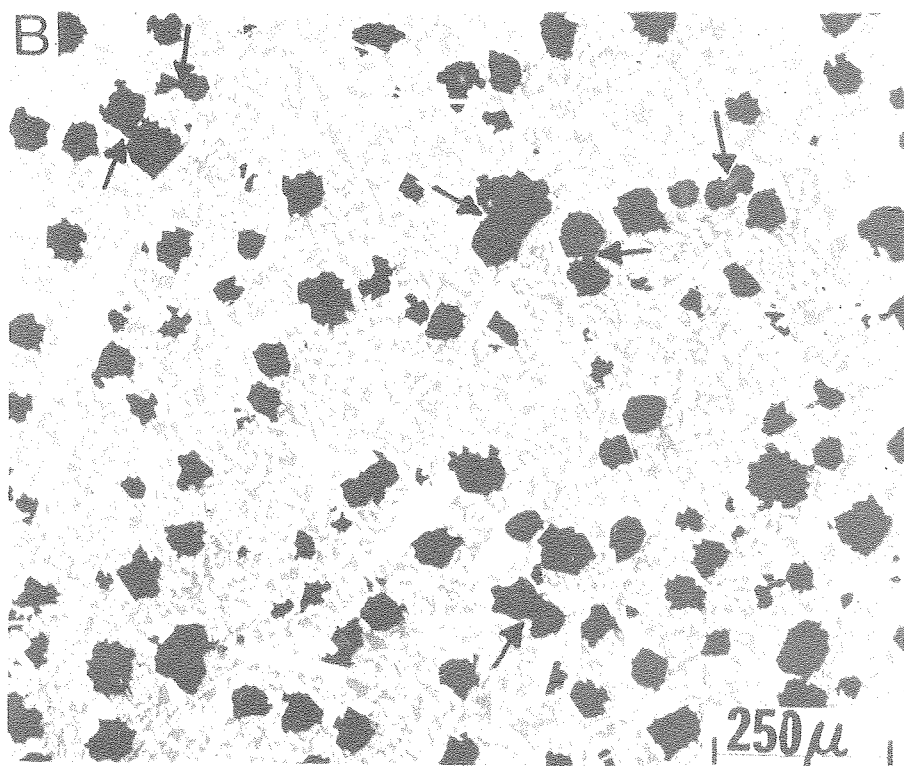
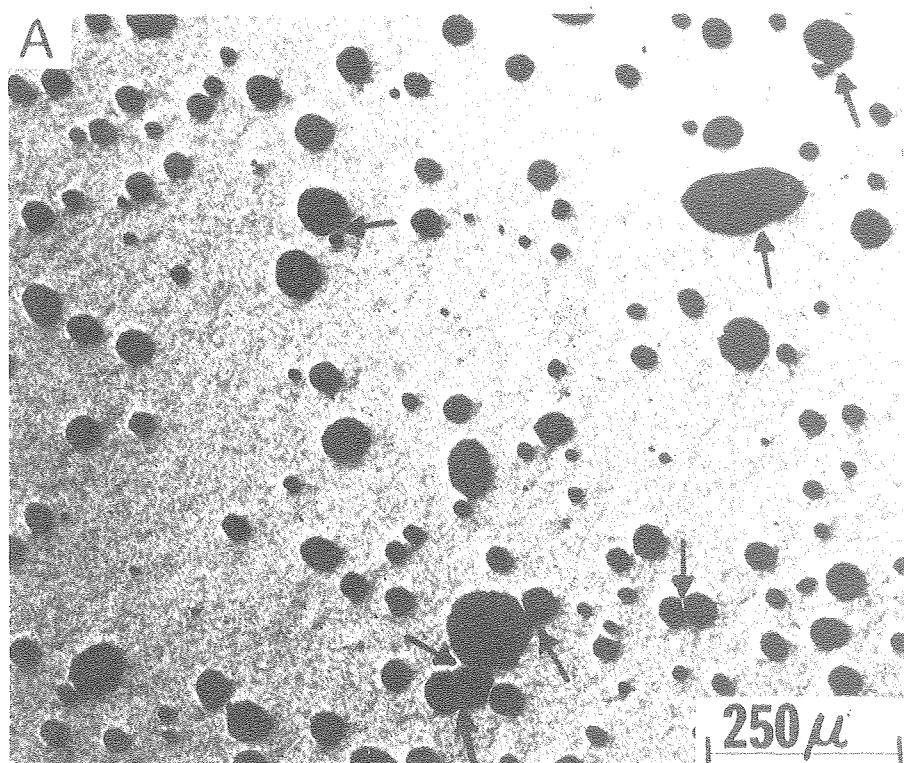
Fig. 100





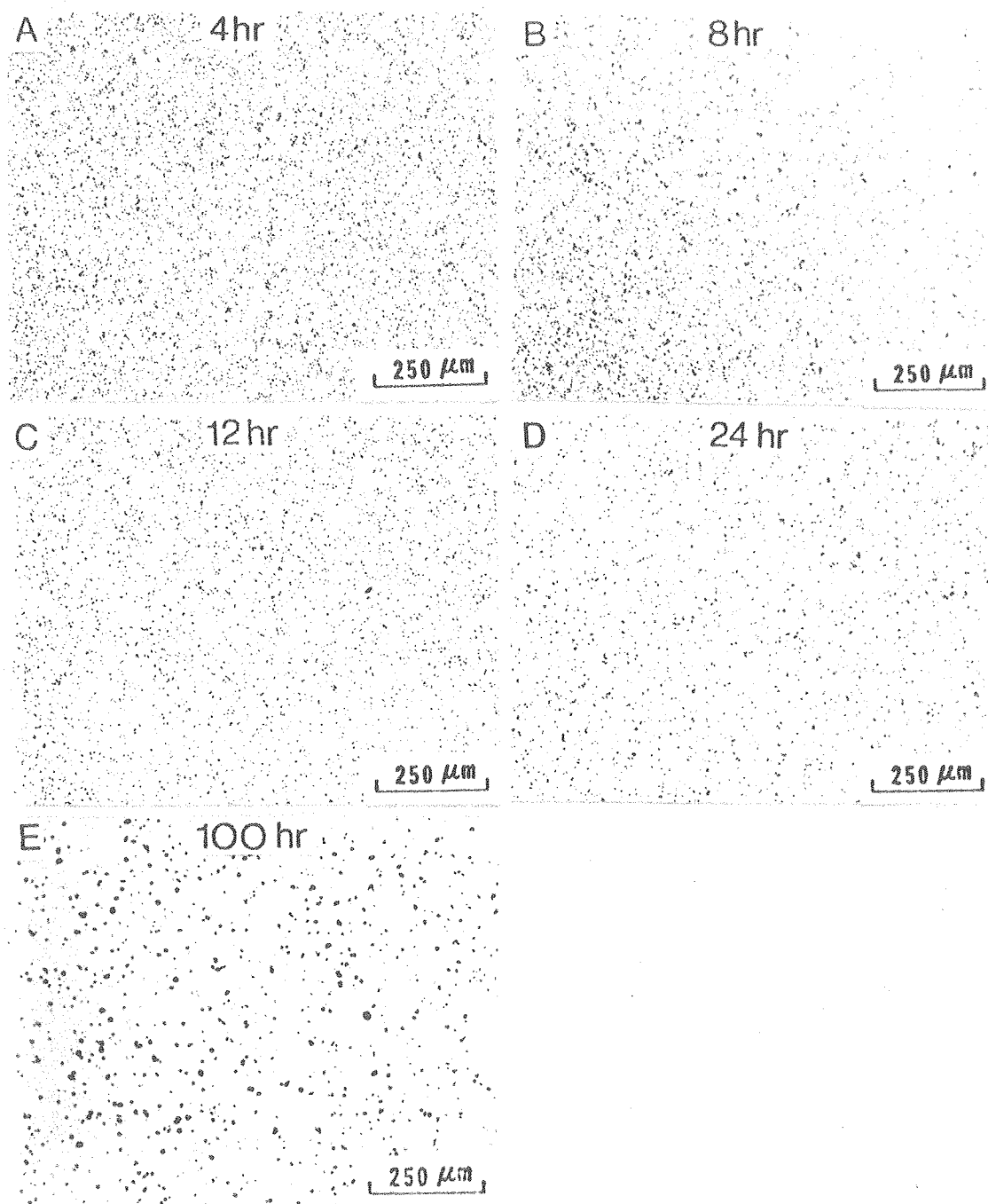
XBB 790-16635

Fig. 101



XBB 790-16245

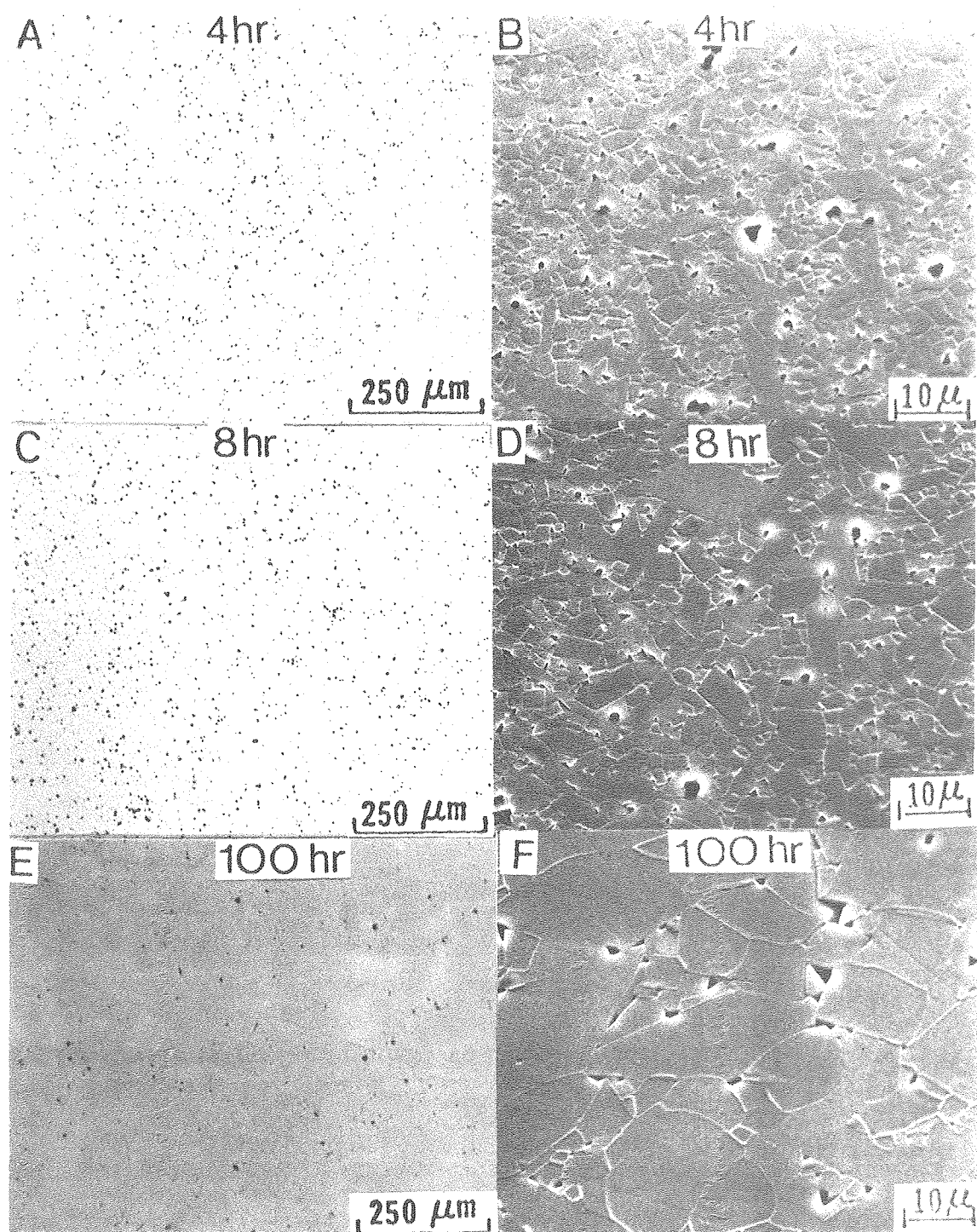
Fig. 102



XBB 760-10592

Fig. 103



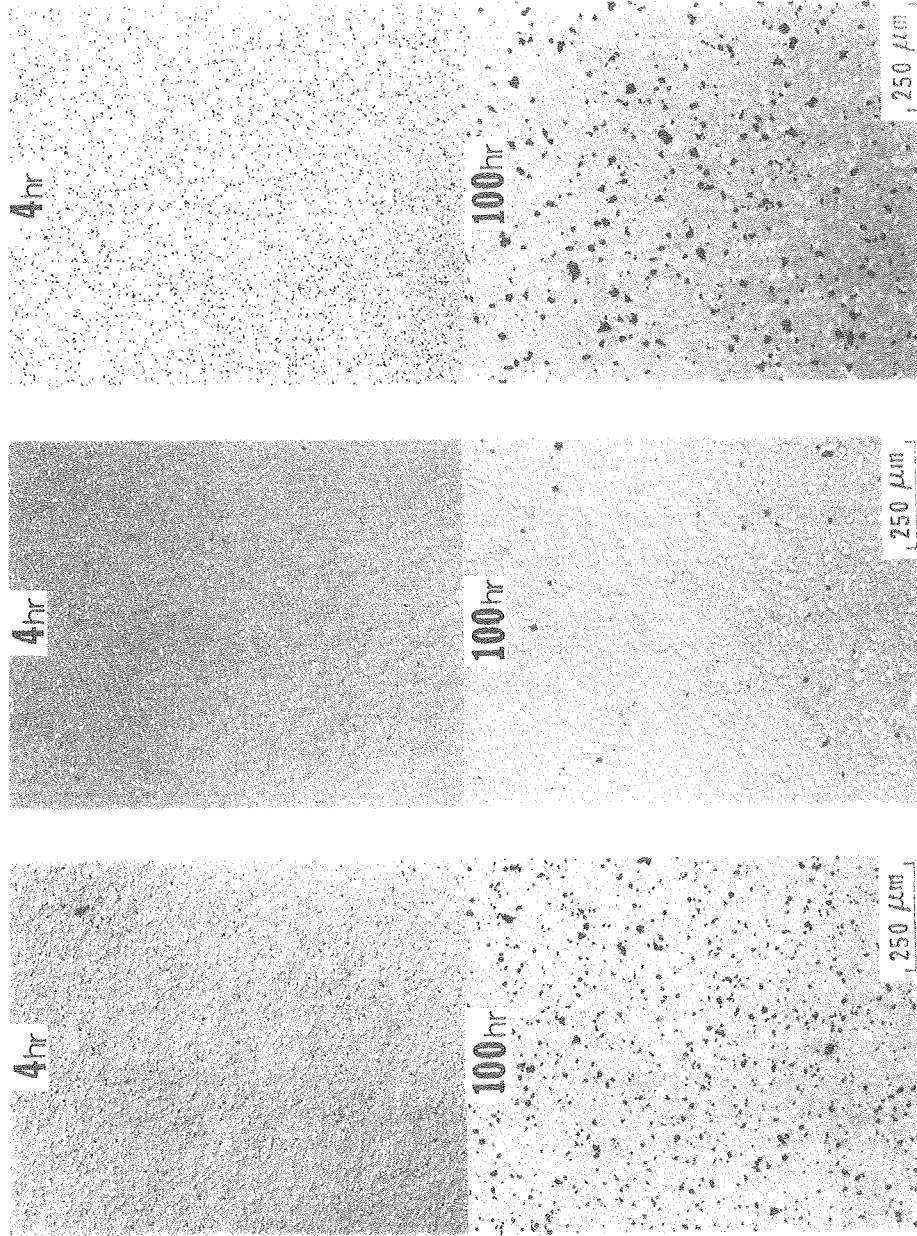


XBB 760-10581

Fig. 104

# COMPOSITION: 80/20 "GEL"

AIR                      VACUUM                      ARGON



XBB 790-15916

Fig. 105

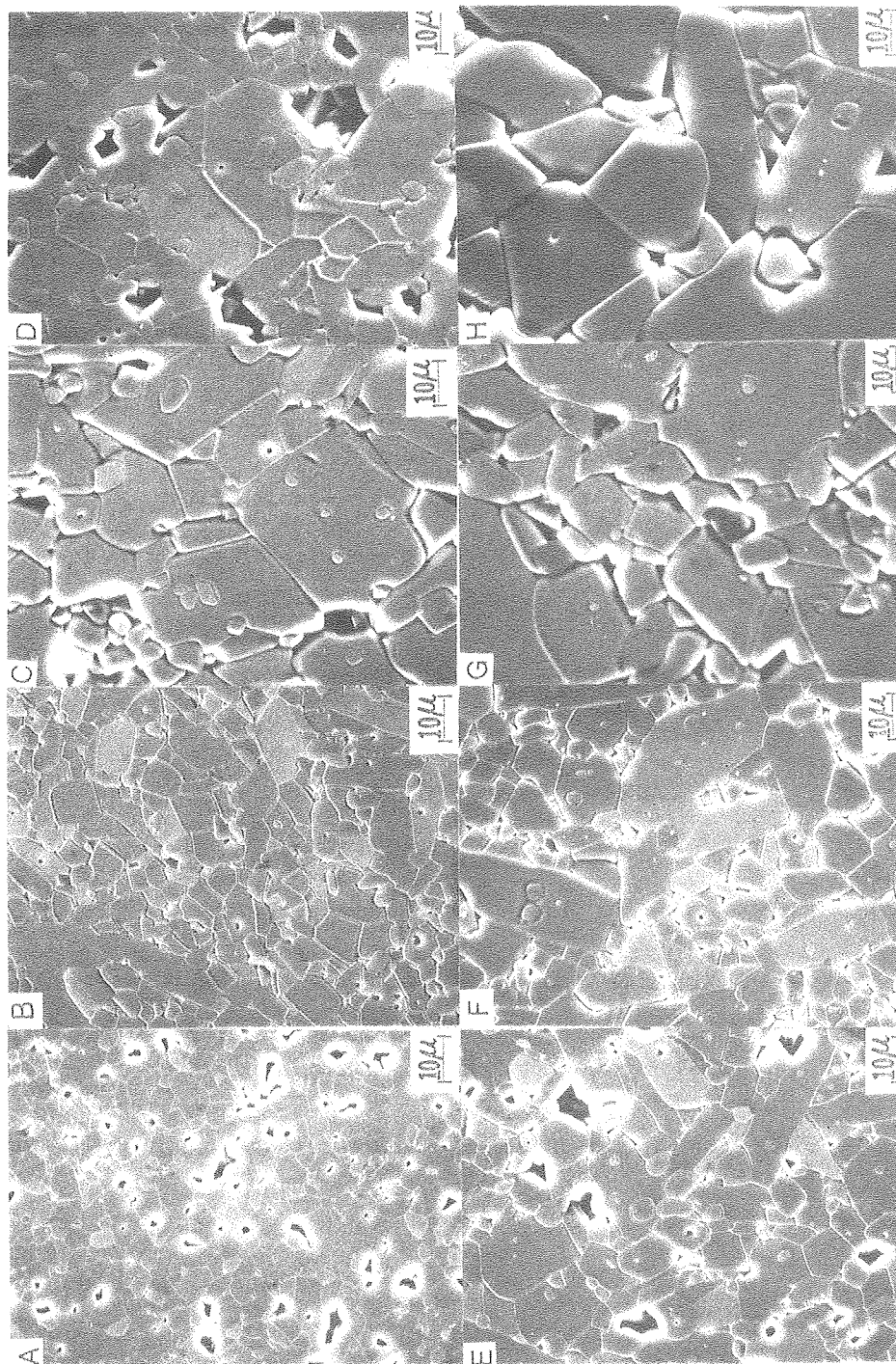
COMPOSITION: 80/20

SEALED Mo

ARGON

VACUUM

AIR



XBB 760-11026

Fig. 106

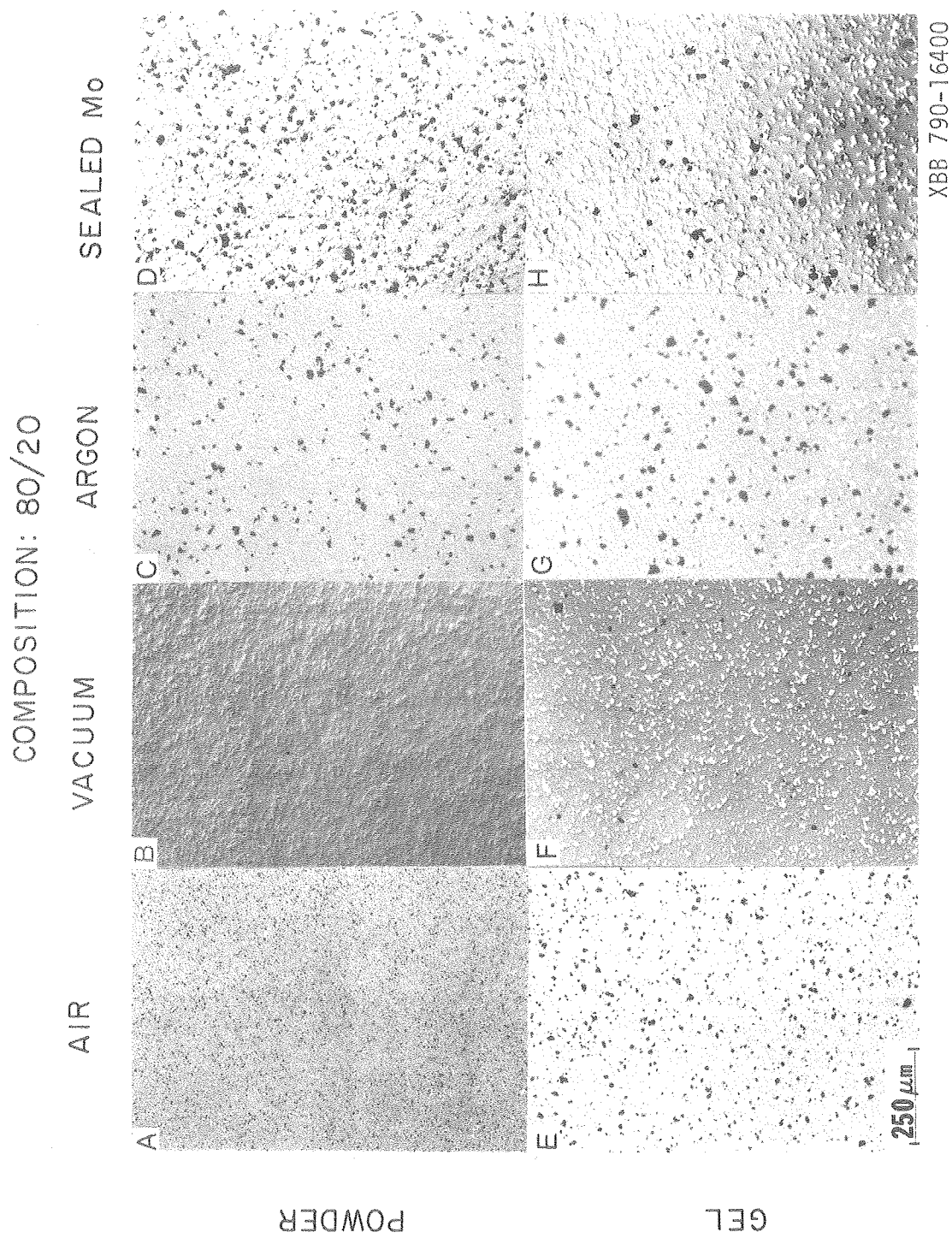
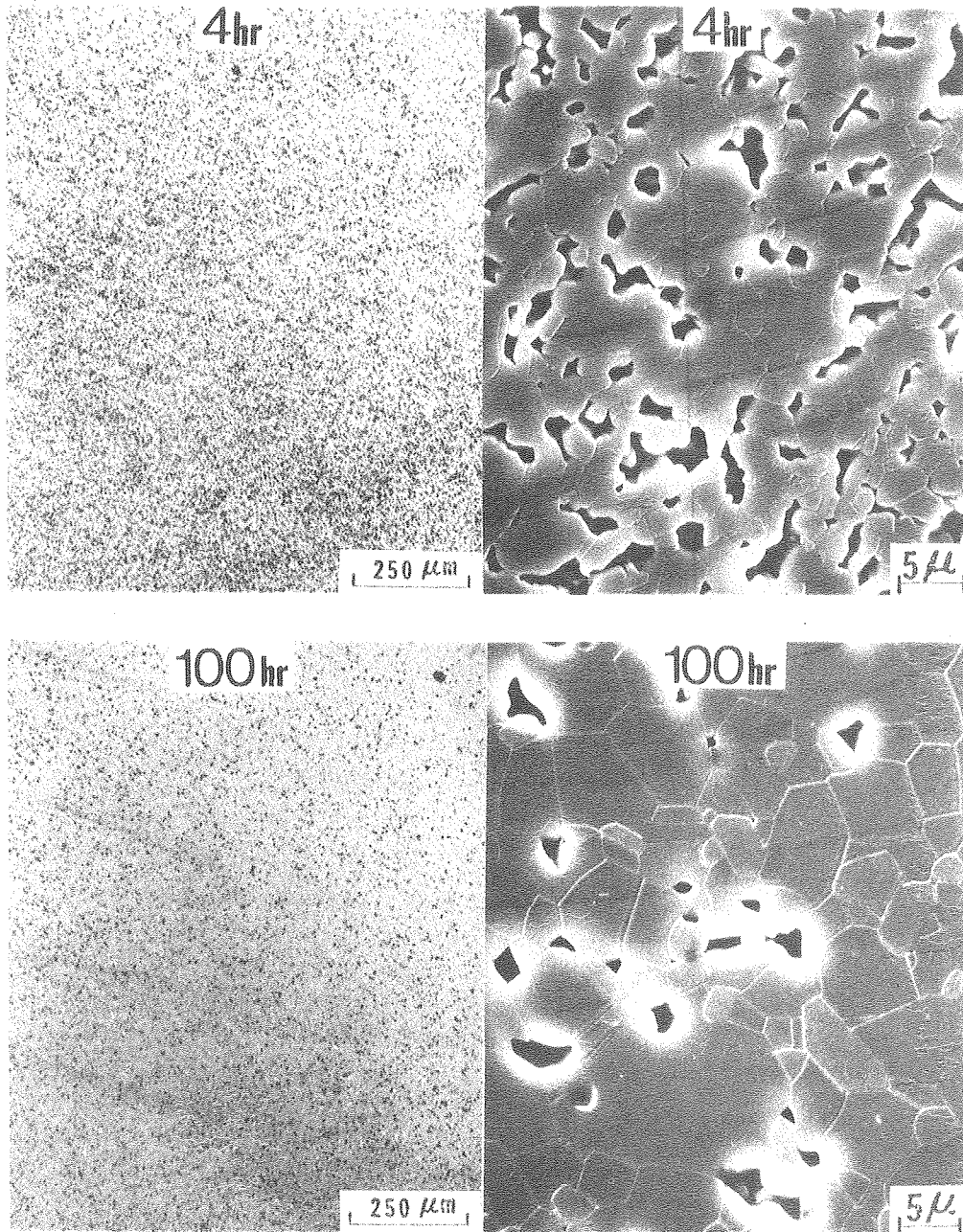


Fig. 107



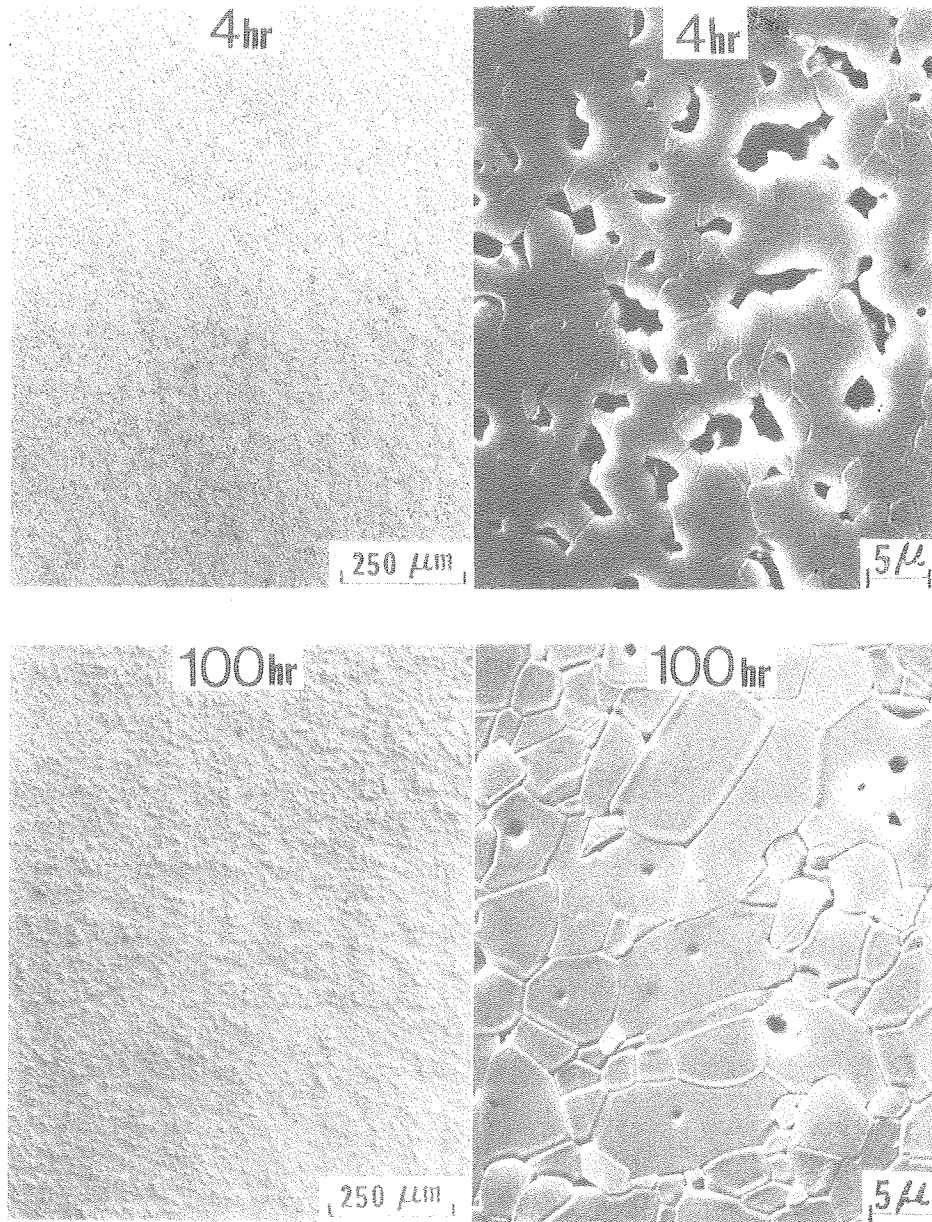
# COMPOSITION: 80 IP AIR



XBB 790-15915

Fig. 108

# COMPOSITION: 80 IP VACUUM



XBB 790-15914

Fig. 109